
Qualitative and Absolute Quantitative Studies of the Cell-Nanoparticle Interaction

Dissertation

zur Erlangung des Doktorgrades Dr. rer. nat.
eingereicht an der Johannes Gutenberg-Universität, Mainz

Anita Höcherl

geb. in Landsberg am Lech

Mainz, Februar 2012



Qualitative and Absolute Quantitative Studies of the Cell-Nanoparticle Interaction

Dissertation

zur Erlangung des Grades eines ‚Doktor rerum naturalium (Dr. rer. nat.)‘

der Fachbereiche

- 08 Physik, Mathematik und Informatik
- 09 Chemie, Pharmazie und Geowissenschaften
- 10 Biologie
- Universitätsmedizin

eingereicht in Fachbereich 09 der Johannes Gutenberg-Universität Mainz

Max Planck Graduate Center

mit der

Johannes Gutenberg-Universität, Mainz

Angefertigt am Max-Planck Institut für Polymerforschung

vorgelegt von

Anita Höcherl

Mainz, Februar 2012

Diese Arbeit wurde im Zeitraum Aug 2008 bis Februar 2012 am Max-Planck-Institut für Polymerforschung in Mainz im Arbeitskreis Physikalische Chemie der Polymere angefertigt.



Max-Planck-Institut für Polymerforschung
Max-Planck Institute for Polymer Research



Amtierender Dekan:

Gutachter

1. Gutachter:

2. Gutachter:

Datum der mündlichen Prüfung: 27.04.2012

“The role of the infinitely small in nature is infinitely large“.

Louis Pasteur

Für meine Familie

Abstract

Polymeric nanoparticles (NPs) are promising tools for biomedical applications as their selective internalization into cells gives rise to sophisticated drug-delivery applications. However the particle-cell interaction is influenced by a multitude of factors which include the particles' size, surface charge, softness, hydrophobicity or the resulting specific protein coating. Thorough studies of the particle-cell interaction are required in order to provide the detailed knowledge that is required for the design of tailored nanocarriers as drug-delivery systems.

The presented work focused on the effect of polymer properties on the interaction of polymeric NPs with an epithelial cell model system (HeLa cells). Hereby the cellular uptake of poly(methyl methacrylate) (PMMA), polystyrene (PS) and poly(L-lactide) (PLLA) nanoparticles with similar physico-chemical properties was investigated. The particles were synthesized in miniemulsion (ME) applying a radical polymerization (PS and PMMA) or a solvent-evaporation (PLLA) technique. In order to vary just one parameter, *i.e.* in this case the type of polymer, the ME synthesis was done such that size and surface charge were kept similar between all samples. The particles were characterized for their size, zeta potential, dye content, morphology and the glass transition temperature T_g . Their uptake into HeLa cells was studied in a semi-quantitative (flow cytometry) and in a qualitative (electron and confocal laser scanning microscopy) manner. It was observed that PLLA particles were taken up by the cells with high efficiency, exceeding that of PMMA and PS particles. Upon co-incubation of PS and PLLA particles with cells in a unique competitive setup, the two particle species had a mutual influence on their uptake behavior. Upon simultaneous incubation, a reduced internalization of PLLA and an increased uptake of PS particles was observed. Neither the co-incubation of PMMA and PLLA nor of PMMA and PS yielded a similar effect. It was concluded that the phenomenon could be based on the softer quality of the amorphous PLLA particles or on the presence of carboxyl groups on the surface. Likely a specific protein coating of PLLA or PS was involved, as well. Isotitration calorimetry studies revealed a strong interaction of the polylactide particles with serum proteins. Electron microscopy studies of the PS-PLLA co-incubation indicated a one-by-one internalization mechanism – the particles were predominantly located separately inside organelles. Only after long incubation times co-localization appeared, presumably due to merging of the endocytotic vesicles. It was concluded that PS and PLLA particles competed for resources during the process of internalization, and that likely a specific protein coating was involved.

Semi-quantitative studies of the cellular uptake by flow cytometry as presented above require a standardization factor f based on the fluorescence intensity of the different NP species. The factor f for semi-quantitative measurements is commonly derived from bulk measurements of

the dye content or the fluorescence intensity; these methods are not without flaws – and in any case the ultimate goal is absolute quantitation.

Therefore this work also addressed the flow cytometric measurement of single submicron NPs. Single particle measurement (SPM) offered a way to retrieve precise standardization factors f for the NP fluorescence normalization. Moreover, a method for the absolute quantitation of particles inside cells was devised based on the SPM data.

The precise fluorescence intensity of single NPs as small as 150 nm was determined with a commercially available benchtop cytometer, breaching the detection limit of the cytometer. The effects of sample properties (*e.g.* concentration or fluorescence intensity) and of instrument settings (*e.g.* threshold or laser power) on the flow cytometric measurement were evaluated. A series of fluorescent particles with high loadings of various dyes was synthesized by radical polymerization in the ME. A flow cytometric screening identified those particle samples that should be suitable for SPM *i.e.* that had sufficient signal strength. With three model particles the SPM was successful and their fluorescence was measured precisely. Furthermore the absolute NP concentration per volume was determined.

With the results from SPM a routine for rapid absolute quantitative counting of the endocytosed particles was developed and confirmed by confocal laser scanning microscopy (cLSMy). In the supplementary cLSMy experiments the particles were deliberately counted manually in cells without the application of specific quantifying software. Quantitative flow cytometry revealed that the uptake efficiency of negatively charged PMMA particles in HeLa cells is very low *i.e.* in the range of 10^{-3} % of added particles. The cLSMy data did not fully correspond to the flow cytometry results and spectroscopic analysis pointed towards residues of the serum-supplied incubation medium as the reason, due to absorption in the wavelength range of the particles' emission.

Disregarding the standard deviation, the new flow cytometry routine demonstrated the dimensions of the intracellular NP count and turned relative values into absolute values of the count of particles.

Zusammenfassung

Polymere Nanopartikel (NP) bieten besonders im medizinischen Sektor vielversprechende Ansätze für innovative Therapien. Das wird am Beispiel der Chemotherapie deutlich, wo die sog. *Nanocarrier* die hochgiftigen Chemotherapeutika vor dem Organismus verbergen und sie selektiv im Tumorgewebe anreichern könnten. Die Wechselwirkungen von Nanopartikeln mit biologischen Systemen sind jedoch komplex und Partikeleigenschaften wie Material, Größe, Ladung oder die Beschichtung mit adsorbierten Proteinen spielen dabei eine wichtige Rolle. Deshalb sind zur gezielten Synthese von Nanopartikeln detaillierte Kenntnisse über die NP-Zell-Interaktion notwendig.

Diese Arbeit beschäftigte sich vorrangig mit den Materialeigenschaften von polymeren Nanopartikeln und deren Einfluss auf die Interaktion mit humanen Epithelzellen (HeLa). Dazu wurde die zelluläre Aufnahme von NP aus Polymethylmethacrylat (PMMA), Polystyrol (PS) und Poly(L-lactid) (PLLA) verglichen. Die Synthese erfolgte über radikalische Polymerisation (PS und PMMA) bzw. über eine Lösungsmittel-Verdampfung (PLLA) in der Miniemulsion (ME). Um den direkten Einfluss des Polymers zu erforschen wurden die NP mit möglichst identischen physico-chemischen Eigenschaften hergestellt und hinsichtlich Größe, Zeta-Potential, Farbstoffgehalt, Morphologie und Glasübergangstemperatur T_g charakterisiert. Zunächst wurde die Partikelaufnahme in die HeLa-Zelllinie semi-quantitativ mittels Durchflusszytometrie (engl. *flow cytometry*, FCy) und qualitativ mittels Transmissionselektronen- (TEM) sowie konfokaler Laser-Raster-Mikroskopie (engl. *confocal laser scanning microscopy*, cLSMy) untersucht.

Dabei zeigten PLLA-Partikel eine deutlich höhere Aufnahmerate als PMMA- und PS-Partikel. Mögliche Gründe dafür könnten in der amorphen Beschaffenheit des PLLA (kein T_g messbar), der Oberflächenfunktionalisierung mittels Carboxygruppen und der daraus resultierenden spezifischen Beschichtung mit Serumproteinen liegen. Diese Hypothese wurde durch isotitrationskalorimetrische Messungen bestärkt, da PLLA-Nanopartikel im Vergleich zu PS und PMMA Partikeln eine höhere NP-Protein-Wechselwirkung zeigten.

Weiterhin wurden in einem kompetitiven Ansatz zwei Partikelsorten gleichzeitig mit Zellen inkubiert. Bei der Co-Inkubation von PLLA- und PS-Partikeln beeinflussten diese sich gegenseitig in ihrer Aufnahmerate, so dass im Vergleich zu Einzelpartikel-Experimenten PLLA-Partikel schlechter und PS-Partikel besser aufgenommen wurden. Dieser Effekt trat bei der Kombination von PMMA- mit PS- bzw. von PMMA- mit PLLA-Partikeln nicht auf. Elektronenmikroskopische Studien der Co-Inkubation von Zellen mit PS- und PLLA-Partikeln zeigten stets einzeln in Organellen lokalisierte Partikel, was auf einen Einzelpartikel-Aufnahmemechanismus hindeutete. Die Co-Lokalisation mehrerer Partikel war nur nach langer Inkubationszeit zu beobachten und war in diesen Fällen eher durch nachträgliche Fusion der Endozytose-Vesikel zu begründen. Es wurde ein Modell entwickelt

gemäß dem PS- und PLLA-Partikel um bestimmte Ressourcen konkurrieren die im Zusammenhang mit der zellulären Aufnahme stehen, wobei die Beschichtung durch spezifische Serumproteine ebenfalls eine wichtige Rolle spielt.

Solche semi-quantitativen Studien der zellulären Partikel Aufnahme mittels FCy sind nur möglich, wenn gleichzeitig ein Standardisierungsfaktor f für die verschiedenen Fluoreszenzintensitäten der getesteten Partikel gegeben ist. Dieser Faktor f für semi-quantitative Messungen wird in der Regel über *bulk*-Messungen des Farbstoffgehaltes bzw. der Fluoreszenzintensität der Partikel erhalten. Diese Messungen sind jedoch aufgrund unterschiedlicher Parameter und zusätzlicher Arbeitsschritte anfällig für Fehler. In diesem Zusammenhang wurde im zweiten Teil dieser Arbeit eine Methode zur Einzelmessung von NP im Durchflusszytometer entwickelt, die eine absolute Quantifizierung der Fluoreszenzintensität und daraus folgend der Partikelzahl pro Zelle erlaubt. Diese Einzelpartikelmessung (engl. *single particle measurement*, SPM) ergab präzise Standardisierungsfaktoren f . Dazu wurden die Messparameter so optimiert, dass es möglich war, die Fluoreszenz einzelner Partikel bis zu einem minimalen Durchmesser von 150 nm zu messen.

Basierend auf der Einzelpartikelmessung wurde die absolute Quantifizierung der NP in Zellen durchgeführt und mittels konfokaler cLSMy bestätigt. Dazu wurden die Bilddaten manuell ausgewertet und mit der Quantifizierung über FCy verglichen wobei sich ein Faktor von etwa 2 ergab. Zusammengefasst zeigte die neu entwickelte Methode zur quantitativen FCy, dass die zelluläre Aufnahme der Nanopartikel im Bereich von 10^{-3} % der eingesetzten Menge liegt. Solche Nachweise sind bisher, vor allem mit polymeren Partikeln die nicht über alternative Methoden nachweisbar sind, schwer zu führen.

TABLE OF CONTENTS

1	Introduction.....	1
2	Theoretical Background.....	5
2.1	Nanoparticle Synthesis in Miniemulsion	5
2.1.1	The Miniemulsion Technique.....	5
2.1.2	Polymeric Materials for Nanoparticles.....	7
2.1.2.1	Polystyrene.....	7
2.1.2.2	Poly(methyl methacrylate)	8
2.1.2.3	Polylactide.....	8
2.2	Cell Biology	9
2.2.1	The Cytoplasmic Membrane	9
2.2.2	Cellular Transport Processes.....	11
2.3	Effect of Particle Properties on the NP-Cell Interaction.....	13
2.4	Instruments and Methods	15
2.4.1	Dynamic Light Scattering	15
2.4.2	Zeta Potential	15
2.4.3	Transmission Electron Microscopy	16
2.4.4	Confocal Laser Scanning Microscopy	17
2.4.5	Flow Cytometry	17
2.4.5.1	Working Principle.....	18
2.4.5.2	History and State-of-the-Art.....	20
2.4.5.3	Studying the Particle-Cell Interaction.....	22
2.4.5.4	Application for Submicron Analysis	22
3	Experimental Part	25
3.1	Materials	25
3.2	Methods.....	27
3.2.1	Synthesis of Nanoparticles in Miniemulsion.....	27
3.2.2	Characterization of Nanoparticles.....	27
3.2.3	Electron Microscopy.....	28
3.2.4	Isothermal Titration Calorimetry	29
3.2.5	Cell Culture.....	29
3.2.6	Confocal Laser Scanning Microscopy	30

3.2.6.1	Qualitative Cellular Uptake Studies.....	30
3.2.6.2	Quantitative Cellular Uptake Studies	30
3.2.7	Flow Cytometry for Single Nanoparticle Detection.....	32
3.2.7.1	The Impact of Experimental Conditions and Particle Features	32
3.2.7.2	Nanoparticle Measurement in Flow Cytometry.....	32
3.2.7.3	Protocol for Particle Fluorescence Measurement	34
3.2.7.4	Protocol for Volumetric Particle Counting	34
3.2.8	Flow Cytometry for Cell Analysis	35

4 Results and Discussion.....38

4.1 Nanoparticles38

4.1.1	Synthesis of Polymeric Particles	38
4.1.2	Synthesis of Amino-Functionalized Polystyrene Particles.....	41
4.1.3	Incorporation of Fluorescent Markers with High Loading	44

4.2 The Effect of Polymer Nature on the Cellular Uptake49

4.2.1	Interaction of Polymeric Nanoparticles with Cells	49
4.2.2	Competitive Uptake after Co-Incubation of Two Particle Species ...	52

4.3 Flow Cytometry for Single Nanoparticle Detection61

4.3.1	The Impact of Experimental Settings and Sample Properties	61
4.3.1.1	Threshold, PMT Amplification and PMT Linearity	62
4.3.1.2	Laser Power.....	64
4.3.1.3	Apparent Sample Concentration	68
4.3.1.4	Particle Scattering Properties (Size and Refractive Index).....	77
4.3.1.5	Fluorescence of the Nanoparticles (Emission Spectra and Intensity)....	79
4.3.2	Screening for Suitable Fluorescent Nanoparticles	85
4.3.2.1	Blank Reference Particles	86
4.3.2.2	BODIPY Dyes	86
4.3.2.3	Perylene Monoimide Dyes	88
4.3.2.4	Various Perylene Dyes.....	90
4.3.2.5	Lumogen F Dyes	92
4.3.3	Particle Fluorescence Measurement	95
4.3.4	Volumetric Counting of Particles	99
4.3.4.1	Counting >200 nm sized Spheres.....	99
4.3.4.2	Counting 100-200 nm sized Spheres.....	100
4.3.4.3	Counting 70 nm sized Spheres	101
4.3.4.4	Particle Counting in the Presence of Serum.....	105

4.4 Absolute Quantification of Nanoparticles in Cells 109

5	Summary and Conclusions	121
6	Literature	124
7	Appendix	133
i.	List of Abbreviations	133
ii.	Supplementary Data.....	135
iii.	Acknowledgments.....	138
iv.	Statutory Declaration.....	139
v.	Curriculum Vitae	140
vi.	Publications.....	141

1 Introduction

“Friend or Foe?” This is the central question in the heated discussion about the field of nanotechnology (NT). The defenders of NT stress the progress and list the possibilities of this technology that include new durable materials and revolutionary medical treatment. But the critics will talk about ‘incalculable risks’ and ‘not foreseeable (long term) consequences’, which is reasonable. In order to join in on the debate it is necessary to know what is actually behind *nanotechnology*. The term nano, which is derived from the Greek *nános* and translates into ‘dwarf’, indicates a small size. And a *nanometer* (nm) is the defined SI unit that corresponds to 10^{-9} m. A talk by R. Feynman in 1959 marked the beginning of what is today termed nanotechnology (NT) ¹. In his famous speech Feynman established the basis and elaborated the possibilities of material modification at the scale of atoms. The term NT itself was only introduced in 1974 by Taniguchi ².

Today’s NT is a diverse field that spreads across different disciplines including chemistry, physics and biology. It is vaguely defined by one common feature: The fabrication or (surface) modification of objects on a submicron scale. In this context the expression ‘nanoparticles’ (NPs) was introduced in recent years to define objects that span less than 100 nm in at least one dimension. Due to their small size they possess a high surface-to-volume ratio. Furthermore, NPs have unique physico-chemical properties that partly result from quantum effects. The applications of NPs are numerous *e.g.* for automobile construction, in inks, as catalyst or as semi-conductor materials ³⁻⁵. Apart from these technical applications NPs are also used in cosmetics, food and medicine ⁶⁻⁷.

Probably the most discussed function of NPs in the medical sector is their application as a drug-delivery system (DDS). In a DDS the particles serve as a carrier system which not only provides protection for a sensitive therapeutic agent, but also allows aimed and efficient transport of the latter into a destined tissue or specific cell type. Most therapeutic agents and medications are sensitive compounds and need to be protected from chemical reactions (*e.g.* oxidation or hydrolysis) and from the body’s immune system (*i.e.* from macrophages) – to which they are exposed if administered orally or into the blood stream. By using natural materials or functionalizing the particle surface, the cells’ transport mechanisms could be triggered so that they efficiently and selectively internalize the nanocarrier. This would notably increase the bioavailability of the active agent. The initial dose could be lowered in comparison to the standard oral administration that is still used for most medicines. Subsequently, treatment costs and the strain for the patient, *e.g.* during chemotherapeutic therapy, could be lowered. This was the motivation behind the development of drug-delivery systems. Today numerous principles of DDS are being evaluated ⁸ such as drug-polymer conjugates ⁹, liposomes, capsules or solid NPs ¹⁰, to name a few. A number of these so-termed ‘nanopharmaceuticals’ have passed the clinical trials and are now authorized for human

use¹¹. However, until today no reliable and less-straining therapy to kill all metastasis of a cancer is available. Common chemotherapy methods may reach all metastases, but these also expose the whole organism to the therapeutics which puts great strain on the patients. Drugs targeted for the brain are another problematic issue, because the blood-brain-barrier (BBB) efficiently prevents the transport of most drugs into the central nervous system. Few nanoparticulate systems were reported to pass the BBB¹²⁻¹³.

This work contributes to the research about NPs and their interaction with cellular model systems, which is a prerequisite for the development of new nanoparticulate DDS. Three different subjects will be covered in the thesis:

1. The effect of polymer nature on the cellular uptake

The general tenor of all DDS is that the only way to load a specific tissue or cell type with the drug in a selective and efficient fashion is to exploit the body's own signaling and cell internalization mechanisms. However, such control requires a deep knowledge of the particle's route inside the body and about the final cellular uptake mechanism, termed endocytosis. This process is directed by complex interactions of NPs with plasma proteins and the extracellular matrix – and is strongly influenced by the cell type, by its physiological state and finally by the physico-chemical properties of the nanocarrier. Studies with carefully synthesized nanoparticles of defined properties could provide this knowledge. Then the nanoparticulate DDS could be customized with the required properties.

In this regard polymeric NPs have become a popular model system for DDS studies as they can be synthesized in a customized way and applied for systematic studies of the cellular uptake mechanisms. All required particle properties (charge, size, surface functionalization, softness, *etc.*) can be tuned as required during synthesis. From the literature, mainly three types of polymers such as polystyrene (PS), poly(methyl methacrylate) (PMMA) and polylactide (PLLA) have been studied in the cell experiments.

Up to now a direct comparison of these polymers regarding their endocytotic properties has not been reported. The variability in NPs and biological model systems further hinders a comparison of the published data. In this thesis different polymeric particles of PS, PMMA and PLLA with similar physico-chemical properties were synthesized and subjected to cell experiments. The HeLa cell line, derived from ovarian cancer tissue, was chosen as a model of epithelial cancer cells. Around 22000 new cases of this cancer subtype alone are expected in 2012 in the US and the mortality rate of this cancer subtype in 2012 is estimated to be 70%¹⁴. The effect of the polymer properties on the particle transport into HeLa cells should be studied by applying similar experimental conditions.

2. Flow cytometry for single nanoparticle detection

A common way to analyze the cellular uptake of NPs is to incorporate a fluorescent marker. Then a combination of flow cytometry (FCy) and confocal laser scanning microscopy (cLSMy) is applied to estimate the amount of internalized particles. The method of cLSMy is a qualitative approach that visualizes the particles and shows their location. A quantitative application of cLSMy as offered by some specific software is time consuming and prone to errors. Therefore, qualitative cLSMy is combined with FCy, a semi-quantitative method that allows the analysis of thousands of cells per s, albeit no information of the precise location of the detected NPs (adhered or internalized) is given.

But a direct correlation between intracellular NP concentration and cell fluorescence measured in a flow cytometer (FC) must not be assumed automatically when NPs of different polymeric material are compared. Emission properties of the same dye may change with the particle material, due to varied chemical labeling efficiency, quenching or spectra shift. Common bulk spectroscopic methods do not provide sufficient characterization of the 'effective' particle emission. A normalization of the particle fluorescence signal is essential in order to study the relative uptake efficiency in FCy. There are several approaches, mostly based on the particles' mean dye content¹⁵ or fluorescence intensity¹⁶. But these techniques are not flawless and errors, *e.g.* due to dye stacking¹⁷, may be introduced, as discussed above. A normalization that neither depends on the incorporated dye (type, amount or stacking) nor on the particle material would be favorable – the more because new dyes and particle materials are being introduced daily. This could be provided by the measurement of single nanoparticles in an FC.

In this thesis the measurement of submicron particles should be established in the same cytometer that would also be used for the cell studies. NP detection in a flow cytometer that was built for detection of micron-sized cells is a tedious task and rarely approached¹⁸. But the reward would be the best possible normalization factor in comparative particle uptake studies. Single particle measurement (SPM) in the flow cytometer would enable to separately measure the mean fluorescence intensity (MFI) of hundreds of single NPs per s.

3. Absolute quantification of nanoparticles in cells

Establishing the measurement of submicron particles in FCy would offer yet more possibilities. Such a method would enable an absolute quantification *i.e.* a count of the internalized particles per cell. Polymeric NPs are commonly tagged with a fluorescent marker and the tunable sensitivity of FCy enables the detection of small up to very large particle doses¹⁹ – but polymer NPs cannot really be quantified, unlike *e.g.* metal spheres²⁰. In the presented new quantification approach by FCy, the difference in MFI *i.e.* the fluorescence signal of particle-loaded and particle-free cells could easily be measured. A calculation of this value with the average MFI of a single NP would then yield the precise number of

internalized particles. In parallel, reference data would be provided in the form of a quantitative particle counting in cLSMy. The analysis should deliberately be done ‘by hand’ *i.e.* by simple counting without the application of automated quantifying software – to have a direct look into the system contrary to the more abstract FCy data.

Once established this new method in flow cytometry can be used for studying relevant questions in nanotechnology, because the semi-quantitative and the absolute quantitative measurement of the nanoparticle internalization into cells is often difficult.

2 Theoretical Background

2.1 Nanoparticle Synthesis in Miniemulsion

2.1.1 The Miniemulsion Technique

This method has become a popular route of nanoparticle synthesis for several reasons. The miniemulsion (ME) provides a system of autonomic reaction spaces inside the droplets, often termed *nanoreactors*, that can be exploited for sensible chemical reactions²¹. The high surface-to-volume ratio gives rise to effective chemical processing along the interface of droplet and dispersed phase²², moreover the synthesis can be done up to a high solid weight content²³. Furthermore the ME is a platform to obtain many different polymeric nanoparticles and -capsules, because a variety of reaction types can be performed (*e.g.* polyaddition, polycondensation, enzymatic or the widely used radical polymerization)²⁴⁻²⁷. Finally the ME allows precise tuning of the particle properties. These include size, charge, size distribution, markers, hydrophobicity, and surface functionalization. Detailed reviews on the possibilities and applications of the miniemulsion technique are available²⁸⁻³⁰. The small size and the high surface-to-volume ratio provide the final nanoparticles with unique properties. Hence, the technical and (bio) medical applications are numerous^{5, 31}.

A system of at least two immiscible liquids is termed emulsion when the phases are dispersed to the point that a phase separation cannot be observed by eye. Hereby an amphiphilic molecule, the emulsifier, reduces the interfacial tension. The phase which forms the larger volume fraction is termed 'continuous' and the other, finely distributed phase is termed 'disperse'. If the continuous phase is aqueous with an organic phase distributed in it, the emulsion can further be specified as oil-in-water (o/w) or as direct. Accordingly, the emulsion is termed water-in-oil (w/o) or inverse if the continuous phase is organic. Another way to classify different types of emulsions is by characteristic properties and droplet size. In particular, a miniemulsion is defined by a droplet size of 50-500 nm and by a kinetic stabilization. A fine dispersion of the discontinuous phase is required to obtain the small droplet size of a ME, resulting in a sharp increase in surface area – which in turn requires a high energy input. This is circumvented by lowering the system's free energy (Gibbs energy) through a decrease of the interfacial tension between the two phases. For this purpose a surfactant (surface active agent) is added. The amount should not exceed the detergent's critical micelle concentration (CMC). But apart from the properties of the surfactant there are additional key points, such as temperature, polarity, and viscosity of the two phases. Being a kinetically stabilized system, the ME will not come into existence spontaneously, but only when an appropriate amount of energy is provided. Mixing the two phases on the plate stirrer creates a temporarily stable macroemulsion which must be subjected to sonication to create a stable miniemulsion with homogeneous droplet size. During sonication high shear forces and local variations in pressure, due to the rise and implosion of cavitations, create the

miniemulsion. The process of NP formation in the o/w-mini-emulsion is demonstrated in Figure 1. Hereby, the starting material for the particles, which can be a monomer or a pre-formed dissolved polymer, is contained in the droplets of the dispersed phase. These droplets are turned into NPs by polymerization or by solvent evaporation³².

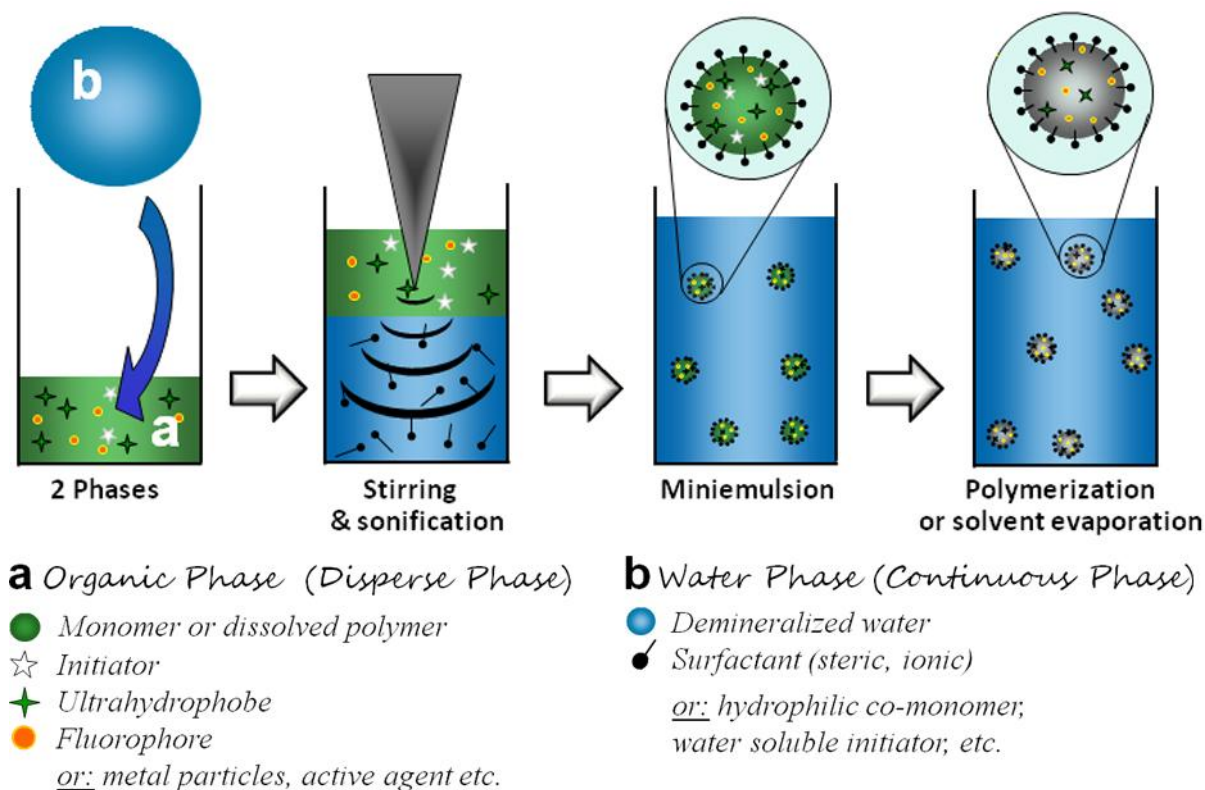


Figure 1. Synthesis of nanoparticles in the o/w-mini-emulsion process.

The solvent evaporation technique is an approach where pre-formed polymer is dissolved in the dispersed phase³³⁻³⁵. The solvent in the droplets is evaporated and the polymer precipitates inside the tenside-stabilized droplets, eventually forming solid nanoparticles.

After creating the ME during sonication, other factors are needed to keep the emulsion stable and preserve the droplet size. Destabilizing mechanisms such as Ostwald ripening (as the size distribution is never perfectly homogeneous) and coalescence need to be suppressed, see Figure 2. By adding an ultrahydrophobe like hexadecane to the dispersed phase, the Ostwald ripening (bigger droplets enlarge at the expense of smaller ones) is prevented. In smaller droplets, the Laplace pressure is comparably higher than in larger droplets, as expressed in the proportionality of the Laplace pressure p_L to the interfacial tension γ and the reciprocal of the droplet radius r . Considering a certain solubility of the monomer in the continuous phase, p_L enforces monomer diffusion from smaller into larger droplets.

$$p_L = \frac{2\gamma}{r} \quad \text{Laplace pressure (I)}$$

As a consequence of possible monomer diffusion, the non-diffusible ultrahydrophobe would be concentrated in the smaller droplet building up an osmotic pressure Π contrary to p_L :

$$\Pi = \frac{c \cdot R \cdot T}{M} = c_{mol} \cdot R \cdot T \quad \text{Osmotic pressure (II)}$$

c and M correspond to concentration [$\text{g}\cdot\text{l}^{-1}$] and molar mass [$\text{g}\cdot\text{mol}^{-1}$] of the osmotic active substance. The ratio $\frac{c}{M}$ displays the molar concentration c_{mol} [$\text{mol}\cdot\text{l}^{-1}$], R the gas constant [$\text{J}\cdot\text{mol}^{-1}\cdot\text{K}^{-1}$] and T the temperature [K].

Ionic or sterically demanding surfactants create a charge repulsion or steric hindrance of the droplets. With the droplet collision prevented, thermodynamically favored coalescence *i.e.* droplet fusion will not occur. In a similar manner the particle dispersion is stabilized.

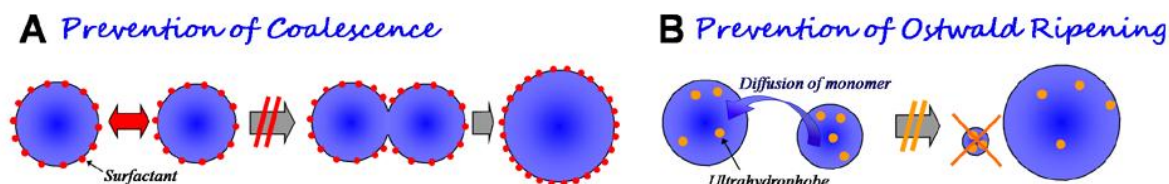


Figure 2. Stabilization of the miniemulsion by prevention of coalescence and Ostwald ripening.

2.1.2 Polymeric Materials for Nanoparticles

The three polymeric materials that were the main focus in the cellular uptake studies of this thesis (see *Figure 3*) are presented in this chapter.

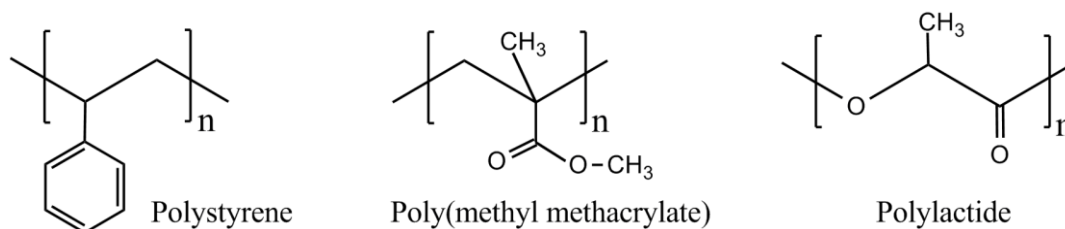


Figure 3. Structural formula of polystyrene, poly(methyl methacrylate) and polylactide.

2.1.2.1 Polystyrene

Radical polymerization of the C=C double bond in vinyl benzene, also termed styrene, yields polystyrene (PS). The T_g is in the range of 100 - 110 °C³⁶. With aromatic rings protruding from the backbone, this polymer is highly hydrophobic and susceptible only to apolar solvents. PS is a hard and brittle plastic and it is one of the most important industrial polymers. Massive plastic objects are produced as well as foamed materials such as *e.g.* Styropor® (BASF). PS furthermore has become the material of choice for commercially available calibration beads and model nanoparticles (NPs). This is one reason why the material is also of high interest for scientists studying the particle-cell interaction. In this field,

microspheres or nanoparticles of PS have emerged as a popular reference model³⁷. The fact that spheres of PS are biologically inert, long-lasting and good to handle adds to the popularity of the system for cell experiments³⁸⁻⁴⁰.

2.1.2.2 Poly(methyl methacrylate)

The polymer poly(methyl methacrylate), abbreviated as PMMA, is mainly synthesized by radical polymerization. It is a hydrophobic material (yet less hydrophobic than polystyrene) with a T_g of about 110 °C. Methyl methacrylate is mostly polymerized in emulsion to obtain components of enamels, glues, or molding compounds for a variety of plastic articles (*e.g.* Plexiglas[®], eyeglasses, car components *etc.*). But of particular relevance in this context is the polymer's biocompatibility, another reason for its application in cosmetic and reconstruction surgery⁴¹ or *e.g.* contact lenses. Reports about cell toxicity^{38, 42-43} are often traced down to other effects (such as residues of methacrylic monomer due to insufficient washing) and not deemed a property of the polymer itself⁴⁴. On the whole PMMA is an inert and non-toxic polymer. It does not have the status of a reference system like does PS, but it offers similar advantages. PMMA (coated) particles of up to 500 nm diameter are widely applied in studies of the particle-cell interaction and in drug-delivery development⁴⁵⁻⁴⁹.

2.1.2.3 Polylactide

The polyester of lactic (or: milk) acid is termed polylactide PLA and is usually retrieved by anionic ring opening polymerization of the dimer lactide. The polymer has a rather low T_g of 50 °C and a melting point T_{melt} of 150 °C. Since the mid nineties PLA has been utilized in the medical sector for tissue implantations and side effects, *e.g.* long-term tissue response, may occur but do not outweigh the benefits⁵⁰⁻⁵¹. In this study PLLA, the L enantiomer form of the polymer, was used. PLA ester bonds are susceptible to hydrolysis especially in acid media. This is why polylactide NPs can be degraded when internalized in cells and transported into low-pH organelles such as the multivesicular bodies or the lysosome. As a general rule PLA is fully biodegradable under physiological conditions. But the degradation time depends on the objects' size and on factors like molecular weight, crystallinity, pH, temperature *etc.*, which is why degradation can last several weeks (microspheres) up to several years (*e.g.* large implants)⁵²⁻⁵⁴. PLA in biomedical applications has the great advantage of a non-toxic degradation product, lactic acid, which is easily disposed of by the body. The latter is part of the energy metabolism of erythrocytes and of low-oxygen muscle tissue (anaerobic glycolysis). Its oxidation product pyruvate can undergo gluconeogenesis or enter the citrate cycle and be disposed. The biodegradability makes PLA an excellent choice for sophisticated implantations and drug-delivery systems as there is no long-term accumulation in the organism. The degradation also provides a mean for over-time release of incorporated active agents. Consequently, a lot of research is being done about the interaction of PLA and PLGA (copolymer with glycolic acid) particles with biological systems^{52, 55-61}.

2.2 Cell Biology

2.2.1 The Cytoplasm Membrane

Most of the basic knowledge in this and the following subchapters is the shared content of several educational books in the field. Therefore all presented facts, if not cited otherwise, can be looked up elsewhere⁶²⁻⁶⁴. Cells are the complex microscopic modules of nature for building macroscopic organisms like *e.g.* a human. Each cell has its defined properties and a function which it executes rather independently. But at the same time all cells need to be coordinated and in constant contact with the rest of the organism. This is ensured by a phospholipid double-layer termed cytoplasm membrane (CM) which defines the border of each cell. Amphiphilic phospholipids form an approx. 6 nm thick double layer with a broad lipophilic core, shielded by a hydrophilic surface. Considering that along this short distance of ~6 nm a membrane potential of -60 to -90 mV is applied, the CM must be recognized as location of high electrical field strength. But as much as the cytoplasm membrane is a passive barrier, it is also an active platform of transportation and of communication. To meet these requirements, the CM contains also cholesterol (regulates membrane fluidity), lipids (*e.g.* for pathway signaling and cell-cell recognition) and a variety of proteins (ion channels, transporters, receptors, signal transducers *etc.*) often coupled with sugars. Proteins embedded in the bilayer are termed transmembrane (integral), in contrary to those merely associated with it (peripheral). Membrane domains of specific composition like lipid rafts (LRs) diffuse freely and form dynamic clusters⁶⁵. Attached to the CM is the extracellular matrix (ECM), a 3D network containing hyaluronic acid, proteoglycans and collagen fibers. On the cytoplasmic side, the CM is covalently bound to the cytoskeleton (CT). A typical lipid bilayer membrane is displayed below (see *Figure 4*).

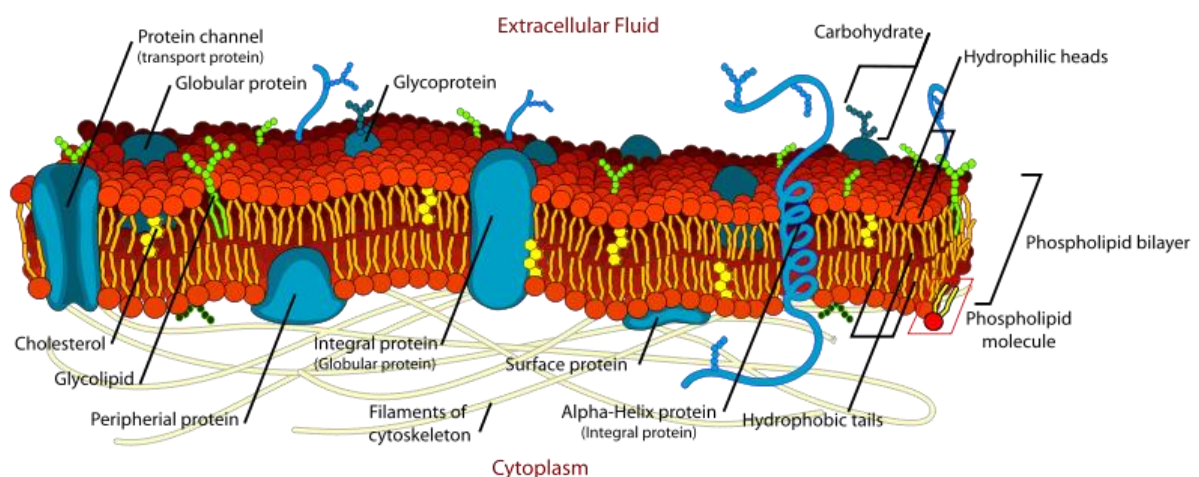


Figure 4. Structure of the eukaryote cytoplasm membrane.

by LadyofHats [Public Domain], via Wikimedia Commons, accessed: feb2012

http://commons.wikimedia.org/wiki/File:Cell_membrane_detailed_diagram_en.svg

The cytoskeleton filaments are the supporting structures of the cell but they are also highly dynamic systems, in a state of constant assembly and disassembly. They are the driving force in cell motility and dynamic membrane expansions like microvilli or pinocytotic fingers. Actin fibers provide mechanical support but were also found to be involved in intracellular vesicle transport⁶⁶. Tubulin, next to its mechanical stabilization function, plays a prominent role in intracellular trafficking as it provides a transportation axis. Motor proteins link to cargo-filled vesicles and transport them by moving along on the cytoskeleton strands⁶⁷⁻⁶⁸.

The CM is highly selectively permeable to maintain vital properties of the cell. Due to the lipophilic nature of the membrane's core, only nonpolar compounds (*e.g.* steroid hormones) or very small molecules (*e.g.* carbon dioxide) can passively diffuse through it. Anything else (including ions, proteins, fatty acids, sugars or amino acids) can only enter or exit a cell through specialized transporters or tunnel proteins. But as the size of nanoparticles greatly exceeds that of a single molecule, NPs require yet alternative transport mechanisms – processes suitable for larger cargo. This form of cellular uptake, termed endocytosis, requires the internalization of membrane surface and is described in detail in the following chapter. Furthermore it is important to note that the CM is a highly flexible and dynamic system, because the lipid bilayer is held together by non-covalent interactions. These bilayered membranes spontaneously form or merge (self-assembly) and are therefore considered a self-healing system. The membranes' capability to fuse is the base of any cellular transport involving lipid vesicles as transport containers. Transmembrane proteins and domains (assemblies of specific lipids or receptor proteins) float freely in x-y direction. The CM is seen as a viscous liquid in which the phospholipids laterally diffuse with up to $2 \mu\text{m}\cdot\text{s}^{-1}$ velocity. These features are described in the fluid mosaic model presented by Singer and Nicolson in 1972⁶⁹. In contrary, transversal diffusion, *i.e.* an exchange of molecules between the two layers, does not take place spontaneously. It is a rare process and mostly under control of specific enzymes. This ensures another vital property of biological membranes – their asymmetry.

Summed up, the cytoplasmic membrane is a highly dynamic environment, with protruding proteins and carbohydrate chains diffusing freely in what appears as a viscous sea of phosphate head groups. Above, the hydrophilic 3D network of the extracellular matrix is situated. A multitude of independent processes (transport, enzyme activity, signaling *etc.*) takes place simultaneously. Finally the cell's CM is not a plain surface wrapped around the cell. The CM undergoes constant ruffling and protrusions are stretched out and retracted.

2.2.2 Cellular Transport Processes

As stated above, membrane-bound molecules (*e.g.* receptors) and larger cargo are not transported inside by carrier or tunnel proteins. Therefore additional ways of internalization are available to the cell and these mechanisms are summed up as endocytosis. Accordingly, similar processes in outward direction are termed exocytosis. Endocytosis by definition includes the internalization of a fraction of membrane and is an energy-dependent process⁷⁰. Any of these mechanisms require excessive bending of the involved membranes, which stresses the importance of membrane flexibility. Some endocytotic pathways start by a CM invagination (pit) followed by the budding of an intracellular transport vesicle which contains the cargo. In reference to the involved structures a distinction is drawn between clathrin- (CLA) and lipid-raft-dependent (LR) uptake⁷¹. Several LR-driven mechanisms, *e.g.* the caveolae-dependent (CAV) route, are known. Other pathways independent of clathrin and of lipid rafts supposedly exist, but little is known yet. Macropinocytosis and macropinocytosis operate on a different principle. Extensions of the CM are formed and enclose a femtoliter-sized volume (which can be liquid or a solid object). The different pathways are displayed schematically in *Figure 5* and detailed information about the various mechanisms is provided below. Once internalized the particles enter a very complex yet organized liquid filled space termed cytoplasm (CP). But unlike depicted in this scheme, a cell's inner is tightly packed with organelles and various structures.

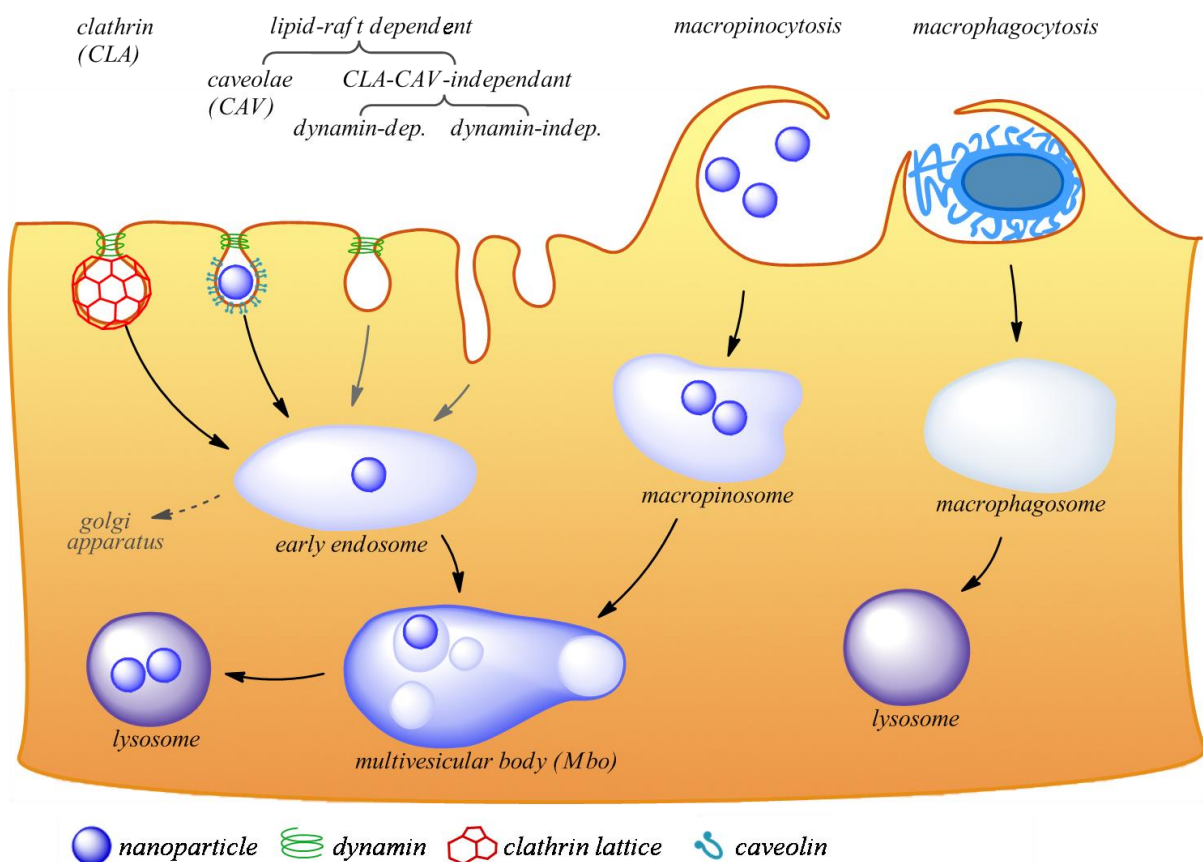


Figure 5. The major endocytotic and intracellular transport paths.

The **clathrin**-dependent uptake certainly is the best studied of all the endocytosis pathways and detailed information is available ⁷². The budding vesicle on the cytoplasmic side is stabilized by a curved lattice made of clathrin trimers (triskelions). The lattice forms around the budding vesicle and envelopes it with a spherical shell, the ‘clathrin basket’. An elongating helix is formed around the vesicle’s neck by the GTPase dynamin which finally pinches the vesicle off the CM. The newly formed clathrin coated vesicle (CCV) sheds off the clathrin coat and undergoes cell trafficking. CLA uptake is the major mechanism of receptor mediated endocytosis and is responsible for the internalization of *e.g.* transferrin ⁷³ and epidermal growth factors ⁷⁴. The dynamics of receptor mediated endocytosis are also influenced by features of the triggering receptors and of the cargo ⁷⁵. As the clathrin baskets cannot exceed a diameter of approx. 130 nm, this pathway is restricted to cargo sized <130 nm. Dynamic domains on the cytoplasmic membrane with high density of cholesterol and sphingolipids are termed **lipid rafts** (LR) ⁶⁵. These dynamic assemblies also maintain a high receptor protein density and today are known as major spots of cell trafficking and signal transduction ⁷⁶.

LRs diffuse freely in the CM and form dynamic assemblies of several hundred nm diameter, making precise size measurements a hard task. Sizes ranging from tens of nm up to a micrometer scale have been reported for lipid rafts ⁷⁷. In late studies the core region is assumed to be as small as 10 nm but these units can form dynamic clusters of larger size ⁷⁸. **Caveolae** are membrane indentions, derived from lipid raft clusters which have recruited an additional protein (caveolin). But no clathrin coat forms around the budding vesicle. In contrary to the clathrin-dependent uptake, no coating structures are involved in the caveolae-dependent pathway. Similar to the clathrin-coated pits the vesicle budding is promoted by dynamin. Caveolae buds are restricted to a diameter of 50-80 nm ⁷⁹. Endocytosis by **macropinocytosis** and **macrophagocytosis** follows yet another principle. Extensions of the CM are formed and put over, enclosing either a volume of surrounding liquid (pinocytosis, also termed ‘cell drinking’) or an object (phagocytosis) ^{71-72, 79}. This mechanism allows the internalization of μm -sized objects. Apart from phagocytosis all the presented internalization pathways are omnipresent *i.e.* available to every type of cells. Of course, some mechanisms are more present in one or another cell line and the status of the used model system is described in detail in the following chapter.

2.3 Effect of Particle Properties on the NP-Cell Interaction

Considering the complexity of the cell membrane and of the endocytotic processes, it is unlikely that the internalization of nanoparticles is completely random. But if there is a scheme, *i.e.* if NPs specifically trigger their internalization by one or another pathway, this can only be explained with characteristic properties of the particles. Indeed, today numerous facts are known to influence the cellular uptake.

A list of particle properties that affect the cellular uptake is given below:

- Size (approx. below 50 nm, 200 nm or 1 μm)
 - Shape (spherical or elongated)
 - Surface properties
 - Hydrophilic or hydrophobic
 - Neutral or charged (positively or negatively)
 - Blank or functionalized (*e.g.* $-\text{NH}_2$ or $-\text{COOH}$)
 - Smooth or uneven (hairy layer)
 - Mechanical property (soft or hard)
 - *Etc.*
- } *Resulting 2° property:*
- Protein coat

SIZE With regard to the different dimensions of endocytotic structures it becomes obvious that the particle's **diameter** must be a major factor in particle-cell interaction. Macropinocytosis may be compatible with small and large particles alike. But the mere size of an *e.g.* >200 nm particle will rule out the clathrin- as well as the caveolae-dependent uptake. As a general rule, the particle's size is in reverse proportion to its uptake efficiency. Most cells prefer 0.1 μm to 1-10 μm sized particles⁸⁰⁻⁸¹, which comes as no surprise. But also within the submicron range there is still a preference – of small (20 nm) NPs towards slightly larger (200 nm) ones⁴⁰. Even if the particles target the same uptake mechanism, *e.g.* if a transferrin-functionalization triggers clathrin-dependent uptake, the particle size still takes effect on endocytosis and exocytosis⁸². Also the **surface curvature** of a spherical particle, defined by its diameter, affects the protein adsorption in a quantitative and qualitative way⁸³⁻⁸⁴.

The size of the NPs in this study was kept in the range of 120 nm, which should be compatible with most of the internalization pathways.

SHAPE Recent studies have shown that the uptake behavior of nanorods, *i.e.* elongated non-spherical particles, is influenced by their aspect ratio⁸⁵. Discussions about how particle shape affects the uptake have only emerged recently, because most of the studied NPs are spherical by the nature of the synthesis. But the interest in other shapes like nanorods⁸⁶ or long filigree nanotubes⁸⁷ is increasing. Therefore this study is entirely based on spherical particles in order to focus on the particle characteristics defined by polymeric properties.

SURFACE PROPERTIES The particle surface is what the cell can 'see' and it therefore plays an important role. For one thing, the NP surface is defined by the material. In the case of *e.g.* polystyrene the surface is **hydrophobic** with aromatic rings protruding. The difference to

other polymers like PMMA may be negligible concerning the hydrophobicity. But the functional groups of PMMA might change the particle's interaction with biological systems. Polylactides are also hydrophobic but the end-carboxylic groups introduce hydrophilicity to the particles – as well as a 'biological' character, by possibly mimicking the functional groups of some biomolecules. Independent of the particle material, the surface hydrophobicity can be adjusted as required by functionalization⁸⁸⁻⁸⁹. Hydrophobicity correlates with an increase in protein coating^{16, 90}. But it also influences the type of proteins that adsorb on the particle surface and form the protein corona⁸³. Additionally functionalization allows tuning the particle's **surface charge**. The latter can be introduced by ionic surfactants or charged comonomers^{33, 91-93}. The uptake of charged NPs is more effective than that of non-charged particles, and the endocytotic efficiency increases with the net surface charge¹⁵. It is also known that positively charged NPs demonstrate a higher endocytosis rate compared to negatively charged ones^{15, 94-96}. **Functional groups** on the NP surface (inherent or introduced by functionalization) also effect the internalization. A comparison between positively charged NPs showed that amino-functionalized particles were internalized by different endocytotic routes (and with higher efficiency) than their non-functionalized counterparts⁹⁷. Other particle characteristics like **smoothness** of the surface are also tunable *e.g.* by a **hairy layer**. Compounds like poly ethylene glycol (PEG) form a flexible 'stealth' coat of protruding hydrophilic chains around the NP⁹⁸. The brush-like coat reduces protein adsorption, the interaction with biological surfaces as well as the cellular uptake efficiency and it prolongs the intravenous lifetime of drug-delivery particles by delaying macrophagocytosis^{58, 99-100}.

MECHANICAL PROPERTIES If a sphere is hard and unyielding or soft and elastic is another criterion for the cellular uptake. It was demonstrated recently that soft particles, *e.g.* those with a T_g below 37 °C *i.e.* below the applied cell experiment condition, are preferred to hard spheres¹⁶. Other studies revealed that the nature of the NP material (*e.g.* the polymer of lactic acid, lactic-co-glycolic acid or caprolactone) influences the protein adsorption pattern – even if the polymer is 'hidden' behind a thick PEG layer⁵⁸.

PROTEIN COATING (2° PROPERTY) A unique protein coat will form around the NP when added to serum supplied incubation medium, as the result of all physico-chemical properties¹⁰¹. As more hydrophobic NPs displayed both a higher protein adsorption and an increased cellular uptake, a thick protein coating might be favoring the cellular uptake in some cases^{16, 83}. On the other hand, a decrease of the particle uptake was observed when the available amount of proteins was increased by adding more serum to the incubation medium (unpublished data). The protein corona is an important factor for biological applications because, finally, this is 'what the cell sees'¹⁰²⁻¹⁰³. Biocompatibility, biodistribution and the endocytotic mechanisms are influenced by the particles' protein coat: The adsorption of proteins termed opsonins enhance the recognition and clearance of NPs from the organism by macrophages of the reticuloendothelial system¹⁰⁴. Conjugating a particulate DDS with targeting peptides¹⁰⁵ or with proteins like albumin changes its pharmacokinetics which can improve its biodistribution, biocompatibility or the cellular uptake¹⁰⁶.

2.4 Instruments and Methods

2.4.1 Dynamic Light Scattering

The size distribution of submicron colloids is commonly measured by dynamic light scattering (DLS), also termed photon correlation spectroscopy. Monochromatic coherent light (laser) is directed through the sample and the intensity of scattered light detected over time. The scattering process is termed elastic, or coherent, if neither phase nor frequency is changed. In contrary, both phase and frequency will be changed in dynamic (inelastic) scattering. Particles in dispersion are in constant movement due to the Brownian motion and their velocity is dependent on their size (and on other properties of the system like temperature or viscosity of the liquid phase). The frequency of the scattered light varies with the particles' velocity, as described by the Doppler effect, and the intensity of scattered light changes over time. This fluctuating scattering signal is detected over time and an autocorrelation function $f(t)$ is established. With some assumptions (spherical particle shape, no interactions, neglect of intramolecular vibrations *etc.*), this function can be displayed simplified as follows (*Formula III*). The signal intensity $f(t)$ is defined by the scattering vector q , the translational diffusion coefficient D , the time t and a pre-exponential factor ρ :

$$f(t) = \rho \cdot \exp(-q^2Dt) \quad \text{Autocorrelation (III)}$$

Once D is known the size or more to the point the hydrodynamic radius r_H of the nanoparticles will be derived. This is based on the Stokes-Einstein-Relation which is as follows (again assuming a spherical particle shape).

$$D = \frac{k_B \cdot T}{6 \cdot \eta \cdot \pi \cdot r_H} \quad \text{Stokes-Einstein (IV)}$$

Another important number about particle size is the polydispersity index (PDI), which defines the percentage standard deviation of the objects' sizes in a colloidal sample. A high PDI value corresponds to a large size distribution and these samples (PDI >0.3) are termed polydisperse. In nanoparticle synthesis the size distribution of the latex should be narrow, monodisperse (PDI <0.2) if possible.

2.4.2 Zeta Potential

Assisted by dynamic light scattering (DLS), the particle's zeta potential (ZP) can be determined as a measure of the surface charge. In the following a short overview on the principles on ZP is given¹⁰⁷⁻¹⁰⁸. Charge is an essential factor concerning particle stability in different solvents *e.g.* in the presence of strong bivalent ions like Mg^{2+} or Ca^{2+} . Furthermore it affects the interaction with cell structures and serum components. But the real Coulomb potential of a charged particle cannot be measured as it is covered by (counter) ions when in solution. Adsorbed on the particle surface is a monolayer of counter ions, termed Stern layer.

This is surrounded by a layer of oppositely charged ions which are not adsorbed but still attracted to the core. This is termed the fixed layer. The outermost sheet forms the so called diffusive layer; fixed and diffuse layer are summarized as electrical double layer. Distant from the attracting core, this outer layer is only weakly adhered to the inner fixed layer. The plane dividing the two layers is termed slipping or shearing plane – because, in an ongoing process, parts of the diffuse layer are being sheared off and adhered again. Temporary holes in the neutralizing layer are formed where the charged interior is revealed. This is why an average charge is present despite the – in theory – neutralizing coat. The resulting potential at the shear plane is termed zeta potential ζ and can be measured by electrophoresis. Charged objects in an electrical field will move with a velocity proportionate to their charge. The correlation between velocity and ZP is given by the Smoluchowski relation:

$$\zeta = \frac{v}{E \cdot \eta \cdot \varepsilon} \quad \text{Smoluchowski (V)}$$

With v = particle velocity, E = electrical field strength, η = solvent viscosity and ε = dielectrical constant.

2.4.3 Transmission Electron Microscopy

A focused electron beam is used to achieve high resolution imaging, but the optical setup follows the basic principles of an optical microscope. Running in vacuum to reduce scattering on gas molecules, the beam is accelerated by a voltage of up to 400 kV and is focused by electromagnetic lenses. In the case of the transmission electron microscope (TEM), a sample of roughly 100 nm thickness is hit by the electron beam in the measurement chamber. The transmitted part of the beam is detected for imaging, which is why the sample thickness should not exceed 100 nm. Multiple scattering disturbs the imaging, too much energy is absorbed and the transmission decreases. The resolution d [nm] of an imaging system, as characterized by Abbe (see *Formula VI*), is linked to the wavelength λ [nm] and thus to the energy of the applied emission source. In detail, d depends on the wavelength and on the numeric aperture $\eta \cdot \sin\alpha$, with α being the aperture angle and η the liquid's refractive index.

$$d = \frac{\lambda}{2\eta \cdot \sin\alpha} \quad \text{Abbe limit (VI)}$$

In theory the energy-rich electron beam with a small wavelength could achieve a high resolution of <1 nm. But factors like lens errors have to be taken into account. In addition the acceleration voltage is mostly kept below 150 kV, to reduce the damage for sensitive samples. The real resolution therefore is usually worse and is, in the case of *e.g.* biological samples, in the range of several nanometers. Whereas the resolution is mostly controlled by the energy density of the beam, the contrast in TEM images is based on different electron densities of the sample. The higher the electron density of a structure in the sample is, the stronger the electron beam is scattered at this spot. As a consequence, the fraction of transmitted beam

electrons that reach the detector is reduced and the electron dense structure appears dark in the image. Therefore, biological samples are often stained with osmium tetroxide OsO_4 . The strong oxidant reacts with the double bonds in unsaturated membrane lipids – forming a permanent bond and staining the membrane. But localizing the particles in a cell sample can still be tedious as each ultra thin slice contains only few NPs. Also some polymers lack the contrast so that differentiating them from similarly sized cell structures can be difficult.

2.4.4 Confocal Laser Scanning Microscopy

Offering a resolution of few hundred nm in combination with fluorescence-based imaging, the confocal laser scanning microscope (cLSM) closes the gap between transmitted light and electron microscopy. The cLSM is particularly useful for studying nanoparticles inside cells, because here the fluorescence-marked nanoparticles are easily localized. Furthermore the cLSM allows studying live cells, throughout several days even, if an incubation chamber is installed. This gives rise to over-time or even live video recording dynamic processes in the cell, *e.g.* cytoskeleton dynamics¹⁰⁹ or nanoparticle trafficking¹¹⁰. Depending on the setup of the machine, several lasers are directed onto the sample. The special property of a cLSM is a perforated blend placed in front of the detector. Due to this blend, only light that is emitted from a designated z-layer of the sample is admitted into the detector (see *Figure 6*). The effect is a non-invasive optical cut of the sample into slices with a z-resolution of approx. 500 nm and a lateral resolution of down to 250 nm. The development of 4Pi-imaging and two-photon excitation has further improved the axial resolution¹¹¹⁻¹¹². In 1999 Stefan Hell presented the STED (stimulated emission depletion) technique thus breaking the lateral resolution down to 6 nm¹¹³. This technique is especially valuable as it can be applied to living cells¹¹⁴.

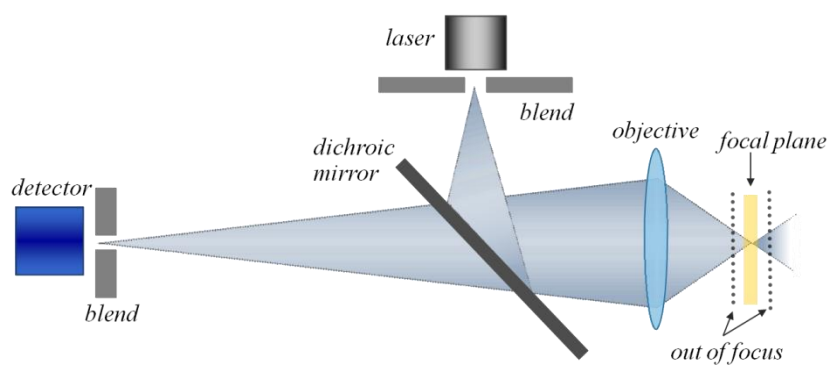


Figure 6. Schematic build of a confocal laser scanning microscope.

2.4.5 Flow Cytometry

Since the first application of flow cytometry (FCy) in the 1970s¹¹⁵, the machines have become widely popular in research and clinical diagnostics. In principle, FCy can be combined with nearly any staining procedure, assay or biotechnological process. Whenever

fluorescence is introduced into a microorganism or a cell it can be exploited in flow cytometry for assessing information about the specimen. To a low extent the technology is applied for other objects than microorganisms and cells¹¹⁶. But with the combination of fluidics and laser triggered fluorescence detection it is the ideal tool to detect NPs in cells. Subtle changes in scattering and emission of a cell can be observed – which are directly linked to the cellular uptake of fluorescing particles.

2.4.5.1 Working Principle

In flow cytometry, a fluidics system is coupled with the detection of fluorescence and of light scattering in small and wide angle position.

For this application the objects of interest must be prepared as a diluted dispersion commonly not exceeding a concentration of several thousand objects per μl . In the machine, a sample stream is injected into the core of a flowing stream of so called sheath liquid (water or physiological buffer) and a laminar flow is established. The two streams do not mix and the sample flow is surrounded by a layer of sheath liquid flow in a concentric setup (Figure 7). This is termed hydrodynamic focusing. This stream of two concentric layers is directed through the measurement chamber, a narrow glass capillary.

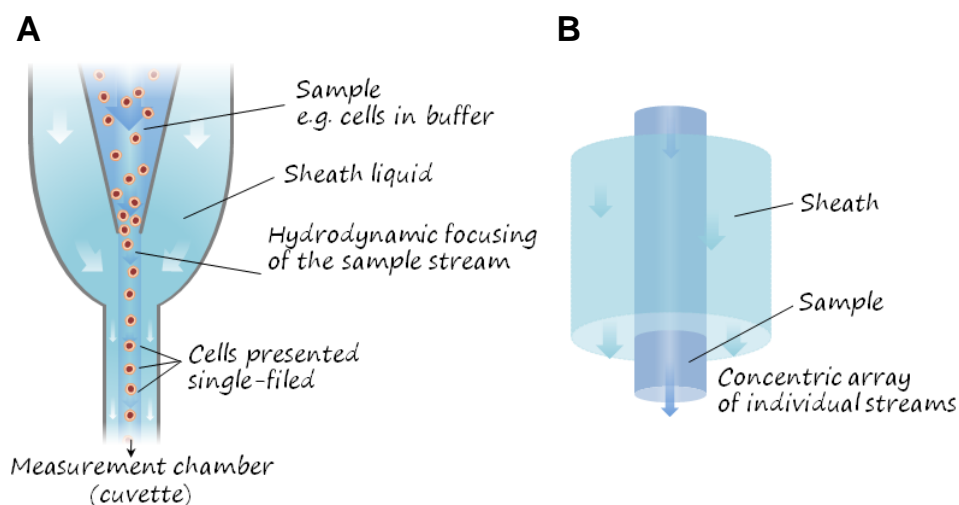


Figure 7. Scheme of the joining of sheath and sample stream in a flow cytometer (A). By hydrodynamic focusing (B) a thin stream of sample is formed and positioned in the center of the cuvette.

In the measurement chamber, the sample stream is hit orthogonally by a laser beam (see Figure 8). It is important to note that the objects, e.g. cells, pass this laser beam single-filed. Placed behind an array of filters and mirrors, several detectors successively detect the properties of each cell passing the laser beam. This includes fluorescence signals but also of wide angle (sideward scatter, SSC) and small angle (forward scatter, FSC) scattering.

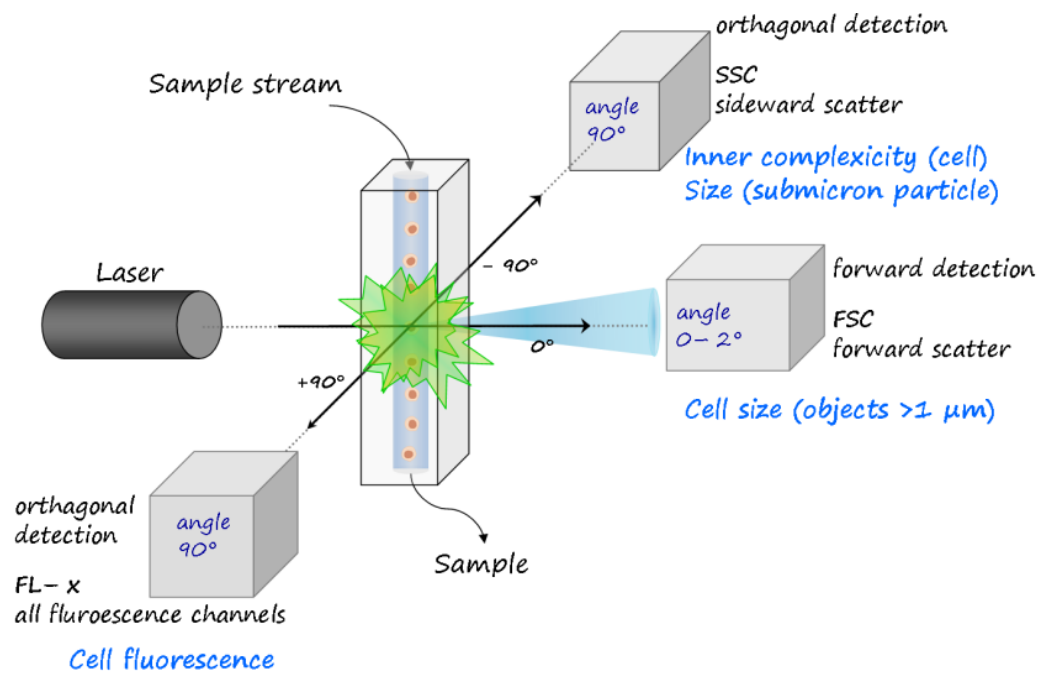


Figure 8. Excitation and detection of fluorescence and scattering in a multi-channel flow cytometer equipped with one to several lasers.

Flow cytometers thus allow for the rapid measuring of individual objects in dispersion. Another obvious advantage is the short exposure of each object to the laser (μs scale), unlike *e.g.* in microscopy where exposure lasts seconds to minutes. Extremely light sensitive objects can be analyzed by flow cytometry. Within one second, several thousand objects can be measured separately and their number per volume can be counted. But only when one object passes through the beam of the reference laser, data acquisition is triggered. In this instant, a digital event is created and the acquired data from every active channel is assigned to this event *i.e.* assigned to this particular object. Each event now represents a comprehensive data set, including fluorescence intensities in various channels and scattering intensities at two fixed positions (small and large angle *i.e.* FSC and SSC). This collected raw data consists of up to hundred thousands of events which represent background (*e.g.* pieces of cell debris) and wanted objects (cells) alike. Before final data interpretation the signals must be sorted from the background events. Fluorescence, granularity (SSC) or the presumable size (FSC or SSC) are features which can be applied to identify the wanted objects. Commonly a threshold condition is set on one of the detection channels so that unwanted signals are excluded from detection. In nearly every system a 488 nm laser is present as standard reference, but often additional lasers (*e.g.* 640 nm, 561 nm, 375 nm) are available.

Summed up, the function of a flow cytometer is based on the interplay of fluidics, optics and electronics (see Figure 9).

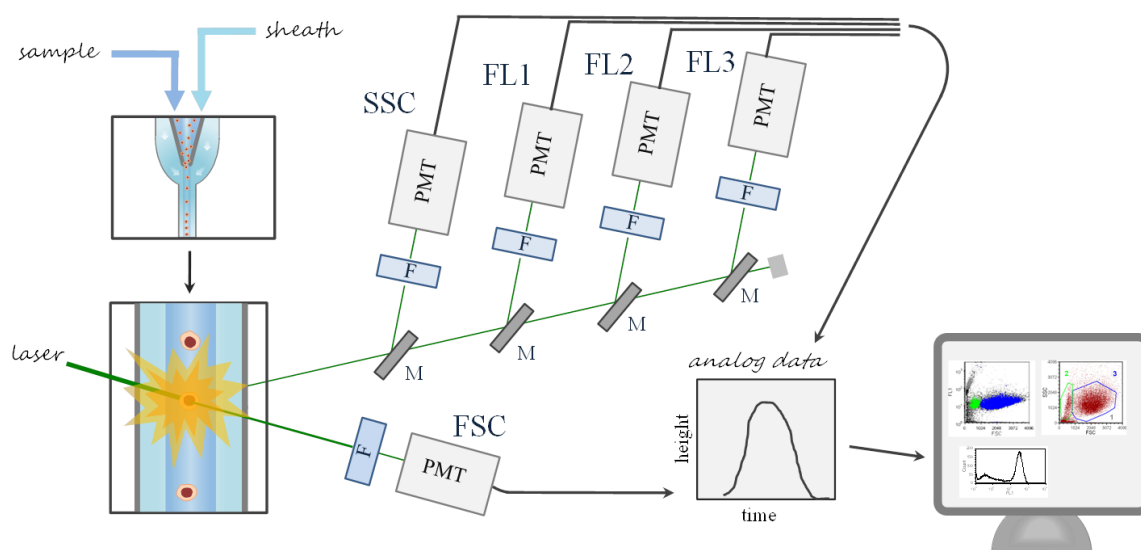


Figure 9. Components of a flow cytometer system: Fluidics The fluidics system focuses the sample in a thin stream that is guided through the cuvette. Optics A laser beam is directed through the cuvette, and resulting scattering and fluorescence pass through an array of mirrors (M) and band or long pass filters (F). Electronics These photons are detected and amplified by photomultiplier tubes (PMT) that yield analog data in the form of a pulse with the parameters of height and duration. The pulse signal is converted into an intensity value and the obtained data sets can be displayed by the software in the form of dotplots, histograms etc.

Some cytometers allow the simultaneous detection of up to 17 colors¹¹⁷. As reference the 488 nm laser will be the base for all scattering measurements. As described above the signal intensity of the scattered 488 nm light is detected FSC and SSC. With more lasers built-in, proper calibration of the machine for multi-channel detection is more difficult. Detection in the different photomultipliers must be precisely timed on a μs scale, to ensure that the detected fraction of photons is not the combined emission caused by several lasers. Additionally, as for all fluorescence-based measurements, a suitable set of fluorophores must be chosen to avoid spectral overlap. But in some cases spectral overlap cannot be avoided and then the error must be reduced to a minimum by correct compensation of the involved detection channels.

2.4.5.2 History and State-of-the-Art

The development of cytometric analysis was originally enforced by the American military, with the intention to measure pathogens of biological warfare *i.e.* anthrax spores in aerosols. This was at the time of World War II and due to military secrecy the results were not published until 1947¹¹⁸. The technique was transferred to liquid samples and in the 1970s the

first flow cytometers were on the market, provided by *e.g.* Partec or Becton Dickinson, and first publications appeared ¹¹⁵. In these days studies focused on objects that could be visualized easily by their large size or autofluorescence. Common biological samples were marine microorganisms that contain autofluorescent pigments as part of the photosynthesis system. One milestone in early flow cytometry was the discovery of an abundant submicron phytoplankton sized roughly 700 nm, which had not been detected by traditional microscopy due to its high light sensitivity ¹¹⁹. But early on staining of biological samples was introduced to better detect the target organisms and to gain additional information. Immunofluorescence markers¹²⁰ or indicator dyes for metabolic activity ¹²¹⁻¹²² were used. Flow cytometry was also discovered for determination of the cell karyotype, which describes the number and features of chromosomes. A variety of applications in the clinical sector has been developed, amongst them the detection of genetic aberrations like aneuploidy ¹²³. Some flow cytometers, later on termed fluorescence activated cell sorters (FACS, ©Becton Dickinson) were constructed for physical sorting of the samples. With this feature, target cells now could automatically be separated from the rest of the sample under physiological and sterile conditions. It might be mentioned here that the expression FACS nowadays is falsely applied as a general term for flow cytometers, disregarding if the sort feature is provided or not. In conformance with the advances in molecular biology and instrument technique, the range of applications in flow cytometry has further increased ¹²⁴. As long as a specimen can be fluorescence-labeled, it can be detected in flow cytometry and analyzed at a rate of thousands per second. In the case of bacteria this means that the organism itself, its genetic material, a specific surface antigen or a metabolic product can be targeted separated from the rest of the sample. The reader is referred to a review by Veal ¹²⁵ or a thorough overview of the available staining methods for cell and microorganism studies in flow cytometry. Cytometric screening for contaminations with pathogenic microorganisms in different media such as food ¹²⁶, blood samples ¹²⁷ or drinking water ¹²⁸ has great potential and has begun to replace the previous labor-intensive and time-consuming culture-based techniques. Amongst the various approaches of specific labeling, immunofluorescence has proven particularly useful since multi-color labeling and multi-channel detection are now widely available. Targeting a surface epitope with a fluorescence-coupled antibody is one easy way to identify and sort biological specimens. Identification of cells is achieved by tracking the specific cell surface molecules termed clusters of differentiation (CD) ¹²⁹⁻¹³⁰. More than 250 of these structures are identified yet and a cell type can be identified by its unique CD pattern. Another application is the screening for blood (cancer) diseases or the status monitoring of diseased patients, by counting the blood cells of interest ¹¹⁷. If the cells are permeabilized also intracellular proteins can be detected. A more recent tool for cell identification which could successfully be transferred to flow cytometry is based on the in-situ recognition of specific nucleotide sequences. This technique termed fluorescence in situ hybridization (FISH) or phylogenetic labeling was first introduced by DeLong ¹³¹. Hereby, fluorescence-marked oligonucleotides are added to permeabilized target

cells. These oligonucleotides recognize a complementary mRNA strand and will only adsorb to exactly this sequence of nucleic acids, which results in highly specific staining.

It is a logical consequence that with the rise of nanoscience and nanoparticles in particular, flow cytometry was also assigned to detect fluorescence-marked NPs in cells.

2.4.5.3 Studying the Particle-Cell Interaction

With the ever growing importance of nanoscience and, in particular, of nanoparticles (NPs), another application was added. The uptake of nanoparticles into cells is studied by detecting the fluorescence-marked NPs in the cells^{57, 132-133}. Even though the tracking of particles by fluorescence is most common, the uptake of especially strongly scattering NPs can also be measured by the cell's increasing SSC¹³⁴. This can be combined with cell immunomarking and viability staining assays, to correlate the uptake rate of nanoparticles with other properties of the cells or to sort the cells by type. Nanoparticle-induced toxicity in flow cytometry is commonly studied by exclusive DNA staining, using *e.g.* 7AAD (7-aminoactinomycin D) or propidium iodide¹³⁵. These dye molecules intercalate within the cell's DNA strand and emit a fluorescence signal that can be detected and quantified by flow cytometry. Healthy live cells, with an intact cytoplasmic membrane and functional membrane-bound transporters, will not be dyed by 7AAD. But apoptotic cells will be slightly stained and dead cells will be stained strongly. The three cell populations can be identified by their distinct fluorescence intensity and the percentage of live, apoptotic and dead cells can be calculated.

2.4.5.4 Application for Submicron Analysis

Despite the many advances in fluorescence-triggered flow cytometry, most machines are designed for analysis of cells. As these cytometers are customized for objects in the μm size range, any submicron detection (triggered on scattering and not on fluorescence) is a difficult task. At low signal intensities the coefficient of variation (CV) is increased due to bad signal resolution¹³⁶ as expressed in *Formula VII* below:

$$CV \sim \frac{1}{\sqrt{\text{signal intensity}}} \quad \text{FL signal CV in flow cytometry (VII)}$$

Few machines offer an angle-dependent detection of the scattered light; these can be applied for scattering-based detection of smaller objects like nanoparticles¹³⁷ or viruses¹³⁸⁻¹³⁹. In scanning flow cytometry (SFC) the scattering is measured angle-dependent from approx. 5° to 120° . Indicatrix data (angle-dependency of the scattering intensity) is correlated with properties of the NPs, to obtain a parametric solution of the inverse scattering problem. A restricted range of object diameter and refractive index needs to be defined. Within these parameters a solution or good assumption of the Mie equation is developed. The reward is a precise measurement not only of submicron particle size but also of the refractive index, light depolarization, shape and some more¹⁴⁰⁻¹⁴². But angle-dependent detection is not necessarily

required for SFC-like results, as demonstrated by Maltsev¹⁴³. With a coaxial orientation of sample stream and laser beam, the scattering was detected over time with a spherical mirror in 0° position – imitating the angle-dependent like of the SFC setup.

What limits non-scanning cytometers to near μm sized objects is for example a large illumination and observation volume (causing high background). Another issue is the broad temporal window for signal detection. When detection is optimized for large objects and not adjusted to nanoparticles, the time span of signal detection is unnecessarily long – which again increases the risk that, simultaneously, noise signals are also detected.

As discussed, a submicron particle of approximately 100 nm diameter has an excessively small volume compared to the dimensions of the sample stream (few μm), of the sheath fluid stream (several hundred μm), of the illuminated volume (laser beam width 20-100 μm diameter) and finally of the observed volume. This is demonstrated in *Figure 10* and *Figure 11* at the base of the CyFlow ML (Partec) which was used in this thesis.

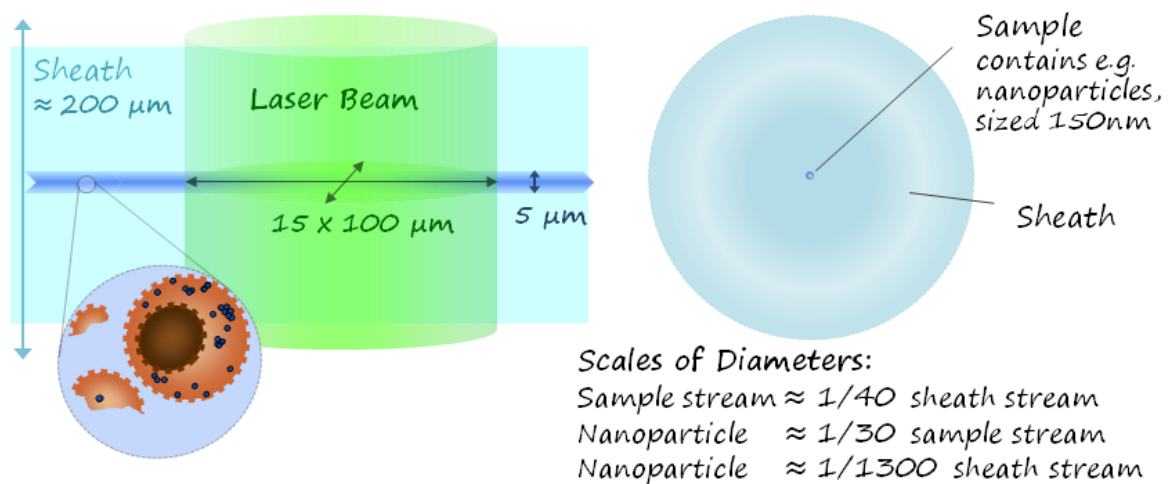


Figure 10. A nearly true scale display of the dimensions in a flow cytometer puts the size of cells and nanoparticles in relation to the diameter of sample stream, sheath stream and the illuminated volume.

The temporal resolution *i.e.* the time span Δt can also be seen as fraction of sample volume ΔV that passes the detection in this short time span. If the sample concentration exceeds the maximal possible resolution, more than one object passes the detection spot within the time span Δt and errors (coincidences) occur.

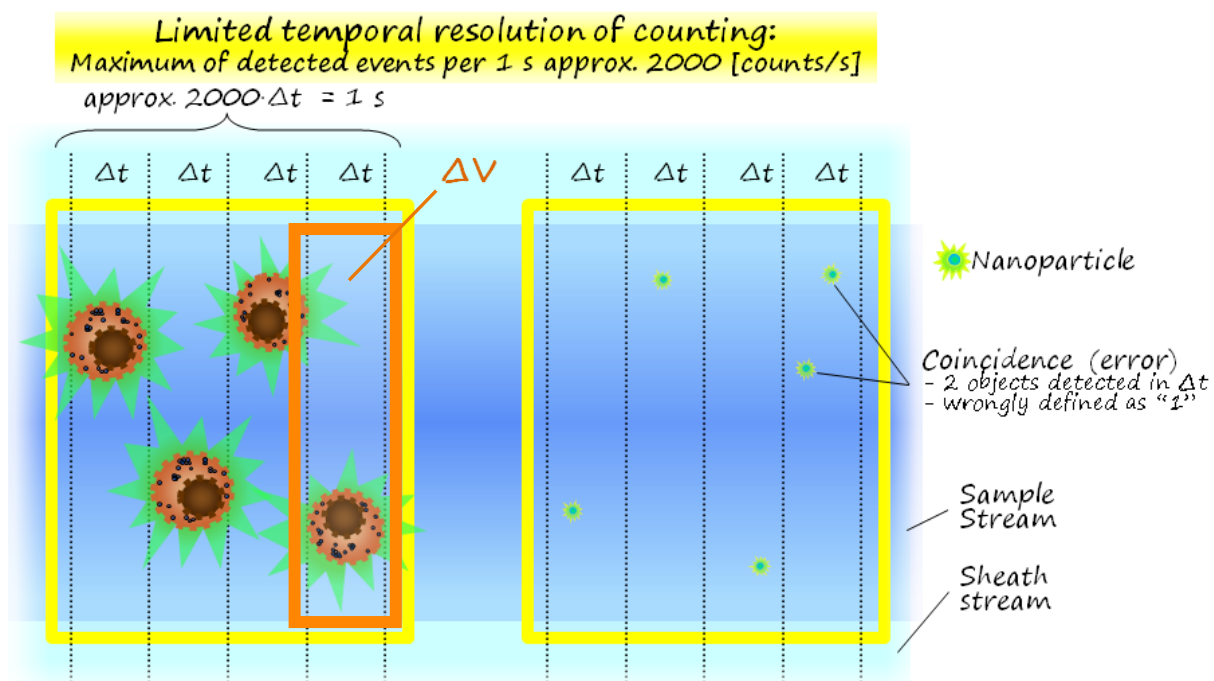


Figure 11. Interpretation of the temporal resolution Δt as a spatial resolution ΔV .

The real potential of non-scanning FCy was demonstrated as early as 1979 in a formidable publication of Shapiro¹³⁹. He is known for his pioneering work in the field and for his book which has become the ‘bible’ of flow cytometry¹⁴⁴. A customized flow cytometer was built and optimized to submicron detection (concerning the width of observation window, observation volume, detection electronics, *etc.*). Particles as small as 91 nm could not only be detected perfectly by their scattering, but also be resolved in a mixture with nearly similarly sized particles.

3 Experimental Part

3.1 Materials

For the majority of cell experiments, the approved fluorescent dye N-(2,6-diisopropylphenyl)-perylene-3,4-dicarbonacidimide **PMI** (BASF) was incorporated in the particles. But for specific applications, namely for the single NP detection in flow cytometry, other fluorescent markers had to be utilized. Preliminary testing had indicated that PMI might not meet the specific criteria for this application. Single NP detection in flow cytometry requires high particle fluorescence signals – which is facilitated by a high quantum yield of the dye and good solubility in monomer and polymer. Furthermore, the fluorophore's excitation and emission maximum should correspond precisely to the flow cytometer's laser wavelength and to the fluorescence detection range. The intention was also to find dyes suitable not only for the FL1 but also for other fluorescence detection channels of the cytometer – which would enable the simultaneous detection of several NP species.

The standard fluorescent dye in particles was the perylene dye PMI (see *Figure 12* & *Table 1*). This fluorophore is photostable, oil-soluble and yields intensive fluorescence after excitation at 488 nm (the standard laser). Additional fluorophores, YA795 and the series MS1A to MS1C, including several **perylene imide modifications**, were synthesized by members of the Max Planck Institute for Polymer Research (MPIP). For the dye samples MS1A to MS1C the aromatic system was expanded to increase the solubility in hydrophobic media and the quantum yield (see *Figure 12*).

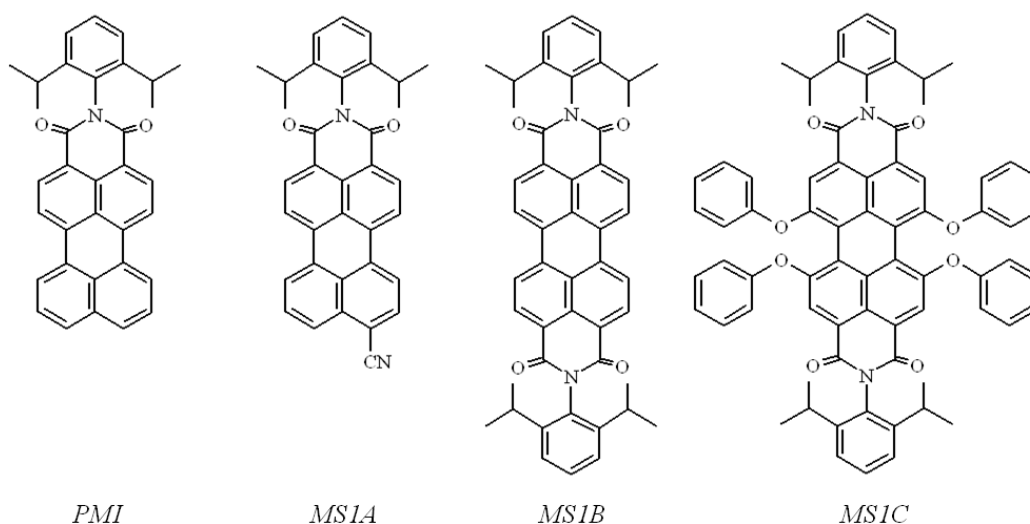


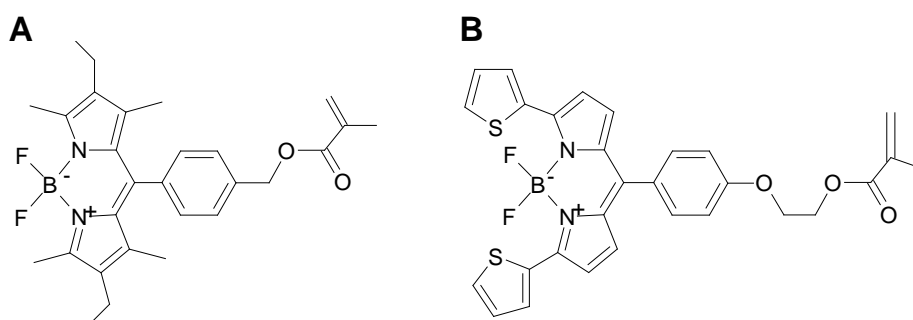
Figure 12. Structure formulas of commercially available PMI and other supplied perylene imide dyes.

To some dyes a spectral red-shift was introduced, promising a possible dye for 562 nm or 640 nm laser excitation. Additional properties of the dyes are listed in *Table 1*.

Table 1. Properties of the utilized perylene imide dyes

Dye	Absorption maximum	Quantum yield	Potential FC detection channels
PMI	490 nm	≈ 0.7	FL1, FL2, FL3
MS1A*	515 nm	> 0.8	"
MS1B	511 nm	≈ 1	"
MS1C	588 nm	≈ 0.96	FL5, FL6
YA795	499 nm	0.75	FL1, FL2, FL3

Methacrylate-modified 4,4-difluoro-4-bora-3a,4a-diaza-s-indacene **BODIPY** dyes (see *Figure 13*) for excitation at 488 nm and 640 nm were provided by Dr. Andrej Turshatov.

**Figure 13.** Structure formulas of the BODIPY fluorophores BP1 (A) and BP2 (B).

The polymerizable BP dyes (see *Table 2*) were chosen because these had been synthesized for STED applications and offered a high photostability. In addition, introducing the dye in form of a comonomer prevented leakage. The BP2 fluorophore, for excitation at 640 nm wavelength, was incorporated into PMMA particles by Dr. Turshatov (see *Table 9*).

Table 2. Properties of the polymerizable BODIPY fluorophores.

BODIPY dye	Absorption max.	Emission max.	FC detection channel
BP1	520 nm	540 nm	FL1, FL2
BP2	640 nm	650 nm	FL5

Furthermore some commercially available perylene dyes from the Lumogen® F plastic colorant series (Kremer, BASF) were incorporated in particles. The ‘yellow’ dye (LFY) for the 488 nm laser and the ‘red’ dye (LFR) for excitation at 562 nm were chosen (see *Table 3*).

Table 3. Properties of commercially available Lumogen dyes.

Lumogen® F	Absorption max.	Emission max.	Quantum yield η	FC detection channel
Yellow	473 nm	1° 500 nm, 2° 570 nm	0.85-0.9	FL1, FL2
Red	578 nm	600 nm	> 0.9	FL5

3.2 Methods

3.2.1 Synthesis of Nanoparticles in Miniemulsion

All particles were synthesized in miniemulsion (ME) and the latter was obtained by sonication under ice cooling with a W450 sonifier (Branson). To form the particles, the ME was then transferred into a flask and stirred over night at either 40 °C (open lid for solvent evaporation) or 72 °C (radical polymerization with the lid corked).

Nanoparticles made of PS and PMMA were synthesized by radical polymerization in the oil-in-water ME. 6 g of distilled monomer (styrene or methyl methacrylate, both Merck), 250 mg hexadecane (HD, Aldrich) and 100 mg 2,2-azobis(2-methylbutyronitrile) (V-59, WAKO Chemicals) were mixed together. For fluorescent particles 4 mg of the dye PMI was added also. After addition of the continuous phase, 24 g water and 72 mg sodium dodecylsulfate (SDS, Merck), the mixture was pre-emulsified for 1 h at 1200 rpm and subjected to sonication under ice cooling at 90% amplitude for 3 min (½" tip, W450 sonifier, Branson). After reaction large aggregates (if any) were removed by centrifugation. Particles, if needed, were washed by dialysis with a 100 kDa pore size membrane against 5 l of demineralized water. The water was changed daily until a conductivity of 3 $\mu\text{S}\cdot\text{cm}^{-1}$ was reached. The spheres used for single particle detection in the flow cytometer were created with the same synthesis protocol. Instead of PMI a variety of other fluorophores (see chapter 3.1) were incorporated.

Poly(L-lactide) nanoparticles were prepared by the solvent evaporation technique as described elsewhere³³. The polymer, 150 mg of PLLA (Fluka, M_w 101700 $\text{g}\cdot\text{mol}^{-1}$), and 0.1 mg PMI (for the fluorescent particles) were dissolved in 5 g chloroform and mixed with the aqueous phase, consisting of 72 mg SDS and 24 g water. After stirring for 1 h the macroemulsion was sonified under ice cooling for 3 min (pulsed 30 s/ 10 s sonication/ pause, ¼" tip, running at 70% power, W450, Branson). The nanoparticles were purified by dialysis as described above.

Amino-functionalized PS particles were obtained in radical polymerization with the comonomer aminoethylmethyl methacrylate (AEMH, Merck), as presented earlier¹⁴⁵. Hereby 120 mg of AEMH were dissolved in a 0.833% solution of Lutensol AT50 (Lut-50, BASF) at room temperature. Lut-50 is a non-ionic surfactant consisting of a linear $\text{C}_{16}/\text{C}_{18}$ chain and a block of 50 ethylene glycol units. For the discontinuous phase 100 mg V-59, 250 mg HD, 5.88 g styrene and a fluorescent dye (if required) were mixed. Under constant stirring the two phases were combined and stirred at 1400 rpm for 1 h. The samples were subjected to sonication with the ½" tip under ice cooling. Details of the sonication were varied (tip dipping height or duration). Filtration through tissue wipers removed large aggregates if required.

3.2.2 Characterization of Nanoparticles

The particle size was determined by photon cross correlation spectroscopy with a Nanophox machine (Sympatec). A submicron particle sizer NICOMPTM 380 (PSS-NICOMP) was utilized to measure the ζ -potential of the particles in 1 mM solution of potassium chloride.

Moreover, the particles were incubated in PBS or in serum-supplied medium prior to the zeta and DLS analysis to test the dispersion's stability in biological media. The morphology was studied by transmission electron microscope with an EM-912 or EM-902 (both Zeiss). Thereto drops of diluted latex were set on a carbon-coated copper grid and left to dry. PLLA and PMMA samples were carbon-coated for a better protection of the samples in the electron beam. The molecular weights of the polymers were determined by gel permeation chromatography (GPC). 5 mg of freeze-dried particles were dissolved in 1 ml of chloroform (PLLA) or tetrahydrofuran (PMMA and PS) and subjected to GPC at a flow rate of 1 ml·s⁻¹. The glass transition temperature T_g and the crystallinity of the polymeric NPs were analyzed by differential scanning calorimetry (DSC). Applying a heating rate of 10 K·min⁻¹ the temperature was raised from between -140 °C to 360 °C. For the particle fluorescence normalization factor, the emission of NPs was analyzed in a TIDAS FL3095 SL 3D fluorescence spectrometer (J&M). Hereby aqueous dispersions with solid contents ranging from 0.4 to 4 mg·g⁻¹ were measured, as described by Lorenz et al.¹⁶. At an excitation wavelength of 420 nm, emission intensity at 530 nm was recorded and plotted in a chart with the solid content. After background subtraction a linear fit crossing the zero-point was applied. The resulting slopes S_{Pol} were divided by the slope of polystyrene (S_{PS}) to retrieve the normalization factor $f_{1(Pol)}$:

$$f_{1(Pol)} = \frac{S_{Pol}}{S_{PS}} \quad \text{Normalization factor 1 for NP fluorescence (VII)}$$

An additional normalization factor $f_{2(Pol)}$, based on the dye content $m_{dye(Pol)}$ (mg_{dye}·g_{polymer}⁻¹), was obtained. The dye loading $m_{dye(Pol)}$ was measured in UV-Vis absorption spectroscopy performed on dissolved NPs in organic solvent⁹³. For the final calculation $f_{1(Pol)}$ was used.

$$f_{2(Pol)} = \frac{m_{dye(Pol)}}{m_{dye(PS)}} \quad \text{Normalization factor 2 for NP fluorescence (VIII)}$$

$$Fl_{2Pol} = \frac{Fl_{Pol}}{f_{2(Pol)}} \quad \text{Normalized fluorescence (IX)}$$

3.2.3 Electron Microscopy

Morphology and intracellular localization of particles were analyzed in a transmission electron microscope EM-912 or EM-902 (both Zeiss). Cells were incubated for 4 h or 24 h at a total particle concentration of 300 µg·ml⁻¹. For further preparation the samples were handed to members of the electronic microscopy team in the group. The cells high pressure frozen (HPF Compact 1, Wohlwend Engineering GmbH) using hexadecane as transfer medium. Remaining water in frozen cells was freeze substituted by acetone and heavy metals were added for contrasting (osmium tetroxide 0.2% and uranyl acetate 0.1%). The water content in the substitution media was kept at 5%¹⁴⁶. After substitution and embedding in EPON the samples were ultrathin sectioned.

3.2.4 Isothermal Titration Calorimetry

Particle protein-interaction was studied in an isothermal titration calorimetry (ITC) setup with fetal calf serum at 22 °C and physiological pH 7.2. Analysis was done with a CSC-4200 machine utilizing the software ITC RUNTM and BindworksTM 3.1 (all Calorimetry Sciences Corporation). The 75 µg·ml⁻¹ particle dispersion was provided in the measurement chamber and 10%-vol. fetal calf serum FCS (Invitrogen) was titrated into the chamber. The experiment routine was set to 50 titration steps of 5 µl each, with 300 s of pause between the steps. The titration of a 10% protein solution into water under similar experimental conditions was used as blank reference and subtracted from the data in order to calculate the share of enthalpy caused by protein-particle interaction. The total heat, *i.e.* the summarized energy set free during 50 injection steps, was taken as a measure for the intensity of the particle-protein interaction.

3.2.5 Cell Culture

All experiments were performed with the HeLa cell line as purchased from the Leibniz Institute, German Collection of Microorganisms and Cell Cultures (DSMZ). The cells were kept in Dulbecco's modified Eagle medium (DMEM) supplemented with 100 U penicillin, 100 µg·ml⁻¹ streptomycin and 10%-vol. fetal calf serum (FCS) in a humidified incubator at 37 °C and 5% CO₂ (all Invitrogen). In a three month cycle the cells were replaced with a freshly thawed batch. Unless specified this medium termed 'DMEM 10%' was used in all incubation experiments. Cells in culture were splitted at confluence utilizing 0.5% trypsin (Invitrogen). For all cytometric experiments, excluding the absolute quantitative studies, cells were seeded in six-well plates at a density of 0.2·10⁶ cells per well in 3 ml cell medium and allowed to attach over night. Prior to the particle incubation step the volume was reduced to 2 ml. For qualitative cLSM studies either 0.04·10⁶ cells were seeded in Ibidi chambers (Ibidi) or 0.08·10⁶ HeLa cells were seeded on untreated glass cover slides placed in 6 well plates. Said Ibidi chambers are cell culture treated µ-dishes providing 3.5 cm² of growth area. For the electron microscopy studies, 0.01·10⁶ cells were seeded in 24-well plates containing the sapphire discs for cryopreparation.

3.2.6 Confocal Laser Scanning Microscopy

3.2.6.1 Qualitative Cellular Uptake Studies

Studies with the cLSM were done to show in particular the intracellular localization of particles, but also to exclude extracellular adsorption to the cell membrane. The cells, grown on glass slides, were incubated for 1 h or 4 h with $75 \mu\text{g}\cdot\text{ml}^{-1}$ of particles in DMEM10%. The samples were washed, transferred into custom-made sample holders and topped with 1 ml PBS. Prior to the measurement, $0.5 \mu\text{l}$ solution of CellMaskTM Orange CMO (Molecular Probes) were added for specific plasma membrane staining. The studies were done on an Olympus IX71 with a 60x oil objective equipped with a 488 nm and a 543 nm laser. Particle fluorescence in Ch1 at 510-540 nm and CMO emission in Ch2 at 570-590 nm were detected in serial scan mode. Additional cLSM studies were performed using a Leica TCS SP5 equipped with a 63x oil objective. The cells, grown in Ibidi chambers, were incubated for 4 h with $800 \mu\text{l}$ of $75 \mu\text{g}\cdot\text{ml}^{-1}$ particles in DMEM 10%. Washing and staining with CMO prior to the measurement was executed as described above. The fluorescence signals of the particles (497-541 nm) and the membrane staining (604-655 nm) were detected in serial scan mode after excitation at 488 nm or 561 nm.

3.2.6.2 Quantitative Cellular Uptake Studies

The Leica instrument was also utilized for all quantitative cLSM studies, with the 488 nm and the 640 nm laser for excitation. After some preliminary tests, each cLSM experiment was coupled to a flow cytometry measurement, so that all samples could be seeded from the same batch of cells. In the general experimental setup, all samples were seeded 1x for the cLSM and in triplicate for the FC measurement. For cLSM and FC studies $0.04\cdot 10^6$ HeLa cells were seeded in 6-well plates and Ibidi slides, respectively. The used HeLa cells have a doubling rate of 48 h¹⁴⁷. Therefore the cell number on the next day, when the particles were added, was assumed to be approximately $0.06\cdot 10^6$ to calculate the number of added NPs per single cell.

In a first set of experiments the cells were grown in Ibidi chambers and incubated for 1 h and 2 h with NPs. The cells were topped with $600 \mu\text{l}$ DMEM 10% containing $500 \mu\text{g}\cdot\text{ml}^{-1}$ of polymer. Great care was taken to avoid any spilling – of the cell suspension or of the particle-supplied medium – beyond the Ibidis' central growth area. The intention hereby was to ensure constancy in the experimental conditions (cell density in the central growth area, particle concentration and liquid column above the cells) and thus increase the precision of the quantitative data. The cell membrane was stained with $0.3 \mu\text{g}\cdot\text{ml}^{-1}$ Alexa680-coupled wheat germ agglutinin WGA₆₈₀ (Invitrogen). Cells were fixed in 3.75% formaldehyde (FA) and topped with 1% FA for storage at 4 °C. Particle emission was detected at 512-565 nm and WGA₆₈₀ was detected at 667-776 nm. For other experiments the particle concentration was reduced and a different membrane staining was applied. Incubation was performed for 2 h with $500 \mu\text{l}$ of $300 \mu\text{g}\cdot\text{ml}^{-1}$ NPs in DMEM 10%. In one step cells were fixed and stained with 1.5 nM DiD (Invitrogen) in 3.75% FA. For a perfect direct comparison between cLSM and

FC, the left-over cells in the FC tubes were imaged in the cLSM. Hereby the cells were transferred into un-coated Ibidi μ -slides, where they re-attached to the ground firmly enough for high resolution cLSM imaging. Particle emission was detected at 512-565 nm and DiD was detected at 650-776 nm.

In order to count the internalized particles, z-stacks of whole cells with a narrow step size of 250 nm were run on randomly chosen cells. Only transmission and the membrane staining were used to localize the cells, with the particle detection switched off. Further imaging and particle counting was done with Photoshop CS3 (Adobe) as demonstrated in *Figure 14* below. The outlines of the cells were highlighted and 10-20 subsequent layers of one z-stack were projected into one plane named smart object (SO) see *Figure 14A*. In every SO, all shapes corresponding to internalized particles were tagged with colored dots, using a different color in each SO (*Figure 14B -E*).

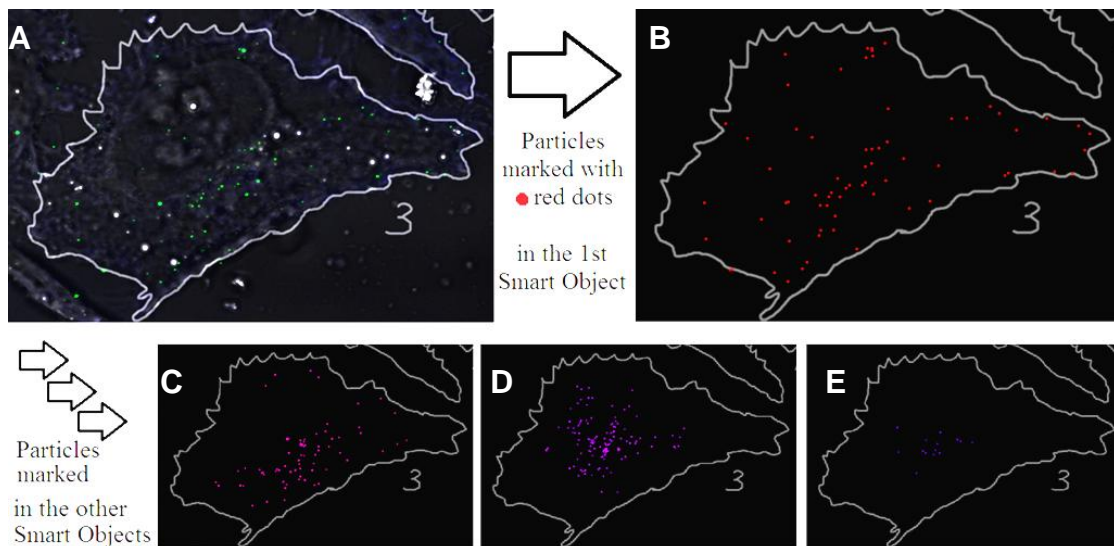


Figure 14. The cell outline is traced and the first SO, i.e. a summarized projection of 5-20 subsequent layers of the z-stack, is created (A). This SO displays all the particles (green) located in the defined cell volume. Based on this image, the location of every single particle is tagged with a colored dot. A mask image of the particle distribution and number is obtained (B). The process described in A & B is performed for the whole cell scan, resulting in a total of 4 cell-particle mask images (B-E). In every SO the particles are marked in a different color (shifting red-pink-purple-blue).

Finally the number of dots i.e. the total number of internalized nanoparticles was counted. This method also yielded two maximum projections of the internalized particles, one of all the smart objects and one the original z-stack images. Particles co-localizing in x-y location (and situated above each other in axial direction) were marked as ‘dots directly next to each other’. This was in concession to the automated count feature in Photoshop, which cannot resolve two dots if they overlap by more than $\frac{1}{4}$.

3.2.7 Flow Cytometry for Single Nanoparticle Detection

The ultimate goal of the single particle studies in flow cytometry was to implement a method for the fluorescence measurement of NPs and for their absolute intracellular quantification. In the first part of the project numerous experiments were performed to lay the base and gather crucial information that can crudely be described as ‘*how the sample behaves in the present system*’. After that, the implementation and routine application of innovative protocols for the measurement and quantification of nanoparticles via flow cytometry could be addressed.

3.2.7.1 The Impact of Experimental Conditions and Particle Features

During these prerequisite measurements, a variety of different experimental conditions and particle properties were tested. In addition instrument settings had to be changed over time to adjust to latest findings, further increasing the variety of conditions.

Major key points for the measurement of nanoparticles in flow cytometry are given below:

- PMT signal amplification
- Laser power
- Threshold
- Sample concentration
- Measurement speed
- Properties of the particles
 - *Size*
 - *Refractive index of the material*
 - *Excitation & emission range of the incorporated dye*
 - *Overall fluorescence intensity*

The deliberate variation of experimental conditions (*e.g.* sample concentration, laser power or particle fluorescence) was used to gather basic information. This consequently led to a high variability of applied experimental conditions of the individual measurements. Therefore all relevant information about the experimental setup is given on-site in the presentation and discussion of the results. These measurements were done to clarify three issues:

- How do individual settings and sample properties affect the detected data?
- Which of the detected signals originate from particles – and which from background?
- If so, do they truly represent single particles – and not coagulates or coincidences?

3.2.7.2 Nanoparticle Measurement in Flow Cytometry

Once the preliminary research was done, the appropriate experimental conditions were known and could be applied in all following experiments. All measurements were done with a

CyFlow ML (Partec) equipped with a 40-200 mW tunable 488 nm and a 640 nm laser. A 562 nm and later on a 375 nm laser were also added. The blue laser was run at 200 mW for maximal dye excitation. Scattered light was detected in logarithmic amplification in sideward (SSC) and forward (FSC) direction using a 490 band pass filter. If not described else, the threshold was set on the SSC and kept constant in all experiments. Fluorescence was detected in channel FL1 with a 527BP±10 band pass filter. Additional series with a more suitable detection range were executed when a 537BP±20 nm filter was available. Particle populations were identified in a SSC-FL1 dot plot (*Figure 15 top*). The raw fluorescence intensity of a single particle (MFI_{NP-raw}) was read out as the median value (see *Figure 15 bottom*). Nanoparticles can only be identified by their fluorescence in channel FL1, as their SSC signal most of the time disappears in the background.

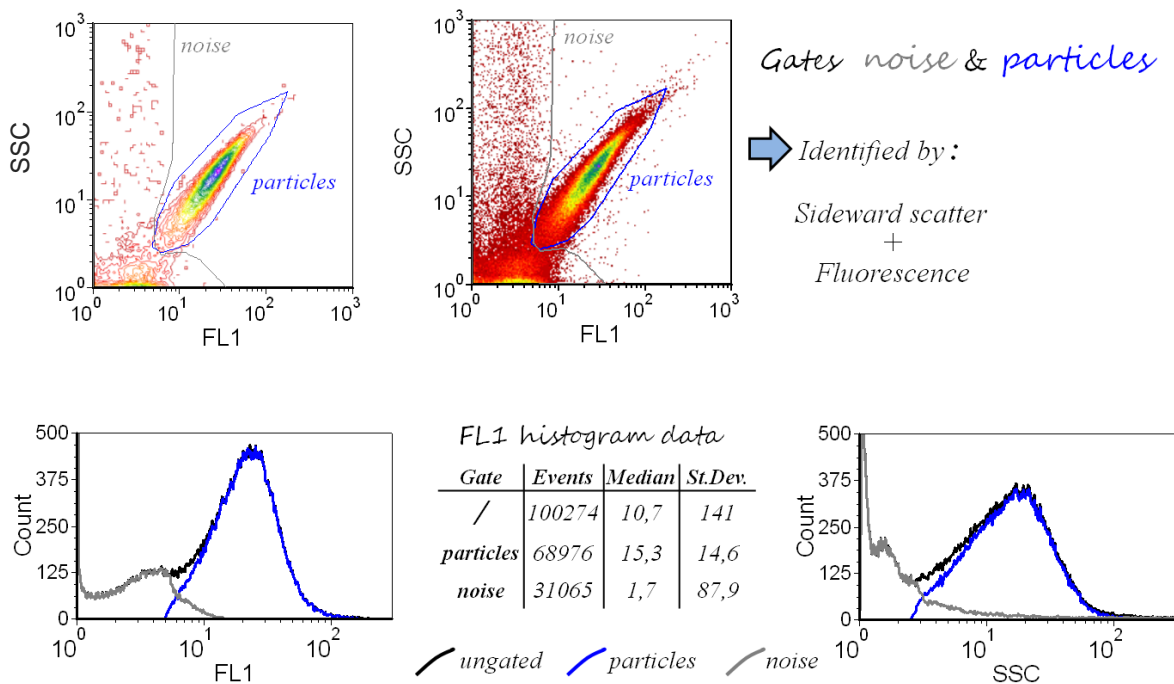


Figure 15. Exemplary flow cytometry data of nanoparticles under ideal conditions: The NPs are gated from the SSC-FL1 density dot plot (top) into histograms of FL1 fluorescence (bottom l.) and SSC scattering (bottom r.). The histograms include the complete data set ‘un-gated’ (black) and the data marked by gate ‘particles’ (blue) and the gate ‘noise’ (grey). The resulting values of mean fluorescence intensity (FL1 median) are listed in the central table.

All events outside the defined particle gate in the SSC-FL1 plot (mostly but not exclusively with weaker FL1 signals than the particles) were defined as noise MFI_{noise} .

Subtraction of the background MFI_{noise} yielded the effective particle fluorescence MFI_{NP} :

$$MFI_{NP} = MFI_{NP-raw} - MFI_{noise} \quad \text{Effective particle fluorescence (X)}$$

3.2.7.3 Protocol for Particle Fluorescence Measurement

For the measurement of single NPs under very clean conditions an ultra-fine in-line filter of 15 nm pore size ‘filter_{15nm}’ (Planova) was installed in the sheath circle flow. A model with 0.3 m² surface was later on switched for one with 1 m² surface with a better flow rate. The supplied sheath liquid was switched for 0.2 μm filtered water and an additional filter unit of 0.2 μm pore size ‘filter_{0.2μm}’ (Millipore) was installed in front of the Planova filter. The highly pure sheath should provide low background conditions and also served as dilution medium of the particle dispersions. Experiments were done with low velocity of $v_{exp} = 0.5 - 1$ [μl sample per s] to ensure maximal thinning and precision of the sample stream. In dependence on the calculated concentration (number of NPs per μl of latex, $N_{0(NP)}$), the dilution factor was set to $40 \cdot 10^6$ till $50 \cdot 10^6$. This ensured an average concentration of 1000 NPs per 0.5 μl in the diluted sample. These experimental conditions, used for high precision analysis of particles, are referred to as ‘settings #1’.

3.2.7.4 Protocol for Volumetric Particle Counting

For absolute particle counting in the medium before and after incubation with cells, the *true volumetric count mode* of the CyFlow ML was utilized. Being the supernatant of a cell experiment (with cell fragments, proteins and particles), these samples were less clean. Therefore they displayed a higher noise level than particle dispersions in clean water. The filter_{15nm} was replaced by a filter_{0.2μm} that is less susceptible to flow interruption which would hamper the counting. Similar conditions as in the cell experiments (concerning instrument settings and sheath liquid) were applied. The cell medium with the NPs was diluted in 0.2 μm filtered phosphate buffered saline without Ca²⁺/Mg²⁺ (PBS, Invitrogen).

A calculation factor F was introduced because the particle population partly overlaps with the noise. By gating only the part of the particle population that assuredly does not overlap with the noise events, referred to as gate ‘NP’, precision was improved (see *Figure 16 green gate NP*). In order to obtain the total particle count, the number of events in gate ‘NP’ was multiplied with a specific factor. This factor F expresses the ratio of events contained in the gates ‘NP’ and ‘all NP’. Gate ‘all NP’ includes the (nearly) complete NP population and can only be derived from a measurement using ‘settings #1’ *i.e.* under very clean conditions. If too much background is present, too many noise events will wrongly be included by the gate ‘all NP’. Factor F is a unique property of the particle dispersion, as it is dependent on the distribution of the NPs’ fluorescence intensity and size. But once measured, it can be applied in every calculation so long as the experiments draw on the same particle dispersion. Problems in samples with a bad signal-noise ratio can be circumvented.

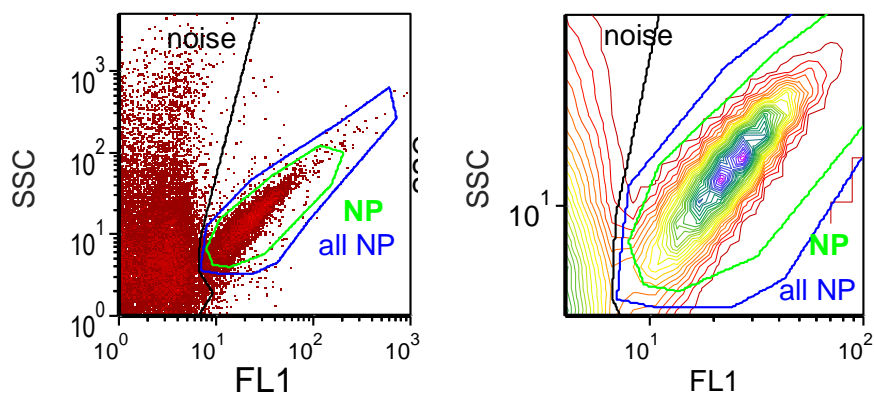


Figure 16. Flow cytometer high precision measurement of BODIPY-marked PMMA particles utilizing ‘settings #1’, depicted in SSC-FL1 plots as density dot plot (left) and as contour plot at higher magnification (right). Gate ‘noise’ (black) marks the background signal and gate ‘all NP’ (blue) marks the vast majority of detected nanoparticles. The fraction of nanoparticles which are fully separated from the background signals (i.e. discernible by strong FL1 signals) are indicated by gate ‘NP’ (green). Gate ‘NP’ is used when particles are measured utilizing ‘settings #2’.

These experimental conditions are referred to as ‘settings #2’. The level of background is slightly increased, but in turn the absolute quantification of the particles in water and in protein-supplied cell medium is not hampered by flow instability.

3.2.8 Flow Cytometry for Cell Analysis

After incubation, HeLa cells were detached with 0.5% trypsin, washed and transferred into PBS for the measurement. Mean fluorescence intensity of the cells was detected in a CyFlow ML running the FloMax software (both Partec) and evaluation was done with FCS Express 3.0 (De Novo). For excitation and scattering a 488 nm laser was used and emission was detected in channel FL1. The normalization factor $f_{1(\text{Pol})}$ (see chapter 3.2.2) enabled measuring the relative uptake efficiency of the different polymeric nanoparticles. Factor $f_{1(\text{Pol})}$ was applied in the competitive and the kinetic uptake studies, to compare the uptake efficiencies of the particle species. The fluorescence intensity of particle-loaded cells was determined by flow cytometry as mean fluorescence intensity (Fl_{Pol}). Hereby Fl_{Pol} represents the data after subtraction of the control value (signal of the particle-free cell samples). Fl_{Pol} was divided by $f_{1(\text{Pol})}$ to calculate the normalized fluorescence intensity FlI_{Pol} :

$$FlI_{\text{Pol}} = \frac{Fl_{\text{Pol}}}{f_{1(\text{Pol})}} \quad \text{Normalized cell fluorescence using } f_{1(\text{Pol})} \quad (\text{XI})$$

Kinetic Cellular Uptake Studies

Temporal uptake kinetics were studied by incubating the cells with the standard particle concentration of $75 \mu\text{g}\cdot\text{ml}^{-1}$ in a volume of 2 ml. The cells were incubated with particles for up to 24 h, then washed, detached and prepared for FC analysis.

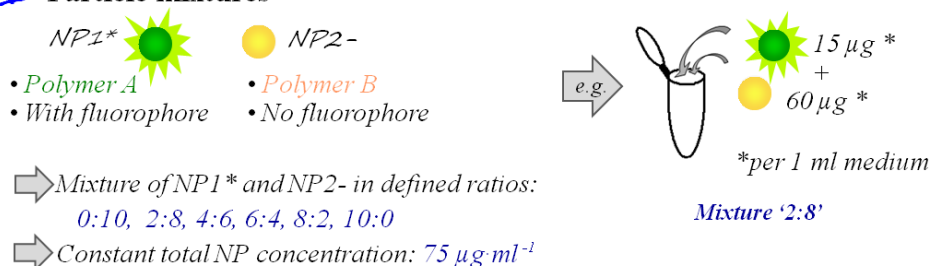
Competitive Cellular Uptake Studies

A mix of 2 particle species (one with and one without fluorophore) was incubated with the cells for 4 h to determine how the co-incubation of different polymeric particles mutually affects the particles' cellular uptake (competitive setup). It was hypothesized that upon simultaneous incubation of two particle types, mutual influence on their cellular uptake can occur because the two materials now are in competition. The NPs were mixed in varying ratios prior to the cell experiment (see *Table 4*) and the experiments were performed as described in *Figure 17*. The total content of particles was $75 \mu\text{g}\cdot\text{ml}^{-1}$ in an incubation volume of 2 ml. All data shown is the mean value of two independent experiments in which each data point was done in triplicate.

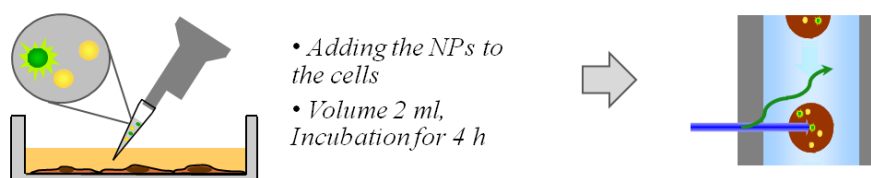
Table 4. Mixtures of fluorescent (NP1+, polymer 1) and non-fluorescent (NP2-, polymer 2) particles for flow cytometry analysis in a competitive setup.

	Mixture solid content per ml (NP1+) : (NP2-)					
	10 : 0	8 : 2	6 : 4	4 : 6	2 : 8	0 : 10
NP1+	75 μg	60 μg	45 μg	30 μg	15 μg	0 μg
NP2-	0 μg	15 μg	30 μg	45 μg	60 μg	75 μg

1 Particle mixtures



2 Cell experiment: Incubation and FCy measurement



3 Repeat experiment vice versa: With a reverse set of NPs



Figure 17. Setup and execution of the competitive cellular uptake experiments.

Quantitative Cellular Uptake Studies

For flow cytometry experiments the cells were seeded in Ibidi plates (triplicate setup) and allowed to attach over night. In the later series each FC experiment was coupled to a corresponding cLSM experiment, as explained in chapter 3.2.6.2. The cells were incubated with the particles and prepared for the FC analysis. In a first set of experiments a particle concentration of $500 \mu\text{g}\cdot\text{ml}^{-1}$ in the volume $600 \mu\text{l}$ was applied. In the following series the particle dose was set to $300 \mu\text{g}\cdot\text{ml}^{-1}$, volume $500 \mu\text{l}$, to reduce the number of internalized NPs. FC measurements were done with the CyFlow ML (Partec) running a 488 nm laser at 200 mW. The 'settings #2' were applied as described above, with minor adjustments to FCS and SSC settings due to the large size of cells. By using similar instrument settings (laser power and photomultiplier PMT fluorescence signal amplification) as for the single nanoparticle detection, comparability with the data from single particle measurements was ensured. Each measurement was done in triplicate, repeated at least two times and >3000 cells were detected for data acquisition. The mean fluorescence intensity of particle-free control cells (MFI_{-NP}) was subtracted from the MFI value of the cells exposed to particles (MFI_{+NPs}). The resulting value ΔMFI was divided by the mean fluorescence intensity of a single particle MFI_{NP} . This way the number of internalized particles per cell could be obtained.

4 Results and Discussion

4.1 Nanoparticles

For the competitive cell uptake studies a set of three different polymeric particles (PMMA, PS and PLLA) was synthesized. Based on these particles with similar physico-chemical properties, the effect of the polymer nature on the endocytosis into HeLa cells was singled out. Furthermore, NPs with high fluorescence intensity were required for the introduction of the single particle measurement in flow cytometry. The synthesis of PS particles with the maximal possible dye loading was part of this project. The utilized dyes were provided by scientists within the Landfester and the Müllen groups at the Institute. Furthermore functionalized PS particles with amino groups on the surface were synthesized. The larger NPs were well suited for introduction of the SPM method at the flow cytometer, as their large size would make their detection in the FC easier. With SPM established, the amino-functionalized particles would provide a proven system to be used in the absolute quantification of NPs in cells. Unlike the other synthesized SDS-stabilized particles, these amino-functionalized NPs offered a high cellular uptake efficiency – which could further improve the precision of the absolute NP quantification method.

4.1.1 Synthesis of Polymeric Particles

The influence of polymer properties on the cellular uptake of a nanoparticle species was studied with PS, PMMA and PLLA particles with similar physico-chemical properties. In addition it was studied how these affect the uptake of each other by co-incubation of two different particle species (competitive setup). For this purpose the miniemulsion technique was applied to create two sets (fluorescent and blank) of PMMA, PLLA and PS particles with the surfactant SDS. No coagulum was formed in the flasks of PS or PMMA samples after polymerization. The size distribution was narrow and the solid weight content indicated almost 100% conversion *i.e.* 18-20%-wt. of expected 20%-wt. No coagulates were observed in the PLLA samples after synthesis and the size distribution was narrow. Several batches with similar properties were created following the identical synthesis protocol. These were summarized and termed as described in *Table 5*. The particles for the cell experiments were washed and characterized. Zeta potential, polymer molecular weight, glass transition temperature, dye content and stability of the washed NPs after incubation with serum proteins were determined (see *Table 5*).

Table 5. Physicochemical characteristics of the particle species for the competitive experiments, before and after incubation in the cell medium for 24 h.

Sample	Polymer type	ζ [mV]	Dye Content [mg·g _{Pol} ⁻¹]	Diameter [nm]	M _w [g·mol ⁻¹]	T _g [°C]
PS1	Polystyrene	- 42 ±3	0	107 ±18	313·10 ³	98
PS2		- 41 ±3	0.28	112 ±18		
PS2_a.i.		- 32 ±7	0.28	148 ±26		
PLLA1	Poly(L-lactide)	- 38 ±6	0	115 ±21	77·10 ³	not found
PLLA2		- 37 ±6	0.38	116 ±22		
PLLA2_a.i.		- 30 ±8	0.38	159 ±31		
PMMA1	Poly(methyl methacrylate)	- 40 ±4	0	127 ±24	509·10 ³	122
PMMA2		- 39 ±5	0.29	112 ±20		
PMMA2_a.i.		- 29 ±7	0.29	143 ±28		

'a.i.' stands for 'after incubation' in cell medium containing 10% of fetal calf serum.

DLS analysis as well as electron microscopy studies had revealed an average size of 115±15 nm, as shown in *Figure 18* and in *Table 5*. The zeta potential values were also in a comparable range, so that the variations should not significantly affect the cellular uptake. The particles were well suited for the competitive experiments, as significant changes of the uptake mechanisms only appear to very small (<40 nm) or very large (>300 nm) particles¹⁴⁸.

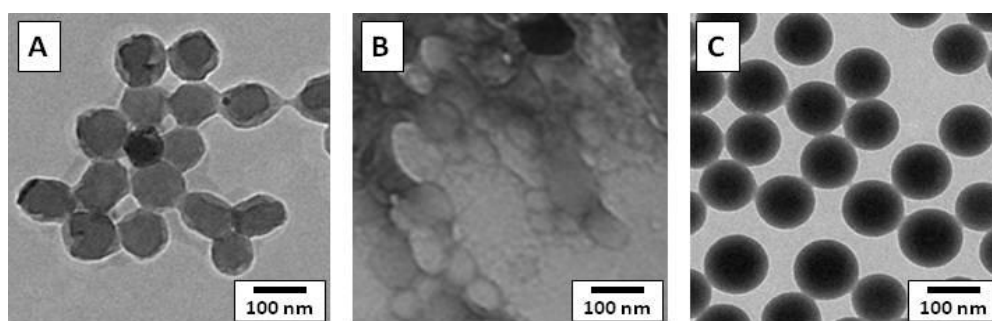


Figure 18. TEM images of dialyzed particles of PMMA (A), PLLA (B) and PS (C). PMMA and PLLA samples were carbon-coated for better stability in the electron beam.

To compare the fluorescence based data of the cell uptake experiments, the fluorescence intensity of the different particle species was normalized using specific normalization factors. These factors $f_{1(\text{Pol})}$ (based on the particle fluorescence) and $f_{2(\text{Pol})}$ (based on the particle dye content) were derived as described in chapter 3.2.2. For $f_{1(\text{Pol})}$, the emission of aqueous particle dispersions (with varied solid content) was measured and plotted in a chart with the solid content. Linear fits on these graphs revealed slope values of 55 (PS2), 57 (PMMA2) and 100 (PLLA2). A division by the slope factor of the PS particles resulted in the factors $f_{1(\text{Pol})}$ of 1.00 (PS), 1.04 (PMMA) and 1.81 (PLLA). Likewise factor $f_{2(\text{Pol})}$ was calculated. The particles' dye content was determined by absorption spectroscopy and all dye loadings

($m_{\text{dye(Pol)}}$) were divided by that of the PS sample. The normalization factors obtained via emission spectroscopy correlated with those from the UV analysis (Table 6).

Table 6. Comparison of the fluorescence normalization factors $f_{1(\text{Pol})}$ and $f_{2(\text{Pol})}$.

Sample	$f_{1(\text{Pol})}$ from dispersed NPs	$f_{2(\text{Pol})}$ from dissolved NPs
PS2	1.00	1.00
PMMA2	1.04	1.04
PLLA2	1.81	1.38

From visual observations the particle dispersions displayed different colors, ranging from yellow-orange (PLLA) to orange (PMMA) and pink (PS) which is due to an influence of the aggregation effect in polymeric material on the optical properties of the incorporated perylene dye PMI. The increasing red shift correlates with a decrease of the $f_{1(\text{Pol})}$ values. Such behavior was already observed in systems of higher similarity than the 3 polymers used in this paper, *i.e.* in copolymeric particles that only differ in the chain length of the methacrylate comonomer¹⁶. For perylene (bis)imide dyes it is known that a decrease in polarity of the surrounding solvent or polymer increases the aggregation of dye molecules. This stacking of the dye is accompanied by a spectra shift¹⁴⁹, so that increased aggregation of the applied dye PMI most likely results in a red shift of absorption and emission. As the fluorescence intensity of the uptake into cells was done with un-dissolved nanoparticles inside of cells all cell experiment data was calculated with the normalization factor $f_{1(\text{Pol})}$ derived from dispersion measurement.

SUMMARY Applying the miniemulsion technique, PS and PMMA NPs were synthesized by radical polymerization, whereas PLLA particles were created by a combination of miniemulsion and solvent evaporation process³³. The anionic surfactant sodium dodecylsulfate SDS provided both a negative zeta potential and a small size distribution of the particles. To compare the uptake of the different species a normalization factor for the different particles' fluorescence intensities had to be introduced. It was demonstrated that the fluorescence intensity of PLLA NPs was highest, followed by PMMA and PS particles, even though all particles had been synthesized with the same dye-polymer ratio. The calculated factors based on the measurement of dissolved NPs did not perfectly concur with those based on the analysis of intact dispersed NPs. It therefore was concluded that the particle material influenced both the dye loading efficiency and later on the fluorescent properties of the incorporated dye. An influence of the polymer properties, such as *e.g.* hydrophobicity, on incorporated perylene was reported earlier^{16, 149}. The particles were perfectly suited for the competitive experiments, as significant changes of the uptake mechanism only appear for very small or very large nanoparticles¹⁴⁸. Moreover the washed particles were stable in the presence of serum proteins.

4.1.2 Synthesis of Amino-Functionalized Polystyrene Particles

Amino-functionalized particles were obtained by addition of 2%-wt. amino ethyl methacrylate (AEMH) as a comonomer in the miniemulsion. The dyes Lumogen F Yellow (LFY) and F Red (LFR), as well as the standard perylene monoimide (PMI), were used for fluorescence marking. Residues in the flasks after synthesis indicated that the polymerization in miniemulsion had been affected by the addition of AEMH. Particle size distribution was measured by DLS (see *Table 8*) and demonstrated that the latices were not monodisperse. Varying the height of the sonication rod during ultrasound treatment (see *Table 7*) did not have an effect neither did more intense stirring prior to the sonication (by using a different agitator) or a longer ultrasound treatment (to counter the increased viscosity of the water phase).

Table 7. DLS data of the amino-functionalized polystyrene particles.

Sample	Specification of the sonication	Supplementary information	
	Distance between rod tip and glass bottom [mm] and duration [min] in this rod position		
PS-AM-1	2 min at 2 mm	no ultrasound applied	
PS-AM-2	"		
PS-AM-3	/		
PS-AM-4	1) 0:10 min at 15 mm, 2) 0:30 min at 15 mm 3) 0:30 min at 2 mm	10 h at 63 °C, then 5 h at 72 °C No ice, sonified in 5-10 °C water	
PS-AM-5	"		
PS-AM-6	1) 0:10 min at 15 mm, 2) 1:50 min at 2 mm		
PS-AM-7	"		
PS-AM-8	"		
PS-AM-9	"		larger agitator used

Table 8. DLS data of the amino-functionalized polystyrene particles.

Sample	Name	Dye [mg]	Particle size [nm]		
			X ₅₀	X ₁₀	X ₉₀
PS-AM-1	AM-1	/	197	162	237
PS-AM-2	AM-2	2 mg LFY	211	178	250
PS-AM-3	AM-3	6 mg LFR	135	111	163
PS-AM-4	AM-4	5 mg LFR	199	165	238
PS-AM-5	AM-5	5 mg PMI	255	216	299
PS-AM-6	AM-6	6 mg PMI	208	173	249
PS-AM-7	AM-7	4 mg PMI	221	184	265
PS-AM-8	AM-8	6 mg LFR	227	196	265
PS-AM-9	AM-9	6 mg LFY	215	184	249

It was observed that all samples had a large size distribution when the DLS data was fitted with a Gauss function. Electron microscopy studies of the first samples (*Figure 19*) confirmed this.

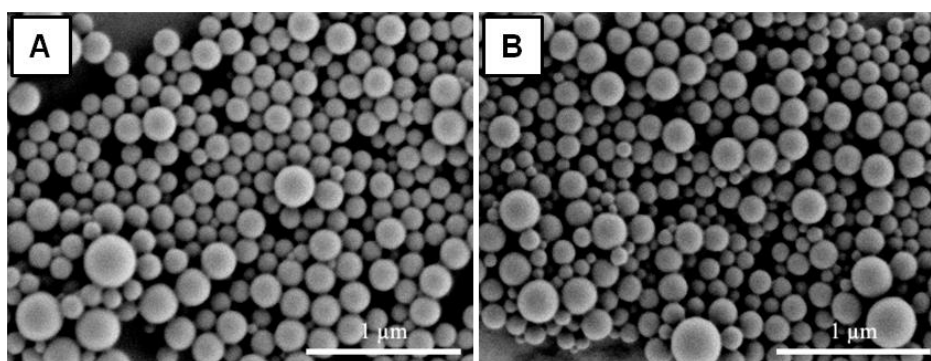


Figure 19. Scanning electron microscopy analysis (SEM) of PS-AM-1 (A) and -2 (B).

A sedimentation step of 1:5 diluted PS-AM-1 demonstrated that the mean particle size in the supernatant could be reduced to 190 nm and the size distribution narrowed (data not shown). In the PS-AM series the average particle sizes were around 190-220 nm, only two samples stood out with a mean diameter that was particularly small (PS-AM-3, 135 nm) or large (PS-AM-5, 255 nm). For sample PS-AM-3, which was obtained without ultrasound, the DLS analysis had indicated a more homogenous size distribution and a small particle size. The SEM image showed that the majority of particles in PS-AM-3 were in the range of 100 nm, with a few NPs in between that seemed significantly larger (*Figure 20*).

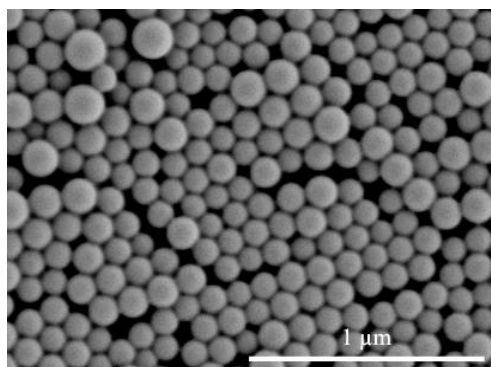


Figure 20. SEM analysis of sample PS-AM-3.

The sample was analyzed in a Nicomp DLS machine which offers an algorithm for size calculation that is more suitable for multi-modal distributions. It was found that in this sample, a bimodal distribution with average particle sizes of 100 and 300 nm was present (*Figure 21A*). The majority of particles were sized around 100 nm, which is slightly smaller than the previous analysis where the bimodal distribution was not taken into account. When weighting the particle numbers, it became obvious that the 2nd population contained only few particles compared to the 100 nm population (*Figure 21B*).

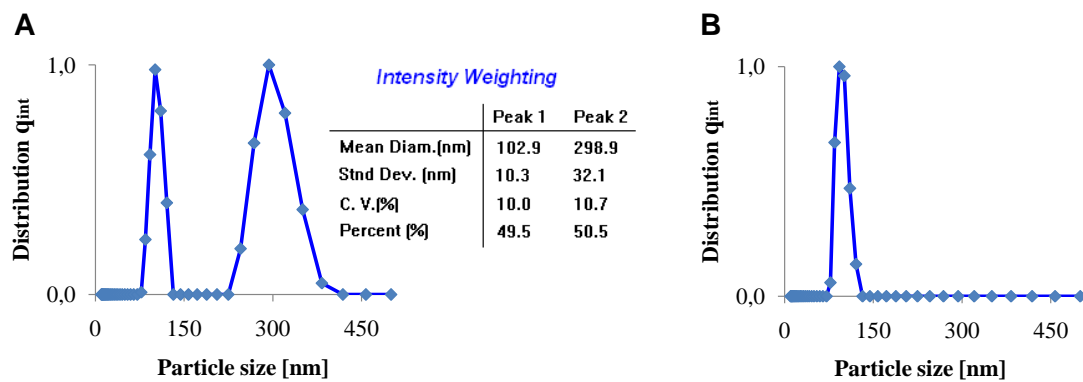


Figure 21. DLS measurement of sample PS-AM-3 in a Nicomp machine. Shown are the intensity weighted size distribution graph and data table (A) as well as the number weighted graph (B).

Sample PS-AM-5 with particularly large particles was also imaged in SEM, see *Figure 22*. Most spheres were sized around 200-300 nm, whereas a few seemed to measure approx. the double diameter (>500 nm). With their larger size these spheres should yield strong signals and were therefore well suited for a test of single particle measurement in the FC.

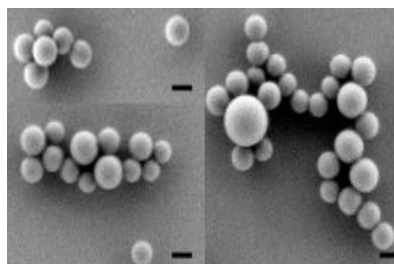


Figure 22. SEM images of sample PS-AM-5, scale bar 200 nm.

SEM indicated that in sample PS-AM-5 the size distribution was indeed bimodal and this was confirmed by DLS (see *Figure 23*). However in the EM images the particles were slightly smaller than the Nicomp DLS analysis showed, due to the differences in hard core diameter (TEM) and hydrodynamic diameter (DLS).

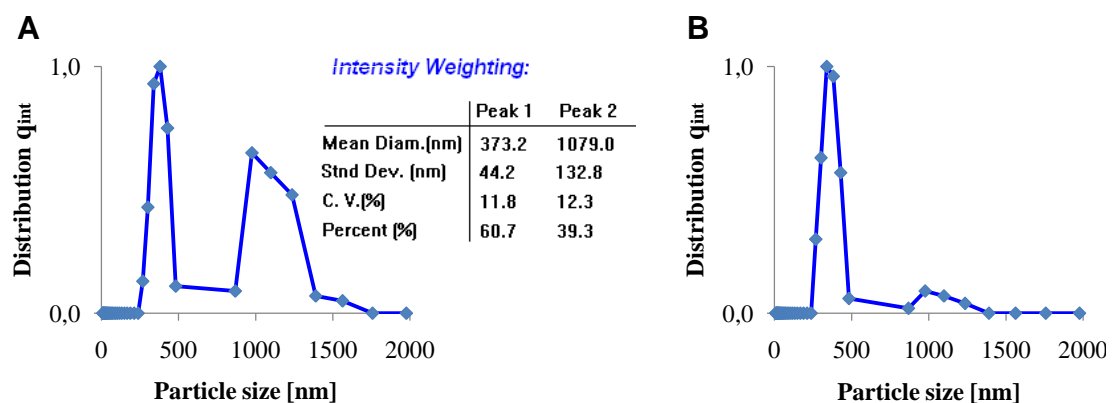


Figure 23. DLS measurement of sample PS-AM-5 in a Nicomp machine. Shown are the intensity weighted size distribution graph and data table (A) as well as the number weighted graph (B).

In FC studies the bimodal nature of this sample could be confirmed because two populations of particle events were distinguished by scatter and fluorescence. A similar analysis of PS-AM-2 particles via flow cytometry demonstrated that there was indeed only one population (with a broad but monomodal size distribution as confirmed by the Nicomp DLS analysis). Furthermore it was observed that PS-AM-5 created a stronger scattering signal and therefore had to be larger than PS-AM-2, even though probably slightly smaller than appeared in the DLS. The observations in FC matched the Nicomp DLS data in that both methods demonstrated the bimodal size distribution of PS-AM-5 (*Figure 23*).

SUMMARY It is common practice to add functional groups to the nanoparticles' surface but in the competitive studies of this thesis the nature of the pure polymer was the center of interest. Therefore a series of particles was synthesized without functionalization. Specific properties such as amino or carboxyl groups affect the particle-protein interaction¹⁵⁰ and increase the cellular uptake efficiency⁹⁶. Functional groups further provide the base coupling methods such as *e.g.* the EDC reaction (N-ethyl-N'-(3-dimethylaminopropyl) carbodiimide hydrochloride) to conjugate compounds¹⁵¹⁻¹⁵² or proteins¹⁵³⁻¹⁵⁶ to the spheres' surface. In this thesis the synthesis of functionalized PS spheres were created using 2%-wt. (referred to the monomer) of the amino comonomer 2-aminoethyl methacrylate hydrochloride (AEMH). The chosen steric surfactant Lutensol AT50, a PEG compound, provided sufficient stabilization for the miniemulsion. A broad monomodal particle distribution, in some cases a bimodal one, was observed which was not influenced by variations of the sonication process. The two fractions could be separated by *e.g.* sedimentation, field flow fractionation or chromatography.

4.1.3 Incorporation of Fluorescent Markers with High Loading

One of the aims in this thesis was to establish the measurement of single submicron particles in flow cytometry. This would give access to a normalization factor for precise comparisons of different particle species regarding their efficiency in cellular uptake. However, if applied properly it would also give rise to particle characterization and to an absolute quantification of NPs in cells. The crucial part in FC single particle measurement (SPM) has always been the signal-to-noise ratio and this aspect could be improved by using spheres of maximum fluorescence intensity. For this purpose polymeric NPs were synthesized with high loadings of different dyes to validate the (maximal) solubility of the fluorophores' in the monomer. Furthermore the fluorophores' suitability for flow cytometry SPM should be tested. Synthesis was done following the standard recipe with 1.2%-wt. of SDS. Larger particles (PS-Lut-1) were obtained with 3.33%-wt. of Lutensol AT50, which is known to yield larger spheres with narrow size distribution⁹¹. This sample was also synthesized with a high dye loading, so that the large size and the high dye content together should yield a particularly strong fluorescence signal. The synthesis of sample PMMA-BP1-2 was done with 1.5%-wt. of SDS. Additional PMMA particles were provided by members of the group of Prof. Dr. Landfester. These were

also synthesized with 1.2%-wt. of SDS. The PMMA-AT3 particles were applied in early STED microscopy and in FC single particle detection. The sample CH235-3 with the BP1 dye was used in SPM to test the lower detection limit. The particle samples are listed in *Table 9*.

Table 9. Properties of the studied nanoparticles with different fluorescent markers.

Particle	Dye added [per 6 g monomer]	Dye absorption maximum	Latex color	Solid content %-wt.	Particle size [nm]		
					X ₅₀	X ₁₀	X ₉₀
PS-AM-2	2 mg LFY	578 nm	yellow	19	211	178	250
PS-AM-8	6 mg LFR	"	rose	20	227	196	265
PS-LFY-1	2 mg LFY	488 nm	yellow-green	20	112	93	134
PS-LFY-2	4 mg LFY	"	yellow	20	125	101	153
PS-LFY-3	8 mg LFY	"	yellow	20	114	93	140
PS-LFY-4	12 mg LFY	"	orange	19	118	99	141
PS-SDS-4	4 mg MS1B	511 nm	orange	19	124	101	153
PS-SDS-5	4 mg MS1C	588 nm	purple	19	115	93	143
PS-SDS-7	18 mg Ya795	499 nm	yellow	12	154	129	184
PS-Lut-1	32 mg MS1B	511 nm	orange	17	178	153	206
PMMA-BP1-2	10 mg BP1	520 nm	peach	19	155	133	180
CH235-3*	48 mg BP1	520 nm	orange	20	65±6 nm		
PMMA-AT3**	4 mg BP2, ca.	620 nm	blue	1.47	121±10 nm		

* The samples PMMA-AT3 and CH235-3 were provided by members of the work group.

** The sample was provided after dialysis.

Particle size and solid content of the dispersions were found to be in the expected range except in the case of PS-SDS-7 (12%-wt.) and PS-Lut-1 (17%-wt.). Due to the large amount of dye in these recipes the miniemulsion was less stable and the synthesis impaired.

With the PS-LFY series, the influence of the particle fluorescence intensity on the signal strength in the flow cytometer was to be studied. It was obvious that the changes in dye concentration in the samples PS-LFY-1 to -4 had affected the dye. The samples with more dye had a slightly red-shifted color. The absorption of the dissolved particles was measured in THF to retrieve the relative (compared to sample PS-LFY-1) dye content, see *Figure 24*.

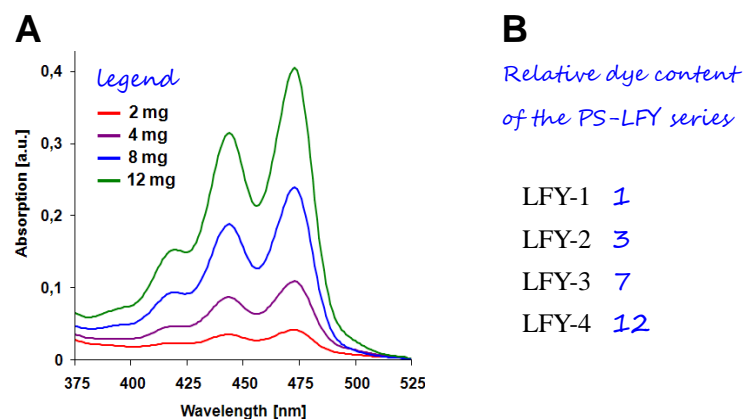


Figure 24. The absorption of the PS-LF series at 472 nm was measured (A) and the relative dye content, referring to sample LFY-1, was calculated (B).

The calculation yielded relative dye contents of 1 (LFY-1), 3 (LFY-2), 7 (LFY-3) and 12 (LFY-4), see *Figure 24B*. Quenching and spectra shifts can alter the effective emission intensity of nanoparticles, especially if detection is only done in a narrow bandwidth (as is in the used flow cytometer). But the amount of fluorophore is generally a good approximation for the particles' fluorescence intensity¹⁵⁷⁻¹⁵⁸. In this case the absorption analysis did not fully correlate with the amount of dye added in the synthesis. Likely the measurement was less precise for the samples LFY-1 and -2, as they contained only little dye and the absorption peak was very narrow.

The sample PMMA-BP1-2 was chosen as the main particle for the quantitative cell studies for several reasons: i) the diameter of 160 nm was an ideal compromise of small particle size (at the lower detection limit of the cytometer) and a yet tolerable signal-to-noise ratio; ii) the sample was monomodal with a narrow size distribution (see also EM image in *Figure 25*); iii) the dye was added as a comonomer and was therefore covalently fixed; iv) BP1 was also fully photostable and offered the possibility for STED imaging and v) the particle demonstrated high fluorescence intensity in the flow cytometry measurements (see chapter 4.3.3).

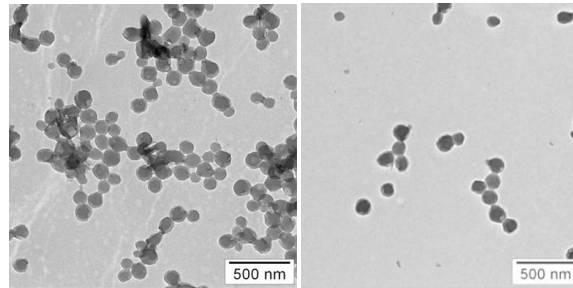


Figure 25. TEM images of carbon-coated PMMA-BP1-2 particles.

The number of NPs per volume had to be calculated so that the lattices could be used for flow cytometric single particle measurement (SPM).

Calculation of the particle concentration

The presented approach was based on the assumption that all NPs were spheres of similar diameter (which was the average size as obtained by DLS) and with a material density in the range of 1 [g·cm⁻³].

$$\blacksquare \text{ Weight percent of the sample (\%-wt.)} \quad \% \text{-wt.} = \frac{m_{\text{Monomer}} + m_{\text{Ultrahydrophobe}}}{m_{\text{cont.Phase}(H_2O+\text{Tenside})}} \quad (\text{XIIIa})$$

$$\text{Approximately} \quad \% \text{-wt.} = \frac{m_{\text{Monomer}}}{m_{\text{cont.Phase}(H_2O)} + m_{\text{Monomer}}} \quad (\text{XIIIb})$$

$$\blacksquare \text{ Particle volume: } V_{NP} [\text{nm}^3] \quad V_{NP} = \frac{4}{3} \pi r^3 = 4.18 \cdot r_{[\text{nm}]}^3 \quad (\text{XIV})$$

$$\blacksquare \text{ Particle mass: } m_{NP} [\text{mg}] \quad m_{NP} = \rho_{[\text{g}\cdot\text{cm}^{-3}]} \cdot V_{NP} \cdot 10^{-18} \quad (\text{XV})$$

■ Particle number in 1 μl : N_{NP} [$\text{NPs}\cdot\mu\text{l}^{-1}$]

$$N_{NP(\text{per } 1\mu\text{l})} = \frac{m_{\text{Polymer}(\text{per } \mu\text{l})}}{m_{NP}} = \frac{\text{wt}\%(\text{per } \mu\text{l})}{m_{NP}} = \frac{\frac{m_{Pol}}{m_{Pol} + m_{H_2O}}}{\rho_{NP} \cdot V_{NP}} \quad (\text{XVI})$$

During the particle synthesis, minor deviations in the sample composition were already introduced by sonication, refilling, filtration *etc.* Therefore some minor components of the recipe, *e.g.* the hexadecane, were neglected in the calculations (see formula XIIIb).

As a further fine-tuning of this model, the calculations were based on the size distribution curve (measured by DLS) instead of using the mean particle size. This way, the calculation of the NP number was less susceptible to broad size distributions.

Calculation of the particle concentration based on the size distribution

This approach was based on the weighted NP size distribution as demonstrated in Table 10. Calculations based on the average NP size are less precise than those based on the weighted size distribution, especially in the case of broader size distributions. Therefore the calculations based on the size distribution were taken as reference for the volumetric counting of particles in the FC. This was required only for the ‘main’ samples PMMA-BP1-2, PS-Lut-1 and PS-SDS-7.

Table 10. Exemplary data how the number of NPs per volume was calculated based on the size distribution.

X [nm]	$q_{\text{int}} \lg$ [a. u.]	$m_{(NP)}$ [mg]	$m_{(NP)} \cdot (Z)$	% m	m_{eff} [mg Pol. per μl]	Number of NPs: $m_{\text{eff}} : m_{(NP)}$
72	0	2.08E-13	0.00E+00	0.00	0.0000	0.00E+00
78	0.05	2.59E-13	1.29E-14	0.04	0.0001	3.21E+08
83	0.24	3.22E-13	7.72E-14	0.25	0.0005	1.54E+09
.
.	.	.	<i>etc.</i>	.	.	.
.
172	0.08	2.83E-12	2.27E-13	0.73	0.0015	5.13E+08
185	0	3.52E-12	0.00E+00	0.00	0.0000	0.00E+00
Sum	31.73	$9.83 \cdot 10^{-11}$	100	0.2		$1.02 \cdot 10^{11}$ in 0.5 μl

X: particle diameter, **$q_{\text{int}} \lg$:** distribution density, **$m_{(NP)}$:** mass of one particle, **$m_{(NP)} \cdot Z$:** Mass of the fraction of a specific size range (weighted by numbers), **%m:** percentage weight share of one fraction, **m_{eff} :** effective mass of one fraction (referring to 0.2 μg which is the amount of monomer that is contained in 1 μl of 20%-wt. latex)

For all other experiments the data derived from the average NP size provided a good approximation of the NP number per volume. The sample concentrations were calculated as required (see Table 11). Amino-functionalized PS particles, due to their polymodal size distribution, were not used for precise NP counting in the flow cytometer. These were used in

the screening for new fluorophores and for other measurements that do not require the precise NP concentration.

Table 11. Sample concentrations [particles per volume] as calculated based on the particle size distribution (A) or on the average particle size (B).

Sample	Size [nm]	% -wt.	Concentration [NPs per 0.5 μ l]	
			A via size distribution	B via average size
PMMA-BP1-2 *	160	22*	$4.49 \cdot 10^{10}$	$5.1 \cdot 10^{10}$
PS-Lut-1	179	17	$2.56 \cdot 10^{10}$	$2.9 \cdot 10^{10}$
PS-SDS-7	154	12	$2.75 \cdot 10^{10}$	$3.1 \cdot 10^{10}$
CH235-3	70	20	/	$5.6 \cdot 10^{11}$
PS-LFY-3	118	20	/	$1.2 \cdot 10^{11}$
PS-AM-2 **	211	20	/	$2.0 \cdot 10^{10}$
PS-AM-5 **	255	20	/	$< 1.6 \cdot 10^{10}$
PS-AM-8 **	227	19	/	$1.6 \cdot 10^{10}$

* A different aliquot of the particles was used later on and meanwhile sedimentated particles were removed and a new solid content was measured.

** Amino-functionalized NPs were added to this list for completion. But as those samples had a broad (PS-AM-2 & -8) or even bimodal (PS-AM-5) size distribution, their concentration could not be calculated precisely. The NP concentration of PS-AM-5 was expected to be lower than in the other 2 amino-functionalized samples, due to the larger particle size.

SUMMARY The proved method of radical polymerization in miniemulsion was applied to synthesize polymeric nanoparticles with a particularly high loading of fluorescent markers. Spheres of PS and PMMA with various dye molecules could be synthesized using SDS as a surfactant. The ionic surfactant ensured a low size distribution but it was observed that an initial high dye loading (0.4% -wt. referred to the monomer) affected the synthesis. High dye concentration resulted in low monomer conversion and large particle size, however the size distribution remained monomodal and rather narrow. Several sets of highly fluorescent PS and PMMA spheres sized between 100-200 nm were obtained to be used in flow cytometry. The detection of single nanoparticles in a non-scanning flow cytometer is difficult due to the bad signal-to-noise ratio and has rarely been reported up to now^{18, 139, 159}.

Incorporating a highly fluorescent dye in polymer nanoparticles is the most convenient way to detect these spheres in a flow cytometer – in particular if their scattering signals do not surpass the background signals. It was of particular importance to provide a fluorophore which has a strong emission in the precise band width range of the FC detection channel – and which retains this emission when incorporated inside the particle with a high concentration.

Incorporating highly fluorescent dye is the most suitable way to detection of polymer spheres in the FC whose scattering signals do not surpass the background level.

4.2 The Effect of Polymer Nature on the Cellular Uptake

Numerous properties of a particle (*e.g.* shape, size, softness, hydrophobicity, surface charge, protein corona) act in combination to guide the particle-cell interaction. These factors are responsible for the route of entry, the uptake efficiency and in consequence the intracellular fate of a particle. But a direct comparison of the raw particle material regarding its endocytotic properties is rarely approached and specific information in the literature is rare. This project, which was focused on PS, PLLA and PMMA particles, could provide such a comparison.

The effect of the polymer nature on the particle-cell interaction was singled out, amongst others by a competitive experimental setup. In a unique competitive setup, two particle species were co-incubated with the cells. The cellular uptake was studied in a qualitative (cLSMy and TEM) and a semi-quantitative (FCy) way. The basic idea behind the co-incubation experiments was that any cellular uptake mechanism should have a certain capacity or maximum rate of endocytosis. Therefore, when two particle species are incubated simultaneously and possibly even target the same endocytotic pathway, they might compete for a limited resource. This might concur with a competition for certain coating proteins that are rare in the fetal calf serum and thus available only in small quantities. Or the limited resource could be those domains on the cell surface where binding of the NPs occurs. The competitive experimental setup could reveal that the particles mutually affect their uptake, *e.g.* in such a way that the internalization of one particle species is hindered.

Parts of this topic are published in the paper ‘Hoecherl A. *et al*, *Competitive cellular uptake of nanoparticles made from polystyrene, poly(methyl methacrylate) and polylactide*’¹⁶⁰.

4.2.1 Interaction of Polymeric Nanoparticles with Cells

Prior to the co-incubation, the 3 particle species were incubated separately with cells and imaged by cLSMy. The particles’ intracellular localization should be investigated and furthermore NPs that were merely adhered to the cell surface should be identified. Intracellular localization of all 3 species was proven and no extracellular NPs were found adhered to the cytoplasmic membrane. This was especially important for the cytometry studies, as this method cannot differentiate between internalized particles and those only attached to the cell surface. Smaller particle aggregations were spread throughout the cell, likely gathered in endosome-like structures, see *Figure 26*. In the case of PLLA (*Figure 26B*) the accumulations appear to be slightly larger. In general, all NPs were found intracellular but the stronger PLLA signals indicated larger particle accumulations than for the PMMA and PS samples. The negative control displayed no particle signals.

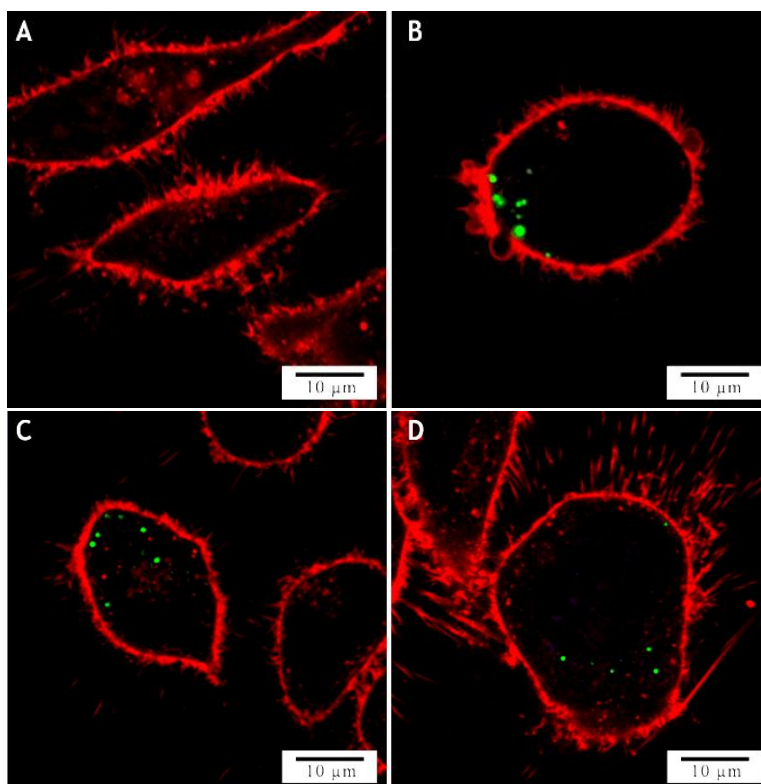


Figure 26. Uptake of fluorescent nanoparticles made from PLLA (B), PMMA (C) and PS (D) in HeLa cells after 4 h incubation time with 75 μg of polymer. (A) depicts the control sample without NPs. The cytoplasmic membrane (red) was stained with Cell Mask Orange and the NPs are pseudo-colored in green.

For a more quantitative approach the uptake of the 3 analyzed particle species was studied by flow cytometry which allows for the rapid analysis of thousands of cells. Prior to the competitive studies, the cellular uptake of PS, PLLA and PMMA particles was studied in single species experiments. The cellular uptake in dependence of incubation time (*Figure 27*) and of particle concentration (*Figure 28*) was measured. As an important factor of particle-cell interaction, the adsorption of serum proteins on the different polymeric particles was studied by DLS and by zeta potential measurements.

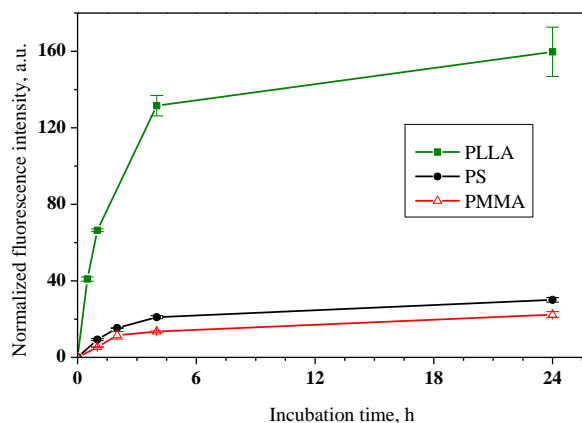


Figure 27. Uptake kinetics of PLLA2 (square), PMMA2 (triangle) or PS2 (dot) into HeLa cells after 0 to 24 h incubation with $75 \mu\text{g}\cdot\text{ml}^{-1}$ of NPs. The median values of fluorescence were normalized by the NP fluorescence utilizing factor $f_{I(\text{Pol})}$ to retrieve the normalized fluorescence intensity $F_{I(\text{Pol})}$. The graph of $F_{I(\text{PLLA})}$ shows the highest signal intensities and thus the greatest uptake for PLLA particles.

From Figure 27 it can be seen that more PLLA particles were internalized in the cells in comparison to the other polymeric NPs. After 24 h of incubation the uptake of PLLA particles was approximately 5 times higher as compared to those of PS and PMMA. The increased uptake of PLLA spheres correlated with larger intracellular particle accumulations compared to PMMA and PS, as visualized by cLSM (Figure 26).

This superior internalization rate could be based on an enhanced interaction of PLLA with the cells. The main differences between PLLA or PMMA and PS particles are the following: The lowest molecular weight, the absence of T_g and the presence of covalently bound carboxyl groups on the surface of PLLA particles (see Table 5). All these factors might affect the interaction of the serum proteins with the particle, resulting in different thickness and chemical composition of the protein corona around the particle¹⁶¹.

In order to study the protein adsorption, all particles were incubated without cells in DMEM10% *i.e.* in the standard cell medium supplied with 10% FCS. After separation of the particles by centrifugation, the average size and zeta potential were measured and compared with the data measured before incubation. The obtained values are summarized in Table 5. After incubation with serum supplied cell medium, the adsorption of the serum proteins on the particle surface caused a decrease of zeta potential. A value of approximately -30 mV after incubation was measured for all three types of particles. The adsorption of proteins on the particle surface lead to an increase of the average diameter and of the size polydispersity. The difference in size is slightly higher for the PLLA particles as compared to the other ones. It was concluded that the amount of protein adsorbed onto the PLLA surface was higher as compared to PMMA and PS particles.

The concentration-dependent uptake of three types of polymer particles was studied by a 4 h incubation experiment with particle concentrations in the range of 15 to $75 \mu\text{g}\cdot\text{ml}^{-1}$. These concentrations correspond to the amount of fluorescent particles in the competitive studies.

Previously it was shown that the saturation effects of SDS coated particles will not occur at such low particle concentrations, but rather above several $100 \mu\text{g}\cdot\text{ml}^{-1}$ ¹⁶². As can be seen in *Figure 28* the different polymeric particles did indeed yield a linear course within the range of experimental error. It was concluded that up to a concentration of $75 \mu\text{g}\cdot\text{ml}^{-1}$ the dependence of cellular uptake for all three types of polymer particles was entirely direct and no saturation effect occurred.

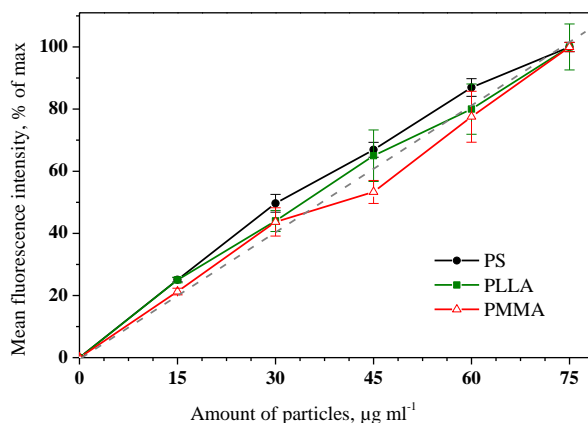


Figure 28. Mean fluorescence intensity of HeLa cells after incubation for 4 h with particles of PLLA (green), PMMA (red) or PS (black). A straight line (dashed grey) running from $P_{min}(0/0)$ to $P_{max}(75/100)$ demonstrates the course of a linear increase in fluorescence with increasing particle concentration. The particle-free control sample was subtracted and fluorescence intensity $Fl_1(Pol)$ was normalized to the respective value of the maximal concentration of $75 \mu\text{g}\cdot\text{ml}^{-1}$ of each polymer.

4.2.2 Competitive Uptake after Co-Incubation of Two Particle Species

For evaluation if the presence of one particle type could influence the uptake kinetic of another type, two types of particles were incubated simultaneously with the cells for 4 h. It could be hypothesized that upon simultaneous incubation of two particle species, mutual influence on their cellular uptake might occur due to the competition of both materials for the cell's endocytosis capacity.

Competitive experiments were performed with the following particle pairs: PMMA+PLLA, PMMA+PS and PS+PLLA. The fluorescence values were normalized to the respective maximum value of the NPs. The PMMA samples displayed particularly weak FL1 signals because of the low particle fluorescence and the low uptake efficiency. The fluorescence signal of cells loaded with PMMA NPs roughly exceeded the signal of particle-free cells by 300%. As a consequence the standard deviation was high. The uptake of PMMA+PLLA and PMMA+PS hardly showed any competition. The obtained graphs followed the linear fit (see *Figure 29*).

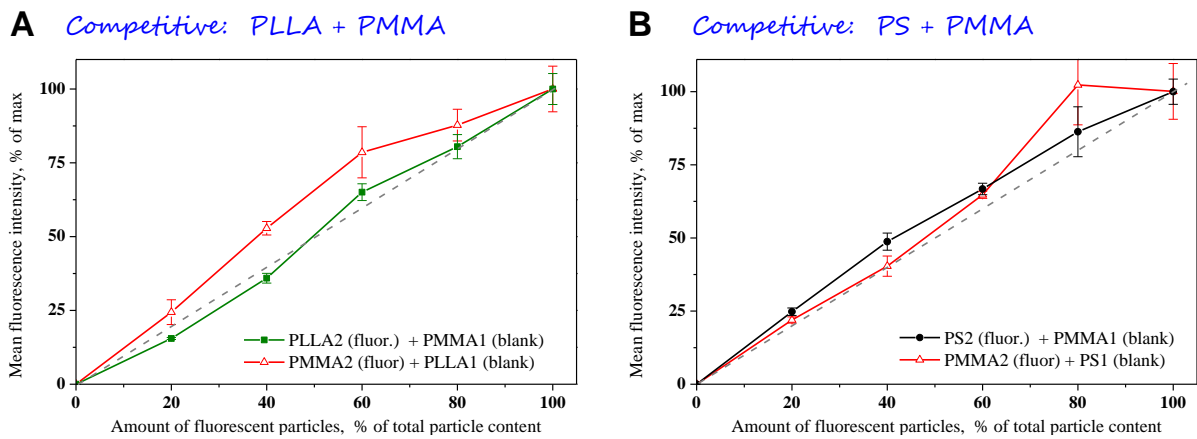


Figure 29. Fluorescence intensity of HeLa cells after the competitive incubation of PLLA+PMMA (A) respectively PS+PMMA (B) particles. The mean fluorescence intensity is displayed as [%] of the sample incubated with only fluorescent particles.

But when PS and PLLA particles were co-incubated together the graphs did not follow a linear fit. Instead the experiment yielded a bended graph which was curved upwards when fluorescent PS particles (PS2) were used and bended downwards when the fluorescent PLLA (PLLA2) NPs were used (Figure 30A). It was an interesting observation that the competitive effect, *i.e.* the curvature of the graph, was markedly reduced when the serum concentration in the incubation medium was increased from 10% to 75% (Figure 30B).

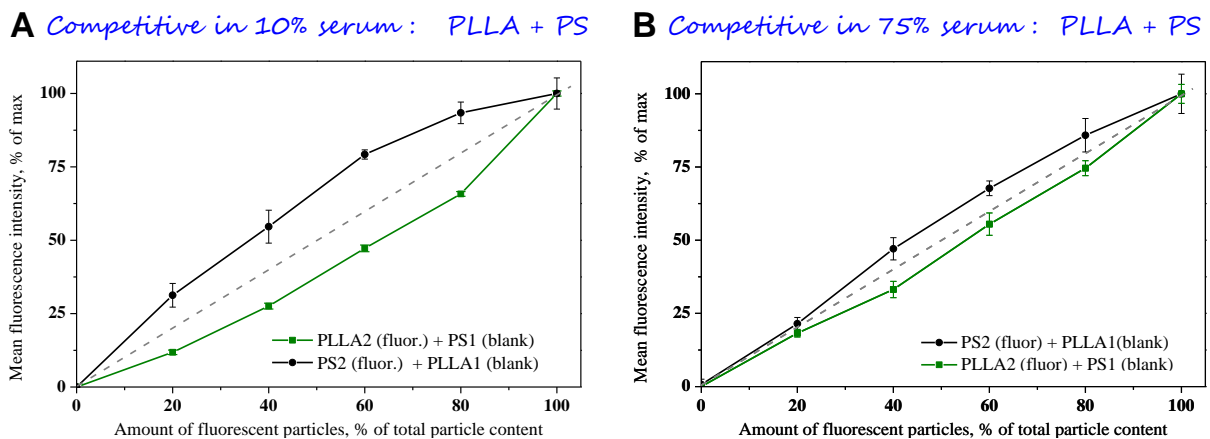


Figure 30. Mean fluorescence intensity of HeLa cells after co-incubation of PS+PLLA particles in cell medium containing 10% (A) and 75% (B) FCS. The mean fluorescence intensity is displayed as % of the sample incubated with only fluorescent particles. The dotted line indicates the linear increase of fluorescence without a competitive effect.

The curvature of the graphs demonstrated the change of particle uptake efficiency from the linear course one would expect. To express this change in a quantitative way, the difference between the effective (measured) and the theoretical (expected, linear) uptake was calculated (Δy). This difference Δy was expressed as the percentage $\Delta Y\%$ of the theoretical value Y_D ($\Delta Y\% = \Delta y \cdot Y_D^{-1}$). This is schematically demonstrated in Figure 31. Depending on if the particle

uptake was relatively high or low, the difference value was displayed with a positive or negative sign.

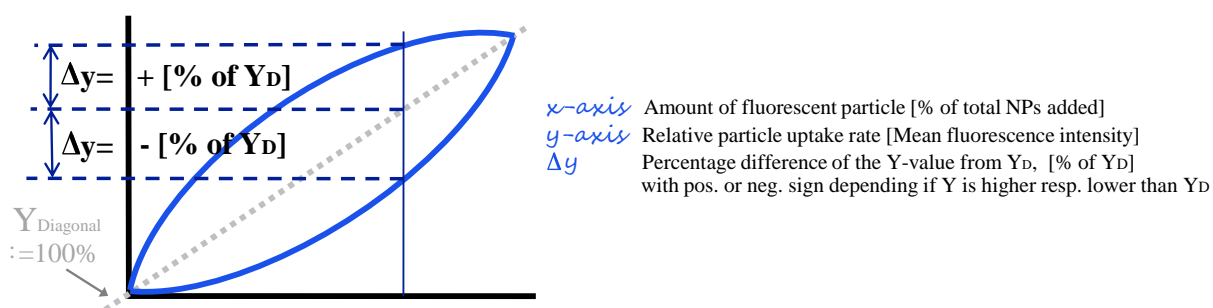


Figure 31. The measured relative particle uptake (blue) was set off against the theoretical particle uptake as represented by the grey dotted diagonal. Hereby, the y-values of the diagonal, representing an imaginary uptake of particles without a competitive effect, were set as 100%.

Following this scheme, the difference in uptake efficiency was displayed in an alternative way (see Figure 32). This more quantitative display revealed that the competitive effect on PS was slightly stronger than on PLLA, as represented by the higher difference in percentage. It also demonstrated that with 75% FCS the effect was markedly decreased suggesting a reduced influence of the particles on each other's uptake efficiency.

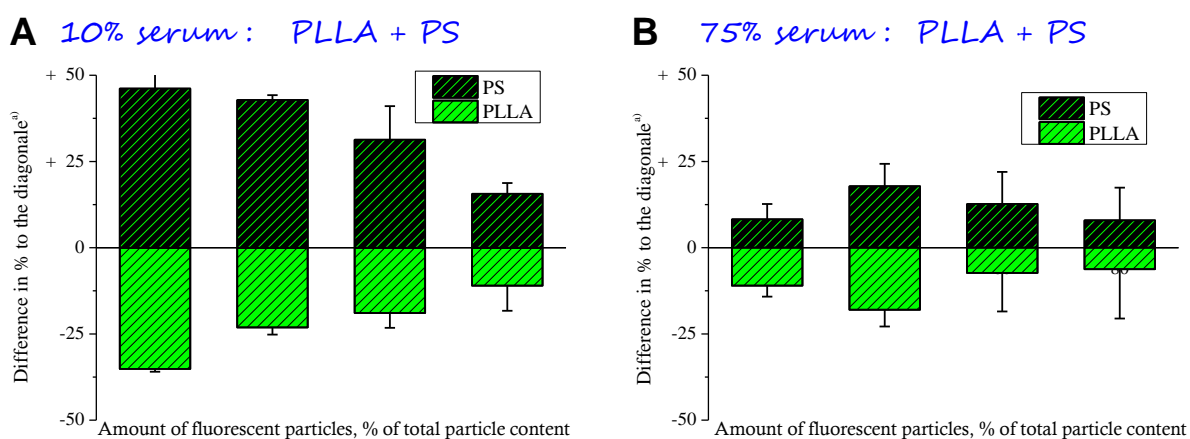


Figure 32. Percentage deviation Δy of the measured particle uptake rates (curved graphs see Figure 31) from a theoretical uptake rate (diagonal, following a linear course). ^{a)}The change of internalization rate is expressed as a percentage deviation (Δy) from the theoretical value (diagonal).

The data suggested that the properties of PS and PLLA particles trigger their endocytosis into HeLa cells in a way that they compete for the same uptake capacities of the cell. Furthermore, the two particle species also seemed to compete for certain endocytosis-favoring proteins in the serum-supplied incubation medium. The competition for coating proteins would be one factor of the observed competitive effect as it would largely influence competition at the cell membrane and, finally, the cellular uptake.

To further pursue this idea of protein coat involvement, the interaction of the three particle species with serum proteins was studied by isothermal titration calorimetry. The NPs were titrated with 10% FCS and the total heat development was measured, see *Figure 33*. Because fetal calf serum is a mixture of many different proteins, the total heat depends on the detailed adsorption pattern *i.e.* on the amount and type of adsorbed protein. In any case the heat development is a measure for the intensity of the particle interaction with proteins. The NPs displaying the competitive effect *i.e.* PS and PLLA developed more heat than the PMMA particles (*Figure 33*). This could not be tied directly to the competitive effect but the stronger particle-protein interaction of the materials PS and PLLA stressed the involvement of serum proteins.

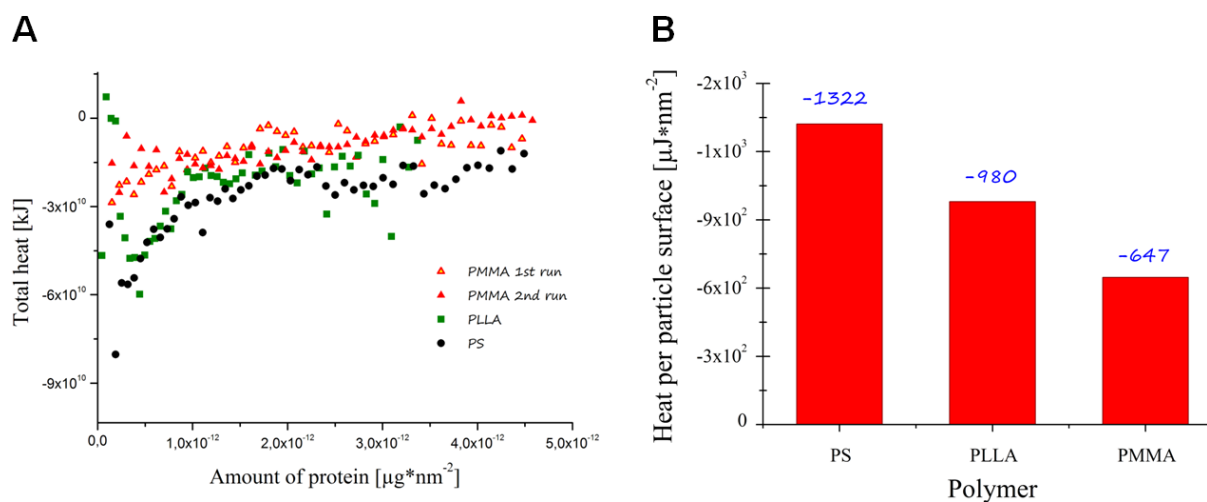


Figure 33. Total heat development of the different polymeric NPs during 50 titration steps against diluted serum, as obtained in the ITC measurement. Particle dispersions of the concentration $75 \mu\text{g}\cdot\text{mL}^{-1}$ were titrated against a 10%-vol. serum dilution.

The strong particle-protein interaction of PS and PLLA samples could be an indicator for the involvement of serum proteins in the competitive effect. Protein coatings that specifically enhance the cellular uptake of NPs have been reported⁸⁴. For example immune globulins, proteins of the complement pathway and coagulation factors were reported in the protein-corona of blank and of carboxyl-functionalized negatively charged PS particles. Concerning these proteins an endocytosis-enhancing effect is being discussed. A decrease in NP endocytosis when the serum was switched for heat-treated serum indicated as much¹⁶³ – because the heating would inactivate the proteins in question. It should be pointed out that the model of this study was a human epithelial cancer cell line (as are HeLa cells) and not capable of macrophagocytosis. All experiments in this thesis were done with heat-inactivated serum, so proteins of the coagulation and of the immune response cascade can be ruled out. But the possibility of other endocytosis-favoring proteins has to be considered.

Finally the hypothesis of the competitive uptake of PS and PLLA particles was investigated by TEM, in cooperation with another member of the electron microscopy team in the group.

to locate the particles inside the cell at high resolution. In particular, it should be studied if PLLA and PS particles were stored in similar compartments inside the cell after co-incubation. The TEM studies gave no proof of extracellular particle coagulates adsorbing to the cell membrane. The observed NPs were at times in proximity to each other, but always separated and not as a dense aggregate, see *Figure 34*. This supported a model where single particles adsorb on the cell surface and compete for the uptake one by one. Unlike the samples for cLSM and FC, the cryo TEM samples were not rinsed prior to the preparation, which is why here many loosely adhered NPs were present around the cell.

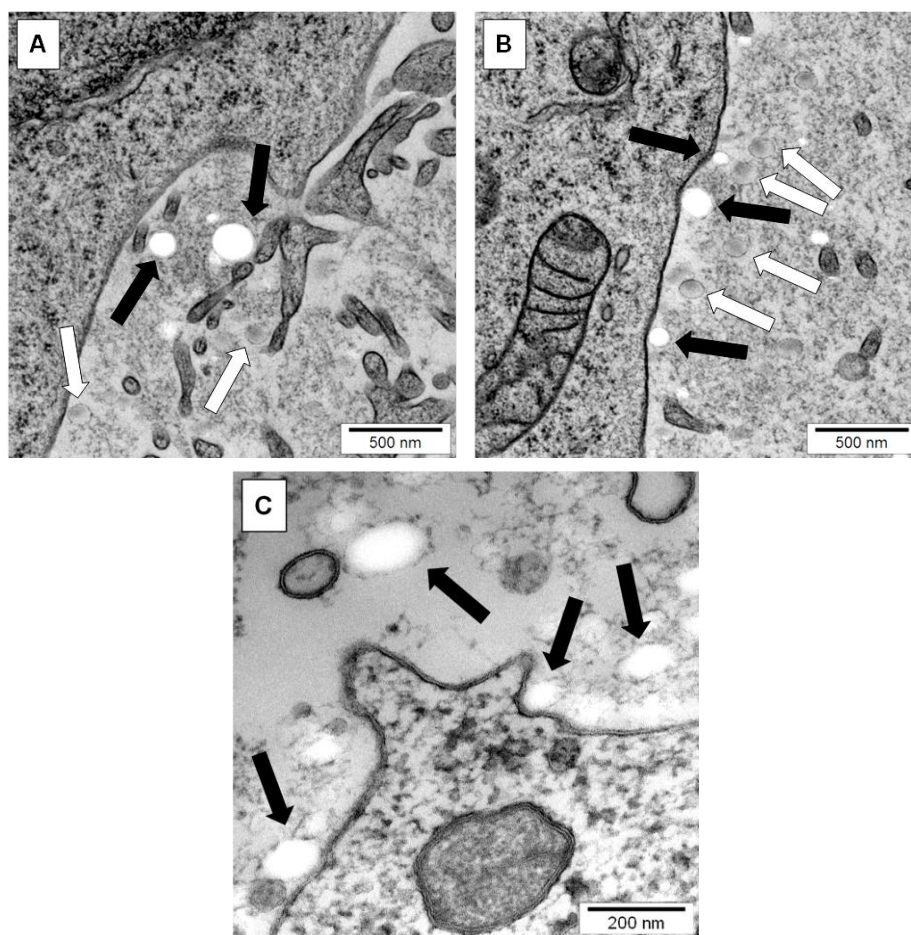


Figure 34. TEM images of the cytoplasmic membrane and extracellular particles which were in close proximity or adhered to it. The images display the cells after incubation with an equal mix of PS and PLLA particles for 4 h (A, B) and 24 h (C). The particles of PLLA (black arrows) and PS (white arrows) are marked.

The high resolution TEM studies confirmed an intracellular co-localization of PS and PLLA NPs after an equal mixture of those had been incubated with the cells. After 4 h incubation time, membrane-enclosed compartments were detected that contained a single particle of PS (*Figure 35A & B*) or PLLA (*Figure 35C & D*). Endosomes or invaginations with more than one particle were not found. Those could not be excluded based on TEM studies. But at least those had to be a rare occurrence if none were spotted in TEM, and should be ruled out as the major mechanism of uptake.

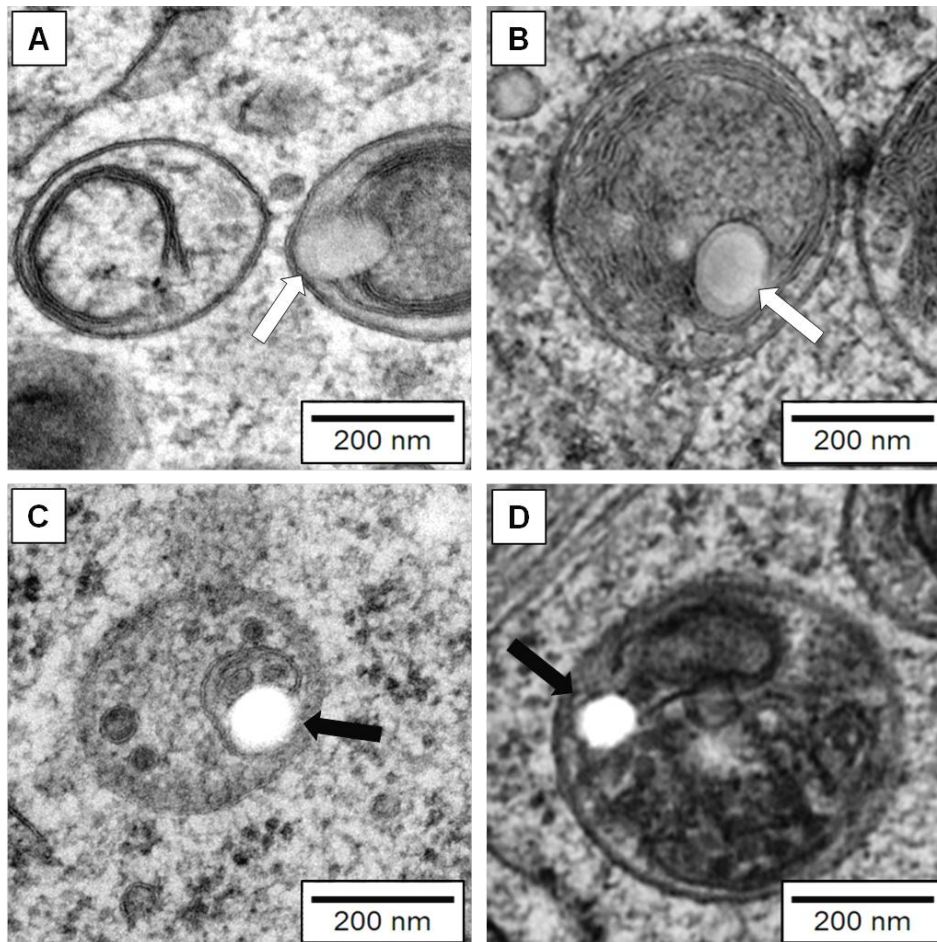


Figure 35. *HeLa cells after 4 h co-incubation with 300 µg of an equal mixture of PLLA and PS particles. Shown are PLLA (black arrows) and PS (white arrows) particles located separated in organelles.*

Even after the long incubation time of 24 h, the TEM studies yielded no proof for the presence of larger particle aggregates inside organelles, as all NPs appeared separated. Not enough cells were analyzed to extract an absolute result. Furthermore some of the observed organelles might contain more nanoparticles than what was visible, considering that the analyzed slices were 80 nm thin. But the overall impression was that the majority of compartments still contained only one particle (*Figure 36C & D*). Few compartments contained <5 NPs (*Figure 36B*) and only one very large organelle with >15 particles was seen (*Figure 36A*). The exact nature of those compartments could not be defined. But the presence of other small particles and multi-membrane structures, in combination with the dark staining, indicated that the NPs were likely gathered in lysosomes or late endosomes (multivesicular bodies), see *Figure 35* and *Figure 36*. The dark color of such organelles is a typical feature of late endosomal structures, as well as the presence of other particles and vesicles¹⁶⁴.

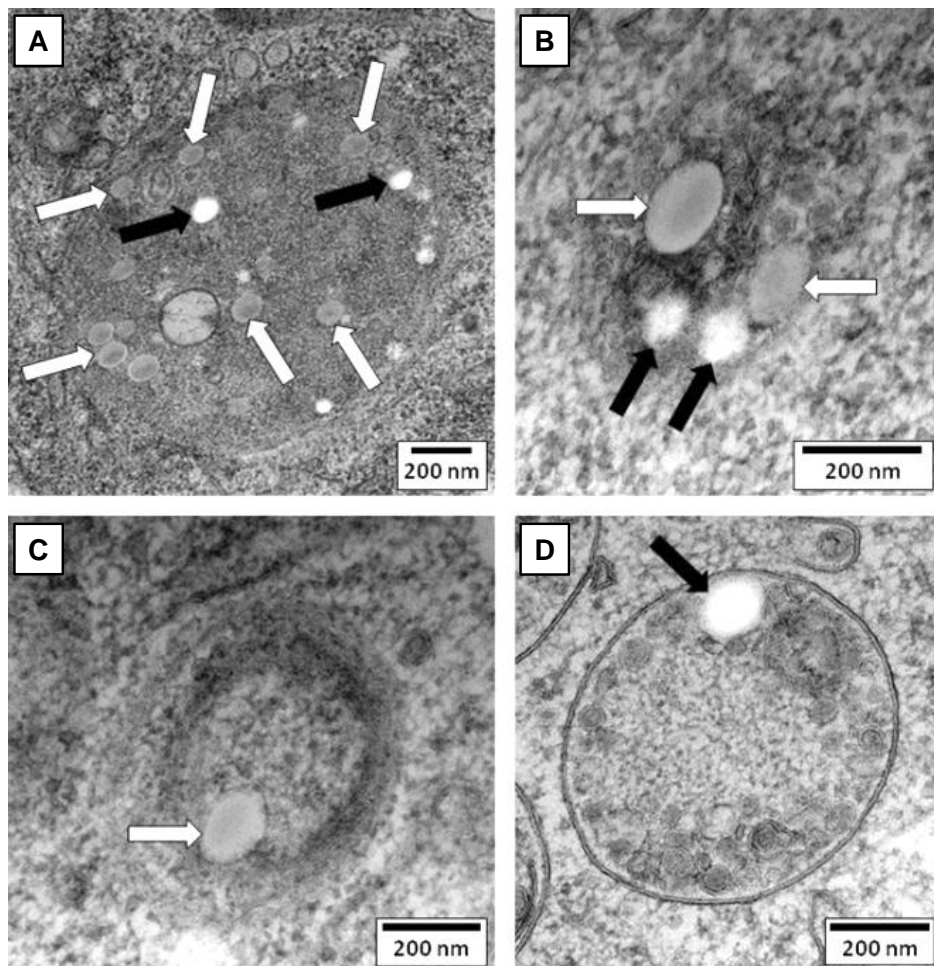


Figure 36. *HeLa cells after 24 h co-incubation with 300 µg of an equal mixture of PLLA and PS NPs. Shown are PLLA (black arrows) and PS NPs (white arrows) co-localizing in a cell organelle likely corresponding to a late endosome or lysosome (A, B). Few membrane-enclosed compartments containing a single PS (C) or PLLA (D) particle were observed.*

The following model for the competitive endocytosis of PLLA and PS nanoparticles was developed (see *Figure 37*).

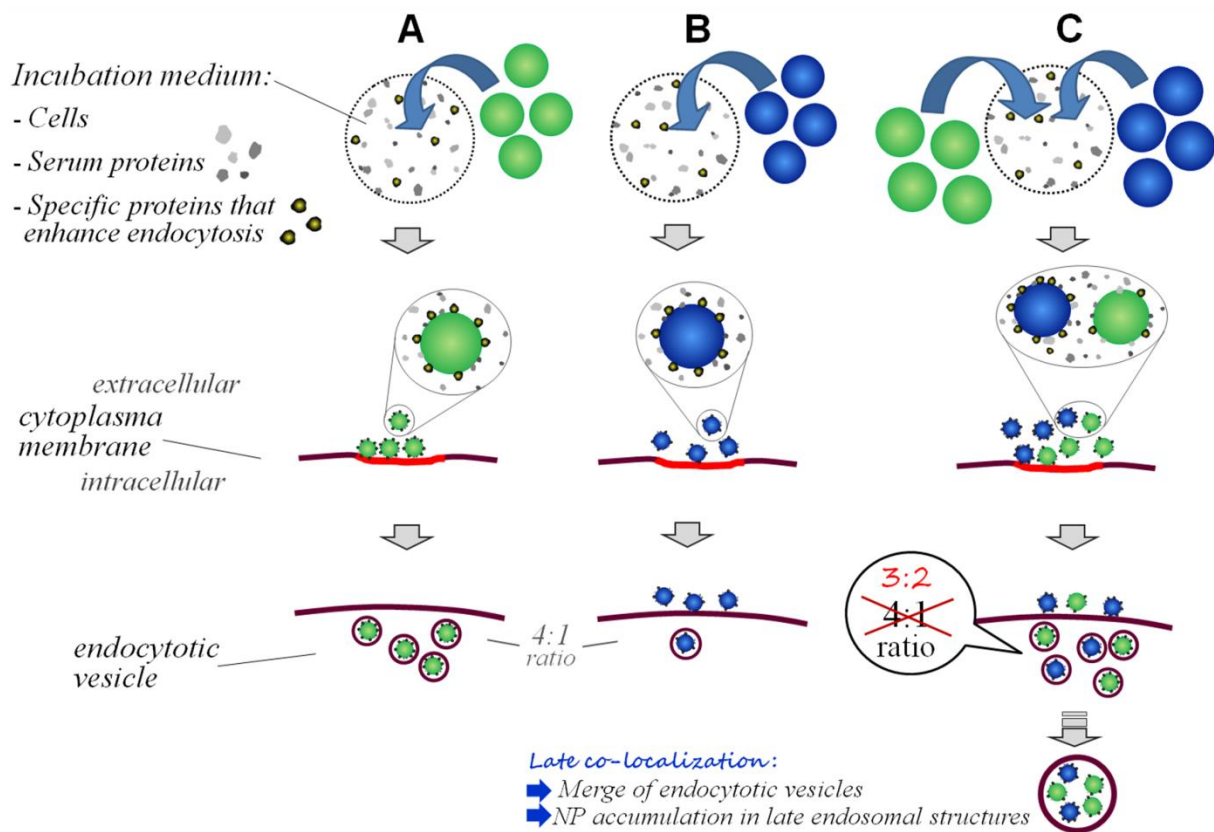


Figure 37. Scheme of the competitive uptake: Upon single species incubation of PLLA (green, A) and of PS particles (blue, B), PLLA exhibit a significantly more effective uptake. Upon simultaneous incubation of the two particles species (C), the uptake of PLLA is comparably reduced whereas PS internalization is increased. Particle concentration in (C) was doubled to better depict the shifting ratio of the uptake efficiencies in the competitive setup. Particles adhere to the CM and are internalized separately. Co-localization of these particles (bottom) is only observed, when the endocytotic vesicles merge after a while to form larger endosomal structures.

SUMMARY Three types of negatively charged PS, PMMA and PLLA nanoparticles with comparable physico-colloidal properties were used to study the influence of polymer nature on the uptake into HeLa cells. Fluorescence microscopy proved that none of the particle species showed any significant adsorption to the extracellular side of the cytoplasmic membrane. This concurred with earlier reports, where particle accumulation on the outer CM side was rarely observed with negatively charged particles⁹⁶.

Single species studies by FCy showed that the internalization rate of PLLA nanoparticles was approx. 5-fold higher than that of PS and PMMA. Presumably that preferential uptake of PLLA particles was due to the surface and the chemical composition of these NPs: Low M_w , polymer ‘softness’ (absence of a T_g) and the carboxylic groups on the surface. The positive effect of carboxyl functionalization on the endocytosis rate of polymeric NPs had been

reported earlier ⁹⁶, but the polymer PLLA even offers these groups without further functionalization.

In the case of co-incubation, only the combination of PS and PLLA resulted in a competitive effect. When given the choice between PS and PLLA particles during co-incubation the cells preferably internalized particles of PS. At the same time the uptake rate of PLLA NPs was decreased accordingly. This suggested that the polymeric spheres compete for resources. These resources would likely be the sites of endocytosis on the cell's surface, or certain proteins that are present in the serum in only small amounts and which enhance endocytosis. Supposedly those two issues are linked, as the affinity of nanoparticles to specific sites (or even receptor molecules) of endocytosis might be significantly governed by the protein corona around the NP ^{45, 83, 161}. In any case the ITC measurements indicated that PS and PLLA particles showed stronger interactions with proteins than did PMMA NPs.

The strong particle-protein interaction of PS and PLLA seemed to link the competitive effect to a shortage of specific endocytosis-favorable coating proteins, as one of several possible reasons. This idea was supported by the observation that a higher serum protein concentration decreased the competitive effect. Furthermore the competition should not be based on the lactide's carboxyl groups, as it did not occur during the co-incubation of PLLA and PMMA NPs.

The hypothesis of the competitive uptake would require that the particles are only internalized one by one and not in groups, which should be verified by EM microscopy. Indeed, TEM imaging revealed mostly single particles, being adhered at the CM and, after 4 h incubation, inside the cell in organelles. Only after 24 h incubation several organelles, presumably late endosomes or lysosomes ¹⁶⁴ were observed that contained more than one particle. After longer incubation time the once separated NPs had been transported to larger containers and accumulated in said compartments. The conclusion was that both PS and PLLA particles were mainly internalized by a mechanism that transports only one particle at a time. This ruled out macropinocytosis as major player, but of course this pathway may still be involved to a certain extent because cells always have several endocytotic mechanisms activated ¹⁶⁵.

4.3 Flow Cytometry for Single Nanoparticle Detection

4.3.1 The Impact of Experimental Settings and Sample Properties

In this chapter the impact of experimental conditions and particle features on the flow cytometry data is investigated. These factors greatly influence the morphology of the obtained data. Wrong settings *e.g.* a high threshold or insufficient amplification can lead to wrong conclusions, and in the worst case, hide the objects of interest from detection. On the other hand, by methodical variation of the experimental conditions conclusions about the sample can be drawn. The work presented in this chapter laid the base for the precise measurement of submicron particles.

The following factors are particularly important for the NP measurement in flow cytometry:

- Threshold
- PMT signal amplification
- Laser power
- Sample concentration
- Measurement speed
- Properties of the particles
 - *Size and refractive index*
 - *Excitation & emission range of the incorporated dye*
 - *Overall fluorescence intensity*

Some of these criteria are linked and should not be looked at isolated, for example PMT amplification & threshold or sample concentration & measurement speed. Based on the listed factors above, several approaches were developed that should help to identify the events representing single nanoparticles. Later on different NPs were analyzed in a fixed set of parameters.

The most relevant properties of the utilized particles are summarized in *Table 12*:

Table 12. *Key properties of the used polymer particles.*

Sample	≈ Diameter	Dye	Laser for excitation	FC channels for detection
PMMA-SDS-4	120 nm	PMI	488 nm	FL1, FL2, FL3
PS-LFY-1	112 nm	LF Yellow	488 nm	FL1
PS-LFY-2	125 nm	LF Yellow	488 nm	FL1
PS-LFY-3	114 nm	LF Yellow	488 nm	FL1
PS-LFY-4	118 nm	LF Yellow	488 nm	FL1
PMMA-BP1-2	155 nm	BP1	488 nm	FL1, FL2
PMMA-AT3	120 nm	BP2	640 nm	FL5
IMMUNO-BRITE™ *	μm-range	<i>n.a.</i>	488 nm	FL1, FL2, FL3
CountCheck Beads **	“	<i>n.a.</i>	488 nm	FL1, FL2, FL3

These PS microspheres were purchased from Beckman Coulter () and Partec (**).*

4.3.1.1 Threshold, PMT Amplification and PMT Linearity

Nanoparticles are very small compared to the total illuminated and detected volume in the cytometer. Therefore the number of noise events exceeds the particle count by far. The rather weak particle signal intensity adds to the complication, as this prevents sorting out noise events by threshold. This is particularly difficult if particle signals fully ‘co-localize’ with noise events, concerning *e.g.* their location in SSC-FSC or SSC-fluorescence plots. In the data of this study, several populations of events were discernible in the dotplots and in the early stage it was not yet clear which of these correlated to particle signals. Therefore threshold and detector signal amplification had to be balanced carefully.

The settings needed to be chosen such that nearly all events are detected – and no particle signals might be falsely lost. Therefore in the beginning, experiments with varying photomultiplier amplification (of channel FL1 and SSC) and varying thresholds were applied. Once the particle signals were identified, signal amplification and threshold could be fine-tuned to ensure ideal NP detection. The importance of the threshold setting for the measurement of nanoparticles is demonstrated by *Figure 38*. PMMA-SDS-4 particles (120 nm, dye PMI) were measured with the threshold on the FSC (0.5, 3, 6 & 15) or the SSC (10). In *Figure 38* the measurements (A) to (D) demonstrate that the threshold has great impact on the acquired data. Each run contained a similar number of events, $80 \cdot 10^3$, but the data set was very different. If a threshold is not defined properly the results can be misleading. At low threshold settings as in (A) and (E), mostly events of low signal intensity were detected, as these are vastly exceeding in numbers in every sample, but in images (B) to (D) these events were excluded from detection by the higher threshold. Only then, outnumbered events *e.g.* those with a strong signal intensity, became visible. This was apparent in the additional peak in the FL1 histogram at approx. 10-fold signal intensity (blue arrows in images B-D). This population emerged only when the threshold was higher *i.e.* on FSC3. The high fluorescence intensity suggested that this peak depicted NP-derived signals. It was concluded that a moderate threshold, between FSC3 and 6, could be suited. It allows to detect both populations (see FL1 histogram in images B & C) and should be suitable for most samples. With the chosen settings, existing event populations were fully visible in the dotplots *i.e.* none were cut off. This included false-positive fluorescence events *e.g.* when measuring a reference sample like pure water. As a consequence of these sensitive settings the count rate reached several thousand events per second, resulting in large data files.

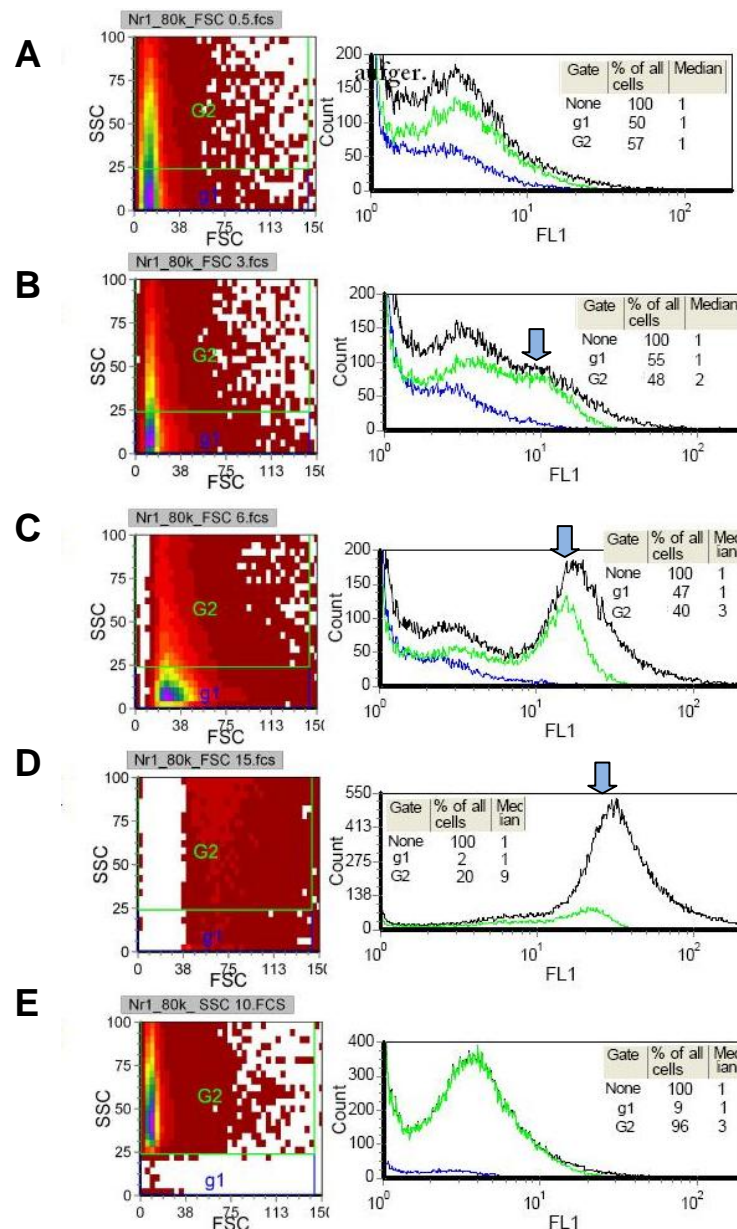


Figure 38. Measurement of nanoparticles (PMMA-SDS-4, 120 nm, dye PMI) at high concentration. Different threshold settings on the FSC, including value 0.5 (A), 3 (B), 6 (C) and 15 (D), were compared to a SSC threshold of value 10 (E). Each run comprised 80-10³ events. In the scatter dotplots (l.) a region of lower (g1, blue) and of higher SSC signal strength (G2, green) was gated. Histograms of FL1 (r.) display the complete data set (black) and the gated events in region g1 (blue) and G2 (green).

In theory, the PMT amplification could be increased at will, as long as the threshold is adapted accordingly; but in fact the photomultipliers are not fully linear in the complete range of voltage. The FL signals of two objects with different fluorescence intensities have to be amplified by exactly the same factor. The voltage range where the PMT works correct (Volt_{lin}) was identified with specific calibration beads ‘IMMUNO-BRITE™ Fluorospheres’ as described in a white paper publication by Beckmann Coulter¹⁶⁶. The set consisted of blank

reference beads and 4 bead species with varied fluorescence intensity. The latter contained a dye which emits at 525 to 700 nm after excitation at 488 nm. A mix of the beads Nr. IV & V was measured and the voltage was varied from 145 to 500 in small steps. Plotting the ratio of the beads' mean fluorescence intensities against the voltage yielded the linear voltage range of the photomultipliers (see *Figure 39*).

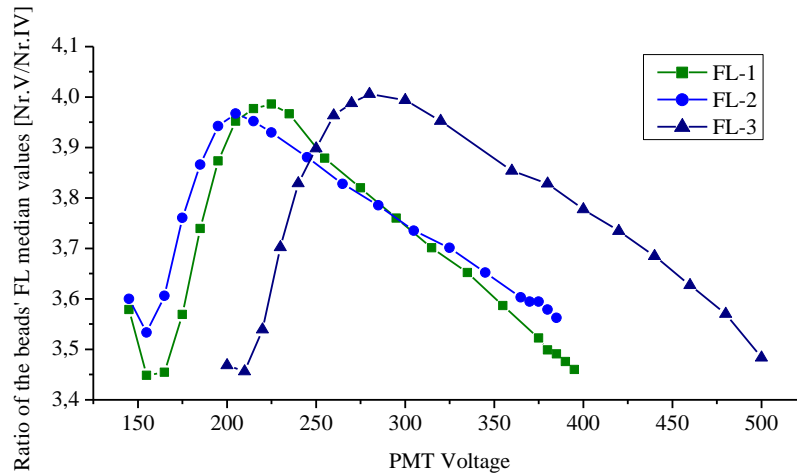


Figure 39. Measurement of the beads Nr. IV and Nr. V: The ratios (Nr. V / Nr. IV) of the FL median values were plotted against the PMT voltage. The graphs' inflection points mark the begin of the linear work range of the PMT of channel FL1 (square), FL2 (circle) and FL3 (triangle).

The inflection points were well visible and marked the start of the linear ranges ($Volt_{lin}$) of the respective photomultipliers. The tilted course of $Volt_{lin}$ was neglected as it is dependent on the different signal processing in the flow cytometers of Partec and Beckman Coulter.

A similar experiment was exercised with the beads Nr. II and III that possess lower fluorescence intensity and thus allowed to probe higher voltage settings (data not shown). Here the PMTs of FL1 and FL2 could be regulated up to 500. This was the possible maximum because above 500 V the beads exceeded the upper detection limit.

The combined results of these experiments showed that the PMTs worked in a linear fashion up to 500. Linear ranges $Volt_{lin}$ of 230-500 (FL1), 200-500 (FL2) and 280-500 (FL3) were identified. In the FC experiments the PMT voltage on FL1 and FL2 was always within the linear range.

4.3.1.2 Laser Power

The power of the 488 nm laser could be regulated between 40-200 mW. Up-regulating the laser input should increase all scattering signals. This includes the SSC signals as expected, but also the false positive signals in FL1 that are no real fluorescence signals. Finally, up-regulation of the excitation source would also intensify the FL1 fluorescence signal – possibly to a different extent than the scattering signals. If that was the case, then particle-derived

signals could be distinguished better from the noise by varying the laser power. In addition different laser settings had to be tested to optimize the fluorescence signal-to-noise ratio. Measurements with PS-LFY-3 particles (sized 120 nm, dye LFY) were exercised under variation of the laser power. Settings of 40, 100, 150 and 200 mW were tested (*Figure 40*).

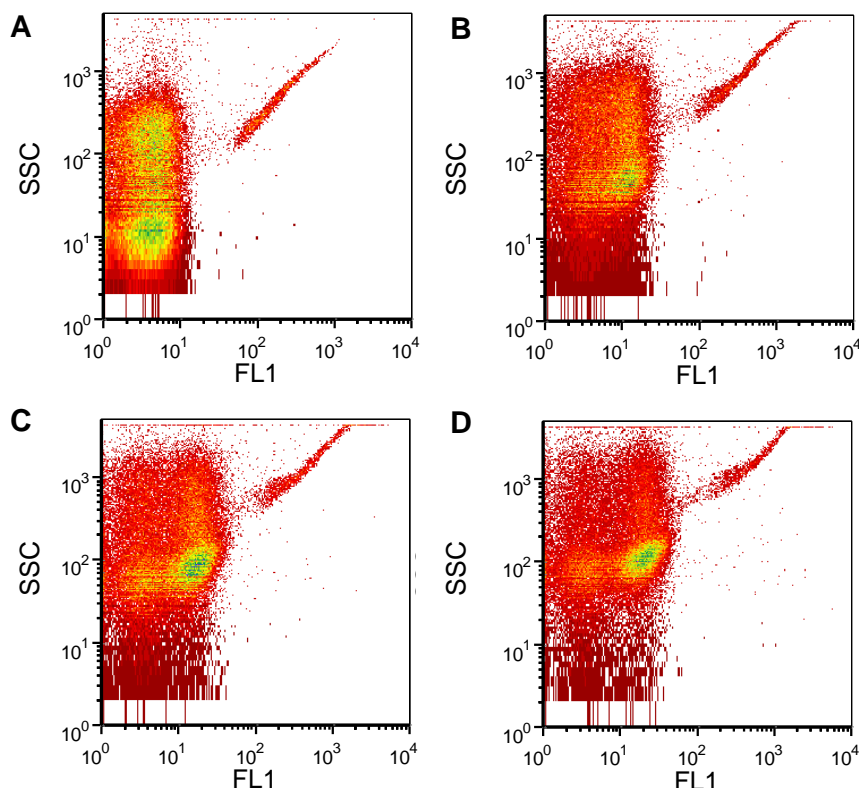


Figure 40. *SSC-FL1 dotplots of the analysis of PS-LFY-3 particles at 40 (A), 100 (B), 150 (C) and 200 mW (D) power of the 488 nm laser.*

A population in the right top corner was observed that as a first impression seemed to be particles (maximum FL1 intensity). But particle signals, at such a high sample concentration, would have to be present in much higher numbers. The presence of this population, that has a 10-100x higher signal strength than all other observed populations, cannot be fully explained. Phenomena like partial μm -sized coagulate formation or a sub-population of especially large spheres could be an explanation. In this early stage of work, with the purpose of laying the base for nanoparticle detection in flow cytometry, this population was not discussed further. In any case, the higher power input increased all signals, as expected, but the focus was on the FL1 channel. The interesting observation was that all FL1 signals were increased, but not to the same extent. Raising the laser power from 40 to 100, 150 and 200 mW had the effect that certain populations (observed at 40 mW) were each split up into two distinct populations (as observed at 200 mW). This is demonstrated in the direct comparison of the 40 mW and the 200 mW sample (see *Figure 41*).

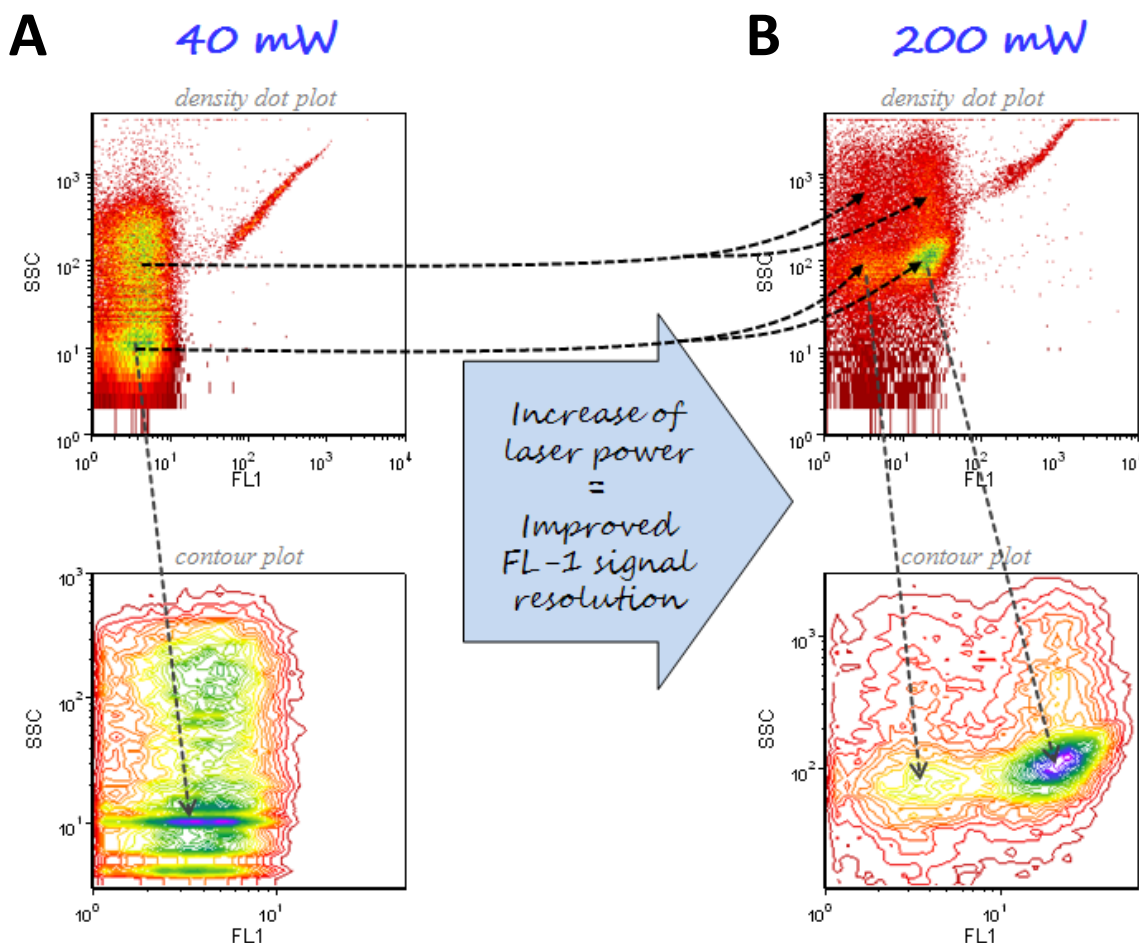


Figure 41. SSC-FL1 dotplots in density (top) and contour (bottom) mode, and the location of important populations are indicated by grey vertical arrows linking the two plots. The results of a measurement of PS-LFY-3 particles at 40 mW (A) and 200 mW (B) are displayed. The black horizontal arrows mark populations that were split into two distinct clouds when the laser power was increased from 40 mW to 200 mW.

At 40 mW, only one population was discernible by FL1 and at 200 mW, this population seemed to be split into two distinct clouds. Obviously, some events had gained more FL1 signal intensity than other events. It was hypothesized that the latter had to be false positive signals, *i.e.* merely scattering of the laser beam that passed the band pass filter of the FL1 channel. In contrary those events with the stronger gain in signal intensity were assumed to be real fluorescence signals, origination from particles that contain the fluorophore. Possibly, the capacity of the dye inside the particles was not fully exploited at 40 mW, leaving room for signal improvement at e. g. 200 mW laser power with more photons available for excitation.

This indicated that the selective up-regulation of particle signals – *i.e.* a significant improvement of the signal-to-noise ratio – was achieved. In *Figure 42A* a pair of high resolution SSC-FL1 contour plots visualizes the improved signal-to-noise ratio as achieved by up-regulating the laser power: Two populations (supposedly NPs and background) were gated with maximum precision by following the contour lines. The pair of 100 mW and 200 mW

power was chosen for this comparison because these settings ensured that no events of low FL1 signal intensity could be lost, whereas at 40 mW laser power it was possible that signals of low FL1 signal intensity were excluded by the minimum threshold.

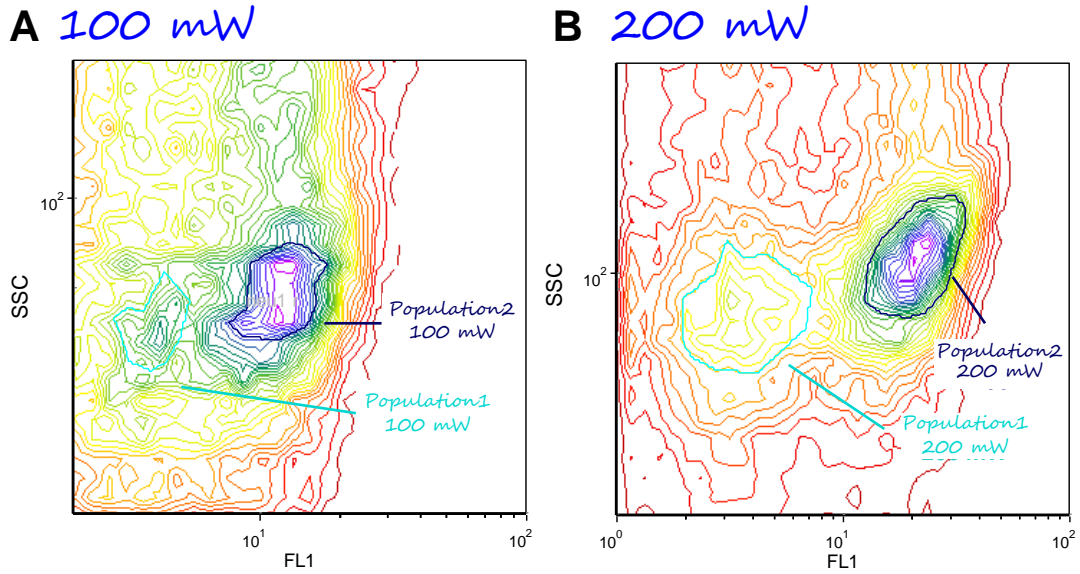


Figure 42. High magnification SSC-FL1 density dotplots, showing the results of a measurement of PS-LFY-3 particles at 100 mW (A) and 200 mW (B). In each dotplot the two populations of interest were gated in turquoise (Population1) and dark blue (Population2).

The mean signal intensities (SSC and FL1) of the gated events in *Figure 42* were interpreted separately for the two populations, see *Figure 43*.

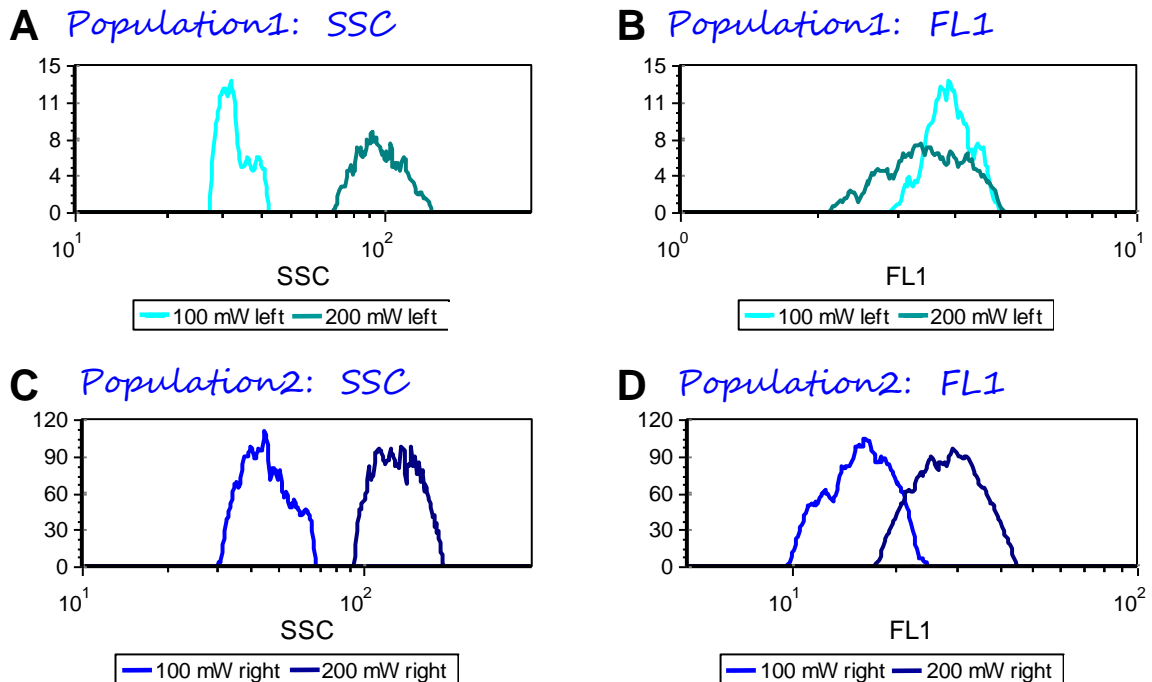


Figure 43. SSC and FL1 signals of the events in 'Population1' (A & B) and in 'Population2' (C & D).

The SSC scatter signals of both populations behaved identically *i.e.* increased by a factor of 3. But the FL1 signal in ‘Population2’ increased by a factor of 2 (from 16 to 29 [a. u.]) when the laser power was up-regulated from 100 to 200 mW. In contrary, the FL1 signal intensity of ‘Population1’, which supposedly represents background events, remained nearly constant. The FL signal intensities of the two populations were indeed amplified with a different factor. This suggested that ‘Population1’ (marked dark blue in *Figure 42A* & *Figure 42B*) included particle-derived signals. The high sample concentration and the strong FL1 signal intensity (4-7x the signal intensity of ‘Population2’) suggested coincidences or coagulates. These experiments showed that 200 mW laser power should provide the best conditions for the detection of single nanoparticles.

4.3.1.3 Apparent Sample Concentration

In flow cytometry the measurement speed (v_{exp}) cannot be fully separated from the sample concentration. At high v_{exp} , a large volume of sample *i.e.* a larger amount of objects passes the detection spot per second – which imitates a higher sample concentration. Therefore sample concentration and measurement speed should only be discussed together. Both factors contribute to a final ‘apparent sample concentration’ *i.e.* the actual number of objects that passes the flow chamber per second. Whenever different sample concentrations were compared in this study, the v_{exp} was kept constant and therefore may be neglected and will not be discussed separately. But there is one important property that should be kept in mind: At high speed, the sample stream will not only flow faster but also grow in diameter. The resulting different locations of objects in the flow chamber (in combination with *e.g.* the detection angle, detection time window and the intensity distribution profile of the laser beam) decrease the measurement’s accuracy. Therefore, all nanoparticle experiments were obtained at a v_{exp} of 0.5, 1 or 2 [$\mu\text{l}\cdot\text{s}^{-1}$].

The first and most difficult task in nanoparticle measurement by FC is to get a clear distinction between events of noise, nanoparticles, coincidences and possibly coagulates. There are several approaches to this task, one of them being to seek the typical characteristics of the possible 3 states: Particle dispersions can be of low (a), medium (b) or high (c) concentration. In theory, case (a) represents a sample with such a low particle content that coincidences will not occur. Therefore, if any events of high fluorescence and scattering intensity are observed, these must originate from coagulates. As a drawback the low particle content leads to a bad signal to noise ratio. The measurement is susceptible to the daily performance of the cytometer. This includes even minor ‘contaminations’ with particles or air bubbles that are irrelevant for standard applications as *e.g.* cell analysis. At a moderate sample concentration (b), many single NPs are detected and the signal-to-noise ratio is good, even though coincidences cannot be excluded anymore. In contrary, for (c) nearly any particle signal is in a coincidence event because the sample is concentrated.

Therefore, varying the sample concentration whilst closely watching the morphology of SSC and FL1 peaks should yield the information where to look for the NP signals in the data. With

increasing NP concentration, each coincidence represents the summed up signal intensity of an increasing amount of particles. As a typical characteristic of the coincidence population, the signal intensity in SSC and FL1 should rise with the sample concentration. Signals originating from NPs could be tracked down this way even if a true single particle measurement (SPM) would still be lacking. Theoretically, if the concentration were reduced enough to allow SPM, a second peak should appear to the left (representing single NPs). Simultaneously, further dilution should gradually remove the coincidence peak.

In an early approach, highly concentrated dispersions of PMMA-SDS-4 (diluted 1:1000, and 1:4000) were measured. At such high concentrations, single particle detection was not expected and the minimum threshold was set accordingly high (FL1:20). In this experiment, mainly coincidences were observed. This first comparison of varying dilutions (see *Figure 44*) demonstrated the impact of sample concentration on the morphology of the cytometry results.

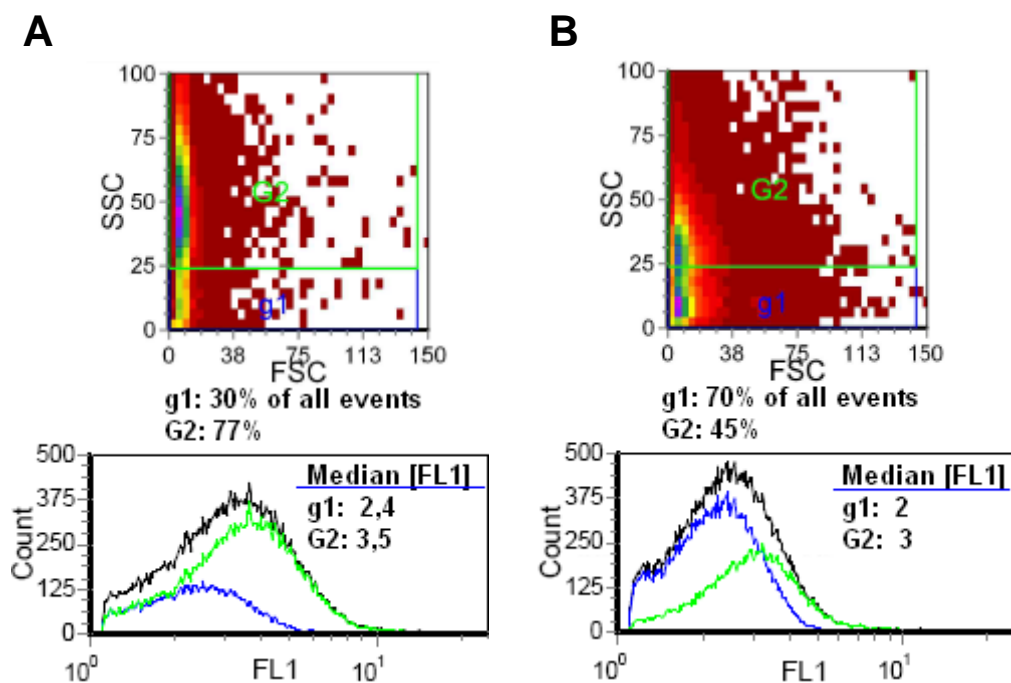


Figure 44. Measurement of washed PMMA-SDS-4 particles (120 nm, dye PMI) diluted 1:1000 (A) and 1:4000 (B), displayed in FSC-SSC dotplots (top) and FL1 histograms (bottom). The gates g1 (blue) and G2 (green) mark particles of lower and higher SSC intensity, respectively. The histograms display the content of gate g1 (blue), G2 (green) and the un-gated data (black).

In the scatter plots of *Figure 44*, two populations of SSC signals above or below 25 [a. u.] were marked by the gates g1 (blue) and G2 (green). The given percentage values, *i.e.* which percentage of the total particle number is contained in the gate, do not add up perfectly because the two gates slightly overlap.

Gate G2 in *Figure 44* demonstrates that increasing the sample concentration nearly doubled the number of events of higher SSC intensity (> 25 a. u.). At the same time the number of

events in gate g1, with a low SSC intensity, was halved. When the sample concentration is too high, several particles pass the detection chamber simultaneously and are therefore summarized as one event termed coincidence E_{err} . The SSC and fluorescence values of those depend on the number of particles which are contained in the E_{err} . The SSC and FL1 signal intensity is accordingly high at high sample concentration and decreases when the sample is diluted.

Another dilution series of fluorescent NPs (PS-LFY-3, dye LFY, size 120 nm) was analyzed. The samples V1-V8 were obtained by a dilution row in triple filtrated (0.2 μm pore size) water, as shown in *Table 13*. Filtrated water was also used as the reference sample.

Table 13. Properties of the PS-LFY-3 dilution series, samples V1-V8.

	Dilution factor	Concentration [NP per 0.5 μl]	Particle flow [NP per s] *
c0	/	$1.04 \cdot 10^{11}$	/
V1	1185	87.763.713	$88 \cdot 10^6$
V2	3555	29.254.571	$29 \cdot 10^6$
V3	$11 \cdot 10^3$	9.751.524	$9.7 \cdot 10^6$
V4	$32 \cdot 10^3$	3.250.508	$3.2 \cdot 10^6$
V5	$96 \cdot 10^3$	1.083.503	$1.1 \cdot 10^6$
V6	$288 \cdot 10^3$	361.168	$360 \cdot 10^3$
V7	$864 \cdot 10^3$	120.389	$120 \cdot 10^3$
V8	$2.592 \cdot 10^3$	40.130	$40 \cdot 10^3$

* NPs that cross the flow chamber i.e. pass the detection spot per second when measuring with a speed of $v_{exp} = 0.5$.

The data sets were displayed in SSC-FL1 plots (*see Figure 45*) where an 8-shaped gate (red) marked the majority of the NP-derived signals. The SSC-FL1 plots showed that several populations were present and that some of these changed their morphology or location in dependence of the sample concentration. Any population that changes with the sample concentration must originate from the sample itself. In contrary, the populations that remained the same in all samples were considered ‘background’ in the FC (air bubbles in the sheath *etc.*) and non-related to particles.

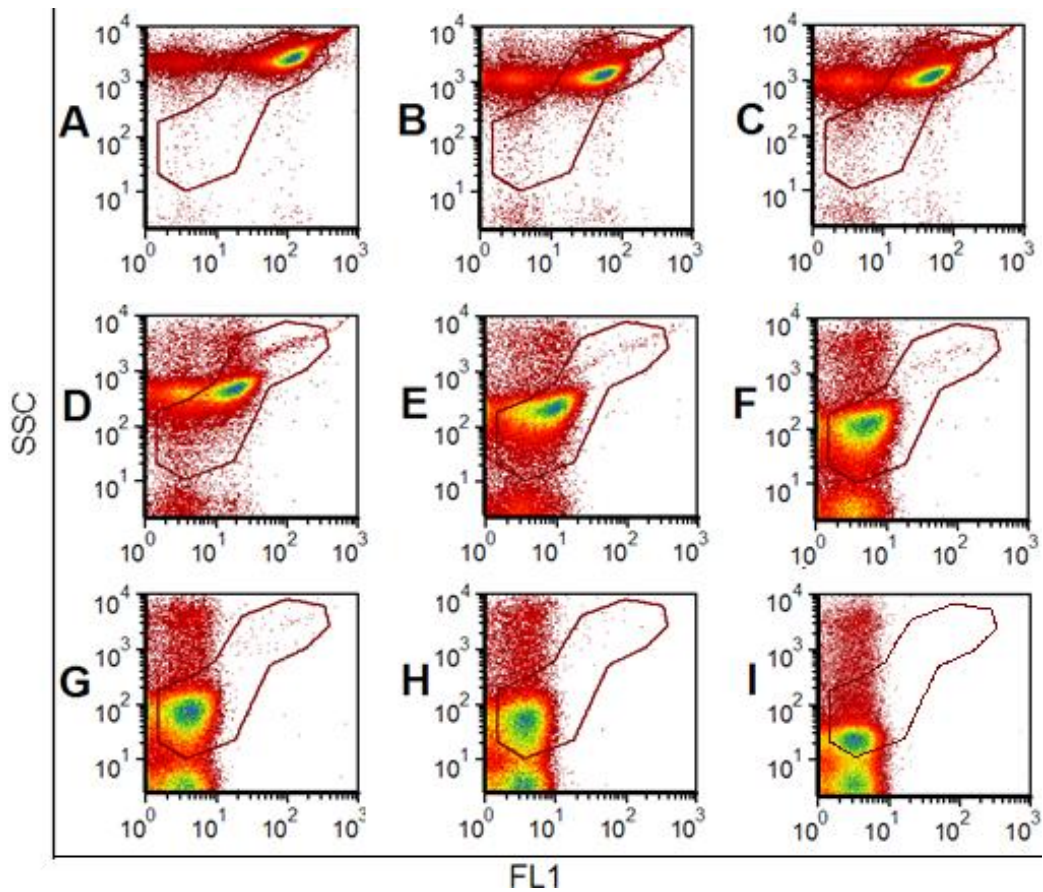


Figure 45: Results of PS-LFY-3 particle dilution series. The SSC-FL1 plots (A)-(H) correspond to the samples V1-V8 as achieved by the dilution row in Table 13, with (A) as the maximal and (H) as the minimal concentration. A sample of filtered water was measured as particle free reference (I).

The reference (see Figure 45I) showed that the standard background signals were located in two main regions as sketched in Figure 46. These populations (a) and (b) had a SSC intensity of $y_1 = 3$ and $y_2 = 20$ [a. u.], respectively. Their fluorescence signals are equally weak. A third population (c), with identical FL1 signal, was considered irrelevant and presumably represented non-fluorescent events of noise of higher SSC intensity.

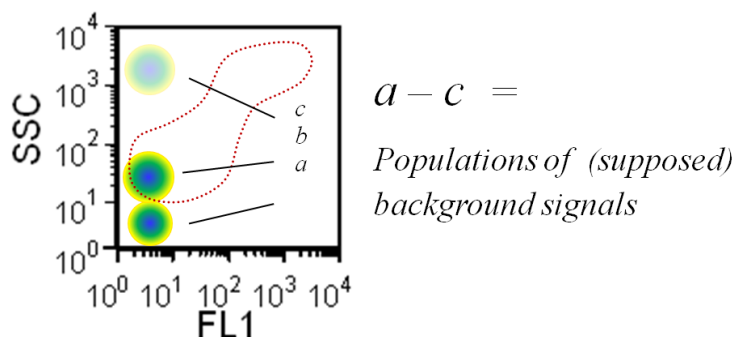


Figure 46. Schematic SSC-FL1 plot of the measurement of filtrated water (reference sample). No particles are contained; hence the spotted populations (a) & (b) correspond to the standard background signals. Population (c) represents noise events of higher signal intensity that are not observed in all samples and will not be discussed further.

The mentioned populations (a) and (b) were also emerging in the samples of lower particle concentration (see *Figure 45F - H*). This proved that either a) hardly any NPs were left in the sample (*H*) or b) there were still many particles but their FL1 signals were indistinguishable from those of the background events.

Consequently the other event population, the one which shifted in dependence of the NP concentration, was defined as ‘particle-derived’. This expression refers to any signals caused by particles and does not specify between single NPs, coagulates or coincidences; such a distinction was not possible at this point.

The SSC-FL1 dotplots in *Figure 46* depicted a cloud that shifted from the right top corner to the left bottom until it apparently disappeared or merged with the upper background cloud (which is termed population (b) see *Figure 46*). This shifting cloud is described in *Figure 47*. The more the sample is diluted, the more this population shifts to lower FL1 and SSC intensities and in the process changes from an elongated to a near circular shape.

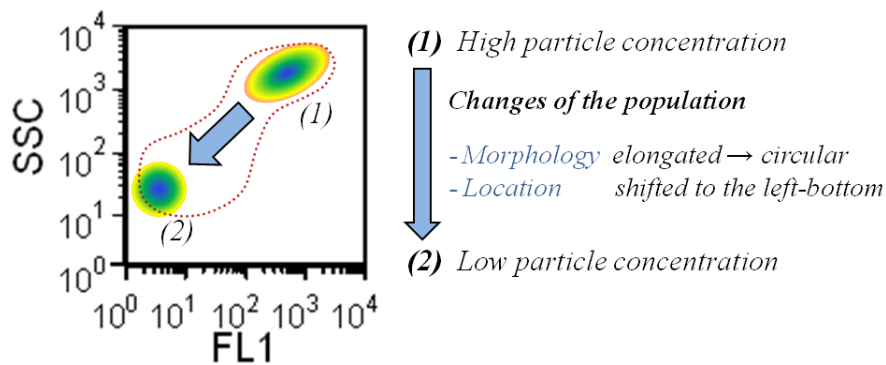


Figure 47. Comparing the population of particle-derived signals at high (1) and at low (2) sample concentrations (schematic display).

For a closer look on the shifting signal intensities, the ‘particle-derived’ events (as defined by the gate in *Figure 47*) were displayed in SSC and FL1 histograms. *Figure 48* shows the signals of SSC (A) and FL1 (B) at varying sample concentrations. Additionally the signal intensities in FL1 and SSC were plotted against the particle concentration in the samples (C). To compare the relative changes in signal intensity of SSC and FL1 in dependence of the particle concentration, these intensities were additionally normalized to 100% (D).

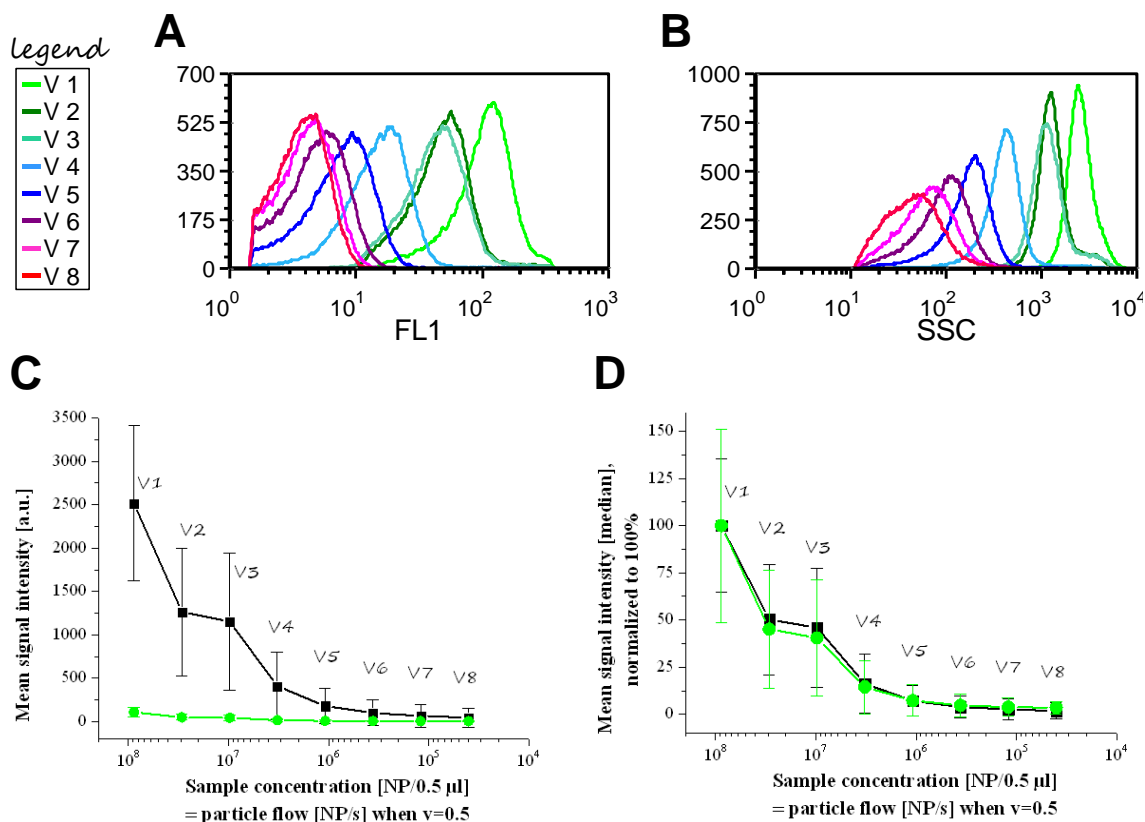


Figure 48. Display of the supposed particle-derived signals (= gate in the SSC-FL1 plots). These signals in sample V1-V8 are displayed in histograms of FL1 (A) and SSC (B). The displayed peaks were normalized to an identical event number so that the shape of the peaks can be compared. Below, the mean signal intensity of FL1 (green) and SSC (black) was read out as median value and plotted against the particle concentration. In (C) the median [a. u.] is utilized. To compare the behavior (i.e. the relation of signal strength vs. particle concentration) of SSC against that of FL1, the median values were normalized to 100% in a second graph (D).

From the histograms in *Figure 48A & B* it was obvious that the coincidence signal intensity decreased with decreasing particle concentration, as expected. Varying the NP concentration is equal to varying the number of particles per coincidence. Furthermore it was also observed that at low particle count, the SSC signals became more imprecise than the FL1 signals. This was obvious by the broader peaks and the higher coefficient of variation in the SSC samples of decreasing concentration.

The scattering of single particles (<200 nm) follows the Mie function and therefore does not behave similar to the FL1 signals. The relation between size and scattering at 90° is directed by the Mie scattering function¹⁶⁷. Coincidences are an overlay of scattering and fluorescence from several objects that are randomly distributed in a 3D space. Defined rules of scattering such as e. g. Mie do not apply here. Still the SSC intensity of a coincidence is reproducible – as long as the number of particles and their scattering properties (size, RI *etc.*) are approximately the same. So if the SSC intensities of coincidences in different samples are similar it may be assumed that these coincidences also contain a comparable number of NPs.

Figure 48D demonstrated that both FL1 and SSC signals of the coincidences were affected in a similar way by the varying particle concentration. The earlier observed shape change of the coincidence population (see Figure 47) therefore is just an artifact of the display mode in the SSC-FL1 scatter.

Finally a direct comparison of the particle-free reference and the PS-LFY-3 particle sample of minimum concentration was done. The diluted sample V8 should yield a count of approx. $40 \cdot 10^3$ [NPs \cdot s $^{-1}$] when measuring with $v_{exp} = 0.5$. Therefore the vast majority of the observed particle-derived signals were coincidences. In Figure 49 the upper population was selectively gated in the reference (A) and in the particle (B) sample. The gated data was displayed in FL1 (C) and SSC (D) histograms.

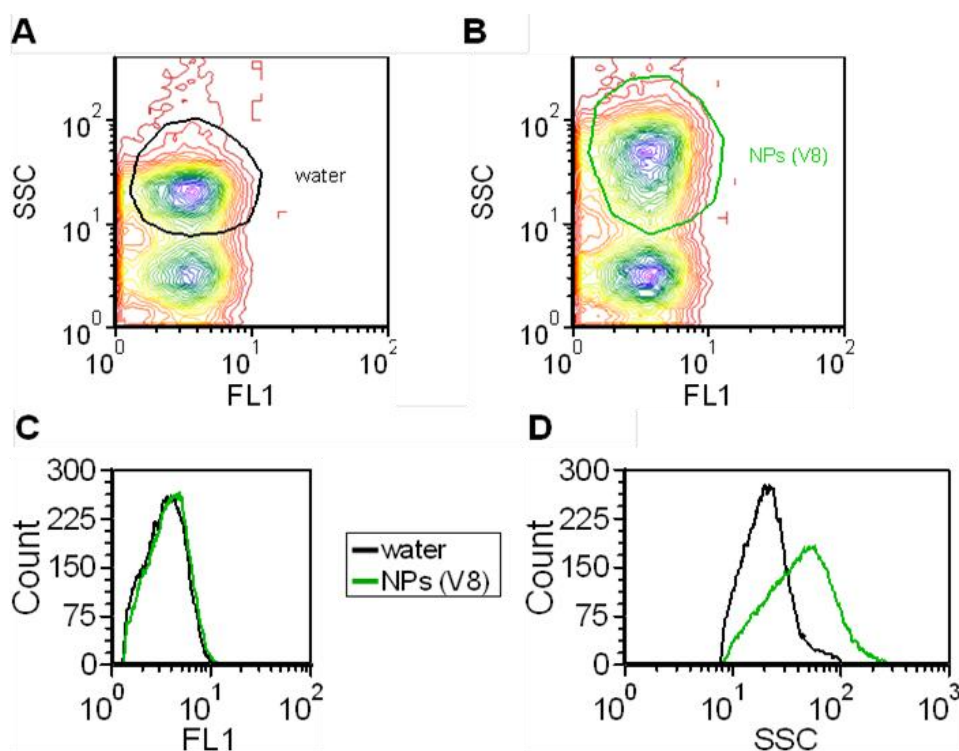


Figure 49. Comparing the reference sample water (A) with sample V8 (B) that contains $40 \cdot 10^3$ NPs per $0.5 \mu\text{l}$. The data sets were gated as given in A & B. The gated data was displayed in histograms of FL1 (C) and SSC (D) in black (water) and green (particle sample). The histograms were normalized to an identical event number.

The SSC signal of the particle sample was stronger than that of the reference, which indicated the presence of NPs. But despite this increased signal intensity, the events could not be isolated from the noise peak. In channel FL1, the peaks were not distinguishable at all (see Figure 49D & C). The conclusion was that at the high dilution V8, the coincidences contained only such a low amount of particles that the total fluorescence signals of even the coincidences were indistinctive from the background. Hence the detection of single PS-LFY-3 NPs would be impossible.

The conclusion was that either the SSC or the fluorescence signal intensity needed to be increased to enable a proper NP detection. The <200 nm sized particles, supplied with 1.33 [$\mu\text{g}\cdot\text{g}^{-1}$ polymer] of LFY dye, created insufficient signal strength of fluorescence and scattering.

The possible presence of nanoparticles in the bottom population (with the low SSC signal, see *Figure 49* above) had to be addressed as well. The SSC and FL1 signals in this population were identical for the reference and for sample V8 (data not shown). The presence of single particles in this population is unlikely for the following reason. The signal of a single NP is within the same dimension as the signal of a smaller coagulate or coincidence. The generally broad distribution of all populations, spanning over one decade, further complicates such a distinction. In any case the two discussed populations are well separated and differ by a factor of >10 in their SSC signal strength. It was already proven that particle-derived signals are present in the top population; hence there should not be any in the 2nd population at 1/10 of SSC signal intensity.

Differentiating single particles and coincidences would only be possible with a strong particle signal as *e.g.* from calibration microspheres. Experiments with micron sized calibration beads (Partec) had confirmed this. *Figure 50* demonstrates that here the distinction between single spheres (Gate 1), duplets (Gate 2) and triplets (Gate 3) was easy. Compared to the single sphere event, the fluorescence intensity of duplets and triplets was increased to 200% and 300%, respectively. For scattering signals, the FSC was utilized instead of SSC, due to the large size of the spheres. The FSC signal of duplets and triplets was increased, but, as expected, did not follow a direct proportional relation.

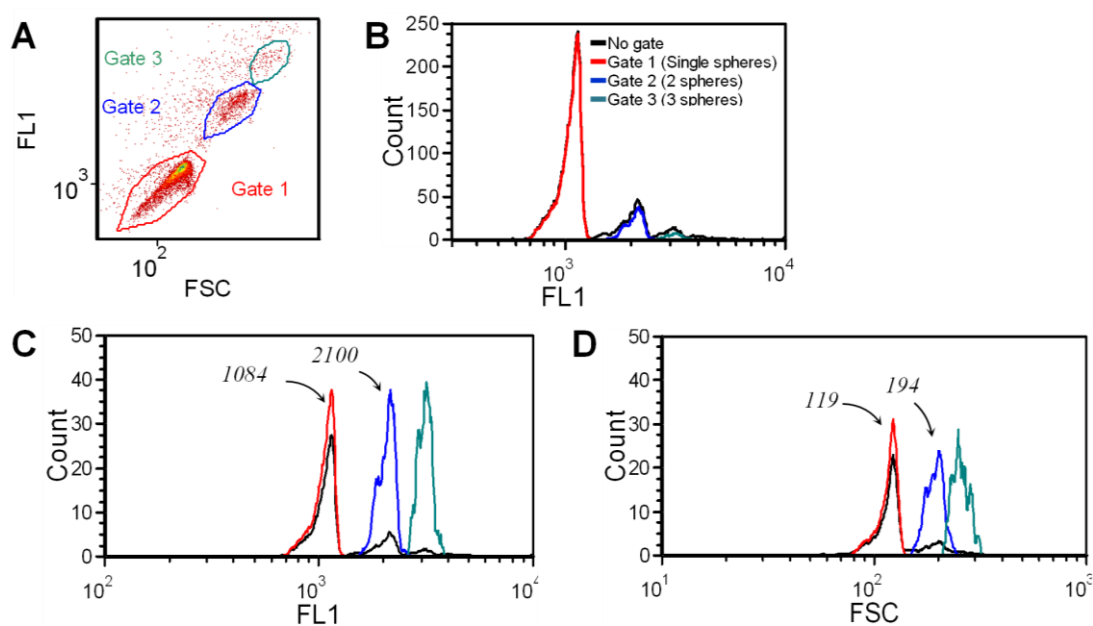


Figure 50. Calibration beads were measured and in a FSC-FL1 plot (A) three distinctive populations termed Gate 1-3 were identified. The gated data was projected into histograms of FL1 (B & C) and FSC (D). In images (C) and (D) the peaks were normalized to an identical event count.

With the nanoparticles and the machine used in this thesis, the fluorescence and scatter signals of single LFY marked nanoparticles were too weak and had a high CV. The resolution of single particle events from coincidences or duplets was not possible under these circumstances.

Based on these findings a criterion was developed which allowed one to evaluate if single particle detection would be possible with a certain particle sample: Possibly only one population is visible and its FL1 and SSC signals decrease with lower sample concentration until the population merges with the background and disappears. Such a sample should not be considered for SPM. But with a suitable sample, at some point a population will be visible that retains a constant fluorescence intensity – despite further sample dilution. The events in this population will retain a constant fluorescence signal intensity until this population disappears (when the sample is diluted such that it hardly contains any particles). If this is the case then the sample is eligible for SPM; these events are representing single particles which can be distinguished from the background.

To provide a supplementary strategy to identify the single particle population, the variation in particle concentration was imitated: A highly concentrated sample was measured shortly to load the NPs into the FC. When a particle-free sample was measured afterwards the cytometer interior was still ‘contaminated’ with remaining NPs. Therefore it was possible to watch live, in the course of the measurement, how the NPs were gradually washed out. The decreasing particle count simulated the subsequent analysis of samples of decreasing concentrations. The unique benefit of this approach was that it provided a seamless transition from high to low sample concentration and to a particle-free sample. The information was collected by taking screenshots from the live measurement (see *Figure 51*).

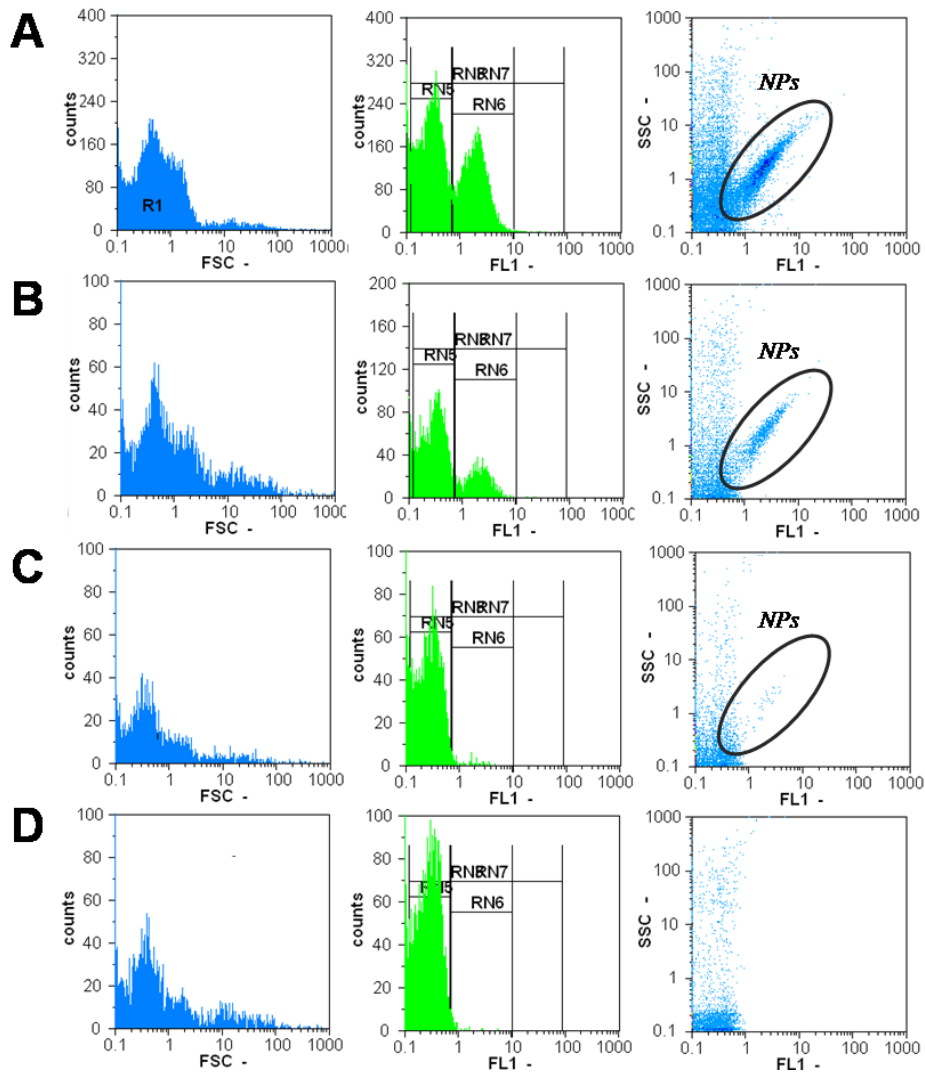


Figure 51. The FC had been loaded with NPs by measuring an over-concentrated PMMA-BP1-2 sample. The remaining particles were gradually washed out throughout 3 min (A-C) during the next run (new sample: water). Below (D) a particle-free reference measurement of water is provided.

In Figure 51 the gates RN5 and RN6 in the FL1 histograms demonstrated that the peaks did not shift position throughout the measurement. RN5 marked the fluorescence signal intensity of the background as this peak was equally present in the control sample (D). The RN6 peak does not further shift to the left and merge with the RN5 peak, but instead remained at the same position until it disappeared (A-C) when there were no more NPs left in the FC. As discussed earlier, this proved that peak RN6 represented a population of single nanoparticles.

4.3.1.4 Particle Scattering Properties (Size and Refractive Index)

In a first approach to identify particle-derived signals by size (or scattering signals), the sample was filtrated prior to the FC measurement. The filtration step, through 0.2 and 0.45 μm pore size membranes, removed all objects larger than the pore size – which should include

coagulates, particle aggregates and contaminating objects. Comparing the data morphology of original and of filtrated samples, particle signals might be identified. The measurement of a non-filtered and a 0.2 μm filtered PMMA-AT3 (120 nm, dye BP2) sample was compared, see *Figure 52*.

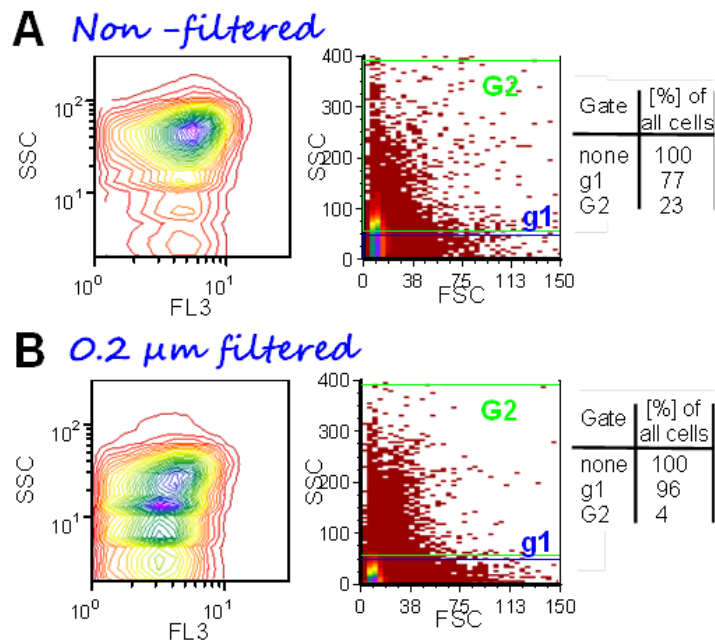


Figure 52. Measurement of PMMA-AT3 particles before (A) and after (B) filtration with 0.2 μm pore size. The SSC-FL3 plots demonstrated that filtration changed the sample morphology. The SSC-FSC scattering plots (center) define two gates for lower (g1, blue) and for higher (G2, green) SSC signal intensities. The percentage of events per gate is given to the right.

Larger objects and particle coagulates should be expected rather in gate G2 than in g1, as G2 defines a higher SSC signal. Before filtration, gate G2 contained approx. 23% [events of the total sum of events], which was reduced to 4% after the sample was filtrated. Simultaneously, the content in gate g1 was increased from 77% to 96%. The 0.2 μm filtration selectively removed G2 events which showed that the G2 events mostly represented objects larger than 0.2 μm (and coincidences). The SSC signal intensity depends not only on the object size but also on parameters like *e.g.* the refractive index RI. The SSC should preferably be used for size comparisons of objects with similar properties (material, RI, shape, etc). The experiment proved that the fluorescence of PMMA-AT3 particles was not suitable for SPM. No specific pattern in the SSC-FL plot, which could be attributed to nanoparticles, was visible (see *Figure 52, left*). A 0.45 μm pore-size filtration yielded similar results (data not shown).

This experiment demonstrated that objects smaller than 0.2 μm (contaminations and particles), and possibly minor coincidences, were located in gate g1. Therefore any single nanoparticle population should as well be sought in the location of gate g1 (using similar experimental conditions).

4.3.1.5 Fluorescence of the Nanoparticles (Emission Spectra and Intensity)

When particles below 200 nm size cannot be distinguished from the background by their scattering signals (which mostly is the case), the other option is the fluorescence signal. In particular, the emission properties of different particles could be exploited to differentiate single particle events from coincidences. This approach is described in the following. For these experiments, two species of particles were mixed that are distinguishable by a certain parameter, the emission intensity or the emission wavelength. In the case of successful SPM the flow cytometry data should reveal two separate populations with the mentioned emission properties. But in the case of coincidences, some of the E_{err} would contain a mix of the two particle species – and thus combine the properties of both species and e.g. yield fluorescence signals in both FL channels. The working principle of two approaches is given in *Figure 53*.

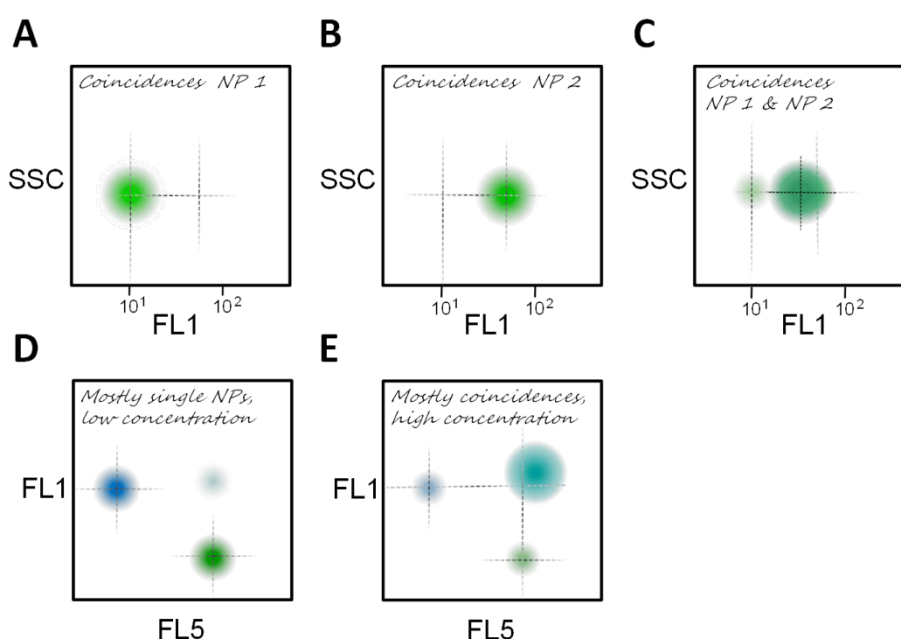


Figure 53. Proof of coincidences by measuring a mix of two NP species with different properties: In one approach (A-C), two particle samples are used which emit in the same FL channel but with different intensity. These are measured separately at similar, high, concentrations so that coincidences occur (A & B). Then an equal mixture of both species with a similar total NP concentration is analyzed; these coincidences should represent a comparable amount of NPs but now contain a mixture of both species (C). A new population appears and whilst its SSC intensity should be roughly similar (because the total particle content is the same) the FL signal should be an intermediate of both species' FL intensities. Alternatively an equal mixture of two NP species that emit in different FL channels (D-E) can be used. When measuring at low concentration (that allows SPM), a separate NP population should be observed in each of the FL channels (D). The two species with different fluorophores can be distinguished in the fluorescence dotplot. At high concentration, coincidences appear as a 3rd population (E) that combines the fluorescence properties of both NPs. Scatter and fluorescence signals of this population should be higher than for the single-species populations.

According to the method described in *Figure 53A & B*, a mix of two particle species with different fluorescence intensities (in the FL1 channel) was measured. By synthesis, particle PS-LFY-4 should contain the 6-fold amount of dye compared to PS-LFY-1. If the fluorescence intensity was roughly in proportion to the dye content, this difference might be sufficient to distinguish the two particle populations by their FL1 signal intensity. For synthesis of the PS-LFY-1 till -4 series, an amount of 2, 4, 8 and 12 mg dye were added per 6 g monomer. Absorption spectroscopy revealed a relative dye content of 1, 3, 7 and 12, normalized to the 2 mg sample. Particle material, refractive index and size were the same so the particles' SSC signals should be similar. The samples PS-LFY-1 till -4 were treated in a similar manner, centrifuged and the pellet was re-dispersed in water. All dispersions were diluted 1:2000 prior to the FC measurement, so that the NP concentrations in the final samples were nearly similar. The fluorescence intensity of the different particle species was first measured separately (see *Figure 54*) to ensure that PS-LFY-1 and -4 were eligible for the described proof for SPM.

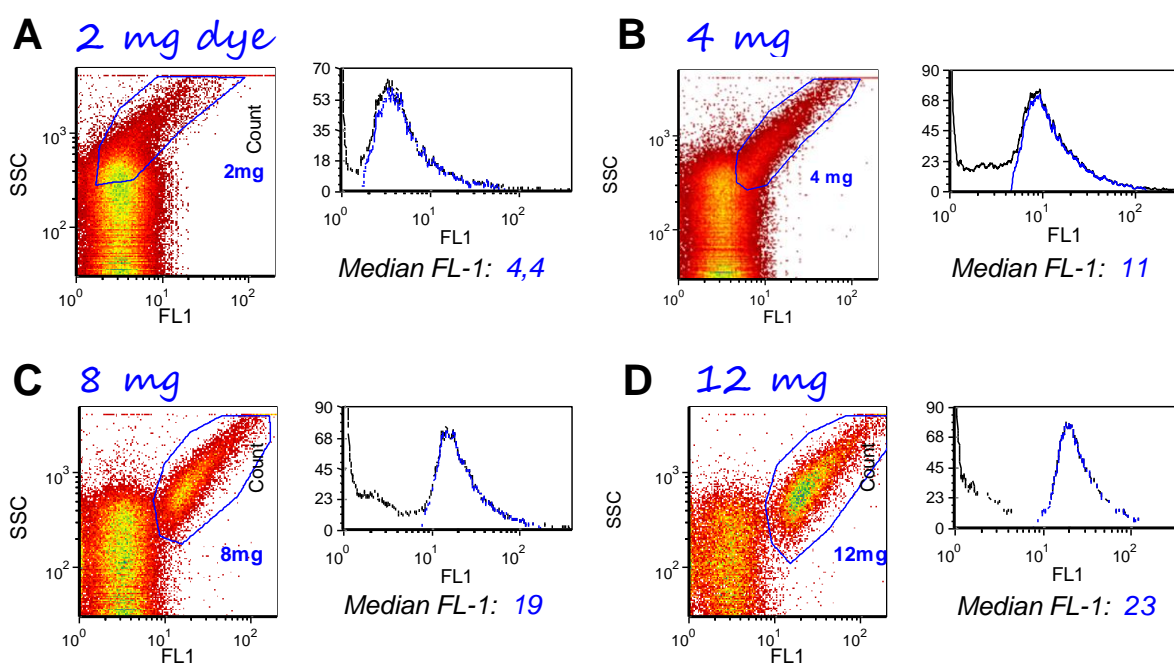


Figure 54. FC measurement of LF yellow marked nanoparticles at 100 mW laser power. The particles were synthesized with 2 mg (A), 4 mg (B), 8 mg (C) and 12 mg (D) of dye per 6 g monomer. Particle-derived signals i.e. coincidences were marked in the SSC-FL1 dotplots (blue gate) and projected into the FL1 histogram to extract the median value.

At this concentration of the particle samples SPM was excluded and the observed fluorescing events could only be coincidences. Under the assumption that the particles have similar size and scattering properties, the SSC signal of a coincidence only depends on the number of NPs it is summing up. Therefore, if the coincidence events in the samples had a similar SSC signal, the average number of NPs per coincidence should also be similar. The SSC values

(data not shown) of the discussed events differed by less than 5%. It was concluded that, in good approximation, the average NP count was the same in all coincidences. Hence the FL1 signal strength of each coincidence was dependent on the FL1 signal intensity of the particles – and therefore increased with the amount of incorporated dye. The fluorescence of the nanoparticles could be compared at the base of coincidence events alone – which is a vital tool for the flow cytometric measurement of all those NPs that have insufficient signal strength for real SPM. The experiment also proved that the FL1 signals of PS-LFY-1 and -4 differed by a factor of approximately 5.

The pair of PS-LFY-1 and 4 was therefore suitable for the above described measurement (see *Figure 53A - C*) where a mix of two particles is measured to prove SPM. The samples PS-LFY-1 (diluted 1: $20 \cdot 10^3$) and -4 (diluted 1: $32 \cdot 10^3$) were measured separately under identical conditions (laser power 100 mW, FL1: 500, threshold on FSC5, $v_{exp} = 1$). Then an equal mixture of both NPs was measured in a similar manner. The total count in each run was $80 \cdot 10^3$ events. The results of this experiment are shown in *Figure 55*.

In *Figure 55* the coincidences in the mixed sample (image *C*, gates *1 & 4*) have a higher SSC signal compared to the separate sample of the dim (*A*, gate *1*) and the highly fluorescent (*B*, gate *4*) particle species. This demonstrated that the coincidences of the mix sample contained slightly more particles. But more importantly, the FL1 signals in the mixed sample (*C*) were higher than those in the weakly fluorescent sample (*A*) but lower than in the highly fluorescent particle sample (*B*). This was the proof that the coincidences contained particles of high (PS-LFY-4) and of low (PS-LFY-1) fluorescence intensity. As was expected, in the mixed sample the coincidences had fluorescence properties (here: the FL1 signal intensity) that lay between those of the two particles species.

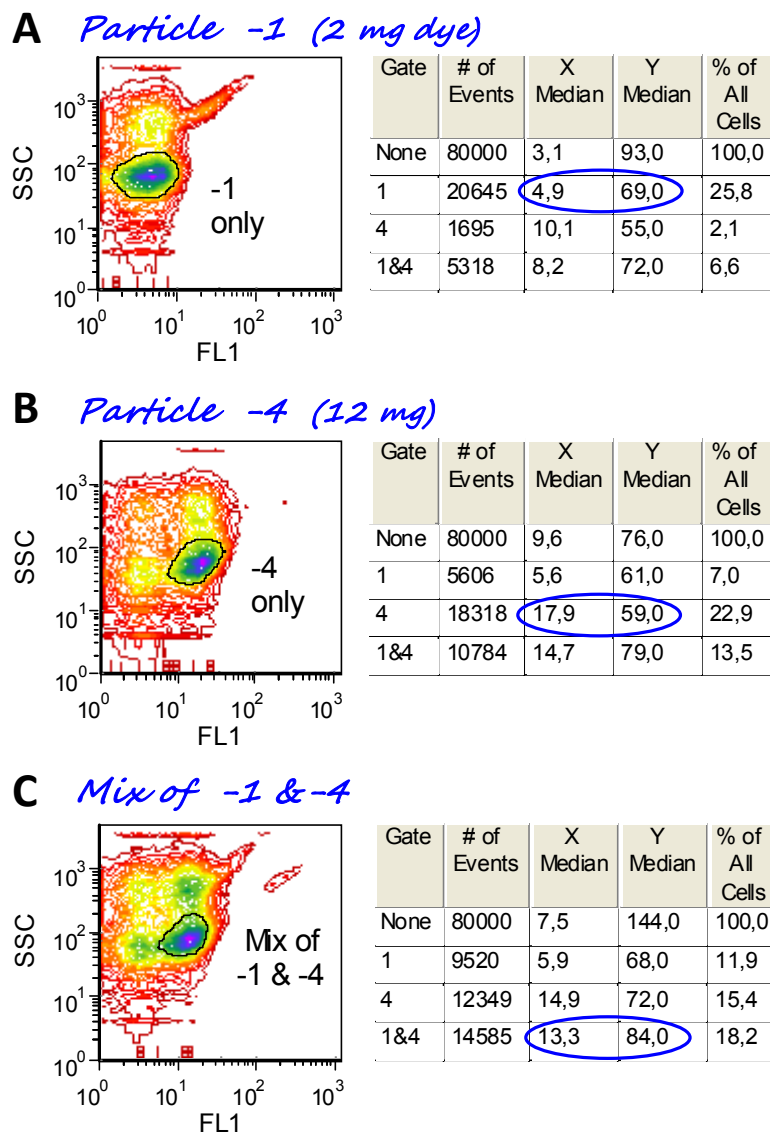


Figure 55. Comparing the separate measurement of PS-LFY-1 (low fluorescence, A) and PS-LFY-4 (high fluorescence, B) against the measurement of a mixture of both particle species (C). In the SSC-FL1 dotplots (left), events of interest, i.e. assumed particle coincidences, were gated with black regions. In the statistics to the right, the SSC (y-median) and the FL1 signal (x-median) of the respective gated regions are highlighted (blue circle).

The identification of coincidences on the base of particles with different fluorescence intensities was successful. It would be even more convenient to do this test by measuring a mix of NPs that emit at different wavelengths *i.e.* that are detected in different FL channels. For this reason the proof of SPM was done with a pair of NPs that had different fluorescent markers: One for detection in channel FL5 (PMMA-AT3 particles with the BP2 dye) and one for detection in channel FL1 (PMMA-SDS-4 particles with the dye PMI).

Both NPs were of similar material and size hence their SSC signals should be similar. An equal mixture of both NPs at high concentration (a 1:2000 dilution guaranteed the presence of coincidences) was measured to prove the presence of coincidences (see Figure 56).

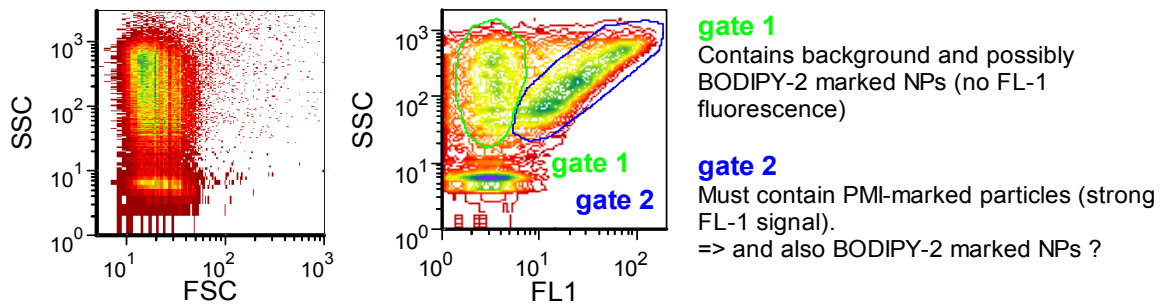


Figure 56. Measurement of a mixture of particles which could be detected separately in the channels FL1 (PMMA-SDS-4) and FL5 (PMMA-AT3). In addition to the scatter plot (l.) the data set is displayed in a SSC-FL1 dotplot. Here the upper populations were marked by gate 1 (green) and gate 2 (blue). Particle coincidences should be contained in at least one of these gates, due to the high scattering intensity.

In order to prove the presence of coincidences, which contain both particle species, the events in gate 1 and gate 2 were displayed separately (see Figure 57).

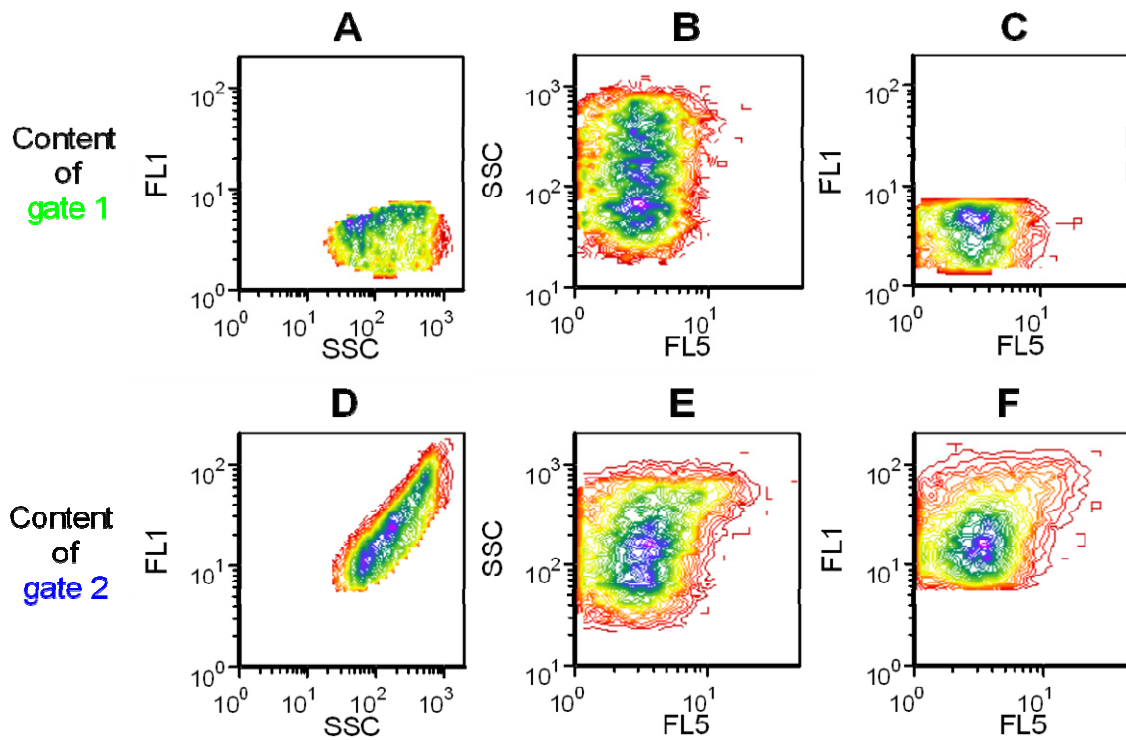


Figure 57. Selective dotplots of the events that were gated as described in the previous figure. Gate 1 contained events of low FL1 (A) and FL5 (B) signal intensity, which was particularly obvious in the FL1-FL5 dotplot (C). In contrary, gate 2 mostly enclosed events of high FL1 (D) and medium FL5 (E) signal strength. The combined FL1-FL5 dotplot (F) demonstrated that gate 2 included events with strong emission in both fluorescence channels. These events were located in the upper right area of the displayed population (black circle).

A distinction between coincidences and single particles was not possible with this set of particles. But the presence of coincidences was proven without a doubt – by the fact that the features of both particle species (fluorescence in FL1 and in FL5) were found combined in one event.

SUMMARY The importance of a careful balance between signal amplification and threshold minimum setting was demonstrated. Concerning nanoparticles, a low threshold on the FSC was suited for detection because it was ensured that no event population is excluded. Once the location of particle signals is known, the threshold can be fine tuned to exclude noise signals more specifically. The studies of higher precision yielded that the threshold is ideally set on the low SSC for NP detection. Furthermore it was shown with LF yellow marked spheres that increasing the laser power can selectively enhance the particles' FL1 signals. Neither the SSC signals (background or particles) nor the background FL1 signals (false positive) were enhanced to the same extent. Therefore most NP measurements were done with 200 mW laser power.

The importance of correct sample dilution in FCy was stressed as the NP count rate is regulated by sample concentration and measurement speed. If the concentration is too high, only coincidences are observed, as demonstrated by a measurement of PMMA-SDS-4 particles. Analysis of a PS-LFY-3 dilution series, however, demonstrated that also coincidences can be a 'controllable' system to some extent. It could be shown that the fluorescence and SSC intensity of a coincidence was precisely linked to the number of NPs it contains. This enables one to judge the number of NPs per coincidence when different polymeric NPss (of similar size and RI) are to be compared. This gives the opportunity to compare particle fluorescence based on coincidences measurements – which is particularly useful if the fluorescence signals are too weak for single nanoparticle detection. The location of NP-derived and of noise events in the SSC-FL1 dotplot was evaluated.

In order to differentiate singlets from duplets, or from small coincidences, a minimum signal intensity (in SSC or FL) is required. Submicron particles of the current size and fluorophore content distribution did not fulfill this criterion; unlike *e.g.* μm sized calibration beads. However, the differentiation between single NP events and small coagulates or coincidences is crucial. Therefore another proof for SPM was provided where a mixture of two particle species was measured. The two NP species differed in one particular property – in the wavelength or in the intensity of their fluorescence emission. If, in the equal mixture, a population of events occurred that combined the properties of both NP species, then these events had to be coincidences. An FCy measurement of the PS-LFY particle series (loaded with 2-12 mg dye per 6 g polymer) had shown that their dye loading ratio was sufficient to notice the difference in the FL1 signals. Hence an equal mixture of the samples PS-LFY-1 and -3 (loaded with 2 and 8 mg dye per 6 g monomer) was measured at high concentration. Events with fluorescence intensities that lay in between that of the two samples were observed and the existence of coincidences was proven. However, such proof would be most useful if it

could be applied for lower sample concentrations, that enable an SPM. Therefore a pair of NPs with different fluorophores, to be detected independently in channel FL1 and FL5, was measured following the same principle. Unlike the approach with varying FL1 intensities, the method with 2 fluorophores would also work at low sample concentrations.

4.3.2 Screening for Suitable Fluorescent Nanoparticles

For flow cytometric applications, the fluorescence of a single particle needs to be strong enough to distinguish it from the background. Therefore a screening method was applied to quickly identify promising particle species that were likely to fulfill this criterion for SPM. Particles were tested at low dilutions of approx. $1:10^6$ (of the 20%-wt. samples). The principle was to watch the signal intensity of coincidences. The 1:1 mio dilution of 20%-wt. samples contains $16 \cdot 10^3$ to $500 \cdot 10^3$ NPs per $0.5 \mu\text{l}$ when the diameter is 220 to 70 nm. If, at such high sample concentration, the coincidence events do not surpass an FL signal intensity of 20 [a. u.], then the sample is not suitable for FC SPM. Several particle samples were tested this way at a laser power of 200 mW with identical settings (FL1: 500, threshold set to SSC30, $v_{exp} = 0.5 \mu\text{l} \cdot \text{s}^{-1}$), if not described else.

This screening method was implemented to help identify promising fluorophores that can be loaded into particles at a high concentration and retain a high fluorescence intensity. Some perylene dyes (including e.g. the dye PMI that was until then used for most of the NP syntheses) were susceptible to a) varied hydrophobicity of the polymer material, b) to high dye concentrations inside the particles (stacking occurred) and they c) displayed a limited solubility in e.g. the styrene monomer. For these reasons the desired fluorescence signal strength of NPs could not be achieved with the PMI dye. Therefore several particles were synthesized and a variety of fluorophores was incorporated (see chapters 3.1 and 4.1.3). An overview of these particles with the incorporated dyes is given in *Table 14*.

Table 14. Properties of the tested nanoparticles.

Sample	≈ Diameter	Dye	Laser for excitation	FC channels for detection
PS-SDS-1	120 nm	none	/	/
PMMA-BP1-2	160 nm	BP1	488 nm	FL1, FL2
CH235-3	70 nm	BP1	488 nm	FL1, FL2
PMMA-AT3	120 nm	BP2	640 nm	FL5
PS-AM-5	>250 nm	PMI	488 nm	FL1, FL2, FL3
PMMA-SDS-4b	120 nm	PMI	488 nm	FL1, FL2, FL3
PS-SDS-4	125 nm	MS1B	488 nm	FL1, FL2, FL3
PS-SDS-5	115nm	MS1C	(488 nm,) 562 nm	FL5, FL6
PS-LFY-3	115nm	LFY	488 nm	FL1
PS-AM-8	230 nm	LFR	562 nm	FL5 (, FL6)

4.3.2.1 Blank reference particles

PS-SDS-1 (blank) particles were measured as reference. The sample PS-SDS-1 (diameter 120 nm) was diluted $1:1 \cdot 10^6$ so that the theoretical count rate was in the range of $100 \cdot 10^3 \text{ s}^{-1}$. Due to limited temporal resolution and coincidence formation less than $4 \cdot 10^3$ particles s^{-1} were detected. As shown in *Figure 58* the median values [a. u.] of 3 (FL1), 5 (FL2) and 1 (FL5) were defined as the average signal intensity of non-fluorescent NPs and of noise such as air bubbles or contaminating objects.

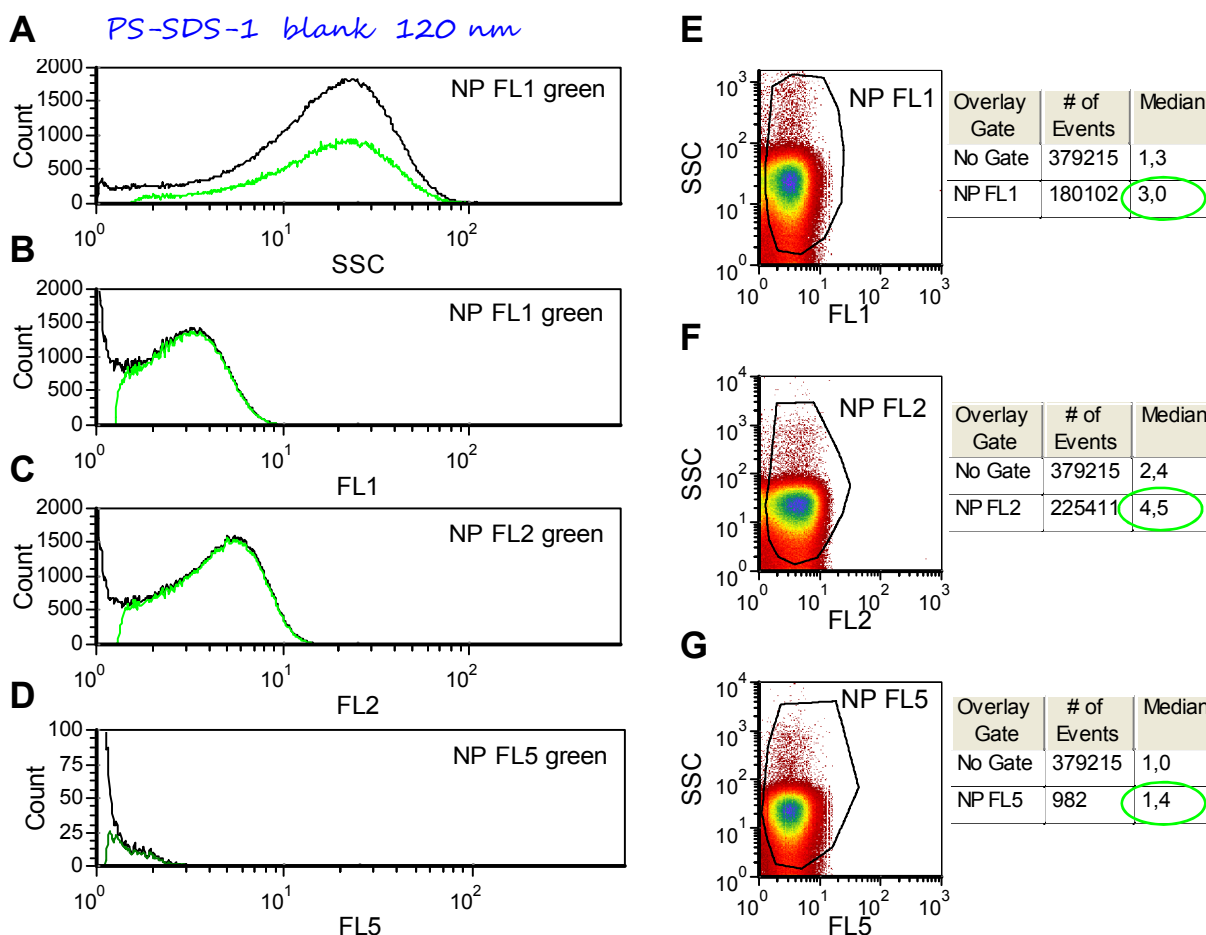


Figure 58. FC measurement of $1:1 \cdot 10^6$ diluted PS-SDS-1 NPs. The data is displayed as SSC (A), FL1 (B), FL2 (C), and FL5 (D) histograms. Gates were applied on the various SSC-FL plots (E-G). The gated events were projected in the histograms (green) to evaluate the FL median (tables).

4.3.2.2 BODIPY Dyes

PMMA-BP1-2 (BP1) These medium sized particles (160 nm) yielded an FL1 median of 48 [a. u.]. At the dilution of $1:1 \cdot 10^6$, the theoretical count was $40 \cdot 10^3 \text{ s}^{-1}$ and 9700 s^{-1} were measured. It was confirmed that this sample was suitable for the SPM. In the SSC-FL1 plot a cloud of particle-derived events was well separated from the background (*Figure 59*).

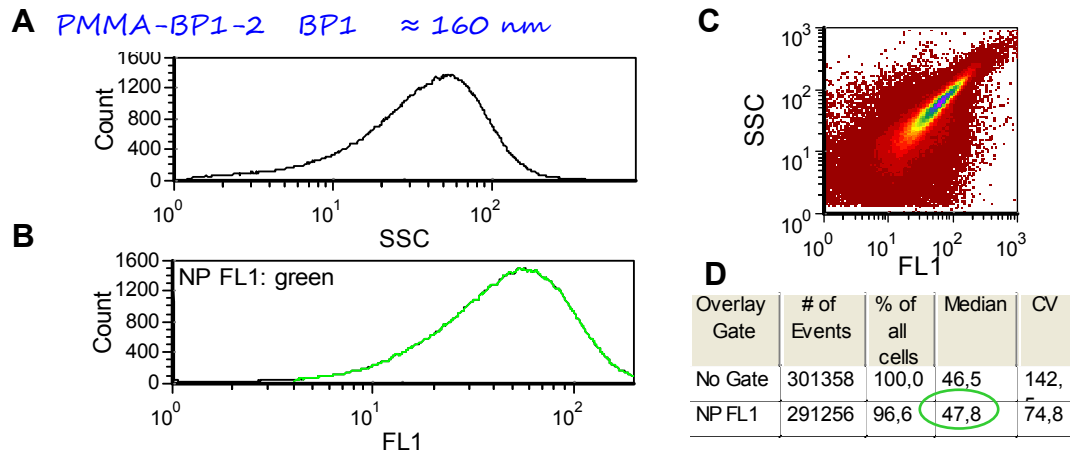


Figure 59. FC measurement of $1:1 \cdot 10^6$ diluted PMMA-BP1-2 particles. Histograms of SSC (A) and FL1 (B) demonstrate the strong SSC and FL1 signals. The population in the SSC-FL1 plot was gated (C) and the FL1 median of the gated events was evaluated (D).

CH235-3 (BP1) The small particles with a diameter of 70 nm yielded a count of 3300 s^{-1} at the dilution $1:1 \cdot 10^6$. The theoretical particle count was $550 \cdot 10^3 \text{ s}^{-1}$ and an FL1 signal in the range of 35 [a. u.] was measured. Considering the high sample concentration (approx. 10-fold higher than that of the previous sample PMMA-BP1-2) and the comparably low FL signal, the particles might have insufficient fluorescence properties for SPM. But on the other hand the rather low SSC signal indicated that these NPs had a strong fluorescence intensity considering their small size. A diagonal upwards shift of the population in the SSC-FL1 dotplot (see Figure 60C) further indicated that these NPs might be suitable for SPM despite the small size.

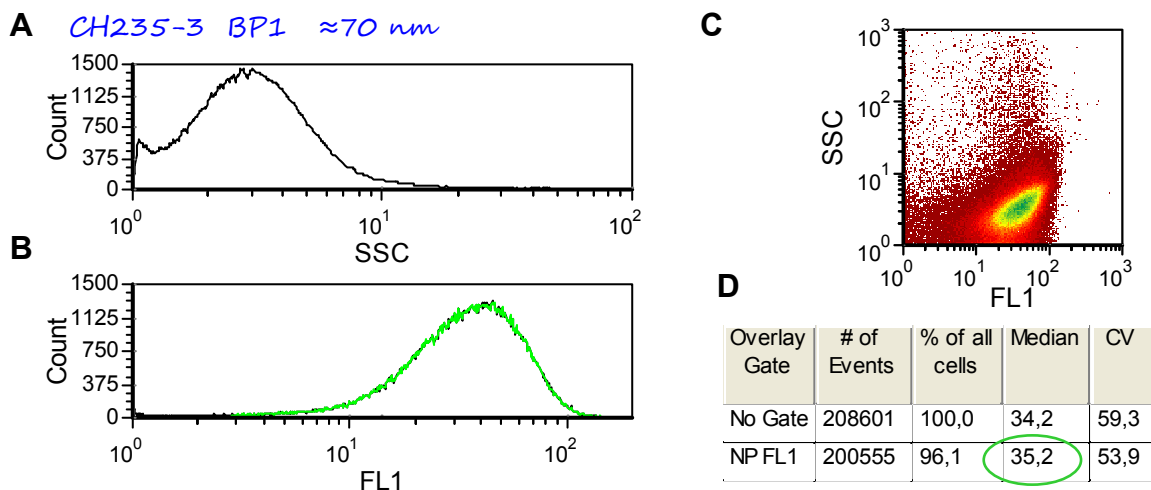


Figure 60. FC measurement of $1:1 \cdot 10^6$ diluted CH235-3 particles. Histograms of SSC (A) and FL1 (B) showed that the particles had strong FL1 signals and comparably weak SSC signals. A gate (not shown) was applied on the visible population in the SSC-FL1 plot (C) and the FL1 median of the gated events was evaluated (D).

PMMA-AT3 (BP2) The particles with a diameter of 120 nm were measured with an increased background. Only a dialyzed sample of these was available and it contained more contaminating particles, hence the strong SSC signal. The fluorescence should be detected in channel FL6 after excitation with the 640 nm laser. But despite high signal amplification (PMT set to 650) no FL6 signal could be detected that was above the background signature. It was concluded that this sample was not suitable for SPM.

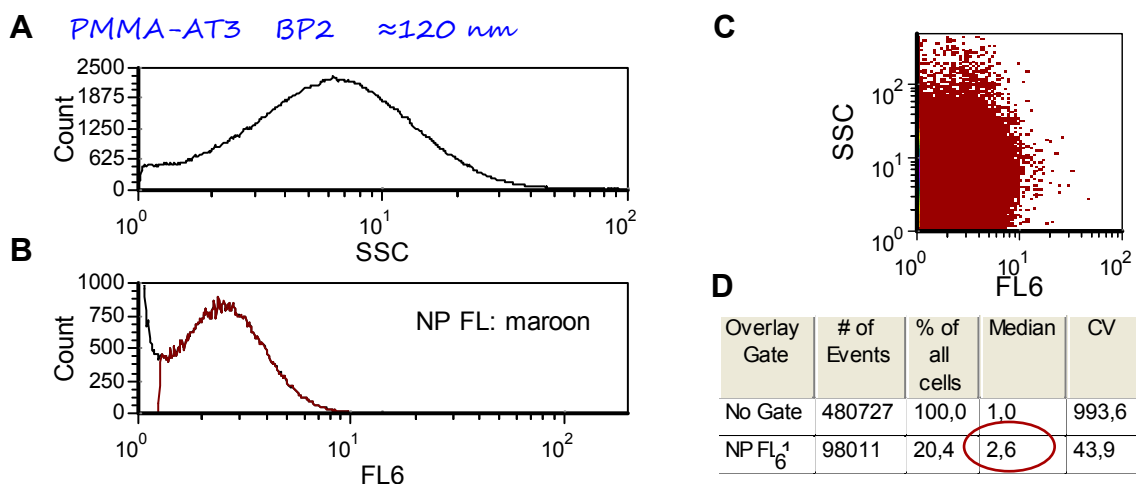


Figure 61. FC measurement of dialyzed PMMA-AT3 particles. Histograms of SSC (A) and FL6 (B) show that the particles had strong SSC signals but hardly any in FL6. A gate (not shown) was applied on the visible population in the SSC-FL6 plot (C) and the FL6 median of the gated events was evaluated (D).

4.3.2.3 Perylene Monoimide Dyes

PS-AM-5 (PMI) These large particles (diameter >250 nm) yielded a count of 4500 s⁻¹. The particles yielded intensive fluorescence but also high scattering signals. It was interesting to note that in both SSC and FL1 a bimodal distribution was observed. The intensity of SSC scatter and the presence of 2 populations confirmed the Nicomp DLS data. The NP signals could be distinguished very well from the background. These NPs were perfectly suitable for SPM, but in any case the intention of this work was the SPM of particles smaller than 250 nm.

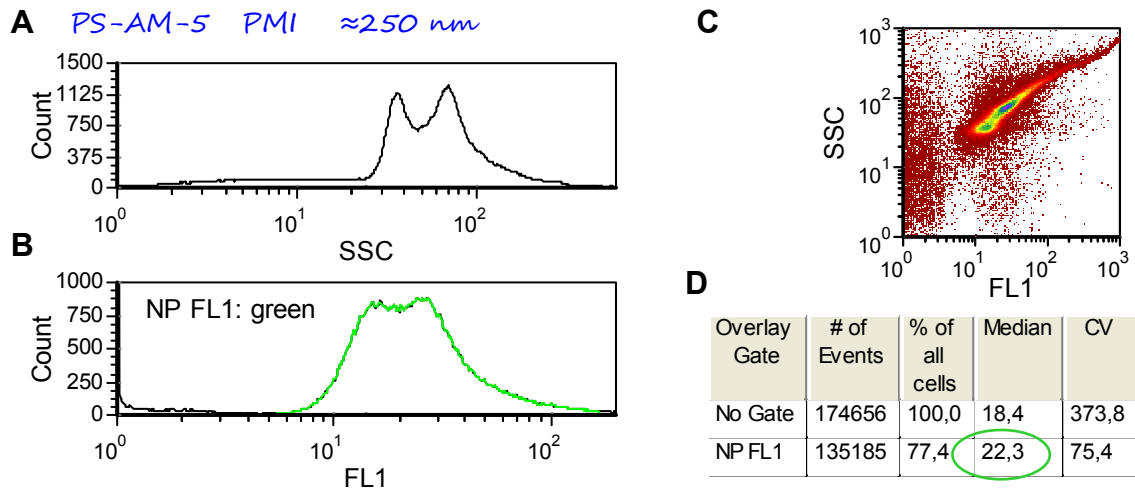


Figure 62. FC measurement of $1:1 \cdot 10^6$ diluted PS-AM-5 particles. SSC (A) and FL1 (B) histograms show that the particles had strong SSC and FL1 signals. A gate (not shown) was applied on the population in the SSC-FL1 plot (C) and the FL1 median of the gated events was read out (D).

PMMA-SDS-4b (PMI) For the sake of comparison, this screening was also demonstrated with NPs that were synthesized for non-quantitative cell uptake experiments. The sample had been synthesized following the standard recipe and contained only a small amount of the PMI dye. These particles (diameter approx. 120 nm) should have yielded a count of approx. $100 \cdot 10^3$ s⁻¹, but only 4800 s⁻¹ were measured. With a FL1 median of 6 [a. u.] the sample demonstrated only weak fluorescence (see Figure 63). The signal intensity was only doubled compared to that of the background events (see Figure 58 above). With this weak fluorescence signal despite the high concentration, the sample was not suitable for SPM.

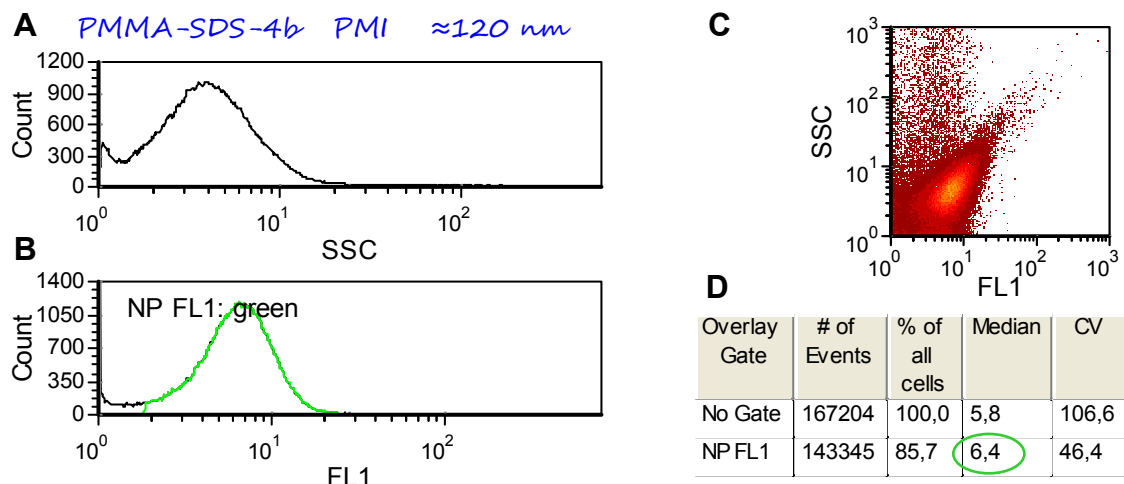


Figure 63. FC measurement of $1:1 \cdot 10^6$ diluted PMMA-SDS-4b particles. Histograms of SSC (A) and FL1 (B) show that the particles had low SSC but in particular low FL1 signals. A gate (not shown) was applied on the visible population in the SSC-FL1 plot (C) and the FL1 median of the gated events was read out (D).

4.3.2.4 Various Perylene Dyes

PS-SDS-4 (MS1B) The particles with a diameter of approx. 120 nm yielded a median value of 10 [a. u.] in the FL1 channel. Of the expected $10 \cdot 10^3$ approximately 5000 NPs·s⁻¹ were measured in the 1:10·10⁶ dilution (see Figure 64). The FL1 intensity hardly exceeded the SSC intensity, which indicated that the fluorescence of these NPs was too low for SPM. But obviously the dye MS1B emitted stronger than the dye PMI (see PMI-marked particles of similar size in Figure 63). Due to the enlarged Π -system, a better solubility in the monomer and less stacking effects of the MS1B dye were expected. The dye should therefore be used for another synthesis of highly fluorescent NPs with high dye loading (PS-Lut-1).

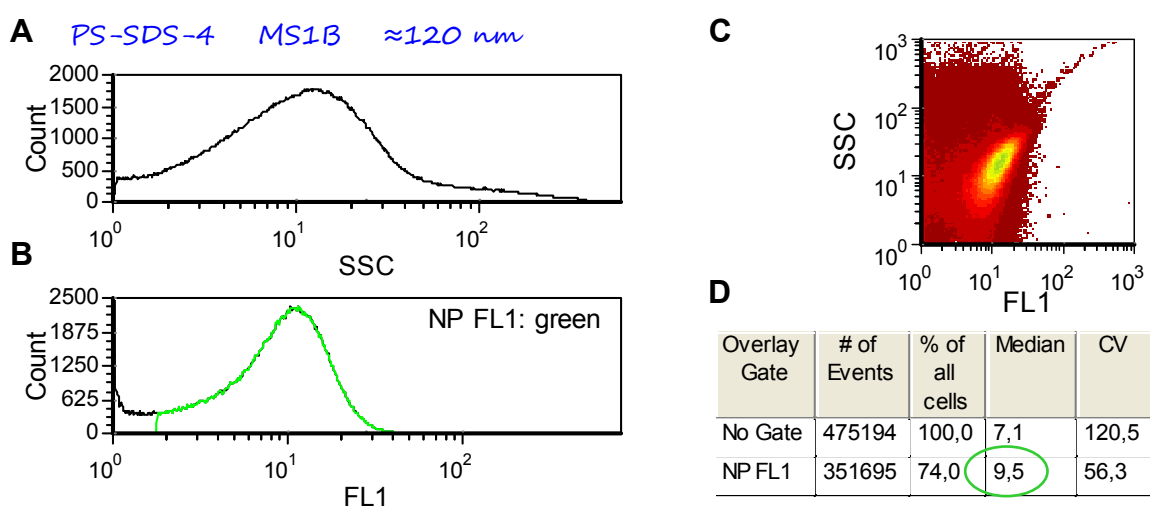


Figure 64. FC measurement of 1:10·10⁶ diluted PS-SDS-4 particles. Histograms of SSC (A) and FL1 (B) show that the NPs had medium SSC and FL1 signals. A gate (not shown) was applied on the visible population in the SSC-FL1 plot (C), and the FL1 median was evaluated (D).

PS-SDS-5 (MS1C) In this sample (120 nm diameter) approximately 4000 NPs·s⁻¹ were measured. The theoretical count was $25 \cdot 10^3$ NPs·s⁻¹ when diluted 1:5·10⁶. Median values of 3 (FL1) and 2 (FL5) were measured after excitation at 488 nm and 562 nm. This corresponds to the signals of background events. This dye was not suitable for excitation at 488 nm, as expected, but it neither was suitable for the 562 nm laser (see Figure 65).

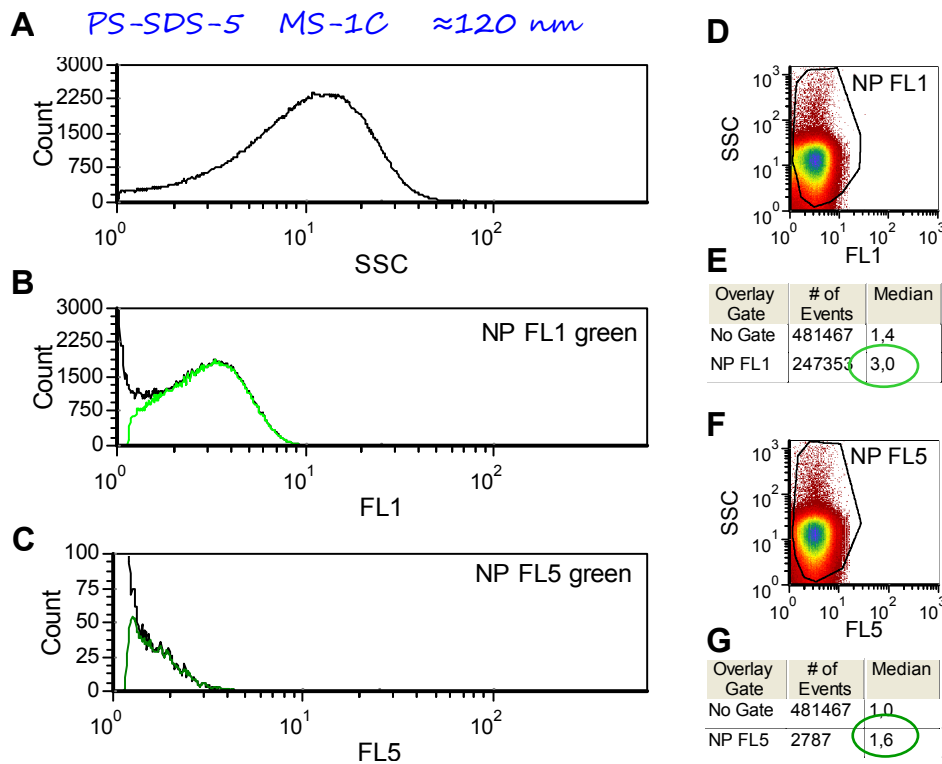


Figure 65. Measurement of PS-SDS-5 NPs. Histograms of SSC (A), FL1 (B) and FL5 (C) demonstrate that the NPs had a medium SSC. As demonstrated in the SSC-FL dotplots (D & F), the signals in FL1 and FL5 were weak. Populations were gated in the SSC-FL (D & F) and projected into the histograms (green graphs) to evaluate the median values (E & G).

A comparison with sample PS-SDS-4 (see Figure 66) showed that the dye MS1B yielded measurable emission signals in FL1 and a weak tendency in FL2. In these channels, an elongated population appeared that was stretched along the diagonal. But MS-1C gave no significant fluorescence signals at all, as observed not only by the low median values but also by the circular shape of the population in each dotplot. The signals did not even exceed the level of background and PS-SDS-5 or rather the dye MS1C was found unsuitable for SPM.

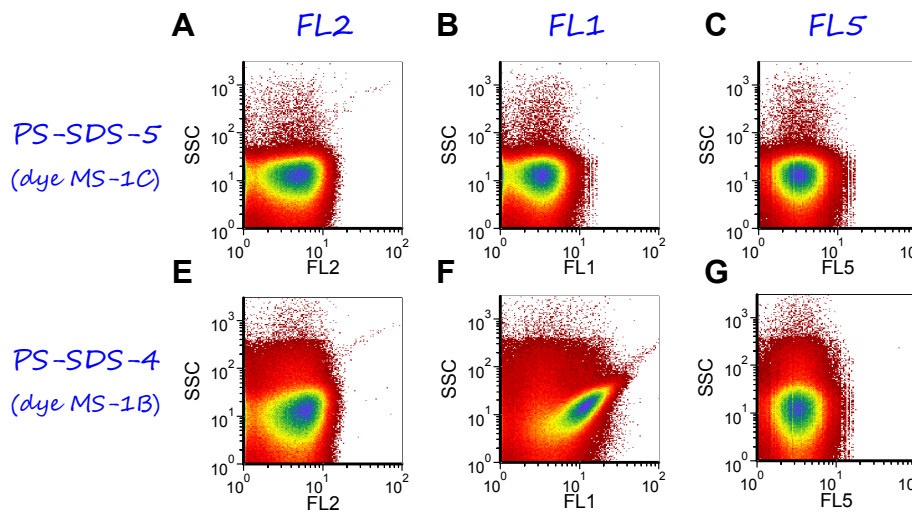


Figure 66. Comparison of PS-SDS-5 (top) and PS-SDS-4 (bottom) in FC after excitation at 488 nm and 562 nm. The data is displayed as SSC-FL dotplots of the channels FL2 (A & E), FL1 (B & F) and FL5 (C & G).

A direct comparison of PS-SDS-4 and -5 in Figure 66 demonstrated that neither of the NP species had significant emission in channel FL2 (A & E) or FL5 (C & G). The only significant fluorescence signal was detected in channel FL1 with the sample PS-SDS-4 (F). The particle signal could be identified, which demonstrated that, in principal, the dye MS-1B is suitable for SPM applications. But for full separation of the particles from the background, a new batch of particles with a higher load of MS-1B should be synthesized (see sample PS-Lut-1).

4.3.2.5 Lumogen F Dyes

PS-LFY-3 (LFY) These particles with a diameter of 120 nm yielded $4500 \text{ NPs}\cdot\text{s}^{-1}$ instead of calculated $116\cdot 10^3$ at a dilution of $1:1\cdot 10^6$. The median was 6 [a. u.] and therefore too low for an approach of SPM, in particular at such a high concentration.

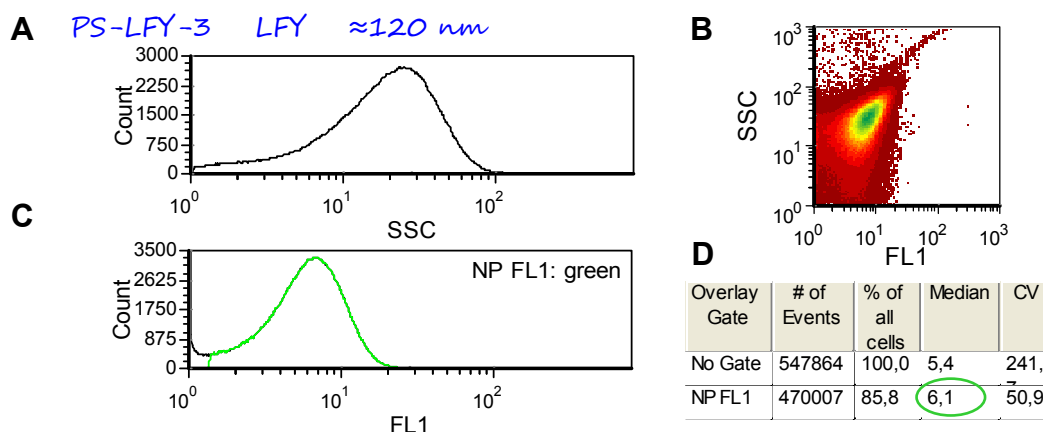


Figure 67. Measurement of 1:1 mio diluted PS-LFY-3 particles ($\approx 120 \text{ nm}$, dye PMI). Histograms of SSC (A) and FL1 (B) show that the particles had median SSC but in particular low FL1 signals. A gate (not shown) was applied on the population in the SSC-FL1 plot (C) and the FL1 median of the gated events was evaluated (D).

PS-AM-8 (LFR) As LFR was already known to be of medium fluorescence intensity, and the power of the 562 nm laser cannot be up-regulated, the LFR-marked particles were not expected to yield a strong signal. Therefore a $1:1 \cdot 10^6$ dilution of the larger PS-AM-8 particles (220 nm, dye LFR) was chosen for the measurement. For these large NPs (see *Figure 68*) a strong SSC signal in the form of a second peak above background level confirmed their presence (A). They yielded an FL5 median of 1 which is the signal intensity of background events (C & F). Of the expected $16 \cdot 10^3$ approximately 4500 particles were detected. It was observed that the fluorophore was partially excited by the 488 nm and showed minor emission in channel FL2 (D). No stronger FL5 signal was detected; these particles and the dye LFR in general were not suitable for SPM.

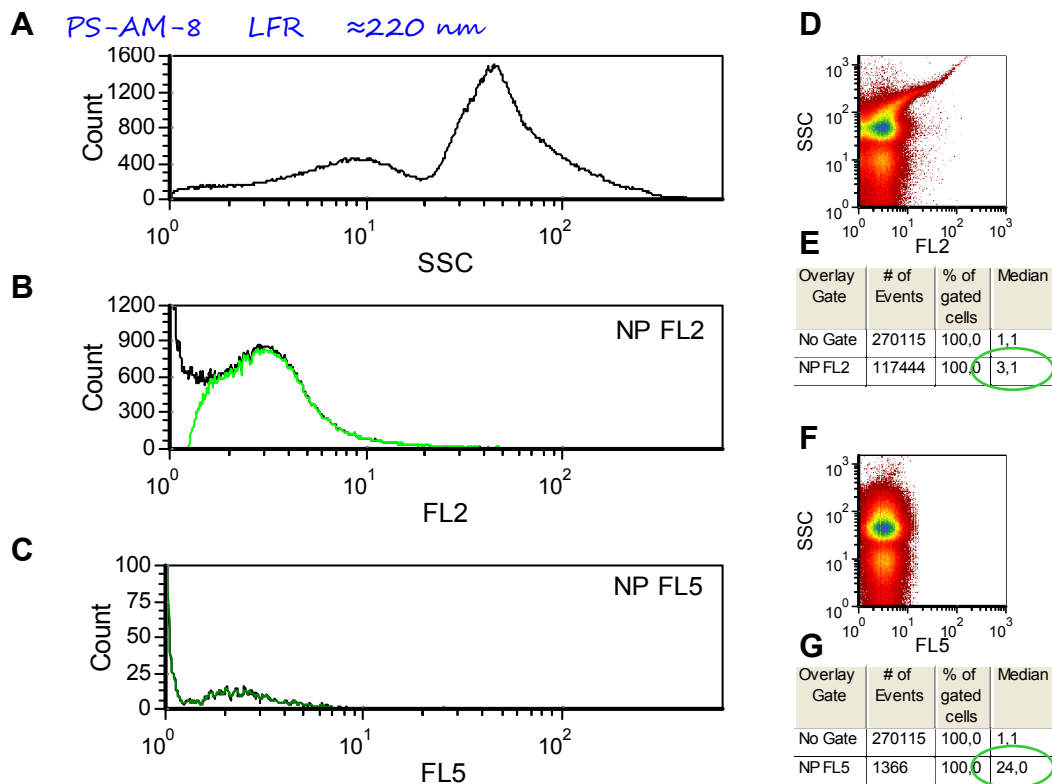


Figure 68. Fcy data of PS-AM-8 particles. The SSC histogram (A) showed that the particles had a very high SSC signal and were even visible as a separate peak. The FL5 histogram (C) and dotplot (F) however demonstrated that the NPs had no significant FL5 fluorescence signal. It was observed that the fluorophore was also excitable at 488 nm because some fluorescence signals in channel FL2 (B & D) appeared. The visible population in the SSC-FL1 (D) and SSC-FL5 (C) plots was gated, projected into the histograms (green graphs) and the median values were evaluated (E & G).

SUMMARY It was crucial to distinguish those nanoparticles that were possibly suitable for SPM from those that would never be due to their low fluorescence signal. For this purpose a screening method was developed, where promising particles were measured at high sample concentrations that should be roughly similar. Blank spheres without dye provided reference values. It was found that, as was already known, the particles PMMA-BP1-2 (dye BP1) had a strong fluorescence signal. The much smaller CH235-3 particles, also with the dye BP1, had a slightly weaker signal despite the higher concentration. Despite the rather high FL1 fluorescence intensity, compared to the SSC signal, it could not be defined if these particles were suitable for SPM or not. Other particles like PMMA-SDS-4b (dye PMI), PS-SDS-4 (dye MS1B), PMMA-AT3 (dye BP2), PS-SDS-5 (dye MS1C) or PS-LFY-3 (dye LF yellow) could be excluded. These created low signals that never exceeded the reference value by more than a factor of 3. Also the large particles PS-AM-8 (dye LF red) gave weak FL signals despite their size of approx. 200 nm. Presumably the dye LFR yielded no strong signals in the available detection channel, as was indicated already by cell experiments with other LFR marked particles (data not shown). The large PS-AM-5 particles (dye PMI) in contrary were well visible in both FL1 and SSC channel and found perfectly suitable for SPM. Here the problem was that, due to the obvious bimodal distribution, the precise particle concentration in the volume should be difficult to calculate. Based on these observations it was also decided that the dye MS1B should be introduced into a new particles at a higher concentration to obtain highly fluorescent particles. As described in chapter 4.1.3, this repeated synthesis with MS1B indeed yielded spheres with a strong fluorescence emission (PS-Lut-1).

4.3.3 Particle Fluorescence Measurement

Sufficient dilution, low measurement speed and a low noise level are required for high precision measurements. The latter should be achieved by integrating a 15 nm pore size filter (filter_{15nm}) into the sheath liquid circulation. However this ultra-fine filter frequently disturbed the sample flow at low speed. This hampered the efforts for quantitative measurements which require a stable sample flow throughout 5-10 min time. Hence these sensitive ‘settings #1’ were only used to measure the mean fluorescence intensity of single particles MFI_{NP} in a non-quantitative approach.

With ‘settings #1’ the nanoparticles PMMA-BP1-2 were measured. The noise was low enough to allow precise fluorescence measurements (see *Figure 69*).

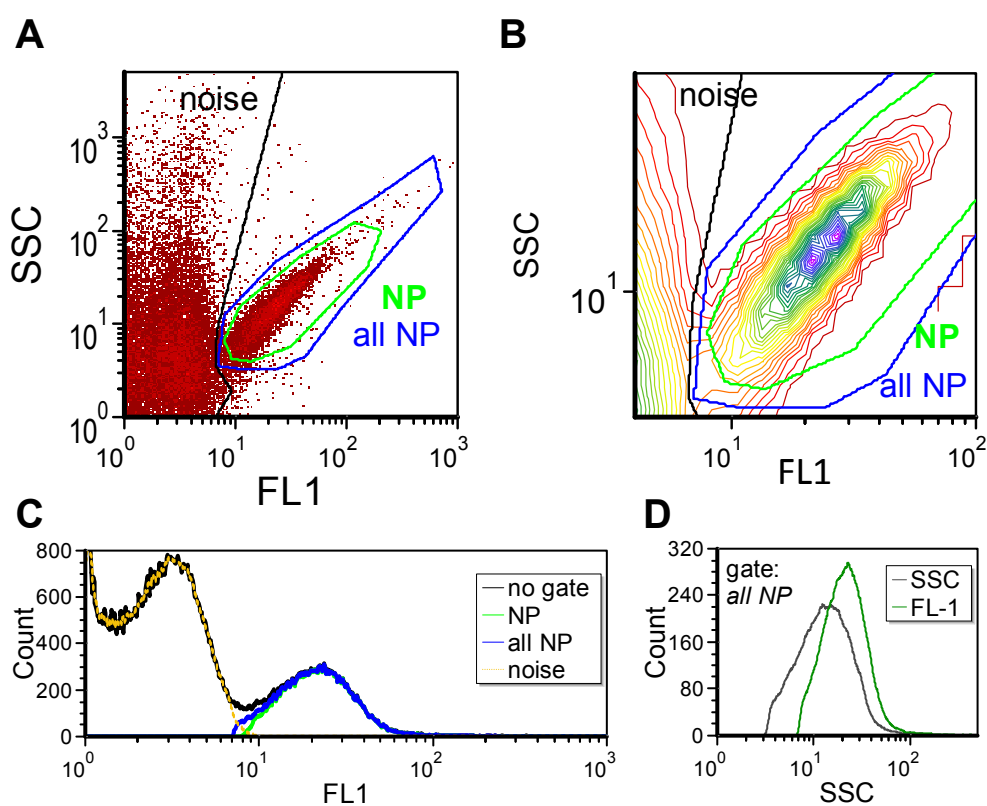


Figure 69. High precision measurement (‘settings #1’) of PMMA-BP1-2 particles, depicted in SSC-FL1 density (A) and contour (B) plots. Gate ‘noise’ (black) marks the background signal and gate ‘all NP’ (blue) marks the vast majority of detected nanoparticles. A fraction of nanoparticles which is fully separated from the background are indicated by gate ‘NP’ (green). This gate ‘NP’ was intended for measurements with a higher background level, e.g. when the NPs are counted using ‘settings #2’.

Based on the data set in gate ‘all NP’ the fluorescence MFI_{NP-raw} could be read out as the median value in channel FL1. Events with a fluorescence signal below the particle signal intensity were gated in the SSC-FL1 dot plot and defined as noise. Particle fluorescence was found to be nearly one magnitude higher than the noise signal intensity, which diminished the

risk of introducing errors due to bad signal-to-noise ratio. Subtraction of the noise resulted in a final PMMA-BP1-2 particle fluorescence MFI_{NP} of 19 [a. u.] (reproducible in >3 independent experiments). As the cytometer needed to be re-adjusted from time to time, the absolute values of NP fluorescence slightly varied. In later measurements, the MFI_{NP} of PMMA-BP1-2 was increased to 22 [a. u.] (data not shown). These values were reproducible. When a quantitative uptake cell experiment was done, the single particle fluorescence was measured each time to confirm the MFI_{NP} .

In a similar manner the particles PS-SDS-7 and PS-Lut-1 NPs were measured, see *Figure 70* and *Figure 71*.

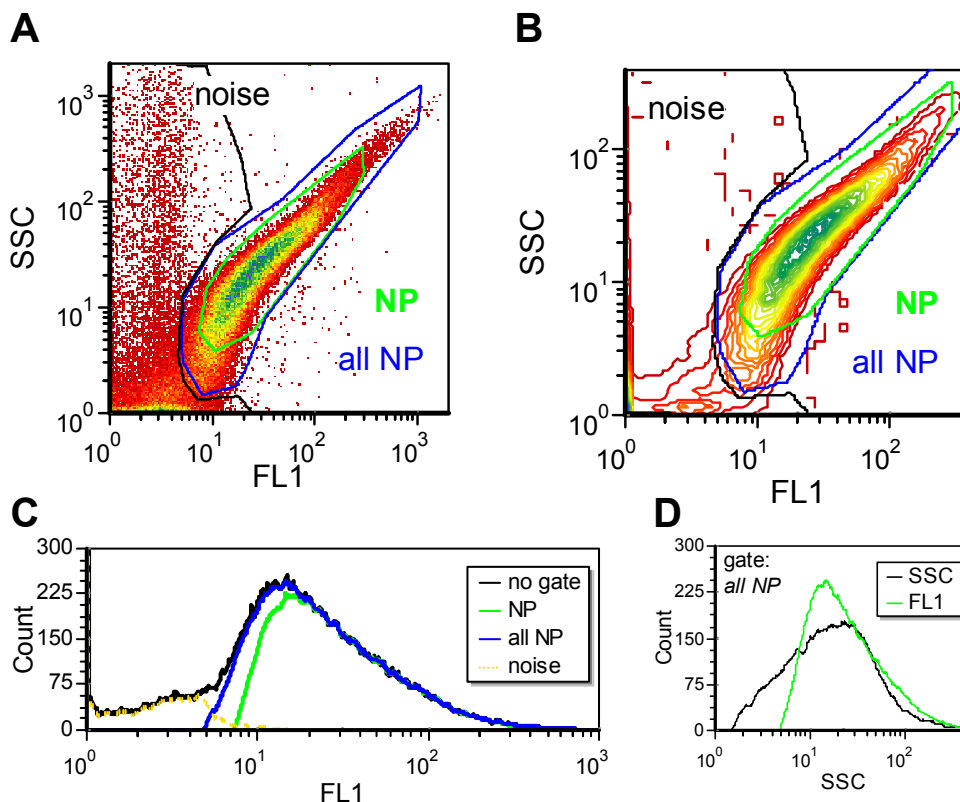


Figure 70. High precision measurement ('settings #1') of $1:40 \cdot 10^6$ diluted PS-SDS-7 particles, depicted in SSC-FL1 density (A) and contour (B) plots. Gate 'noise' (black) marks the background signal and gate 'all NP' (blue) marks the vast majority of detected nanoparticles. A fraction of nanoparticles which is fully separated from the background are indicated by gate 'NP' (green). This gate 'NP' was intended for measurements with a higher background level e.g. when NPs are counted using 'settings #2'.

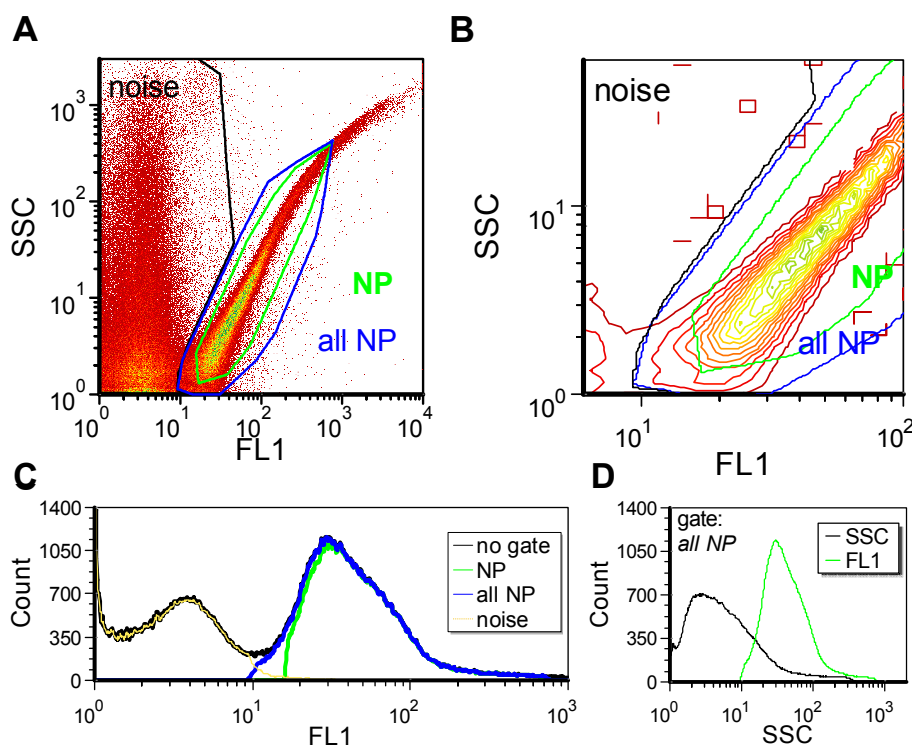


Figure 71. High precision measurement ('settings #1') of 1:50-10⁶ diluted PS-Lut-1 NPs, depicted in SSC-FL1 density (A) and contour (B) plots. Gate 'noise' (black) marks the background signal and gate 'all NP' (blue) marks the vast majority of detected particles. A fraction of these which is fully separated from the background is indicated by gate 'NP' (green). This gate 'NP' was intended for measurements with a higher background level, e.g. when the NPs are counted with 'settings #2'.

The second gate 'NP' was deliberately set to mark only particle events that were well separated from the background. The percentage of NP events in gate 'NP' (when gate 'all NP' is defined as 100%) was calculated. The obtained calculation factor provided the option to count particles in less clean samples with a high background level. The particle count could be obtained in gate 'NP' (which is less sensitive to high background levels), then multiplied with the factor to extrapolate the number of particles that should be inside gate 'all NP'.

The calculation factors (linking gate 'NP' and 'all NPs') and the measured fluorescence intensities of the particles are summarized in *Table 15*.

Table 15. Results of the precise measurement ('settings #1') of the 3 model particles.

Particle	Calculation factor X_{gate} $N_{\text{NP}} \cdot X_{\text{gate}} = N_{\text{all NPs}}$	FL1 mean fluorescence intensity [a. u.]			
		MFI _{NP-raw}	MFI _{noise}	MFI _{NP} (final)	St.dev.
PMMA-BP1-2	1.112	21	2	19	±5%
PS-SDS-7	1.189	20	2	18	±5%
PS-Lut-1	1.114	38	2	36	±5%

The final MFI_{NP} of the two 150 nm sized particle samples was nearly similar *i.e.* 18 and 19 [a. u.], whereas that of the 180 nm sized spheres was doubled *i.e.* 36 [a. u.]. Repeated measurements lead to the conclusion that an MFI standard deviation of approx. $\pm 5\%$ should be considered for the SPM. The fluorescence of all NPs was at least 10-fold the background signal intensity. The SSC-FL1 plots demonstrated that this signal-to-noise ratio was the required minimum for a rough separation of NP and noise signals (*Figure 69, Figure 70 & Figure 71*). A 20:1 signal-to-noise ratio, like with PS-Lut-1 NPs, is ideal.

As mentioned earlier a more suitable band pass filter for the FL1 channel was available. This changed the detection range of FL1 from 527 ± 10 nm to 536 ± 20 nm – thus to a slightly longer wavelength and a larger window. This should both reduce the input of scattered laser light (false positive signals, background) and increase the signal input of BP1 fluorescence. This was particularly important with regard to the precise detection of PMMA-BP1-2 particles in cells. The new band pass filter significantly increased the signal-to-noise ratio, see *Figure 72*.

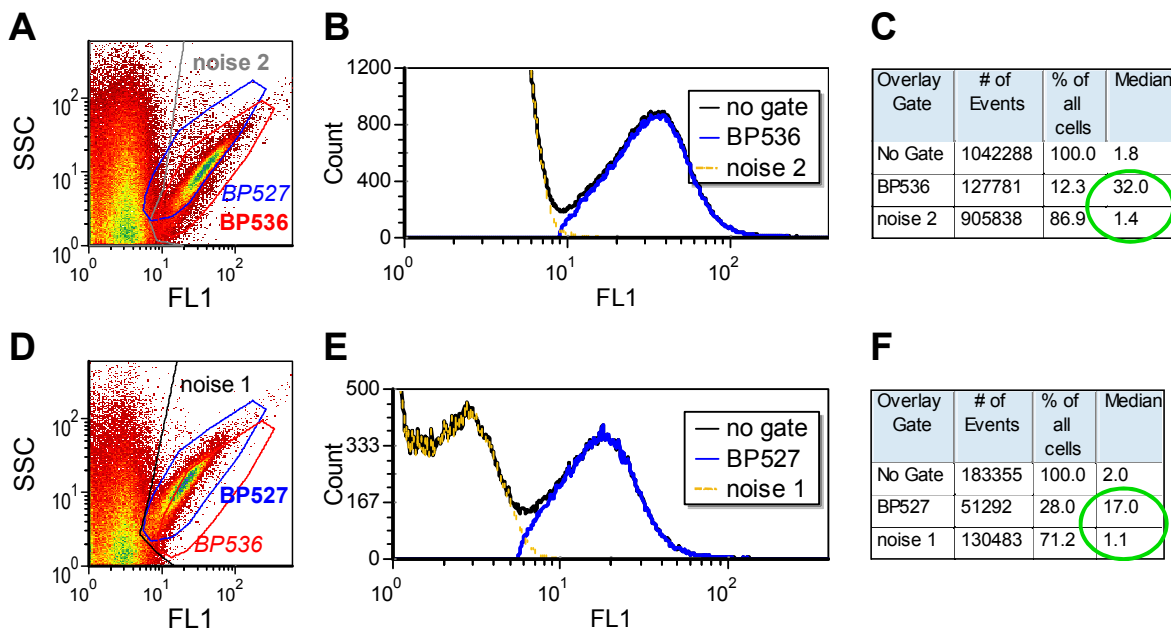


Figure 72. Measurement of $1:60 \cdot 10^6$ diluted PMMA-BP1-2 particles with different FL1 band pass filters. Filter $BP536\pm 20$ was used to obtain the data in A-C and filter $BP527\pm 10$ was used in D-F. The respective SSC-FL1 plots (A & D) and FL1 histograms (B & E) demonstrate how the NP population shifted to higher FL1 values. Regions mark background (noise 2, grey) and NPs (BP536, red) in the data of the $BP536\pm 20$ filter (A-C). In a similar manner gate 'noise 1' (black) and BP527 (blue) were drawn in the other data set (D-F). The gates were projected into the FL1 histograms and the FL1 median of the noise and the particle population was evaluated (C & F, green circle).

The fluorescence signal of single PMMA-BP1-2 particles rose from previously MFI_{NP-raw} 17 to 32 [a. u.]. Changing the band pass filter of FL1 increased the signal of BODIPY-1 marked particles by a factor of ≈ 2 , whereas the background only slightly increased. In the SSC-FL1 plots (Figure 72) the particle events were separated more clearly from the background.

4.3.4 Volumetric Counting of Particles

For the full benefit of SPM in flow cytometry it would also be advantageous if the FC could be utilized to directly count the number of NPs per volume. This cannot be measured directly with other methods and is usually calculated at the base of particle size and solid weight content. Flow cytometry, however, could not only provide a double check on the calculated concentration but would even assign a certain value of sideward scattering ('size') and dye content ('fluorescence intensity') to each particle. It would also enable one to count objects in dispersions that are of low concentration or contain other ingredients (e.g. cell medium supplied with serum). FCy would offer the possibility to count objects in dispersion under experimental conditions that hinder most other analytical methods. In addition, the number ratio of the two populations of a sample with bimodal size distribution could be obtained. This would provide valid information, in particular if coupled with information about the dye content (fluorescence) of the NP populations.

4.3.4.1 Counting >200 nm Spheres

The first approach to volumetric particle measurement was done with large spheres of high fluorescence intensity (PS-AM-5), as those could easily be distinguished from the background. But due to the bimodal size distribution of the sample, the particle concentration per volume could not be calculated precisely so that no reference value N_{calc} was available. Filtered water, which was the dilution medium of all samples, was measured as reference (Figure 73). The measurements were run at velocity of $0.5 \mu\text{l}\cdot\text{s}^{-1}$ with the laser set to 200 mW. To ensure a low background and a steady flow rate the $0.2 \mu\text{m}$ pore size inline filter was used.

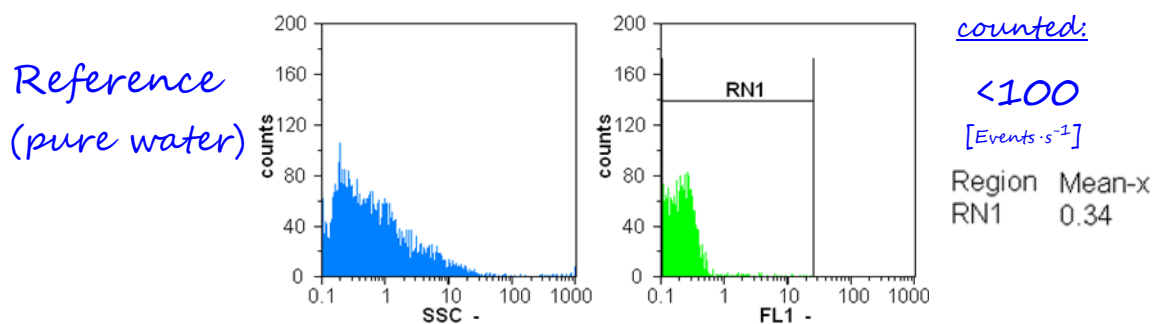


Figure 73. FC measurement of the reference sample filtered water.

In the reference sample the count rate was low and the median of FL1 was below 0.5 [a. u.]. As the settings were very sensitive, the low count rate also demonstrated that the machine was very clean. Under similar conditions PS-AM-5 samples were measured at different concentrations *i.e.* the 20%-wt. latex was diluted 1:20 and 1:50 · 10⁶. The low concentration prevented coincidences and ensured the SPM (*Figure 74*). The double peak in the SSC histogram (gates RN2 & RN3) represented the NPs. This confirmed the observations in TEM and DLS that had indicated a bimodal distribution.

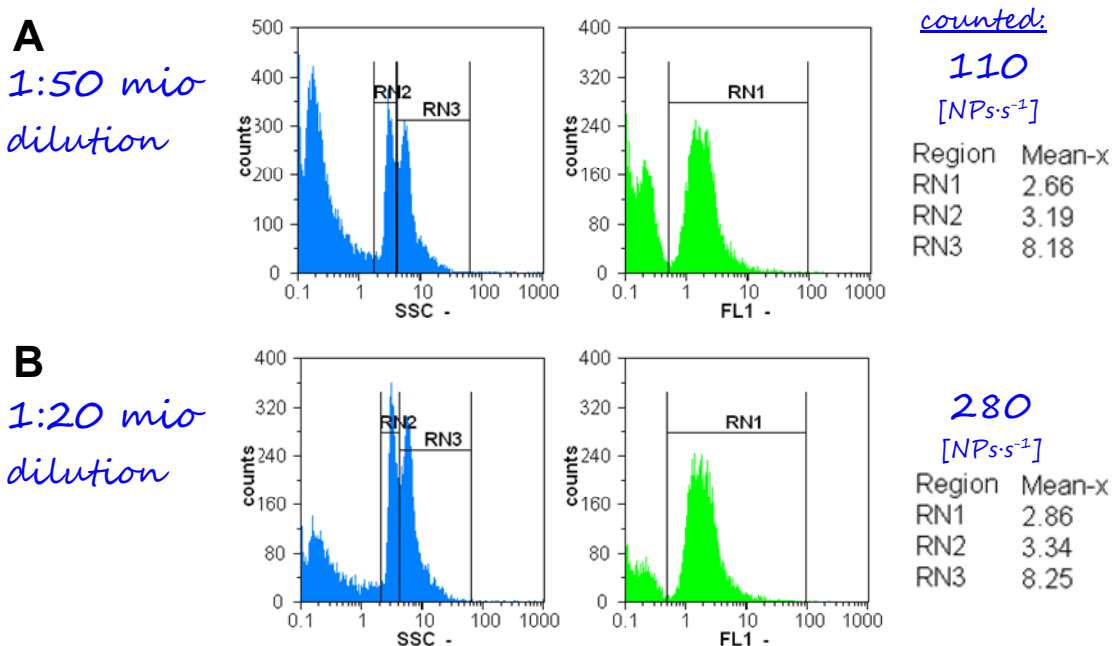


Figure 74. FC measurement of PS-AM-5 particles at a dilution of 1:50·10⁶ (A) and 1:20·10⁶ (B). The count rates provided to the right are referring to a measurement speed of $v_{exp} = 0.5 \mu\text{l}\cdot\text{s}^{-1}$.

When the concentration was increased by 2.5 (from 1:50·10⁶ to 1:20·10⁶ dilution), the particle count likewise increased by 2.5 (from 110 to 280 NPs·s⁻¹). The double peaks were still visible and the signal intensities had not changed, which proved that at both dilutions single NPs were measured. This experiment demonstrated the precision of particle counting and in the next step it should be applied on smaller particles.

4.3.4.2 Counting 100-200 nm Spheres

In order to improve the counting method, the built in *true volumetric counting* (TVC) feature of the CyFlow ML should be used. The counting was done with the most promising particles PMMA-BP1-2 (160 nm), PS-SDS-7 (150 nm) and PS-Lut-1 (180 nm). To test the limit of the cytometer the counting was also attempted with the small 70 nm sized CH235-3 particles. For these samples a precise calculation of the theoretical NP concentration (N_{calc}) was available. Both approaches to volumetric counting were compared: *Over-time* (count_{time}) and *true volumetric counting* (count_{vol}) where the built in feature of the CyFlow ML analyses precisely

200 μl sample volume and automatically calculates the concentration. The results of several independent measurements, run at $v_{exp} = 0.5\text{-}1$ [$\mu\text{l}\cdot\text{s}^{-1}$] with a laser power of 200 mW, are summarized in *Table 16*. A more detailed list with the results of the single measurements is listed in the appendix (see *Table A*).

Table 16. Volumetric counting of the NPs PMMA-BP1-2, PS-SDS-7 and PS-Lut-1. The experimental data $count_{vol}$ and $count_{time}$ is compared with the value that was calculated via the size distribution (N_{calc}).

Sample	$count_{vol}$			$count_{time}$		
	FC results, based on true volumetric counting			FC results, based on v_{exp} and duration		
	[%] of N_{calc}	St.dev.	Nr. of runs	[%] of N_{calc}	St.dev.	Nr. of runs
PMMA-BP1-2	58	± 25	6	74	± 21	8
PS-Lut-1	/	/	/	58	± 20	7
PS-SDS-7	61	± 6	2	69	± 17	5
total of all NP measurements	59	± 21	8	67	± 20	25

The particle concentrations retrieved by calculating the flow speed and measurement duration were too low. The total average of $count_{time}$ was 67 [% of N_{calc}] with a standard deviation of ± 20 (*Table 16*). Calculating the NP concentration with the *true volumetric count* mode was not more precise, with an average $count_{vol}$ of 59 [% of N_{calc}] and a standard deviation of ± 21 . Summed up, counting the particle concentration by flow cytometry yielded values that were 33-40% below the expected value. As this value N_{calc} was based on the sample solid content and on the size distribution, this theoretical calculation might have introduced an error. So did most likely the dilution steps that were needed to dilute a 20%-wt. ($200 \mu\text{g}\cdot\mu\text{l}^{-1}$) latex to the required concentration in the range of $4\cdot 10^6 \mu\text{g}\cdot\mu\text{l}^{-1}$ ($1:50\cdot 10^6$ dilution). Nevertheless the measured values should have been higher and no explanation was found. A systemic error is suspected – as the in total 33 runs of 3 different NP species yielded values below N_{calc} .

4.3.4.3 Counting of 70 nm Sized Spheres

In order to probe the possibilities of this method, the particle measurement protocol should also be applied on the particles CH235-3, which are only 70 nm in diameter. As a double check (if particles or coincidences are detected), these measurements were set up in a way that volumetric counting was also included. For these measurements a 15 nm in-line filter was used to reduce the background to a minimum. The CH235-3 particles could be detected, as demonstrated in *Figure 75* where two concentrations ($1:50\cdot 10^6$ and $1:100\cdot 10^6$ dilution) were compared.

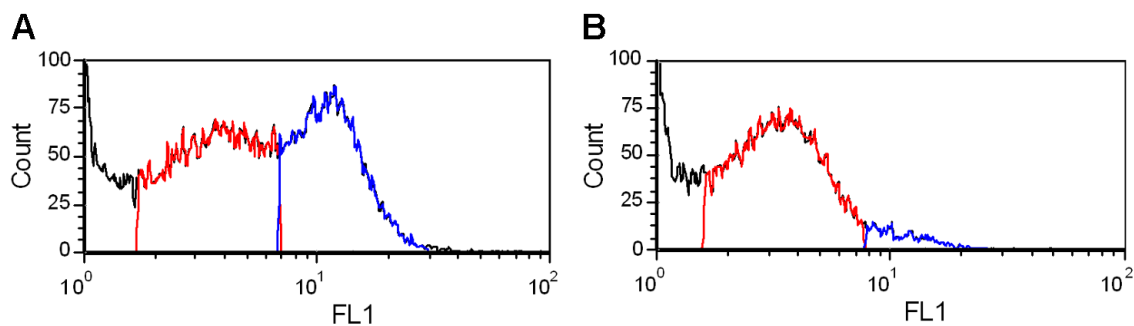


Figure 75. Measurement and counting of CH235-3 particles diluted $1:50 \cdot 10^6$ (A) and $1:100 \cdot 10^6$ (B). The standard settings for NP detection were applied and the ultrafine inline filter with 15 nm pore size was used. Events with lower (gate 'noise', red) and higher ('NPs', blue) FL1 signal intensity were gated.

A population of fluorescent events could be differentiated from the background in the $1:50 \cdot 10^6$ diluted sample (see Figure 75A, blue graph). These events represented either NPs or possibly smaller coincidences and were gated in region 'NPs'. The calculated count N_{calc} [NPs per $0.5 \mu\text{l}$ and 1 s] was $11 \cdot 10^3$ in the $1:50 \cdot 10^6$ dilution and $5.6 \cdot 10^3$ in the $1:100 \cdot 10^6$ dilution. In both samples less than $300 \text{ NPs} \cdot \mu\text{l}^{-1}$ were counted. It was assumed that the filter had hampered the flow rate and consequently the particle counting, even though instabilities of the sample flow could not impair the measurement to such an extent. Furthermore, when the calculations were based on the *true volumetric count* mode which is less susceptible to varying flow rates the results were similar (data not shown).

By raising the SSC amplification from 251 (standard) to 420, the detection of these small particles was improved. At the same time the 15 nm pore size filter was switched for a larger model with 1 m^2 surface area, to avoid flow disturbances. It was concluded that in the previous experiment the settings (which were sufficient to detect 150 nm sized NPs) were not suitable for 70 nm sized NPs. Presumably many 70 nm NPs, and also small coincidences, were lost because their SSC signals were below the minimum threshold (that was set on the SSC).

A $1:100 \cdot 10^6$ diluted sample of CH235-3 ($N_{calc} = 5600 \text{ NPs} \cdot \mu\text{l}^{-1}$) was therefore measured at two different SSC amplification settings, SSC251 and SSC450 (see Figure 76). All other experimental conditions, including the lower threshold that was set on the SSC, were similar.

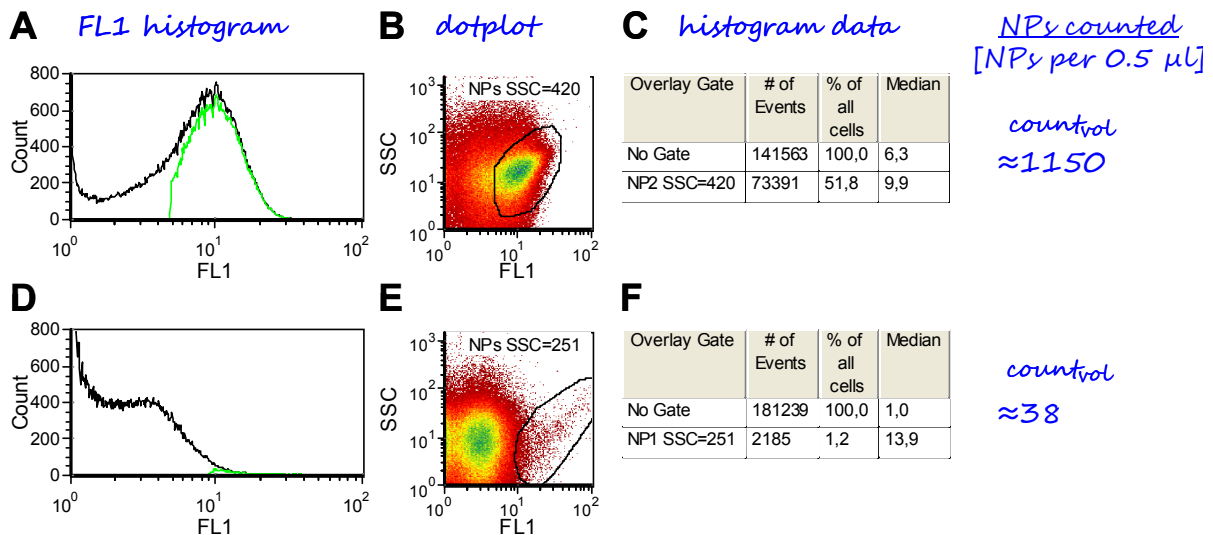


Figure 76. Measurement of the $1:100 \cdot 10^6$ diluted CH235-3 particle sample at a SSC amplification of 420 V (top) and 251 V (bottom), with 251 V being the standard setting for particle measurements. The FL1 histogram (A) and the SSC-FL1 dotplot (B) of the high SSC sample demonstrated that a large number of strongly fluorescent events was detected at SSC420. Those events were gated in region 'NPs SSC=420' (black gate in B, green curve in A). In contrary with low SSC amplification, the according histogram (D) and dotplot (E) showed that the vast majority of detected events was of low fluorescence intensity. Only few events of high fluorescence were detected and could be gated as a separate region 'NPs SSC=251' (black gate in E, green curve in D). The FL1 histogram data and the NP count $count_{vol}$ were also given (C & F).

The histogram data of the high SSC (Figure 76C) and low SSC (Figure 76F) reveal that at SSC251, mostly events of low FL1 intensity were detected and only few of high FL1 intensity. The latter are likely large coincidences. In contrary at SSC420, mostly events of medium fluorescence intensity were observed and the two populations of different FL1 intensity cannot be separated. Already early measurements had demonstrated the effect of the threshold and amplification settings on the data set. Most likely, in the previous experiment with SSC251 the relatively low SSC amplification of 251 sorted out all weaker signals from CH235-3 particles (single NPs and smaller coincidences). As shown in Figure 76D-F, the result is a small (1% of total) and well separated population of highly fluorescent events – the largest of the particle coincidences. In contrary (A)-(C) show a sample with many (50% of total) medium fluorescent events, as marked by the black region. It was concluded that the previously used amplification was sufficient for the other particles, but for the smaller NPs the SSC should be raised to at least 420.

Furthermore a feature of the FCSxpress software to subtract whole data sets might be used to subtract the data of an empty sample (water) from the data set of a particle sample (NPs dispersed in water). Applying this feature on measurements of the 150 nm sized particles in previous tests had proven the relative reliability of this calculation (data not shown).

Measurement of the 70 nm particles was repeated again under the best possible experimental conditions (see *Figure 77*): The more suitable FL1 band pass filter (BP536±20) was used, the large 15 nm pore size filter was placed with an additional 0.2 µm filters before and the SSC amplification was set to 420.

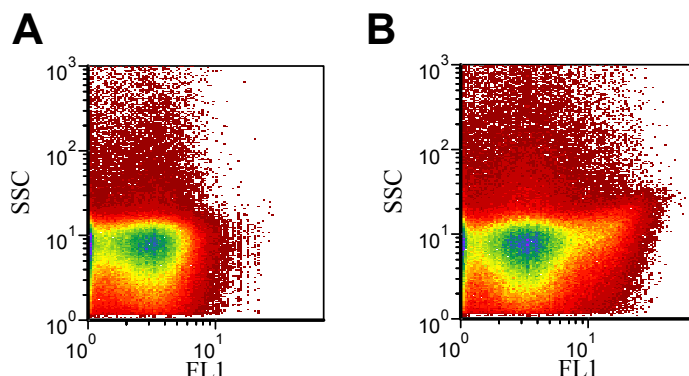


Figure 77. The measurement of CH235-3 (B) particles diluted $1:50 \cdot 10^6$ under ideal conditions is compared with the reference sample water (A).

Also at the high sample concentration of the $1:50 \cdot 10^6$ dilution ($11 \cdot 10^3$ NPs per $0.5 \mu\text{l}$) the particle coincidences were not fully separated from the background (compare *Figure 77A & B*). Judged by the theoretical particle count, the detected fluorescent events were coincidences that summed up 4-6 nanoparticles. The histogram subtraction tool of the FCSxpress software was utilized to calculate the particle and the reference sample in the FL1 channel. A well separated peak of events was retrieved, see *Figure 78*.

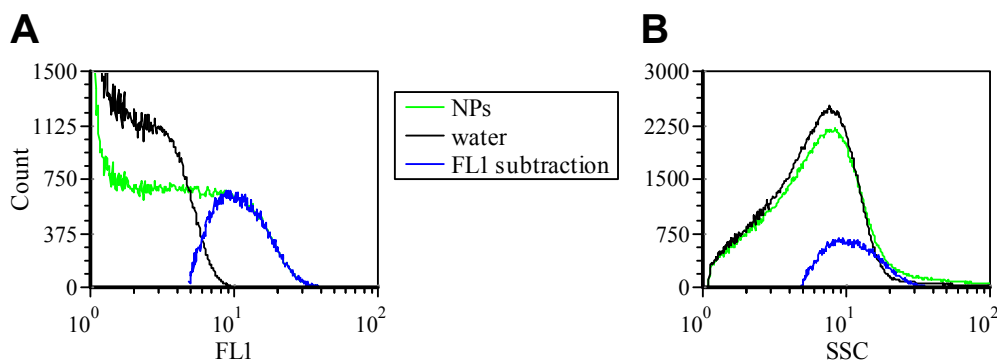


Figure 78. Histogram subtraction in channel FL1 of a sample with CH235-3 particles and a reference sample of pure water. The histogram of FL1 (A) and SSC (B) compare the data of water (black), of the original CH235-3 (green) and of the new (blue) particle data set, from which the control (water sample) was subtracted.

The last measurement showed that sample CH235-3 was not fully suitable for SPM if the background noise could not be reduced. For unknown reason the 15 nm filter with 1 m^2 surface produced a high background. The particle-derived signals in channel FL1 partially overlapped with the background even though still coincidences were measured (the latter have

higher signal intensity than single particles). In the SSC channel no differentiation was possible, as expected (*Figure 78B*). Single CH235-3 particles should have approx. 1/3-1/6 of the current coincidence FL1 signal intensity. But the subtraction method itself seemed reliable as precisely those events with the highest fluorescence were separated by the calculation (see *Figure 78A blue peak*). Presumably this would not be precise enough for absolute quantitation. But this FL1 value obtained by subtraction would be a good approximation of the particle fluorescence.

4.3.4.4 Particle Counting in the Presence of Serum

The previously described counting of particles was done in water, which is a clean dilution medium. However, this method could be further improved if transferred into a much less clean dilution medium *i.e.* into serum supplied cell medium. The volumetric NP counting in incubation medium would offer a variety of possibilities: Most importantly it could a) demonstrate the dispersion's stability in the presence physiological buffer & serum proteins, and b) provide the tool to count NPs in the supernatant before and after incubation with cells (thus yielding the NP internalization efficiency). It would also give rise to other experimental setups like *e.g.* quenching assays of nanoparticles where the fluorescent marker is located at the particle surface).

Therefore the volumetric counting of PMMA-BP1-2, PS-Lut-1 & PS-SDS-7 particles was done after incubation in serum supplied cell medium (DMEM10%). The formation of coagulates should be observed by flow cytometry, as an additional test for the dispersions' stability. After at least 30 min incubation with proteins ($2.5 \mu\text{g}\cdot\text{ml}^{-1}$ of polymer), the particle dispersions were further diluted to a final dilution of $1:133\cdot 10^6$. As a comparison the samples were also diluted $1:133\cdot 10^6$ in water and measured, this data is contained in *Table 16*.

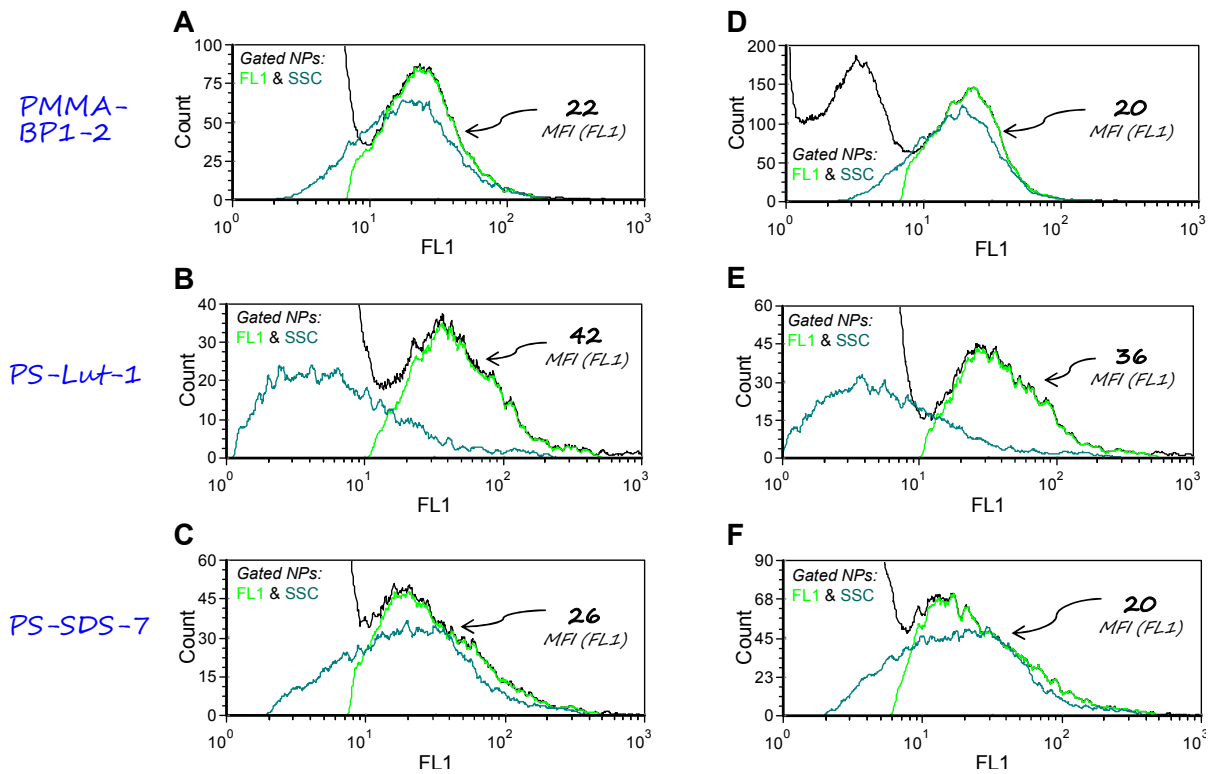


Figure 79. Measurement of $1:133 \cdot 10^6$ diluted samples of PMMA-BP1-2 (A, D), PS-Lut-1 (B, E) and PS-SDS-7 (C, F) in filtered water (left) and after incubation with serum proteins (right). The particle population was gated in the SSC-FL1 dotplots (not shown) and projected into the histograms as green (FL1) and teal (SSC). The black graph in the histograms displays the un-gated data set in FL1.

The FC data after incubation in protein-supplied medium, and after normal dilution in pure water, were compared. It could be demonstrated that counting the particles was still possible even if serum had been added to the respective samples see *Figure 79*.

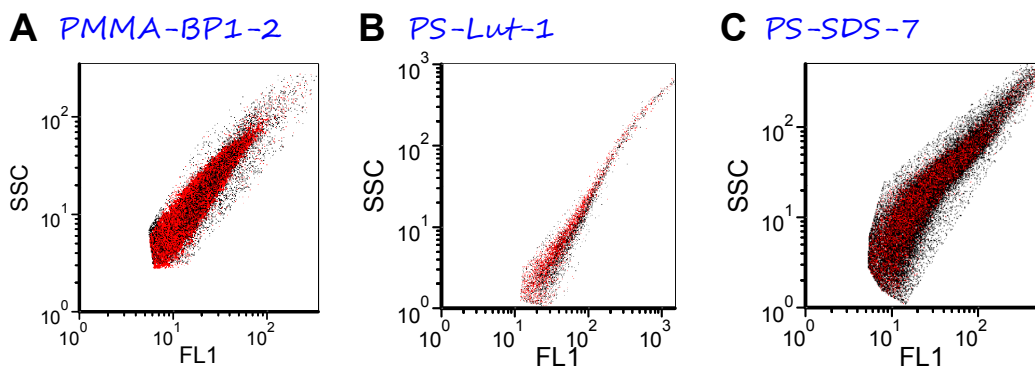


Figure 80. Measurement of $1:133 \cdot 10^6$ diluted samples of PMMA-BP1-2 (A), PS-Lut-1 (B) and PS-SDS-7 (C) displayed as color dotplots. The samples were either diluted in pure water (black) or incubated with serum proteins prior to the FC measurement (red). The co-localization plots reveal a slight shift of the red dots to the left, corresponding to a minor decrease in fluorescence intensity.

Comparing the FL1 histograms and SSC-FL1 dotplots of the protein-free references with the protein-supplied samples (see *Figure 79*) showed that no coagulation appeared. The particles were diluted in PBS buffer solution after they had been incubated in DMEM with 10% FCS. Visual testing and DLS measurements had demonstrated that some of the SDS-stabilized NPs, e.g. PMMA-BP1-2, became unstable when dispersed in PBS (unpublished data). This was because the ionic stabilization of the dispersion, which is particularly vulnerable towards bivalent cations, was disturbed by the buffer solution. Serum components like proteins stabilized the particles by coating them, so that they remained stable when transferred into PBS thereafter.

An interesting observation was the 10% decrease of the FL1 fluorescence intensity. The populations shifted in the SSC-FL1 dotplot (see *Figure 80*), but these minor shifts hardly required a readjustment of the gates. Therefore the particle count should not be effected at all. But apparently the serum components caused a partial loss of the particle fluorescence signals. Either the coat on the NPs or the presence of the serum components in the sample (approx. 10^{-3} %-vol.) affected the FL1 signal strength. Even though proteins are known for absorption in the UV wavelength range due to aromatic amino acids¹⁶⁸, an absorption at 488 nm (that would reduce the incoming laser power) or above 526 nm (which would reduce the detected emission of the dye in channel FL1) has not been reported.

SUMMARY The volumetric counting of large spheres in the range of >200 nm diameter yielded approx. 50% of the expected N_{calc} . This might be based on the fact that the N_{calc} was not correct, because the effective particle concentration could not be calculated in the bimodal sample. Apart from this, the counting seemed to be successful because a clear correlation between the sample dilution and the decreased particle count was observed. The count rate had increased by 2.5 when the concentration was increased by the same factor.

After this first proof of particle counting the method should be applied on three particles of interest: PMMA-BP1-2, PS-SDS-7 and PS-Lut-1. Also, the concentration of these samples could be calculated with increased precision so that a reliable N_{calc} was available. In addition two methods *over-time* ($count_{time}$) and *true volumetric counting* ($count_{vol}$), where the cytometer analyses a fixed sample volume of 200 μ l and automatically calculates the concentration, were compared. Both methods yielded a particle count that was significantly below the expected value of N_{calc} . It was also an interesting finding that the $count_{time}$ method yielded 67% of N_{calc} and therefore was closer to the expected value than the inbuilt $count_{vol}$ feature with 59%. The average standard deviation of both methods was 20-25%.

Finally the smallest available particles CH235-3, with a diameter of 70 nm, should be counted. As these particles were small and close to the detection limit, the count feature should also provide a backup if any detected fluorescent objects are single NPs or still coincidences. The measurement of different dilutions first lead to the conclusion that the up to

now used threshold of SSC10 was suitable for >150 nm NPs but not for the small CH235-3 particles. Many coincidences and single particles were excluded by the SSC threshold criteria. Other analysis with a higher SSC amplification prevented this and a new measurement at ideal conditions was exercised. Diluted $1:50 \cdot 10^6$, this sample should contain approx. $11 \cdot 10^3$ NPs per 0.5 μ l and therefore the detected signals had to be coincidences summing up approximately 4-6 particles. These signals were not fully separated from the background, which gave the final proof that single CH235-3 particles could not be detected properly. With the histogram subtraction feature of the FCSxpress software, the coincidence peak could be isolated. This way the mean fluorescence intensity of 4-6 NPs together in one event and a rough number count of CH235-3 particles was achieved.

Furthermore it was demonstrated for the three particles of interest that the volumetric counting was still possible after the spheres had been incubated with cells in medium containing 10% serum. This would be a useful tool if particles of high uptake efficiency were studied – here the uptake could simply be defined by counting the NPs in the incubation medium before and after incubation with the cells. It was interesting to note that the trace of serum proteins, freely in the sample or possibly adsorbed on the particle surface, seemed to reduce the fluorescence intensity by approx. 10%. This was observed for all three particles.

4.4 Absolute Quantification of Nanoparticles in Cells

The successful measurement of single nanoparticles by flow cytometry enabled the development of a new quantization method. By comparing the fluorescence intensity of particle-loaded cells with that of empty (control) cells, the absolute number of contained NPs could be concluded. Calculating this difference in fluorescence intensity of the two cell samples with the average signal intensity of a single NP should provide the particle count. This new method should be developed and combined with quantitative cLSM experiments, where the particles were directly counted in the cells. The intention of this approach by cLSM was to back up the quantitative FC results with a more direct method – as in contrary to the flow cytometric approach. Confocal laser scanning microscopy was applied to determine ‘by hand’ the number of particles in a cell, *i.e.* without the help of specific quantifying software. For this purpose, HeLa cells were incubated with NPs under similar conditions as in the FCy experiments and analyzed in the cLSM performing z-stacks of the cells. The particles were tagged by hand and counted. The results from flow cytometry and confocal imaging were compared to prove that the new method yielded reliable results.

Pre-testing of suitable experimental conditions

A couple of quantitative FC experiments was done in 24-well plates with 1 ml incubation volume in order to find the best experimental conditions. In particular, a balance should be found between the required minimum (to ensure a certain precision of the measurement) and maximum (to enable manual particle counting in cLSM) amount of internalized nanoparticles. Furthermore the ideal particle loading should happen within a short time frame of a few hours at maximum. Else the NPs get transported to endosomal structures where they accumulate. In visual counting via cLSM it is crucial that the particles are located singled because the resolution is not sufficient to resolve particles in accumulates and in close proximity to each other. Particle concentration and incubation time must be balanced.

Therefore the particles were incubated for 1 h and 2 h with varied concentrations (75, 150 and 300 $\mu\text{g}\cdot\text{ml}^{-1}$) and incubated for 0-24 h at a higher concentration (300 $\mu\text{g}\cdot\text{ml}^{-1}$). The results are presented in *Figure 81*. The fluorescence after 24 h incubation was beyond the scale in FL1, but based on the FL2 data which yields lower signal intensities, approx. 600 NPs were internalized per cell after 24 h (data not shown).

It was decided that the incubation time should be set to 2 h to reduce intracellular NP accumulation. An uptake of 40-50 particles per cell, as was the case after 2 h incubation with 300 $\mu\text{g}\cdot\text{ml}^{-1}$ of polymer, seemed a good choice for further quantitative experiments. Considering that the added 300 μg of polymer correspond to $2.4\cdot 10^6$ particles per cell, the uptake of approx. 40 NPs per cell after 2 h is a very low efficiency ($2\cdot 10^{-3}\%$). After 24 h

incubation the efficiency is improved and approx. 600 particles *i.e.* $25 \cdot 10^{-3}\%$ of the added amount are internalized.

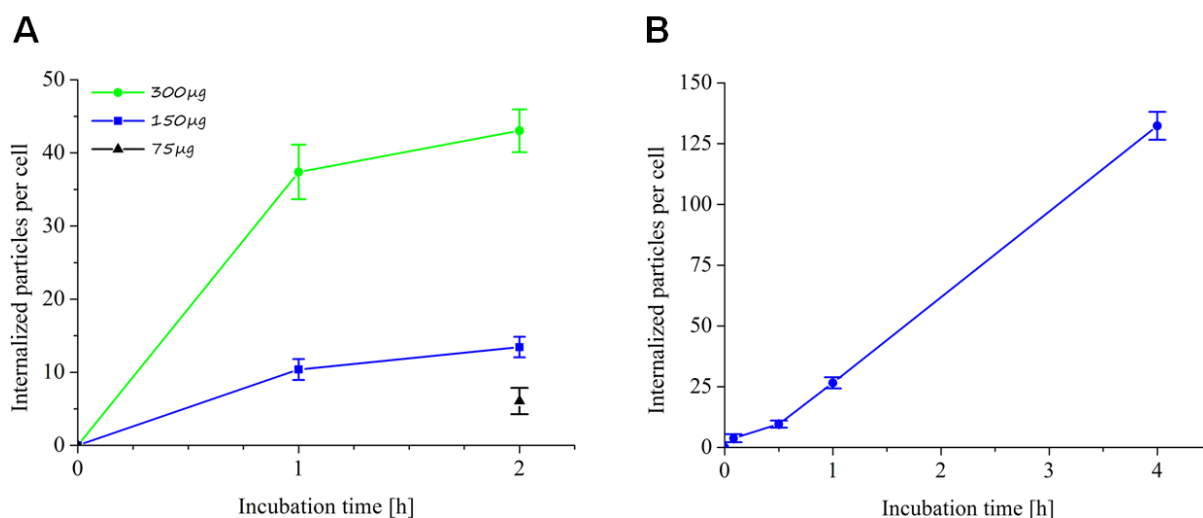


Figure 81. Incubation of cells with PMMA-BP1-2 NPs in 1 ml volume, for up to 2 h (A) at a concentration of 75 μg (triangle), 150 (square) and 300 (circle) $\mu\text{g}\cdot\text{ml}^{-1}$. Additionally the incubation with 300 $\mu\text{g}\cdot\text{ml}^{-1}$ of polymer for up to 4 h (B) is shown.

The uptake of PMMA-BP1-2 particles after 2 h incubation at 300 $\mu\text{g}\cdot\text{ml}^{-1}$ was reproduced again. Another particle eligible for SPM (PS-SDS-7, 150 nm, dye Ya795) was incubated under similar conditions. The results of the quantitative measurements of the two particles are given in Figure 82. These results were compared with the findings of the competitive uptake study that was done with similar particles (see chapter 4.2.1).

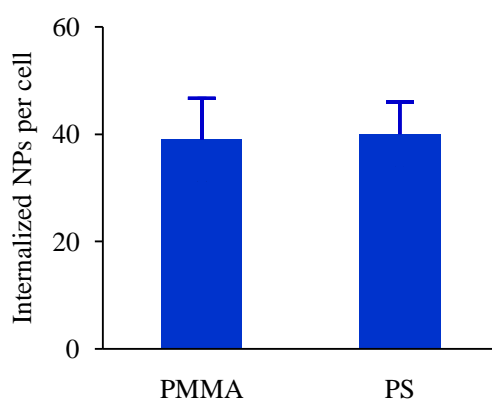


Figure 82. Incubation of cells for 2 h with 1 ml medium containing 300 $\mu\text{g}\cdot\text{ml}^{-1}$ of polymer. The data for PMMA-BP1-2 (PMMA) and PS-SDS-7 (PS) particles were retrieved in 3 and 2 independent experiments, respectively.

For PMMA-BP1-2 and PS-SDS-7 particles the experiments yielded an average uptake of 40 NPs per cell after incubation under similar conditions. This observation complied with the findings of the competitive study (see chapter 4.2.1) where the uptake rate of PS and PMMA NPs was also compared. Even though these measurements were of a semi-quantitative nature,

the observation (that PS and PMMA particles are internalized with roughly similar uptake) concurred with the absolute quantification data. This indicates that the absolute quantization method worked correctly.

All experiments presented in the following were done with the model particle PMMA-BP1-2.

Counting PMMA-BP1-2 particles in the cLSM

As discussed before, confocal laser scanning microscopy was applied to determine ‘by hand’ the number of NPs in a cell *i.e.* without the application of automated quantification software. HeLa cells were incubated with particles under similar conditions as in the FC experiments and analyzed in the cLSM. Z-stacks with narrow step size were obtained to manually count the particles inside one cell. The intention of this approach was to back up the FC results with a method that is direct – in contrary to the flow cytometric approach where the NP count was a result of two measurements and a calculation. Z-stacks of whole cells were run in the cLSM with a narrow step size. Several subsequent layers of one z-stack were projected into one plane termed smart object (SO) and in each of the SO a different color was chosen to tag the internalized NPs with dots. The total amount of dots corresponded to the final particle number in the cell. Particles co-localizing in x-y location (and situated above each other in z-direction) were marked as ‘dots directly next to each other’. This was in concession to the automated count feature in the utilized software Photoshop. The theoretical optical resolution of $\lambda/2$ suggested an ideal resolution of roughly 300 nm. Considering that the particles of question measure 160 nm in diameter, STED mode would be needed to depict single NPs as in theory the resolution in cLSM is insufficient to differentiate between single particles and duplets. But under the assumption that the vast majority of NPs were located separated in the cell, lacking resolution is not an issue. Other factors such as the average intensity, size and shape of the particle signal spots indicated that the fluorescent pixels indeed represented single NPs. A good assumption of the particle number was possible. Taking also into account the dimension and shape of the particle signal in the z-axis, the error could be further reduced. Particles were only incubated for 2 h with the cells to keep endosome fusion low. The high magnification images below showed that the NPs created a fluorescence signal sized roughly 300-400 nm which is the expected size with the given resolution limit (see *Figure 83*).

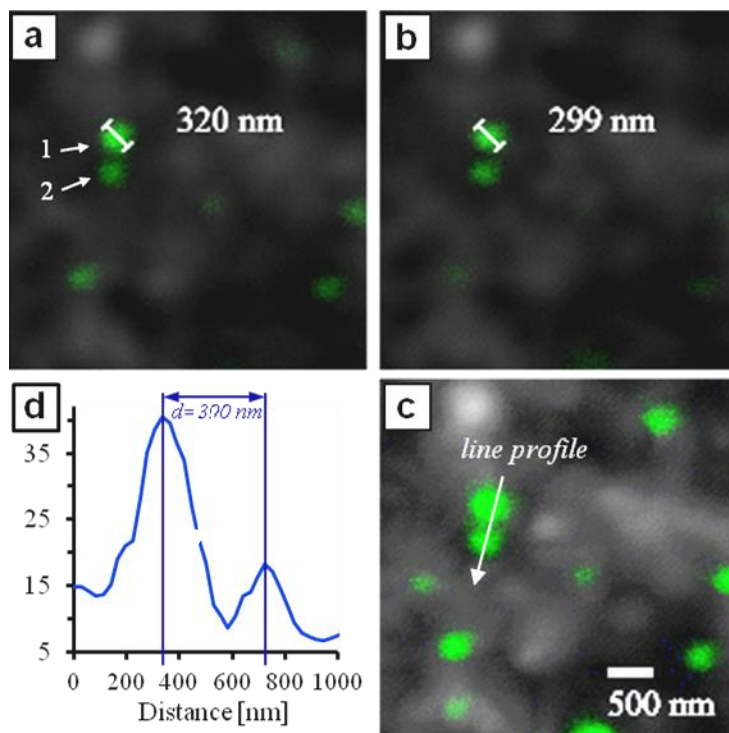


Figure 83. Shown are subsequent images (a & b) of a z-stack with step size 250 nm. Two separate NPs are indicated (1 & 2) and the upper fluorescence signal spot is sized approx. 300 nm. Several layers of the z-stack were projected into one plane (c) and a line profile in x-y-direction was drawn (d) on the particles 1 and 2. The line profile (grey value intensity in y-axis) on the neighboring NPs revealed a core-to-core distance of 390 nm.

2 separate particles were visible and the upper fluorescence signal spot was sized approx. 300 nm. It was concluded that at a particle core-to-core distance of approximately 400 nm, two particles could be separated. This suggested that even at smaller distances it should be possible to differentiate between a particle duplet and a large particle. As the particles are perfectly spherical, most accumulations should be identified by their non-spherical shape. Despite minor imprecision, the overall amount of counted NPs should therefore not differ by more than a factor of 2 from the real particle number in the cell. The main difficulty about this method was to analyze enough cells so that the results would be of statistical relevance. Without using quantification analysis software, this was impossible. Therefore the results of cLSM studies were intended as a good approximation of the intracellular particle numbers.

Quantifying PMMA-BP1-2 nanoparticles in HeLa cells via FC and cLSM

In the first quantitative cLSM experiment the cells were incubated with $500 \mu\text{g}\cdot\text{ml}^{-1}$ of PMMA-BP1-2 particles for 1 h and 2 h, then washed and fixed in the adhered state. Some particles were attached to the cell surface but the majority was intracellular (see *Figure 92*). This behavior was similar to that of the PMMA NPs in the competitive uptake studies.

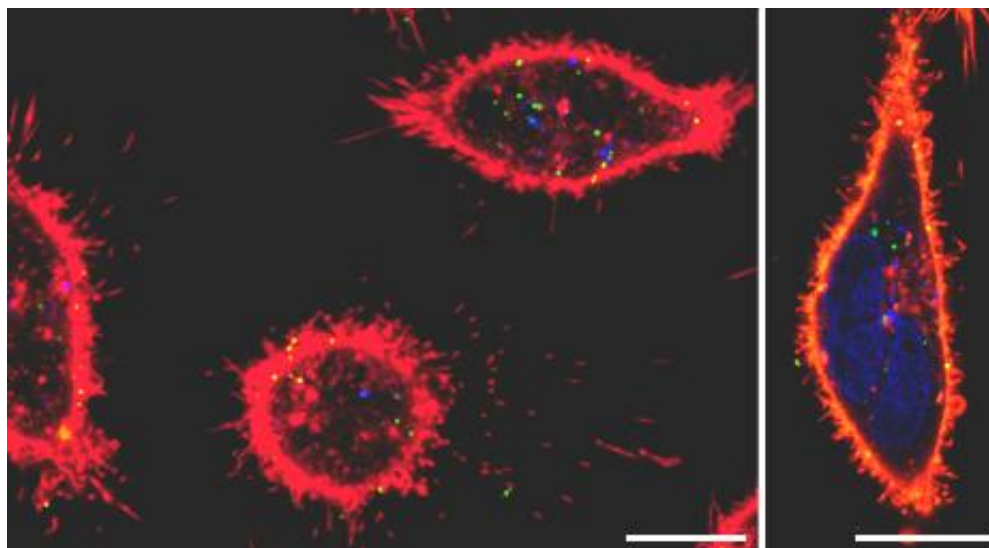


Figure 84. HeLa cells after 2 h incubation with $500 \mu\text{g}\cdot\text{ml}^{-1}$ of PMMA-BP1-2 NPs. False coloring of the membrane marker (red), the NPs (green) and the partial Hoechst staining (blue) was applied. The scale bar is $10 \mu\text{m}$.

It was observed that this technique even allowed an assignment of the particle numbers to a z-axis location in the cell. The color change of the dots from red-pink-purple-blue represented moving through the cell in z-direction. Hereby NPs near the plate bottom were marked in red and those located in the top area of the cell were marked in blue. In some cells the 3D distribution pattern of the differently colored dots even indicated the shape of the cell's spherical nucleus (see Figure 85).

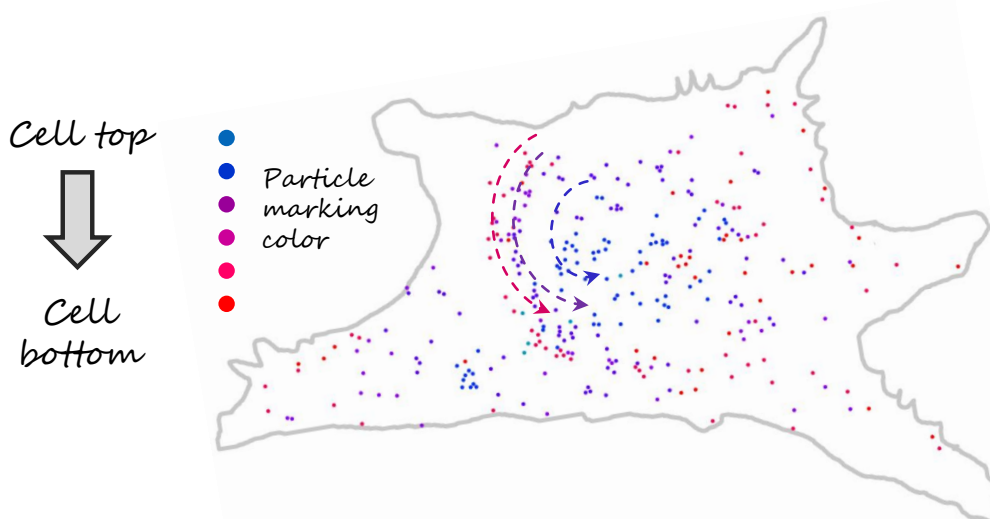


Figure 85. CLSM image analysis of a HeLa cell after incubation with $500 \mu\text{g}\cdot\text{ml}^{-1}$ of PMMA-BP1-2 particles for 2 h. In adhered HeLa cells the nucleus is not as flat as the rest of the cell. The particle distribution in the bottom SO (red), centered SO (purple) and top SO (blue) visualizes the rounded contour of the nucleus in 3D. The spherical shape of the nucleus, contoured by the differently colored dots, is indicated (curved arrows) in the respective color of the NP marking dots.

Analyzing 10 cells in this fashion yielded an approximated count of 246 ± 35 particles per cell. The images of all analyzed cells are given in the supplement section (*Table B & Figure A*). The results are summarized in *Figure 86*.

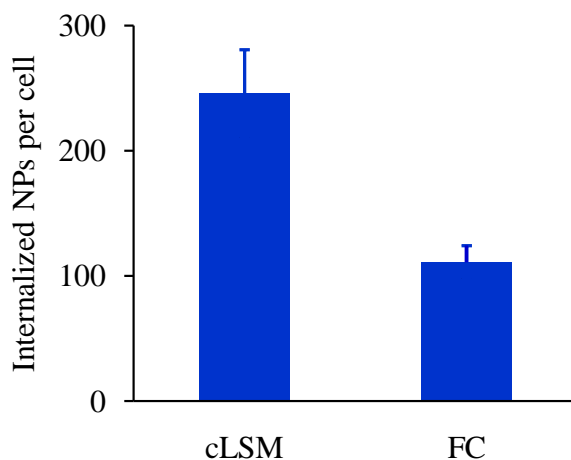


Figure 86. Counting of PMMA-BP1-2 particles in HeLa cells after 2 h incubation. The cLSM samples were incubated in 0.6 ml volume supplied with $500 \mu\text{g}\cdot\text{ml}^{-1}$ and the FC samples were kept in 1 ml containing $300 \mu\text{g}\cdot\text{ml}^{-1}$ of particles. All samples contained in total $300 \mu\text{g}$ of polymer.

The cells for FC and cLSM were seeded at the same day *i.e.* from the identical batch of prepared cells. Also the FC experiments were seeded in Ibidi plates, so that the cell density and the amount of added particles ($500 \mu\text{l}$ of $300 \mu\text{g}\cdot\text{ml}^{-1}$) were also identical. Yet the flow cytometry measurement counted only 50% of particles compared to the cLSM method. The cellular uptake measured by FC (111 ± 12 NPs per cell) did not concur with the results from cLSM (246 ± 35 NPs per cell). Apart from the fact that the cLSM data may not be seen as an absolute value (insufficient cell number for statistics and the above described difficulties in perfect identification of NPs), explanations for this discrepancy were sought.

Possibly the main difference between FC and cLSM samples was that the latter were instantly fixed, and left adhered to the bottom. In contrary the FC samples were trypsinized to detach, washed, centrifuged and then fixed after approx. 30 min. It was reported by other members of this work group that cells, when washed after particle incubation and left in buffer solution, exocytosed again a fraction of the NPs (unpublished). In this case the cells of the FC sample would have lost some particles but not more than 10%. Those of cLSM would not lose any NPs because they were fixed directly after a <3 min washing procedure.

The amount of $6.1 \cdot 10^{10}$ added particles corresponded to approx. $1 \cdot 10^6$ added NPs per cell (assuming the initially $40 \cdot 10^3$ seeded cells had increased to approx. $60 \cdot 10^3$ over night). The measured 111 particles via FCy showed that the uptake efficiency was extremely low *i.e.* in the range of $5 \cdot 10^{-3}\%$ of the added NPs.

In any case the number of internalized NPs was too high for proper cLSM analysis and made the by hand counting of particles a tedious task. Furthermore the optical counting of the

intracellular NPs relied on the assumption that the vast majority of them should be singled in organelles and not accumulated and in close proximity to each other. This was important because the correct counting of the particles in an accumulation by cLSM is a difficult task and prone to yield wrong numbers.

The setup of the second series of quantitative experiments was similar except that the NP concentration was reduced to 500 μl of 300 $\mu\text{g}\cdot\text{ml}^{-1}$ of polymer in the incubation medium.

TEM studies of the particle uptake with similar experimental conditions were done to evaluate the precise intracellular localization of the NPs and to demonstrate that the NPs were located separately. Differentiation between particles and cell structures was difficult due to the light coloring and the low intracellular numbers of the NPs (see *Figure 87*).

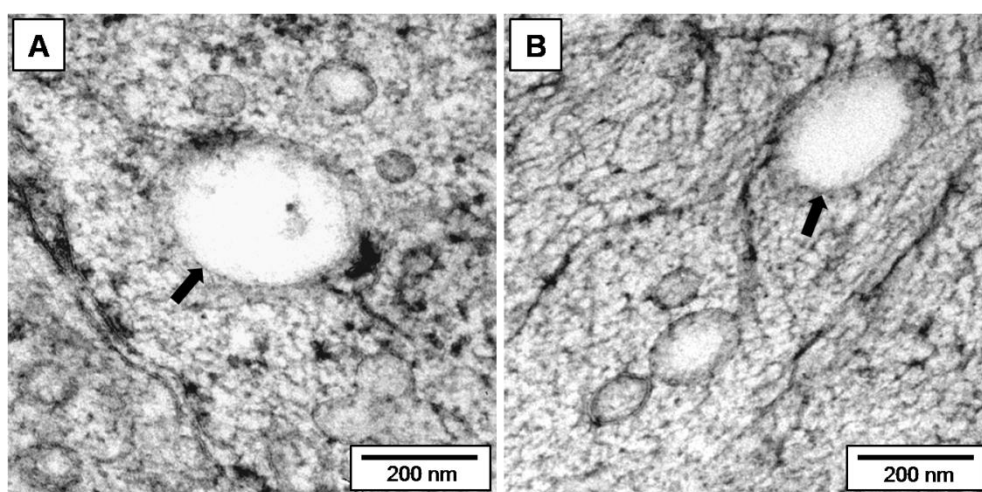


Figure 87. TEM studies of structures likely corresponding to larger PMMA-BP1-2 particles (arrows) in HeLa cells. The cells had been incubated for 2 h with 300 $\mu\text{g}\cdot\text{ml}^{-1}$ of polymer in the volume 500 μl (similar experimental conditions to the FCy and cLSM studies given in *Figure 88*). In concession to the cryo preparation the cells were seeded on sapphire discs in 24-well plates.

The TEM analysis demonstrated that co-localization of NPs had to be very rare, if present at all. The data gathered in the FCy experiments and the corresponding cLSM measurement are given below (*Figure 88*). A detailed listing of the cLSM analysis and the image gallery of the analyzed cells is provided in the appendix (*Table C* and *Figure B*).

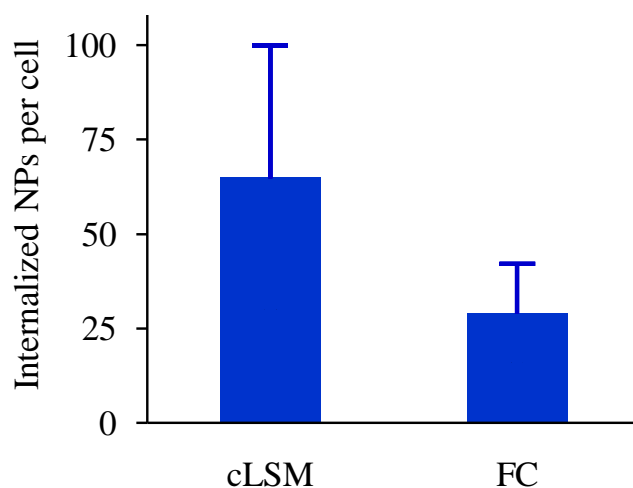


Figure 88. Quantification of PMMA-BP1-2 NPs in HeLa cells after incubation for 2 h with $300 \mu\text{g}\cdot\text{ml}^{-1}$ of polymer in the volume $500 \mu\text{l}$ in Ibidi slides (identical experimental conditions). The results of manual counting in adhered cells by cLSM are given and compared with those obtained in flow cytometric analysis of dispatched cells.

It was observed that, compared to the first FC experiment series, the overall particle uptake was markedly decreased. This was attributed to the reduced NP numbers and to the fact that a different batch of cells was used. The FC data yielded 29 ± 4 NPs per cell whereas the accompanying cLSM experiment suggested 65 ± 36 NPs per cell. The difference to the approximation by cLSM (as a statistically non relevant number of cells could be counted here) was only a factor of 2. Moreover this factor was reproducible and seemed to be a systemic error that might be solved later on.

The precision of the measurement was further increased by narrowing the number of possible reasons for the observed discrepancy (between cLSM and FC): As in the experiment described above, cell density, culture dish, NP concentration and incubation volume were kept identical for the cLSM and the FC samples (as applied already in the previous experiment). Moreover, in the new setup the cLSM cell samples were prepared precisely like were the FC cells – *i.e.* they were equally trypsinized, washed and analyzed in the detached state after FA fixation. These precautions allowed to rule out another three possible reasons for the discrepancy, which were the following: a) the possible loss of particles in FC samples due to trypsination, b) the possible loss of NPs due to the cells' extended incubation in particle-free buffer during the cLSM analysis and c) the risk of false-positive NP counts in cLSM (by mistaking NPs for 'internalized' even though these were in fact located on the culture plate beneath the cell).

Yet other explanations were taken into account. A loss of fluorescence signal intensity was suggested, caused by scattering and adsorption of serum or cell components. The overall FL1 signal loss might therefore be stronger than expected. In this case the intracellular particle count (retrieved with the quantitative FCy method) would indeed be falsely decreased.

Therefore the possibility of any fluorescence loss was evaluated in a spectroscopic measurement using 96 well plates in a plate reader machine. The absorption and emission of empty and of PMMA-BP1-2 loaded cells should be compared. It was assumed that the amount of HeLa cells per sample (also in the lysates) did not differ by more than $\frac{1}{4}$. Particle fluorescence was detected with settings that closely mimicked those of the FC: After excitation at 488 ± 5 nm the emission was detected in the window 545 ± 10 nm. Intact and lysed cells (with & without NPs) were compared to find out if structures of the intact cell scattered the NP fluorescence and reduced the detected FL signal (*Figure 89A*). Additionally the absorption spectra of particles and serum were compared (*Figure 89B*). The particles' fluorescence signal in intact cells was similar to that in the lysate sample (data not shown). This demonstrated that the detected particle fluorescence was not influenced by the presence of ordered cell structures like nucleus, organelles and membranes. Furthermore it was observed that intact cells showed higher absorbance (at 520-570 nm *i.e.* within the emission range of BP1) than did the lysed cells (*Figure 89A*). The strong absorption peak serum supplied incubation medium (see *Figure 89B*) demonstrated that serum components interact strongly with light in the range of 500-600 nm.

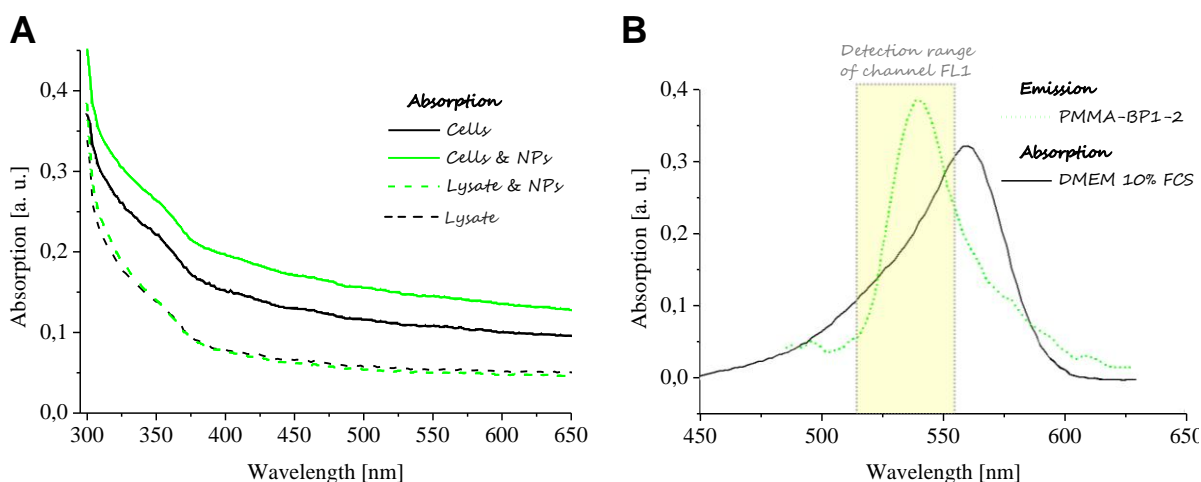


Figure 89. The absorption of cells or cell lysates (A) and of the cell free serum-supplied incubation medium (B) was compared. In (B), the emission spectrum of PMMA-BP1-2 NPs is indicated.

This observation was particularly interesting because the fluorescence of single nanoparticles was decreased in the presence of serum-supplied incubation medium. It could be concluded that serum components significantly reduced the detected emission of PMMA-BP1-2 nanoparticles, seemingly due to absorption in the wavelength range of BP1 emission. In this context it is important to note that cell samples prepared for FC analysis contain residues of serum and incubation medium, as the cells are kept in serum supplied medium during cultivation and during particle incubation. Also, DMEM10% medium is added after trypsination to stop the digestion process. A contribution of serum proteins or other serum

components therefore appears likely. In theory, the phenolsulfonphthalein (a pH indicator also termed phenol red) in the medium might also contribute to the loss of fluorescence signals in channel FL1 – but unlike the serum which made up 10%-vol. of the incubation medium, phenol red is contained in DMEM at a concentration of $15 \text{ mg}\cdot\text{l}^{-1}$ *i.e.* 0.04 mM (see manufacturer information ¹⁶⁹). The basic form of phenolsulfonphthalein absorbs in the emission wavelength range of BP1 ¹⁷⁰⁻¹⁷¹ and therefore should not be neglected. Finally, the protein samples (either in form of intact or of lysed cells) did not demonstrate any significant absorption in the mentioned wavelength range and were therefore ruled out – indeed, cell autofluorescence has mostly been reported for shorter wavelengths due to *e.g.* flavins ¹⁷².

Apart from possible inaccuracy of the quantitative cLSM data, the presence of incubation medium residues in the FC samples might reduce the detected particle fluorescence and thus be responsible for the discussed discrepancy between FC and cLSM data.

These findings point out that the described absolute quantitation should be tuned to full precision if the fluorescence dimming is avoided, *e.g.* by using particles with a more red-shifted emission spectrum.

During some cell experiments the observation was made that the cells split up into two populations (see *Figure 90*).

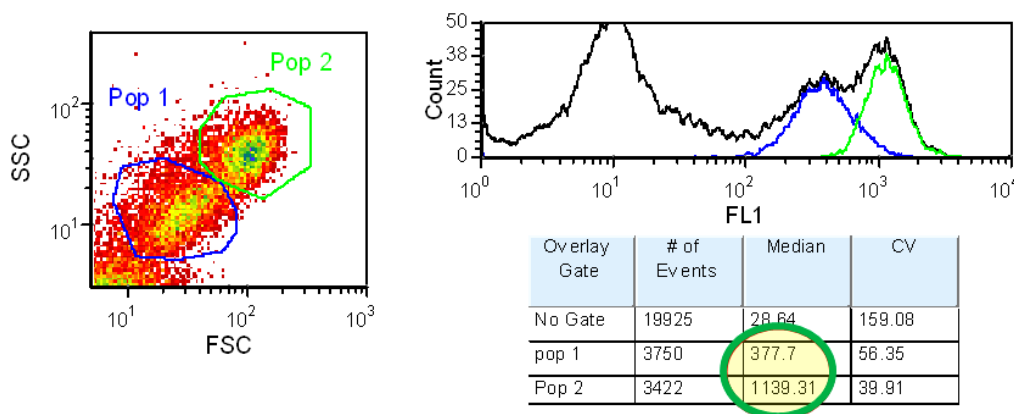


Figure 90. Exemplary data set of HeLa cells without particles, measured at 200 mW under the conditions for quantitative experiments. The SSC-FSC scatter plot (l.) and the FL1 histogram data (r.) distinguish 2 cell populations.

More importantly, it seemed that those populations differed in their particle uptake efficiency by a factor of nearly 3 (see *Figure 91*). All data of the quantitative experiments are based on the average of all cells, *i.e.* no distinction between the two populations was made, see red gate in *Figure 91A*. But separate analysis of the two subpopulations (see *Figure 91B*), if required, were possible because they could always be differentiated in the SSC-FSC plot. The FL1 intensity of the respective particle free cell population, which was required for the calculations, could be derived as demonstrated in *Figure 90*.

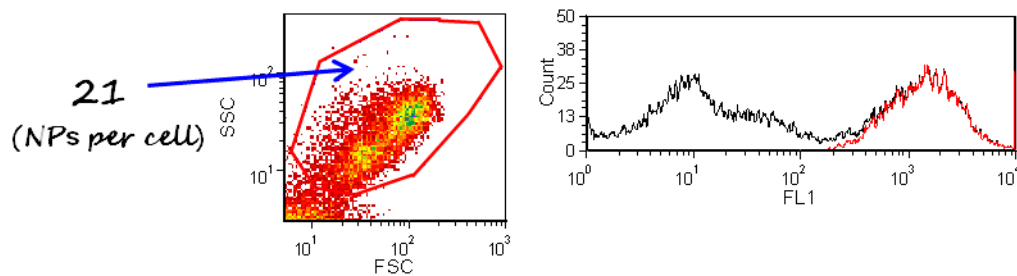
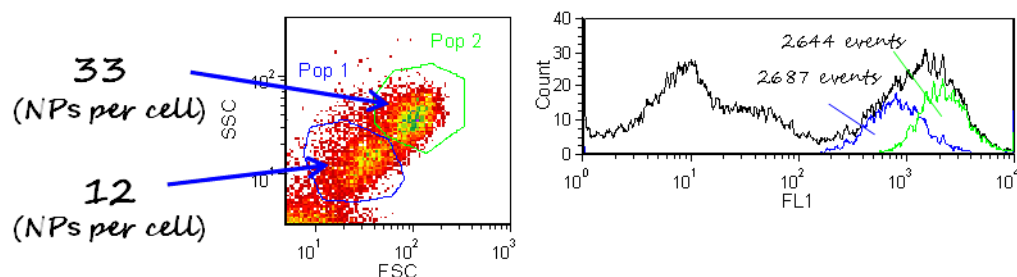
A 1 gate**B** 2 separate gates

Figure 91. Exemplary data set of HeLa cells incubated with $300 \mu\text{g}\cdot\text{ml}^{-1}$ of NPs for 2 h, measured at 200 mW under the conditions for quantitative experiments. Two subpopulations of cells were distinguished in the SSC-FSC plot (l.). The cells were gated into the FL1 histogram (r.) combined in one gate (A) or in 2 separate gates (B).

Unlike in the NP-free sample, a differentiation between two peaks in the FL1 histogram (see Figure 90) was not possible anymore in the samples with NPs (see Figure 91). But the populations could still be gated by the FSC-SSC scatter plot, and transferred into the FL1 histogram (Figure 91B). In general the population split did not occur when the laser power was reduced to 40 mW (data not shown). When measuring at 200 mW, the population splitting occurred in formaldehyde-fixed and live cells alike (data not shown). After ethanol fixation the cell population was more diffuse and a clear split into 2 populations was not observed (data not shown). In total, the effect seemed more pronounced in FA fixed cells, because there the effect already appeared at a lower laser power (100 mW) compared to the non-fixed cell sample (only >150 mW).

If this was not an artifact or coincidence it might be based on certain structures or bio molecules. In this case these structures would be damaged or altered in the FA fixation process in a way that their emission properties would change (FA forms covalent bonds during the fixation process; ethanol does not).

As discussed, this effect did not occur in all experiments and no cause for the phenomenon could be found. A dependence of the effect on the cell cycle was suspected but could not be studied. The discussed effect was not visible anymore when cell samples had been prepared following the protocol for cell cycle analysis (data not shown).

SUMMARY The absolute counting of intracellular NPs was exercised in flow cytometry and in cLSM, which was chosen to provide a direct method of counting the fluorescent NPs. Measurements in cLSM demonstrated that even PMMA-BP1-2 particles located in a 400 nm core-to-core distance could be dissolved as separate particles. Still, as the cLSM was not run in STED mode, it was crucial that the particle-loaded endosomes did not fuse. Therefore a short incubation time of 2 h was chosen. Another requirement was that the cells should contain approximately 40 particles each. This would be a suitable number of internalized NPs for the manual counting in the cLSM.

Therefore incubation time and concentration were balanced in precursory experiments. Incubation for up to 2 h with 75, 150 and 300 $\mu\text{g}\cdot\text{ml}^{-1}$ showed that a maximum of approx. 40 NPs was taken up after 2 h incubation with 300 $\mu\text{g}\cdot\text{ml}^{-1}$. Studies of the uptake over time, at the concentration of 300 $\mu\text{g}\cdot\text{ml}^{-1}$, showed that after 1 h only 25 particles were taken per cell up. After 4 h incubation approx. 130 NPs were internalized.

In the first quantitative testing the FC measurement counted 111 ± 12 and the cLSM counted 246 ± 35 NPs per cell. As, with 500 $\mu\text{g}\cdot\text{ml}^{-1}$ of polymer, the concentration was rather high the particle uptake was also high. Nevertheless the particle counts obtained by the two methods differed by a factor of 2. The reason for this has to be found (apart from the fact that the cLSM data have a high standard deviation due to the low number of analyzed cells). Most likely the reason was that the cLSM cell samples remained adhered until fixation – whereas the FC samples were trypsinized and washed before fixation. This might lead to particle loss.

It was concluded that the best conditions for quantitative studies were 2 h incubation time and a NP concentration of 300 $\mu\text{g}\cdot\text{ml}^{-1}$. With these experimental conditions a set of 4 FCy experiments were done. Coupled to these FCy measurements a complimentary cLSM analysis was done: The cLSM samples were those cells that were left-over in the cytometry tubes. This ensured that the cell samples in the FC and in the cLSM were identical. But again, the FC yielded a lower count (29 ± 4) than the cLSM (65 ± 36 NPs per cell).

After these possibilities were excluded, the most likely explanation for the reduced NP count in the FC was a specific property of the biological sample that reduced the detected emission of the BP1 fluorophore. A spectroscopic analysis of intact and lysed cells demonstrated that neither showed significant absorption at the emission wavelength of BP1. But a sample of serum supplied medium showed a strong absorption peak where the BP1 fluorophore emits. It was concluded that most likely, residues of the serum were contained in the FC samples and absorbed a fraction of the particle fluorescence signals.

Furthermore a split of the cells into 2 populations (distinguished by FL1 and by scattering) was observed in some samples. But it only occurred under specific conditions *i.e.* when the 488 nm laser was up-regulated to >100 mW (FA-fixed cells) or >150 mW (live cells). This difference between live and FA treated cells might indicate that chromophoric cell molecules are involved which are partially altered or destroyed by covalent reaction with FA.

5 Summary and Conclusions

1. The effect of polymer nature of the cellular uptake of nanoparticles

The aim of this thesis was to study essential properties of polymeric NPs that are seemingly overlooked today – those of the polymeric material itself. The variety of materials for nanocarriers is overwhelming and the developed nanoparticulate systems get more and more complex due to surface functionalization, core-shell morphologies, stimuli-response modules or capsule morphology, to name a few. For this study a set of nanoparticles made from PS, PLLA and PMMA, with similar physico-chemical properties and deliberately without further functionalization, were synthesized. Their interaction with HeLa cells was compared and their behavior upon co-incubation of two particle species was studied. It could be shown that the uptake efficiency of PLLA particles was the most effective, which should be linked to the inherent carboxyl groups, the polymer softness (no T_g) and presumably a specific strong interaction with serum proteins. The competitive co-incubation of PS and PLLA particles demonstrated that these two particle species mutually affected their cellular uptake in a way that the relative internalization rate of PS was increased and that of PLLA got decreased. It could be shown that these two species significantly interact with serum proteins and it was observed that a high serum protein concentration markedly reduced the competitive effect. The TEM studies of PS and PLLA co-incubation revealed that the NPs attached to the cell membrane as single particles. Also inside the cell the vast majority of these were located in separate compartments. Based on these findings it was concluded that PS and PLLA nanoparticles adhere to the cell surface one-by-one and compete for the internalization into HeLa cells via a one-particle process. The competition for specific, yet unidentified, coating serum proteins is part of this process. Such details about the basic properties of the polymeric material itself could be applied to more complex nanocarrier systems, to create a finely tuned DDS.

The synthesis of all required NPs was deliberately made a part of this thesis, as it enabled a better knowledge of the colloidal NPs that were used in the cell experiments. The established technique of ME was applied to prepare polymeric nanoparticles from PS, PLLA and PMMA with the ionic surfactant sodium dodecylsulfate. These particles were of narrow size distribution and stable in the presence of serum proteins. Furthermore, large PS NPs with amino-functionalization were synthesized. Due to the presence of 2 %-wt. of the comonomer AEMH in the continuous phase the ME was slightly impaired and the samples showed a bimodal size distribution. It was shown that this could be corrected by appropriate centrifugation steps to selectively remove one of the 2 populations by sedimentation. Other sets of PS or PMMA particles should be synthesized with a maximum amount of incorporated dye. For this purpose, new modified dye molecules were provided by other members of the Landfester and Müllen groups at the Institute. These syntheses were successful and only

samples with the highest dye loading (0.3-0.4%-wt. ref. to the monomer) had a lower conversion. But also these samples had a sufficiently narrow size distribution.

2. Flow cytometry for single nanoparticle detection

The prime intention of preparing NPs with high dye loading was the development of a method to measure single NPs in the flow cytometer. Single particle measurement (SPM) would offer valuable possibilities. For one thing the fluorescence intensity distribution of submicron particles was achieved. Additionally the number of NPs per volume could be counted which so far is only possible with a few sophisticated methods. More often, the NP concentration is calculated based on the particle size and the solid content. Once SPM is established it could be exploited to count the absolute number of internalized NPs in cells in a convenient and swift manner. This so far is impossible with polymeric particles and therefore with a majority of the available nanocarrier materials. Only materials like ferrum can be quantified by other means to count the NPs in a cell.

Only the measurement of the small 70 nm particles remained difficult and their fluorescence could not be obtained with precision. But the measurement of 150 nm sized particles of PS and of PMMA was successful and the mean fluorescence of a single sphere could be determined with a standard deviation below 10%.

The particle number per volume was also counted in the FC and compared with the concentrations calculated at base of the particle size measurement in DLS. The FC analysis did not fully concur with the theoretical values but instead yielded slightly less particles (60%) than was expected. This was successfully applied also on particles that had been incubated with cells in serum supplied medium for several hours – counting polymeric NPs under such conditions is difficult and only few detection methods are available.

3. Absolute quantification of nanoparticles in cells

Three promising particle samples were chosen to be incubated with HeLa cells and then counted in a quantitative manner by FCy and by cLSMy. At the base of the most promising sample, 150 nm sized PMMA spheres stabilized with SDS and marked with copolymerized dye, the quantitative counting method in cells was developed. For a backup of the new flow cytometric quantification the NPs were also counted manually in the cells using cLSMy. No specific automated software was used here and the particles were deliberately counted ‘by hand’ in the cLSM images of the cells. The intention was to get a direct look into the system – as opposed to the more abstract FC method. Flow cytometric quantification repeatedly yielded 50% of the particle count that was observed in cLSMy. This discrepancy was assumed to be a combination of several aspects like loss of particle fluorescence due to absorption by residues of the incubation medium. The FCy data was the average value of several thousand cells and

it was therefore more precise than the findings from cLSMy where a small number of cells was analyzed manually. Spectroscopic analysis of cell samples disproved scattering or absorption of cell contents as a reason for the fluorescence loss, but indicated that serum-supplied incubation medium absorbed in the emission range of BP1.

Despite possible imprecision, which should not exceed a factor of 2, it could be shown that the uptake efficiency of negatively charged non-functionalized NPs was very low. After 2 h of incubation with the HeLa cells, less than $5 \cdot 10^{-3}\%$ of the initially added particles were detected inside the cells. Future studies with fluorophores emitting above 650 nm wavelength should avoid any fluorescence loss and increase the counting precision. The particles' fluorescence signals in the far red range should not be dimmed by biological material as cellular absorbance and autofluorescence are restricted to shorter wavelengths. Compared to the current ways of quantifying polymeric NPs inside cells, this new approach is a significant improvement. The particle fluorescence needs to be measured merely once and then the intracellular counting of these particles is a swift routine measurement.

6 Literature

1. Feynman, R.P., *There's plenty of room at the bottom*. Caltech Engineering and Science, 1960. **23**(5): p. 22-36.
2. Taniguchi, N., *On the basic concept of nanotechnology*. Proc. Intl. Conf. Prod. Eng. Tokyo, Part II, 1974.
3. Chemical Industry Vision2020 Technology Partnership Energetics, I., *Chemical industry R&D roadmap for nanomaterials by design: From fundamentals to function*. 2003.
4. Lee, J., S. Mahendra, and P.J.J. Alvarez, *Nanomaterials in the construction industry: A review of their applications and environmental health and safety considerations*. ACS Nano, 2010. **4**(7): p. 3580-3590.
5. Schmid, K. and M. Riediker, *Use of Nanoparticles in Swiss Industry: A Targeted Survey*. Environmental Science & Technology, 2008. **42**(7): p. 2253-2260.
6. Katz Linda, M., *Nanotechnology and applications in cosmetics: General overview*, in *Cosmetic Nanotechnology*. 2007, American Chemical Society. p. 193-200.
7. Kühling, P.D.W., *Nanotechnologie im Lebensmittelbereich*, B.f.U.-u.N. Deutschland, Editor.
8. Rosen, H. and T. Aribat, *The rise and rise of drug delivery*. Nat Rev Drug Discov, 2005. **4**(5): p. 381-385.
9. Duncan, R. and L. Izzo, *Dendrimer biocompatibility and toxicity*. Advanced Drug Delivery Reviews, 2005. **57**(15): p. 2215-2237.
10. Duncan, R., H. Ringsdorf, and R. Satchi-Fainaro, *Polymer Therapeutics: Polymers as drugs, drug and protein conjugates and gene delivery systems: Past, present and future opportunities*, *Polymer Therapeutics I*, R. Satchi-Fainaro and R. Duncan, Editors. 2006, Springer Berlin / Heidelberg. p. 1-8.
11. Bawa, R., *Nanopharmaceuticals for drug delivery - A review*. Drug Delivery, 2009. **3**.
12. Kreuter, J., *Influence of the surface properties on nanoparticle-mediated transport of drugs to the brain*. Journal of Nanoscience and Nanotechnology, 2004. **4**(5): p. 484-488.
13. Göppert, T.M. and R.H. Müller, *Polysorbate-stabilized solid lipid nanoparticles as colloidal carriers for intravenous targeting of drugs to the brain: Comparison of plasma protein adsorption patterns*. Journal of Drug Targeting, 2005. **13**(3): p. 179-187.
14. Siegel, R., D. Naishadham, and A. Jemal, *Cancer statistics, 2012*. CA: A Cancer Journal for Clinicians, 2012. **62**(1): p. 10-29.
15. Holzapfel, V., et al., *Synthesis and biomedical applications of functionalized fluorescent and magnetic dual reporter nanoparticles as obtained in the miniemulsion process*. Journal of Physics: Condensed Matter, 2006. **18**(38): p. S2581-S2594.
16. Lorenz, S., et al., *The softer and more hydrophobic the better: Influence of the side chain of polymethacrylate nanoparticles for cellular uptake*. Macromolecular Bioscience, 2010. **10**(9): p. 1034-1042.
17. Wurthner, F., *Perylene bisimide dyes as versatile building blocks for functional supramolecular architectures*. Chem Commun (Camb), 2004(14): p. 1564-79.
18. van Gaal, E.V.B., et al., *Flow cytometry for rapid size determination and sorting of nucleic acid containing nanoparticles in biological fluids*. Journal of Controlled Release, 2010. **141**(3): p. 328-338.
19. Hussain, N., *Fluorometric method for the simultaneous quantitation of differently-sized nanoparticles in rodent tissue*. International Journal of Pharmaceutics, 2001. **214**(1-2): p. 55-61.
20. Penn, S.G., L. He, and M.J. Natan, *Nanoparticles for bioanalysis*. Current Opinion in Chemical Biology, 2003. **7**(5): p. 609-615.

21. Musyanovych, A., V. Mailander, and K. Landfester, *Miniemulsion Droplets as Single Molecule nanoreactors for polymerase chain reaction*. *Biomacromolecules*, 2005. **6**(4): p. 1824-1828.
22. Baier, G., et al., *DNA amplification via polymerase chain reaction inside miniemulsion droplets with subsequent poly(n-butylcyanoacrylate) shell formation and delivery of polymeric capsules into mammalian cells*. *Macromol Biosci*, 2011. **11**(8): p. 1099-109.
23. de Arbina, L.L. and J.M. Asua, *High-solids-content batch miniemulsion polymerization*. *Polymer*, 1992. **33**(22): p. 4832-4837.
24. Tiarks, F., K. Landfester, and M. Antonietti, *Preparation of polymeric nanocapsules by miniemulsion polymerization*. *Langmuir*, 2001. **17**(3): p. 908-918.
25. Wang, S.T., et al., *Emulsion and miniemulsion copolymerization of acrylic monomers in the presence of alkyd resin*. *Journal of Applied Polymer Science*, 1996. **60**(12): p. 2069-2076.
26. Crespy, D. and K. Landfester, *Miniemulsion polymerization as a versatile tool for the synthesis of functionalized polymers*. *Beilstein J Org Chem*, 2010. **6**: p. 1132-48.
27. de Brouwer, H., J.G. Tsavalas, and F.J. Schork, *Living Rradical polymerization in miniemulsion using reversible addition-fragmentation chain transfer*. *Macromolecules*, 2000. **33**(25): p. 9239-9246.
28. Schork, F.J., et al., *Miniemulsion polymerization and polymer particles*, in *Advances in polymer science*. 2005, Springer Berlin / Heidelberg. p. 129-255.
29. Asua, J.M., *Miniemulsion polymerization*. *Progress in Polymer Science*, 2002. **27**(7): p. 1283-1346.
30. Landfester, K., *Synthesis of colloidal particles in miniemulsions*. *Annual Review of Materials Research*, 2006. **36**(1): p. 231-279.
31. Salata, O., *Applications of nanoparticles in biology and medicine*. *J Nanobiotechnology*, 2004. **2**(1): p. 3.
32. Landfester, K., et al., *Evidence for the preservation of the particle identity in miniemulsion polymerization*. *Macromolecular Rapid Communications*, 1999. **20**(2): p. 81-84.
33. Musyanovych, A., et al., *Preparation of biodegradable polymer nanoparticles by miniemulsion technique and their cell interactions*. *Macromolecular Bioscience*, 2008. **8**(2): p. 127-39.
34. Mu, L. and S.S. Feng, *Vitamin E TPGS used as emulsifier in the solvent evaporation/extraction technique for fabrication of polymeric nanospheres for controlled release of paclitaxel (Taxol®)*. *Journal of Controlled Release*, 2002. **80**(1-3): p. 129-144.
35. Dessy, A., et al., *Dead sea minerals loaded polymeric nanoparticles*. *Colloids Surf B Biointerfaces*, 2011. **87**(2): p. 236-42.
36. Rieger, J., *The glass transition temperature of polystyrene*. *Journal of Thermal Analysis and Calorimetry*, 1996. **46**(3): p. 965-972.
37. Sanders, E. and C.T. Ashworth, *A study of particulate intestinal absorption and hepatocellular uptake. Use of polystyrene latex particles*. *Exp Cell Res*, 1961. **22**: p. 137-45.
38. Horowitz, S.M., C.G. Frondoza, and D.W. Lennox, *Effects of polymethylmethacrylate exposure upon macrophages*. *Journal of Orthopaedic Research*, 1988. **6**(6): p. 827-832.
39. Jepson, M., et al., *Selective binding and transcytosis of latex microspheres by rabbit intestinal M cells*. *Cell and Tissue Research*, 1993. **271**(3): p. 399-405.
40. Johnston, H.J., et al., *Evaluating the uptake and intracellular fate of polystyrene nanoparticles by primary and hepatocyte cell lines in vitro*. *Toxicol. Appl. Pharmacol.*, 2009. **242**(1): p. 66-78.

41. Bagal, A., et al., *Clinical experience with polymethylmethacrylate microspheres (Artecoll) for soft-tissue augmentation: A retrospective review*. 2007. **9**(4): p. 275-280.
42. Horowitz, S.M., et al., *Macrophage exposure to polymethyl methacrylate leads to mediator release and injury*. Journal of Orthopaedic Research, 1991. **9**(3): p. 406-413.
43. Mang, W.L. and K. Sawatzki, *Complications after implanataion of PMMA (polymethyl methacrylate) for soft-tissue augmentation*. H + G. Zeitschrift für Hautkrankheiten, 1998. **73**(1): p. 42-44.
44. Gough, J.E. and S. Downes, *Osteoblast cell death on methacrylate polymers involves apoptosis*. J Biomed Mater Res, 2001. **57**(4): p. 497-505.
45. Borchard, G. and J. Kreuter, *The role of serum complement on the organ distribution of intravenously administered poly(methyl methacrylate) nanoparticles: Effects of pre-coating with plasma and with serum complement*. Pharmaceutical Research, 1996. **13**(7): p. 1055-1058.
46. Araujo, L., et al., *Uptake of PMMA nanoparticles from the gastrointestinal tract after oral administration to rats: modification of the body distribution after suspension in surfactant solutions and in oil vehicles*. International Journal of Pharmaceutics, 1999. **176**(2): p. 209-224.
47. Voltan, R., et al., *Preparation and characterization of innovative protein-coated poly(methylmethacrylate) core-shell nanoparticles for vaccine purposes*. Pharmaceutical Research, 2007. **24**(10): p. 1870-1882.
48. Xu, H., J.X. Shi, and T. Sun, *Polymethylmethacrylate-grafted titanium dioxide nanoparticles prepared via radical polymerization*. J. Adv. Mater., 2008. **40**(1): p. 27-32.
49. Dhana Lekshmi, U.M., et al., *In vitro characterization and invivo toxicity study of repaglinide loaded poly (methyl methacrylate) nanoparticles*. Int J Pharm, 2010. **396**(1-2): p. 194-203.
50. Garcia, D.A., T.M. Sullivan, and D.M. O'Neill, *The biocompatibility of dental implant materials measured in an animal model*. Materials Science, 1981. **60**(1): p. 44-49.
51. Van der Elst, M., et al., *The burst phenomenon, an animal model simulating the long-term tissue response on PLLA interlocking nails*. 1996. p. 139-143.
52. Anderson, J.M. and M.S. Shive, *Biodegradation and biocompatibility of PLA and PLGA microspheres*. Advanced Drug Delivery Reviews, 1997. **28**(1): p. 5-24.
53. Buddy and Ratner, *Biomaterials science: An introduction to materials in medicine*. Vol. 2nd edition. 2004: Elsevier Inc.
54. Bergsma, J.E., et al., *Late degradation tissue response to poly(L-lactide) bone plates and screws*. Biomaterials, 1995. **16**(1): p. 25-31.
55. Panyam, J. and V. Labhasetwar, *Sustained cytoplasmic delivery of drugs with intracellular receptors using biodegradable nanoparticles*. Mol. Pharm., 2004. **1**(1): p. 77-84.
56. McClean, S., et al., *Binding and uptake of biodegradable poly-DL-lactide micro- and nanoparticles in intestinal epithelia*. European Journal of Pharmaceutical Sciences, 1998. **6**(2): p. 153-163.
57. Leroux, J.-C., P. Gravel, Luc Balant, Bernard Volet, Beatrice M. Anner, Eric Allémann, Eric Doelker, Robert Gurny, *Internalization of poly(D,L-lactic acid) nanoparticles by isolated human leukocytes and analysis of plasma proteins adsorbed onto the particles*. Journal of Biomedical Materials Research, 1994. **28**(4): p. 471-481.
58. Gref, R., et al., *'Stealth' corona-core nanoparticles surface modified by polyethylene glycol (PEG): influences of the corona (PEG chain length and surface density) and of the core composition on phagocytic uptake and plasma protein adsorption*. Colloids and Surfaces B: Biointerfaces, 2000. **18**(3-4): p. 301-313.
59. Tobío, M., et al., *Stealth PLA-PEG nanoparticles as protein carriers for nasal administration*. Pharmaceutical Research, 1998. **15**(2): p. 270-275.

60. Bala, I., S. Hariharan, and M.N. Kumar, *PLGA nanoparticles in drug delivery: The state of the art*. Crit Rev Ther Drug Carrier Syst, 2004. **21**(5): p. 387-422.
61. Yu, J.J., et al., *Bio-distribution and anti-tumor efficacy of PEG/PLA nano particles loaded doxorubicin*. J Drug Target, 2007. **15**(4): p. 279 - 284.
62. Alberts, B., Bray, Dennis, Lewis, Julian, Raff, Martin, Roberts, Keith, Watson, James D., *Molecular biology of the cell*. 3 ed. 1994.
63. Berg, J.M., Tymoczko, J. L., Stryer, L., , *Biochemie*. 5 ed. 2003: Spektrum Akademischer Verlag. 1200.
64. Campbell, N.A., Reece, Jane B., *Biologie*. 5 ed, ed. J. Markl. 2003: Spektrum Akademischer Verlag.
65. Pralle, A., et al., *Sphingolipid-cholesterol rafts diffuse as small entities in the plasma membrane of mammalian cells*. J Cell Biol, 2000. **148**(5): p. 997-1008.
66. Merrifield, C.J., et al., *Endocytic vesicles move at the tips of actin tails in cultured mast cells*. Nat. Cell Biol., 1999. **1**(1): p. 72-74.
67. Fort, A.G., et al., *In vitro motility of liver connexin vesicles along microtubules utilizes kinesin motors*. J Biol Chem, 2011. **286**(26): p. 22875-85.
68. Sivaramakrishnan, S. and J.A. Spudich, *Coupled myosin VI motors facilitate unidirectional movement on an F-actin network*. J Cell Biol, 2009. **187**(1): p. 53-60.
69. Singer, S.J. and G.L. Nicolson, *The fluid mosaic model of the structure of cell membranes*. Science, 1972. **175**(23): p. 720-31.
70. Gagescu, R., J. Gruenberg, and E. Smythe, *Membrane dynamics in endocytosis: structure--function relationship*. Traffic, 2000. **1**(1): p. 84-8.
71. Kirkham, M. and R.G. Parton, *Clathrin-independent endocytosis: New insights into caveolae and non-caveolar lipid raft carriers*. Biochimica et Biophysica Acta (BBA) - Molecular Cell Research, 2005. **1745**(3): p. 273-286.
72. Mousavi, S.A., et al., *Clathrin-dependent endocytosis*. Biochem. J., 2004. **377**: p. 1-16.
73. Hanover, J.A., M.C. Willingham, and I. Pastan, *Kinetics of transit of transferrin and epidermal growth factor through clathrin-coated membranes*. Cell, 1984. **39**(2 Pt 1): p. 283-93.
74. Vieira, A.V., C. Lamaze, and S.L. Schmid, *Control of EGF receptor signaling by clathrin-mediated endocytosis*. Science, 1996. **274**(5295): p. 2086-2089.
75. Mettlen, M., et al., *Cargo- and adaptor-specific mechanisms regulate clathrin-mediated endocytosis*. J Cell Biol, 2010. **188**(6): p. 919-33.
76. Simons, K. and D. Toomre, *Lipid rafts and signal transduction*. Nat Rev Mol Cell Biol, 2000. **1**(1): p. 31-39.
77. Edidin, M., *Shrinking patches and slippery rafts: scales of domains in the plasma membrane*. Trends in Cell Biology, 2001. **11**(12): p. 492-496.
78. Edidin, M., *The state of lipid rafts: From model membranes to cells*. Annu. Rev. Biophys. Biomolec. Struct., 2003. **32**: p. 257-283.
79. Mayor, S. and R.E. Pagano, *Pathways of clathrin-independent endocytosis*. Nat Rev Mol Cell Biol, 2007. **8**(8): p. 603-612.
80. Desai, M.P., et al., *Gastrointestinal uptake of biodegradable microparticles: Effect of particle size*. Pharm. Res., 1996. **13**(12): p. 1838-1845.
81. Desai, M.P., et al., *The mechanism of uptake of biodegradable microparticles in Caco-2 cells is size dependent*. Pharm. Res., 1997. **14**(11): p. 1568-1573.
82. Chithrani, B.D. and W.C.W. Chan, *Elucidating the mechanism of cellular uptake and removal of protein-coated gold nanoparticles of different sizes and shapes*. Nano Letters, 2007. **7**(6): p. 1542-1550.
83. Cedervall, T., et al., *Detailed identification of plasma proteins adsorbed on copolymer nanoparticles*. Angewandte Chemie International Edition, 2007. **46**(30): p. 5754-5756.

84. Lundqvist, M., et al., *Nanoparticle size and surface properties determine the protein corona with possible implications for biological impacts*. Proceedings of the National Academy of Sciences, 2008. **105**(38): p. 14265-14270.
85. Chithrani, D.B., *Intracellular uptake, transport, and processing of gold nanostructures*. Mol Membr Biol, 2010. **27**(7): p. 299-311.
86. Alkilany, A.M., et al., *Gold nanorods: Their potential for photothermal therapeutics and drug delivery, tempered by the complexity of their biological interactions*. Adv Drug Deliv Rev, 2011.
87. Chen, J., et al., *Functionalized single-walled carbon nanotubes as rationally designed vehicles for tumor-targeted drug delivery*. J Am Chem Soc, 2008. **130**(49): p. 16778-85.
88. Wangoo, N., et al., *Facile synthesis and functionalization of water-soluble gold nanoparticles for a bioprobe*. Anal Chim Acta, 2008. **610**(1): p. 142-8.
89. Santos, J.L., et al., *Functionalization of poly(amidoamine) dendrimers with hydrophobic chains for improved gene delivery in mesenchymal stem cells*. J Control Release, 2010. **144**(1): p. 55-64.
90. Gessner, A., et al., *Nanoparticles with decreasing surface hydrophobicities: influence on plasma protein adsorption*. International Journal of Pharmaceutics, 2000. **196**(2): p. 245-249.
91. Landfester, K., et al., *Miniemulsion polymerization with cationic and nonionic surfactants: A very efficient use of surfactants for heterophase polymerization*. Macromolecules, 1999. **32**(8): p. 2679-2683.
92. Guangwei He, Q.P., *Synthesis of polystyrene and polystyrene/poly(methyl methacrylate) nanoparticles*. Macromolecular Rapid Communications, 2004. **25**(17): p. 1545-1548.
93. Holzapfel, V., et al., *Preparation of fluorescent carboxyl and amino functionalized polystyrene particles by miniemulsion polymerization as markers for cells*. Macromolecular Chemistry and Physics, 2005. **206**(24): p. 2440-2449.
94. Harush-Frenkel, O., et al., *Surface charge of nanoparticles determines their endocytic and transcytotic pathway in polarized MDCK cells*. Biomacromolecules, 2008. **9**(2): p. 435-443.
95. Harush-Frenkel, O., et al., *Targeting of nanoparticles to the clathrin-mediated endocytic pathway*. Biochemical and Biophysical Research Communications, 2007. **353**(1): p. 26-32.
96. Dausend, J., et al., *Uptake Mechanism of oppositely charged fluorescent nanoparticles in HeLa cells*. Macromolecular Bioscience, 2008. **8**(12): p. 1135-1143.
97. Jiang, X.E., et al., *Specific effects of surface amines on polystyrene nanoparticles in their interactions with mesenchymal stem cells*. Biomacromolecules, 2010. **11**(3): p. 748-753.
98. Jokerst, J.V., et al., *Nanoparticle PEGylation for imaging and therapy*. Nanomedicine (Lond), 2011. **6**(4): p. 715-28.
99. Fenghua Meng, G.H.M.E., Jan Feijen., *Polyethylene glycol-grafted polystyrene particles*. Journal of Biomedical Materials Research Part A, 2004. **70A**(1): p. 49-58.
100. Avgoustakis, K., *Pegylated poly(lactide) and poly(lactide-co-glycolide) nanoparticles: preparation, properties and possible applications in drug delivery*. Curr Drug Deliv, 2004. **1**(4): p. 321-33.
101. Zhou, J.D., et al., *Differential plasma protein binding to metal oxide nanoparticles*. Nanotechnology, 2009. **20**(45): p. 455101.
102. Lynch, I., et al., *The nanoparticle-protein complex as a biological entity; a complex fluids and surface science challenge for the 21st century*. Advances in Colloid and Interface Science, 2007. **134-135**: p. 167-174.

103. Lynch, I., A. Salvati, and K.A. Dawson, *Protein-nanoparticle interactions: What does the cell see?* Nat Nano, 2009. **4**(9): p. 546-547.
104. Patel, H.M., *Serum opsonins and liposomes: Their interaction and opsonophagocytosis.* Crit Rev Ther Drug Carrier Syst, 1992. **9**(1): p. 39-90.
105. Delehanty, J.B., et al., *Peptides for specific intracellular delivery and targeting of nanoparticles: Implications for developing nanoparticle-mediated drug delivery.* Therapeutic Delivery, 2010. **1**(3): p. 411-433.
106. Miele, E., et al., *Albumin-bound formulation of paclitaxel (Abraxane® ABI-007) in the treatment of breast cancer.* International Journal of Nanomedicine, 2009. **4**: p. 99-105.
107. Dörfler, H.-D., *Grenzflächen und kolloid-disperse Systeme.* 2002, Berlin: Springer Verlag.
108. Müller, R.H., *Zetapotential und Partikelladung in der Laborpraxis.* 1996, Stuttgart Wissenschaftliche Verlagsgesellschaft mbH.
109. Kapitein, L.C., K.W. Yau, and C.C. Hoogenraad, *Microtubule dynamics in dendritic spines.* Methods Cell Biol, 2010. **97**: p. 111-32.
110. Jiang, X., et al., *Endo- and exocytosis of zwitterionic quantum dot nanoparticles by live HeLa cells.* ACS Nano, 2010. **4**(11): p. 6787-97.
111. Nagorni, M. and S.W. Hell, *4Pi-confocal microscopy provides three-dimensional images of the microtubule network with 100- to 150 nm resolution.* J Struct Biol, 1998. **123**(3): p. 236-47.
112. Glaschick, S., et al., *Axial resolution enhancement by 4Pi confocal fluorescence microscopy with two-photon excitation.* J Biol Phys, 2007. **33**(5-6): p. 433-43.
113. Klar, T.A. and S.W. Hell, *Subdiffraction resolution in far-field fluorescence microscopy.* Opt Lett, 1999. **24**(14): p. 954-6.
114. Willig, K.I., et al., *Dual-label STED nanoscopy of living cells using photochromism.* Nano Lett, 2011.
115. Van Dilla, M.A., et al., *Cell microfluorometry - A method for rapid fluorescence measurement.* Science (Washington D C), 1969. **163**(3872): p. 1213-1214.
116. Lauer, S.A. and J.P. Nolan, *Development and characterization of Ni-NTA-bearing microspheres.* Cytometry, 2002. **48**(3): p. 136-45.
117. Chattopadhyay, P.K. and M. Roederer, *Good cell, bad cell: Flow cytometry reveals T-cell subsets important in HIV disease.* Cytometry Part A, 2010. **77A**(7): p. 614-622.
118. Gucker, F.T., Jr., H.B. Pickard, and C.T. O'Konski, *A photoelectric instrument for comparing the concentrations of very dilute aerosols, and measuring low light intensities.* J Am Chem Soc, 1947. **69**(2): p. 429-38.
119. Chisholm, S.W., et al., *A novel free-living prochlorophyte occurs at high cell concentrations in the oceanic euphotic zone.* Nature, 1988. **334**.
120. Muldrow, L.L., R.L. Tyndall, and C.B. Fliermans, *Application of flow cytometry to studies of pathogenic free-living amoebae.* Applied and Environmental Microbiology, 1982. **44**(6): p. 1258-1269.
121. Dorsey, J., et al., *Rapid analytical technique for the assessment of cell metabolic activity in marine microalgae.* Cytometry, 1989. **10**(5): p. 622-628.
122. Phinney, D.A. and T.L. Cucci, *Flow cytometry and phytoplankton.* Cytometry, 1989. **10**(5): p. 511-521.
123. Muehlbauer, P.A. and M.J. Schuler, *Detection of numerical chromosomal aberrations by flow cytometry: A novel process for identifying aneugenic agents.* Mutation Research/Genetic Toxicology and Environmental Mutagenesis, 2005. **585**(1-2): p. 156-169.
124. Porter, J., et al., *Go with the flow - use of flow cytometry in environmental microbiology.* FEMS Microbiology Ecology, 1997. **24**(2): p. 93-101.
125. Veal, D.A., et al., *Fluorescence staining and flow cytometry for monitoring microbial cells.* Journal of Immunological Methods, 2000. **243**(1-2): p. 191-210.

126. Comas-Riu, J. and N. Rius, *Flow cytometry applications in the food industry*. J. Ind. Microbiol. Biotechnol., 2009. **36**(8): p. 999-1011.
127. Vollmer, T., et al., *Bacterial screening by flow cytometry offers potential for extension of platelet storage: results of 14 months of active surveillance*. Transfus. Med., 2011. **21**(3): p. 175-182.
128. Hammes, F., et al., *Flow-cytometric total bacterial cell counts as a descriptive microbiological parameter for drinking water treatment processes*. Water Research, 2008. **42**(1-2): p. 269-277.
129. Cheriyan, V., C. Thomas, and P. Balaram, *Augmentation of T-cell immune responses and signal transduction proteins in oral cancer patients: potential for IL-2-mediated immunotherapy*. Journal of Cancer Research and Clinical Oncology, 2011: p. 1-10.
130. Jonitz, A., et al., *Differentiation capacity of human chondrocytes Embedded in alginate matrix*. Connect Tissue Res, 2011.
131. DeLong, E.F., G.S. Wickham, and N.R. Pace, *Phylogenetic stains: Ribosomal RNA-based probes for the identification of single cells*. Science, 1989. **243**(4896): p. 1360-1363.
132. Mailänder, V. and K. Landfester, *Interaction of nanoparticles with cells*. Biomacromolecules, 2009. **10** (9): p. 2379–2400
133. Gratton, S.E.A., et al., *The effect of particle design on cellular internalization pathways*. Proc. Natl. Acad. Sci. U. S. A., 2008. **105**(33): p. 11613-11618.
134. Zucker, R.M., et al., *Detection of TiO₂ nanoparticles in cells by flow cytometry*. Cytometry Part A, 2010. **77A**(7): p. 677-685.
135. Schmid, I., C.H. Uittenbogaart, and J.V. Giorgi, *Sensitive method for measuring apoptosis and cell-surface phenotype in human thymocytes by flow-cytometry*. Cytometry, 1994. **15**(1): p. 12-20.
136. McCutcheon, M.J. and R.G. Miller, *Fluorescence intensity resolution in flow systems*. J Histochem Cytochem, 1979. **27**(1): p. 246-9.
137. Sem'yanov, K. and Valeri P Maltsev, *Analysis of sub-micron spherical particles using scanning flow cytometry*. Particle & Particle Systems Characterization, 2000. **17**(5-6): p. 225-229.
138. Hirschfeld, T., M. Block, and W. Mueller, *Virometer: an optical instrument for visual observation, measurement and classification of free viruses*. J. Histochem. Cytochem., 1977. **25**(7): p. 719-723.
139. Hercher, M., W. Mueller, and H. Shapiro, *Detection and discrimination of individual viruses by flow cytometry*. J. Histochem. Cytochem., 1979. **27**(1): p. 350-352.
140. Takeda, K. and et al., *Simultaneous measurement of size and refractive index of a fine particle in flowing liquid*. Measurement Science and Technology, 1992. **3**(1): p. 27.
141. Chernyshev, A.V., et al., *Measurement of scattering properties of individual particles with a scanning flow cytometer*. Appl Opt, 1995. **34**(27): p. 6301-5.
142. Fiorani, L., et al., *Scanning flow cytometer modified to distinguish phytoplankton cells from their effective size, effective refractive index, depolarization, and fluorescence*. Appl. Opt., 2008. **47**(24): p. 4405-4412.
143. Maltsev, V.P., et al., *Absolute real-time measurement of particle size distribution with the flying light-scattering indicatrix method*. Appl. Opt., 1996. **35**(18): p. 3275-3280.
144. Shapiro, H.M., *Practical flow cytometry*. 2003: John Wiley & Sons, Inc.
145. Holzapfel, V., et al., *Preparation of fluorescent carboxyl and amino-functionalized polystyrene particles by miniemulsion polymerization as markers for cells*. Macromolecular Chemistry and Physics, 2005. **206**(24): p. 2440-2449.
146. Walther, P. and A. Ziegler, *Freeze substitution of high-pressure frozen samples: The visibility of biological membranes is improved when the substitution medium contains water*. J. Microsc.-Oxf., 2002. **208**: p. 3-10.

147. DSMZ. German collection of microorganisms and cell cultures; Available from: <http://www.dsmz.de>. (last accessed: February 2012)
148. Rejman, J., et al., *Size-dependent internalization of particles via the pathways of clathrin- and caveolae-mediated endocytosis*. *Biochem. J.*, 2004. **377**(1): p. 159-169.
149. Chen, Z.J., et al., *Self-assembled pi-stacks of functional dyes in solution: structural and thermodynamic features*. *Chem. Soc. Rev.*, 2009. **38**(2): p. 564-584.
150. Gessner, A., Lieske, A., Paulke, Bernd-R., Müller, Rainer H. , *Functional groups on polystyrene model nanoparticles: Influence on protein adsorption*. *Journal of Biomedical Materials Research Part A*, 2003. **65A**(3): p. 319-326.
151. Chung, Y.-I., et al., *The effect of surface functionalization of PLGA nanoparticles by heparin- or chitosan-conjugated Pluronic on tumor targeting*. *Journal of Controlled Release*, 2010. **143**(3): p. 374-382.
152. Hwang, D.W., et al., *A nucleolin-targeted multimodal nanoparticle imaging probe for tracking cancer cells using an aptamer*. *Journal of Nuclear Medicine*, 2010. **51**(1): p. 98-105.
153. Park, J.H., et al., *Raman detection of localized transferrin-coated gold nanoparticles inside a single cell*. *Anal. Bioanal. Chem.*, 2011. **401**(5): p. 1631-1639.
154. Abdelrahman, A.I., et al., *Surface functionalization methods to enhance bioconjugation in metal-labeled polystyrene particles*. *Macromolecules*, 2011. **44**(12): p. 4801-4813.
155. Yan, Y., et al., *Preparation of carboxyl magnetic fluid and surface modification by bovine serum albumin*. *Sci. Technol. Rev.*, 2010. **28**(19): p. 73-7676.
156. Acharya, S., F. Dilnawaz, and S.K. Sahoo, *Targeted epidermal growth factor receptor nanoparticle bioconjugates for breast cancer therapy*. *Biomaterials*, 2009. **30**(29): p. 5737-5750.
157. Zupke, O., et al., *Preservation of dendritic cell function upon labeling with amino functionalized polymeric nanoparticles*. *Biomaterials*, 2010. **31**(27): p. 7086-7095.
158. Thurn, K.T., et al., *Endocytosis of titanium dioxide nanoparticles in prostate cancer PC-3M cells*. *Nanomedicine*, 2011. **7**(2): p. 123-30.
159. Zhu, S., et al., *Progress in the development of techniques based on light scattering for single nanoparticle detection*. *Science China Chemistry*, 2011. **54**(8): p. 1244-1253.
160. Hoecherl, A., et al., *Competitive cellular uptake of nanoparticles made from polystyrene, poly(methyl methacrylate) and polylactide*. *Macromol. Biosci.*, 2012. **12**(4): p. 454-464.
161. Aggarwal, P., et al., *Nanoparticle interaction with plasma proteins as it relates to particle biodistribution, biocompatibility and therapeutic efficacy*. *Advanced Drug Delivery Reviews*, 2009. **61**(6): p. 428-437.
162. Lorenz, M.R., et al., *Synthesis of fluorescent polyisoprene nanoparticles and their uptake into various cells*. *Macromolecular Bioscience*, 2008. **8**(8): p. 711-727.
163. Lesniak, A., et al., *Serum heat inactivation affects protein corona composition and nanoparticle uptake*. *Biomaterials*, 2010. **31**(36): p. 9511-9518.
164. Huotari, J. and A. Helenius, *Endosome maturation*. *EMBO J*, 2011. **30**(17): p. 3481-3500.
165. Zhao, F., et al., *Cellular uptake, intracellular trafficking, and cytotoxicity of nanomaterials*. *Small*, 2011. **7**(10): p. 1322-1337.
166. Charie, L.A. and J. Quintana (2007) *Fundamentals of standardization for flow cytometric measurements.*, by Cellular Analysis Business Center, Beckman Coulter, Inc.
167. Rezenom, Y.H., et al., *Separation and detection of individual submicron particles by capillary electrophoresis with laser-light-scattering detection*. *Analyst*, 2007. **132**(12): p. 1215-22.

168. Kalb Jr, V.F. and R.W. Bernlohr, *A new spectrophotometric assay for protein in cell extracts*. Analytical Biochemistry, 1977. **82**(2): p. 362-371.
169. Life TechnologiesTM, <https://www.lifetechnologies.com> (accessed last: February 2012)
170. Pizarro, G. and E. Ríos, *How source content determines Intracellular Ca²⁺ release kinetics. Simultaneous measurement of [Ca²⁺] transients and [H⁺] displacement in skeletal muscle*. The Journal of General Physiology, 2004. **124**(3): p. 239-258.
171. Posati, T., et al., *Selective internalization of ZnAl-HTlc nanoparticles in normal and tumor cells. A study of their potential use in cellular delivery*. Applied Clay Science, 2012. **55**(0): p. 62-69.
172. Benson, R.C., et al., *Cellular autofluorescence - is it due to flavins?* Journal of Histochemistry & Cytochemistry, 1979. **27**(1): p. 44-48.

7 Appendix

i. List of Abbreviations

7AAD	7-Aminoactinomycin D
AEMH	Amino ethylmethyl methacrylate
...BP±...	Band pass filter, <i>e.g.</i> 527BP±10 [nm] range
BODIPY, BP	4,4-Difluoro-4-bora-3a,4a-diaza-s-indacene
CD	Cluster of differentiation
Ch	Detection channel
CLA	Clathrin
cLSM	Confocal laser scanning microscope
cLSMy	Confocal laser scanning microscopy
CM	Cytoplasmic membrane
CMC	Critical micelle concentration
CMO	CellMask™ Orange
CP	Cytoplasm
CT	Cytoskeleton
CV	Coefficient of variation
CVA	Caveolin
DDS	Drug-delivery system
DiD	Membrane staining dye (Invitrogen)
DLS	Dynamic light scattering
DMEM	Dulbecco's Modified Eagle Medium
DMEM10%	Prepared incubation medium, DMEM supplemented 10%-vol. fetal calf serum, 100 U penicillin, and 100 µg·ml ⁻¹ streptomycin
DSC	Differential scanning calorimetry
ECM	Extracellular matrix
E _{rec}	Receptor-mediated endocytosis
$f_{1(Pol)}$	Fluorescence normalization factor (derived from the fluorescence of dispersed NPs)
$f_{2(Pol)}$	Fluorescence normalization factor (derived from the dye content of the NPs)
FA	Formaldehyde
FACS	Fluorescence activated cell sorter (abbreviation is © Becton Dickinson)
FC	Flow cytometer
FCS	Fetal calf serum
FCy	Flow cytometry
filter _{0.2µm}	Filter with 0.2 µm pore size (Millipore)
filter _{15nm}	High throughput filter with 15 nm pore size (Planova)
FISH	Fluorescence in situ hybridization
FL	Fluorescence channel in a flow cytometer
Fl _{1(Pol)}	Normalized fluorescence of particle-loaded cells, utilizing factor $f_{1(Pol)}$
Fl _{2(Pol)}	Normalized fluorescence of particle-loaded cells, utilizing factor $f_{2(Pol)}$
Fl _{Pol}	Fluorescence of particle-loaded cells, not normalized
FSC	Forward scatter

GPC	Gel permeation chromatography
HD	Hexadecane
ITC	Isothermal titration calorimetry
LR, LRs	Lipid raft, ~s
Lut-50	Lutensol AT50, non-ionic surfactant with one C ₁₆ or C ₁₈ and 50 PEO units
MFI	Mean fluorescence intensity value, as measured in the flow cytometer
MFI _{+NP}	MFI of cells containing nanoparticles
MFI _{-NP}	MFI of particle-free cells (cell control sample)
ΔMFI	Increase of the cells' MFI due the internalization of fluorescent nanoparticles, MFI _{+NP}
MFI _{noise}	MFI of the background <i>i.e.</i> of the respective control sample
MFI _{NP-raw}	MFI of a single nanoparticle (before subtraction of the background MFI _{noise})
MFI _{NP}	Final MFI of a single NP (after subtraction of the background), MFI _{NP-raw} – MFI _{noise}
MFI _{Pol}	Final MFI of particle-loaded cells (after subtraction of the background <i>i.e.</i> of the MFI
mRNA	Messenger ribonucleic acid
N _{0(NP)}	Number of NPs per μl of latex, calculated value
NP, NPs	Nanoparticle, ~s
NT	Nanotechnology
(o/w)	Oil-in-water
PBS	Phosphate buffered saline
PDI	Polydispersity index
PEG	Poly ethylene glycol
PLLA	Poly(L-lactide)
PMI	N-(2,6-Diisopropylphenyl)-perylene-3,4-dicarbonacidimide
PMMA	Poly(methyl methacrylate)
PMT	Photomultiplier
PS	Polystyrene
SDS	Sodium dodecylsulfate
SO	Smart Object
SPM	Single particle measurement (in flow cytometry)
SSC	Sideward scatter
STED	Stimulated emission depletion
Surfactant	Surface active agent
TEM	Transmission electron microscope
T _g	Glass transition temperature
T _{melt}	Melting point
WGA ₆₈₀	Alexa680-coupled wheat germ agglutinin
(w/o)	Water-in-oil
ZP	Zeta potential
ΔMFI	Difference in fluorescence, MFI _{+NP} - MFI _{-NP}
GPC	Gel permeation chromatography
HD	Hexadecane
ITC	Isothermal titration calorimetry
LR, LRs	Lipid raft, ~s
Lut-50	Lutensol AT50, non-ionic surfactant with one C ₁₆ or C ₁₈ and 50 PEO units
MFI	Mean fluorescence intensity value, as measured in the flow cytometer
MFI _{+NP}	MFI of cells containing nanoparticles
MFI _{-NP}	MFI of particle-free cells (cell control sample)
ΔMFI	Increase of the cells' MFI due the internalization of fluorescent NPs, MFI _{+NP} - MFI _{-NP}
MFI _{noise}	MFI of the background <i>i.e.</i> of the respective control sample

ii. Supplementary Data

Table A. Volumetric counting of the particles PMMA-BP1-2, PS-SDS-7 and PS-Lut-1. The experimental data $count_{vol}$ and $count_{time}$ are compared with the theoretical count value which was calculated via the size distribution (N_{calc}).

Particle	dilution of the original latex [$\cdot 10^6$]	N_{calc}	$count_{vol}$	$count_{vol}$	$count_{time}$	$count_{time}$
		[per 1 μ l] calculated via size distribution	[per 1 μ l] FC, via true volumetric counting	[%] = percentage of N_{calc}	[per 1 μ l] FC, via measurement time & speed	[%] = percentage of N_{calc}
PMMA-BP1-2	1:60	727	721	99%		
	1:40	1090			618	57%
	1:133	675			227	69%
	1:133	675			682	101%
	1:40	1442			1498	96%
	1:50	1796			1750	97%
	1:40	2246	1042	46%	895	40%
	1:50	1796	1408	78%	1201	67%
	1:50	1796			1702	95%
	1:40	2246			1666	74%
	1:50	1796				
	ca. 1:30	3062	1057	35%		
ca. 1:60	1531	715	47%			
ca. 1:60	1531	660	43%			
PS-SDS-7	1:133	414			423	100%
	1:40	962			1378	70%
	1:50	1102			1050	95%
	1:50	1102			794	70%
	1:30	1836	1029	56%	906	49%
	1:60		596	65%	539	59%
PS-Lut-1	1:133	385			208	54%
	1:133	385			265	69%
	1:40	1048			1282	82%
	1:80	524			640	85%
	1:50	1024			669	65%
	1:50	1024			318	31%
	1:50	1024			550	44%
	1:10	5120			2208	43%

Table B. Data table of the cLSM counting of PMMA-BP1-2 particles in HeLa cells at a concentration of 500 μg of polymer per ml.

Sample	Cell Nr. #	[Particles per cell]				
		Single FC samples / single cells in cLSM	Total average of samples / of cells	St.Dev. $\pm\%$	St.Dev. $\pm\text{NPs}$	
FC	>5000 cells	97, 115, 121	111	11%	12	
cLSM	Stack 19, Cell 1	1	275	246	35%	86
	Stack 19, Cell 2	2	244			
	Stack 19, Cell 3	3	275			
	Stack 19, Cell 4	4	291			
	Stack 19, Cell 5	5	249			
	Stack 16, Cell 1	6	407			
	Stack 12, Cell 1	7	99			
	Stack 23, Cell 4	8	231			
	Stack 23, Cell 1	9	125			
	Stack 24, Cell 3	10	264			

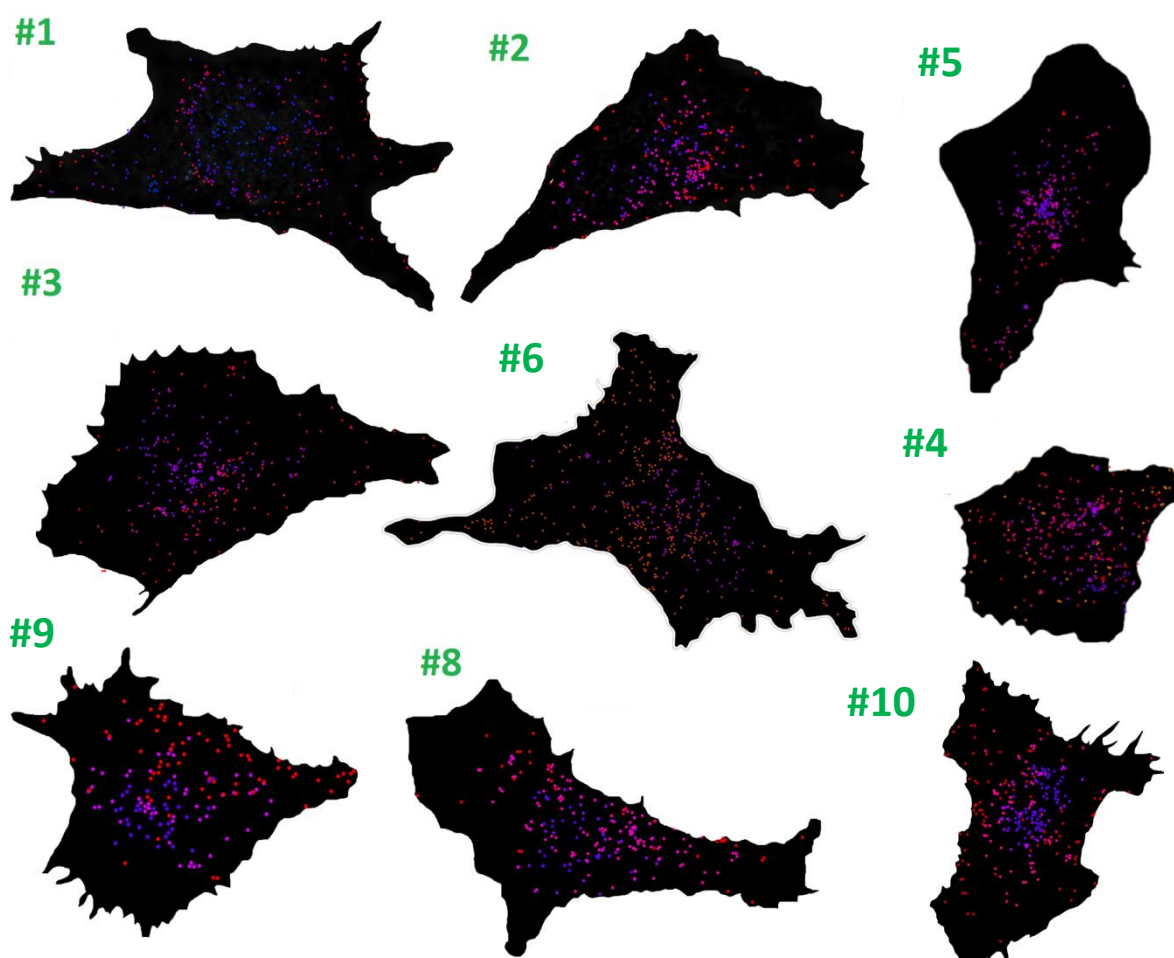


Figure A. Image data (excl. cell #7) of the cLSM counting of PMMA-BP1-2 particles in HeLa cells after incubation for 2 h at a concentration of 500 μg polymer per ml.

Table C. Data table of the cLSM counting of PMMA-BP1-2 particles in HeLa cells incubated at a concentration of 300 μg of polymer per ml for 2 h.

		[Particles per cell]				
	Sample	Cell Nr. #	Single FC samples / single cells in cLSM	Total average of samples / cells	St.Dev. $\pm\%$	St.Dev. $\pm\text{NPs}$
FC *	>2500 cells		35,29,32	29	20%	6
cLSM **	Day1, #3, S23	1	51	65	56%	36
	Day1, #3, S27	2	37			
	Day2, #2, S05	3	60			
	Day2, #2, S07	4	33			
	Day2, #2, S09	5	30			
	Day2, #2, S13	6	126			
	Day2, #2, S15	7	113			
	Day2, #2, S17	8	67			

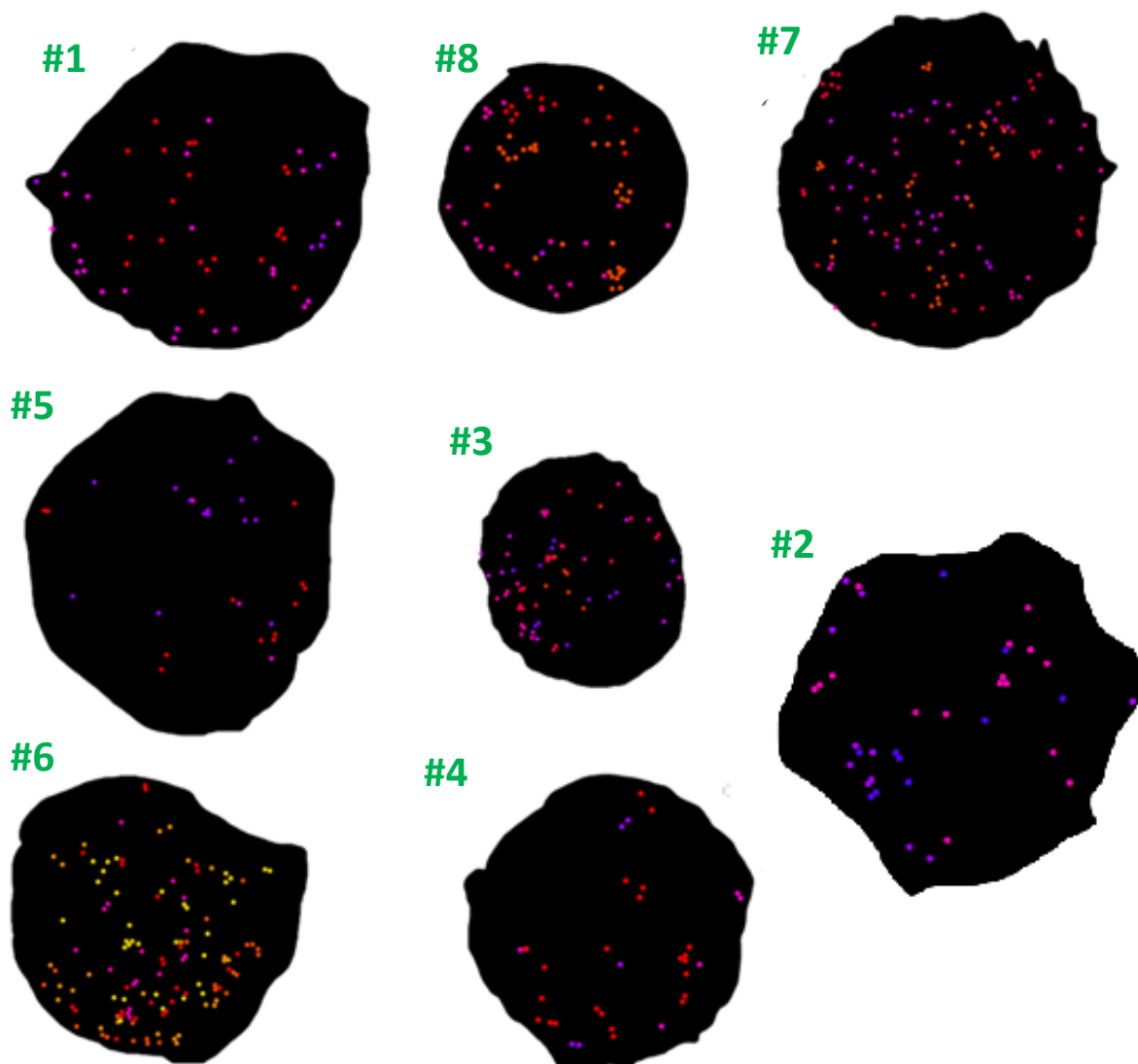


Figure B. Image data of the cLSM counting of PMMA-BP1-2 particles in HeLa cells incubated at a concentration of 300 μg polymer per ml for 2 h.

iii. Acknowledgments

First and foremost, I am indebted to my supervisor, for giving me the opportunity to work on this fascinating topic in her group and I thank her for her enthusiasm and the excellent scientific support. Moreover I am grateful to my other supervisors for the helpful discussions, for the guidance and encouragement.

But this project would also have been impossible if not for all the colleagues and friends who have rescued me from peril many times. In particular, I am addressing my fellow office colleagues, the participants in the coffee and lunch breaks and most of all the cell biology team. I wish to thank all members of the group; I enjoyed the good atmosphere and the great working environment.

I also thank the *Deutsche Forschungsgesellschaft* (DFG), Schwerpunktprojekt SPP1313, for funding and for the opportunity to participate in related workshops.

Furthermore I am grateful to have been a fellow in the Max-Planck Graduate Center (MPGC) which offered not only funding but also numerous additional opportunities. My particular thank goes to the MPGC officials, for the excellent job they did. I thank the other grantees for the good times during free-time activities and the fruitful working atmosphere during seminars and workshops.

I am most especially grateful to my dearest friends, to my siblings, and to my parents, who shared the good and the less good moments. You never ceased to support me.

iv. Statutory Declaration

I hereby declare that I wrote the submitted dissertation without any unauthorized external assistance and used only sources acknowledged in the work. All textual passages which are appropriated verbatim or paraphrased from published and unpublished texts as well as all information obtained from oral sources are duly indicated and listed in accordance with bibliographical rules. In carrying out this research, I complied with the rules of standard scientific practice as formulated in the statutes of Johannes Gutenberg-University Mainz to insure standard scientific practice.

Mainz 23.02.2012



Anita Höcherl

v. Curriculum Vitae

Personal information

Name Anita Höcherl
Place of birth Landsberg am Lech

Education

08/2008 - 11/2011 Doctorate studies at the Max-Planck-Institute for Polymer Research with the Johannes-Gutenberg University, Mainz
Scholarship holder of the Max-Planck-Graduate Center with the Johannes-Gutenberg University (MPGC), Mainz
Degree: Dr. rer. nat.

10/2003 - 05/2008 Academic studies at the University of Ulm
Degree: Master of Science (Biochemistry)

09/1990 - 06/2003 School education, degree: Allgemeine Hochschulreife

vi. Publications

- Articles**
- 2012 ‘Measuring Single Nanoparticles in Flow Cytometry Enables Absolute Quantization of the Intracellular Particle Number’
A. Höcherl, K. Landfester, M. Mailänder (to be submitted)
- 2011 ‘Competitive Cellular Uptake of Nanoparticles made from Polystyrene, Poly(methyl methacrylate) and Polylactide’
A. Höcherl, M. Dass, K. Landfester, V. Mailänder, A. Musyanovych
Macromol. Biosc. (2012.), 12(4), p.454-464
- 2008 ‘Synthesis of Fluorescent Polyisoprene Nanoparticles and their Uptake into Various Cells’, *M. R. Lorenz, M.-V. Kohnle, M. Dass, P. Walther, Paul, A. Höcherl, U. Ziener, K. Landfester, V. Mailänder*
Macromol. Biosc. (2008), 8(8), p.712-727
- Talks**
- 2010 ‘Studying the Cellular Uptake of Nanoparticles’
Seminary of the ‘Nanobiotechnology Group’ AK Sönnichsen,
Institute of Physical Chemistry, University of Mainz
- Posters**
- 2011 ‘Submicron Particles in Non-scanning Flow Cytometry – From single Particle Measurement to Absolute Particle Counting in Cells’,
A. Höcherl, V. Mailänder, K. Landfester
Polymers in Medicine and Biology 2011, Santa Rosa, US
- 2010 ‘Competitive Cellular Uptake of Nanoparticles made from Polystyrene, Poly(methyl methacrylate) and Polylactide’,
A. Höcherl, A. Musyanovych, V. Mailänder, K. Landfester
BioNanoMed 2010, Krems, Austria
- 2010 ‘Mechanisms of Endocytosis in MSC and HeLa Cells’,
A. Höcherl, X. Jiang, J. Schmitz-Wienke, C. Röcker, A. Musyanovych, K. Landfester, G. U. Nienhaus, V. Mailänder
DFG Workshop ‘Zell-Internalisierung, Nanopartikeldesign und Oberflächenfunktionalisierung’, Jena 2010
- 2009 ‘Functional Polymeric Nanoparticles for Biomedical Application’,
A. Ziegler, A. Höcherl, S. Lerch, H. Keller, V. Mailänder, A. Musyanovych, K. Landfester
Frontiers in Polymer Science, Mainz 2009
- 2008 ‘Effect of Polymer Nature on the Cell-Particle Interaction’,
A. Höcherl, V. Mailänder, K. Landfester, A. Musyanovych
DFG Workshop ‘Zellbiologie & Biofunktionen’, Hamburg 2008